MATHEMATICAL MODELING OF DISBONDED COATING AND CATHODIC DELAMINATION SYSTEMS

By

KERRY N. ALLAHAR

A DISSERTATION PRESENTED TO THE GRADUATE SCHOOL
OF THE UNIVERSITY OF FLORIDA IN PARTIAL FULFILLMENT
OF THE REQUIREMENTS FOR THE DEGREE OF
DOCTOR OF PHILOSOPHY

UNIVERSITY OF FLORIDA

2003

ACKNOWLEDGMENTS

I would like to sincerely thank my advisor, Professor Mark E. Orazem, for his technical guidance throughout my graduate research. I will always appreciate his patience during the events that transpired while I pursued the doctoral degree. I would also like to thank Dr. Narisi Sridhar and Dr. Kevin Ogle for their expertise in the electrochemical systems studied. I would like to express my appreciation to the members of my committee, Professor Anthony Ladd, Professor Raj Rajagopalan, Professor Chen-Chi Hsu, and Dr. Jason Butler, for their contribution in my proposal presentation and dissertation defense.

I would like to thank the members of the electrochemical engineering group, Madhav Durba, Mike Membrino, Chen Chen Qui, Pavan Shukla, Doug Reimer, and Nellian Perez-Garcia. I was fortunate to be a member of this group.

I wish to acknowledge the financial supporters of my research at the University of Florida. The work on disbonded coatings was supported by the Gas Research Institute through grant 5097-260-378. The work on cathodic delamination was supported by IRSID, Arcelor Innovation of France.

I would like to express my heartfelt thanks and gratitude to my wife, my parents, and my brothers who have always encouraged and facilitated my academic pursuits. I would like to pay tribute to my deceased Grandmother for giving me the opportunity to live and pursue graduate study in the United States of America.

TABLE OF CONTENTS

LIST OF TABLES

LIST OF FIGURES

NOTATION

Roman

A_c cross-sectional surface area of control volume , cm^2

A_s surface area available for electrochemical reactions in a control volume, cm^2

a coating thiskness, cm

a_{del} exponent used in power law rate for the propagation of the front in a cathodic delamination system, dimensionless

a_j parameter used in design equation for the solution potential drop associated with a disbonded coating system where $j = 1, .., 4$

$b_{\alpha,j}$ fitting parameter for blocking factor used in CADEM where $j = 1, ..., 8$, dimensionless

$b_{\epsilon,j}$ fitting parameter for porosity where $j = 1, ..., 7$, dimensionless

$b_{\omega,j}$ fitting parameter for surface coverage used in CADEM where $j = 1, ..., 7$, dimensionless

$b_{\zeta,j}$ fitting parameter for poisoning parameter used in CADEM $j = 1, ..., 7$, dimensionless

$\boldsymbol{C}_K$ global solution vector for system corresponding to K

$\boldsymbol{C}_N^{(n)}$ global solution vector for the cathodic delamination system at time-step n

c_i concentration of species i, mol/cm^3

$c_{i,\infty}$ bulk concentration of species i, mol/cm^3

D_i diffusion coefficient of species i, cm^2/s

D_i^* diffusion coefficient of species i in porous medium, cm^{2}s^{-1}

E_k effective equilibrium potential for reaction k

F Faraday's constant, 96487 C/equiv

$\boldsymbol{F}_N$ global function vector for the cathodic delamination system

g gap, cm

$\boldsymbol{i}$ current density, A/(cm^2)

$\boldsymbol{i}_\mathrm{d}$ diffusion current density, A/(cm^2)

i_e net electrochemical current density at node in a control volume, A/cm^2

i_k current density corresponding to reaction k, A/cm^2

$\boldsymbol{i}_\mathrm{m}$ migration current density, A/(cm^2)

$i_{\mathrm{lim,O_2}}$ mass-transfer-limited current density for oxygen reduction reaction, A/cm^2

$i_{\mathrm{lim,O_2}}^{\mathrm{coat}}$ mass-transfer-limited current density for oxygen reduction at metal-coating interface, A/cm^2

$i_{\mathrm{o,k}}^{\mathrm{coat}}$ exchange current density corresponding to reaction k at metal-coating interface, A/cm^2

i_o exchange current density, A/cm^2

i_s current density entering a control volume, A/cm^2

$\boldsymbol{J}_N$ global jacobian matrix for the cathodic delamination system

$\boldsymbol{K}_K$ global coefficient matrix for system corresponding to K

k_f, k_b forward and backward rate constant for first order reaction

k_{del} rate constant used in power law for the propagation of the front in a cathodic delamination system, cm/s

$\boldsymbol{N}_i$ flux of species i, mol/(cm$^2 \cdot$ s)

n number of electrons transferred in electrochemical reaction

Q quasipotential variable, A/cm

r overall rate of reversible reaction

r_d disbondment length, cm

r_f, r_b forward, and backward rate of reversible reaction

r_h holiday radius, cm

R universal gas constant, 8.314 J/(mol $\cdot$ K)

R_i net rate of production of species i by homogeneous reactions, mol/(cm$^2 \cdot$ s)

$\boldsymbol{R}_K$ global load vector for system corresponding to K

T absolute temperature, K

t time, s

t_{del} elapsed time used in power law rate for the propagation of the front in a cathodic delamination system, s

u_i mobility of species i, cm$^2 \cdot$ mol/(J $\cdot$ s)

V potential at metal-electrolyte interface $\Psi - \Phi$, V

V^o equilibrium potential for a given reaction, V

V_{corr} corrosion potential, V

$\boldsymbol{v}$ local velocity of electrolyte, m/s

x_{del} point of inflection of front region in cathodic delamination system, cm

z_i charge number of species i, equiv/mol

Greek

α_a, α_c anodic and cathodic transfer coefficients

β symmetry factor used in activated complex theory

β_k Tafel slope corresponding to reaction k, V/decade

ϵ porosity, dimensionless

ϵ_{c} coating porosity, dimensionless

ϵ_{m} gel-medium porosity, dimensionless

ε permittivitty of medium, F/cm

ζ poisoning parameter for zinc dissolution at metal-coating interface, dimensionless

η_s surface overpotential, V

κ conductivity of electrolyte, $\Omega^{-1}\text{cm}^{-1}$

$\xi_{o,K}$ convergence criterion used in system corresponding to K, dimensionless

$\lambda_{i,fro}$ parameter for nonlinear change of c_i in front region, dimensionless

$\lambda_{i,sem}$ parameter for nonlinear change of c_i in semi-intact region, dimensionless

Φ solution potential, V

ϕ dimensionless solution potential

χ_i gradient of c_i in delaminated region, mol/cm^4

Ψ metal potential, V

ω surface area parameter for electrochemical reaction at metal-coating interface, dimensionless

Superscripts

coat metal-coating interface

o assumed value

Subscripts

C crevice system

D disbonded coating system

Fe iron dissolution

HA holiday-adjacent system

H_2 hydrogen evolution

i species index

j computational node index used in DISCOM

m, k node index used in 2-D domain

N cathodic delamination system

O_2 oxygen reduction

m node index used in CADEM

m_{max} external boundary node index used in CADEM

W system for initial solution potential distribution in CADEM

Zn zinc dissolution

Special symbols

$\triangle r$ grid spacing in cylindrical coordinate r-direction, cm

$\triangle x$ grid spacing in the carthesian coordinate x direction, cm

$\triangle y$ grid spacing in the carthesian coordiant y direction, cm

$\triangle z$ grid spacing in the cylindrical coordinate z-direction, cm

Abstract of Dissertation Presented to the Graduate School
of the University of Florida in Partial Fulfillment of the
Requirements for the Degree of Doctor of Philosophy

MATHEMATICAL MODELING OF DISBONDED COATING
AND CATHODIC DELAMINATION SYSTEMS

By

Kerry N. Allahar

December 2003

Chair: Mark E. Orazem
Major Department: Chemical Engineering

Cathodic protection is used in oil and gas industries to mitigate corrosion associated with defective coatings on coated pipelines. A disbonded coating is a defect that includes a coating break exposing a bare metal surface, the holiday, with the surrounding coating totally disbonded from the metal. A mathematical model of the steady-state conditions in a disbonded coating system is presented in this dissertation. The model explicitly accounted for electroneutrality and the transport of species by diffusion and migration. The electrochemical reactions considered were corrosion, oxygen reduction, and hydrogen evolution. The influences of applied potential, bulk electrolyte resistivity, and geometric parameters on the system were determined. The model presented is more sophisticated than previous steady-state models for disbonded coating systems presented in literature.

A cathodic delamination system comprises a defect where the coating surrounding a holiday is partially disbonded. This system involves the propagation of a front along the metal-coating interface. The spatial distributions of potential at the buried metal-coating interface for experimental cathodic delamination systems have been reported. These results have been interpreted in literature in terms of a qualitative mechanism for cathodic delamination. A mathematical model is presented in this dissertation that simulated the propagation of the front during cathodic delamination at a zinc-coating interface. The key to this model involved the hypotheses that the porosity and the polarization kinetics at the metal-coating interface were pH dependent. The simulations provided qualitative agreement with published experimental results. This model is the first mathematical model proposed for the propagation of the front during cathodic delamination and provides a foundation for more sophisticated models.

CHAPTER 1
INTRODUCTION

The total annual direct cost of corrosion in the United States was estimated to be 276 billion dollars in 1998, accounting for 3.1 percent of the gross domestic product.[1] This estimate was consistent with the estimation that the total annual direct cost of corrosion generally ranges from 1 to 5 percent of a country's gross domestic product.[1] The indirect cost of corrosion was conservatively estimated to be equal to the direct cost.[1] The high cost of corrosion in the U.S. is a major concern to the industrial sector. Corrosion control methods are used to mitigate the corrosion of metals and reduce the high direct and indirect costs of corrosion. Corrosion control methods in the U.S. for the year 1998 accounted for approximately 120 out of the total 276 billion dollar cost of direct corrosion. These methods and the average cost are given in Table 1.1. The most common method of protection against corrosion employs organic coatings, which involves the isolation of the metal from its environment using a physical barrier.

Organic coatings are used in pipeline-related industries to protect pipe sur-

Table 1.1: Summary of annual costs of corrosion control methods in the United States for the year 1998.[1]

Method	Average Cost billion dollars	Average Cost percent
Organic Coatings	107.2	89.2
Metallic Coatings	1.4	1.16
Metals and Alloys	7.7	6.4
Corrosion Inhibitors	1.1	0.92
Polymers	1.8	1.5
Anodic and Cathodic Protection	0.98	0.82
Total	120.18	100

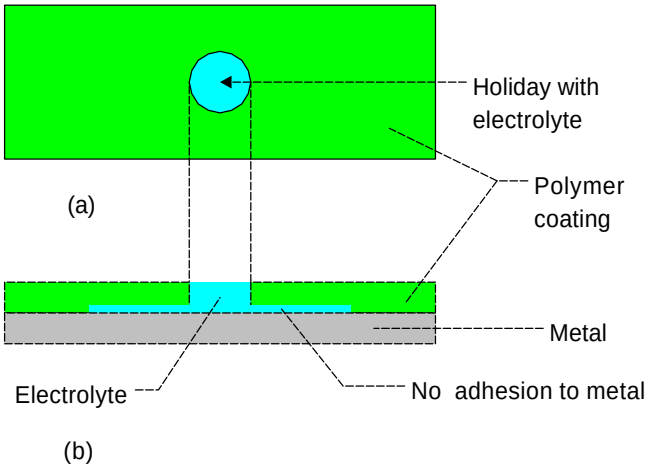

Figure 1-1: Schematic diagram of a disbonded coating system. (a) top view and (b) cross-sectional view.

faces. External corrosion at the pipe surface can still persist at the inevitable breaks in the coating exposing bare metal. Also, there can be corrosion at the metal-coating interface. Cathodic protection is used to mitigate the corrosion at exposed surfaces and at the metal-coating interface.

An electrochemical system that is of interest for metals covered by organic coatings involves an exposed metal surface and the surrounding coating. The exposed metal surface is referred to in literature as a holiday or defect. The surrounding coating is referred to as a disbonded coating when all adhesion to the metal surface is lost and a delaminated coating when there is partial adhesion to the metal surface (see Figures 1-1 and 1-2). The holiday-disbonded coating system and the holiday-delaminated coating system are referred to as the disbonded coating system and cathodic delamination system, respectively, in this work.

The motivation for the research presented was to gain, through development of appropriate mathematical models, an understanding of the phenomena that contribute to the disbonded coating and cathodic delamination systems. Two mathematical models, DISCOM and CADEM, are presented. DISCOM calculated the steady-state conditions in a disbonded coating system and CADEM simulated the propagation of a front along a zinc-coating interface during cathodic delamina-

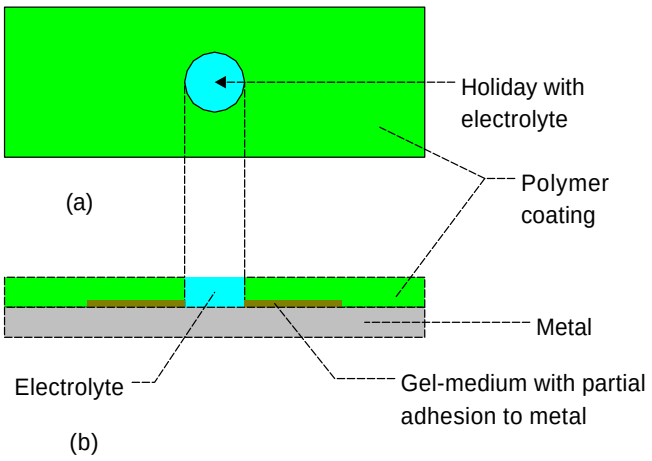

Figure 1-2: Schematic diagram of a cathodic delamination system. (a) top view and (b) cross-sectional view.

tion. The fundamental electrochemical concepts relevant to the systems of interest are presented in Chapter 2. The literature associated with mathematical modeling of disbonded coating systems is presented briefly in Chapter 3.

Two mathematical models for the steady-state conditions in disbonded coating systems have been presented in literature to date.[2–5] A model presented by Chin and Sabde considered oxygen reduction and assumed that the contribution by hydrogen evolution was negligible.[2,3] The model[2,3] also used the assumption that the diffusion coefficients of all species were equated to 10^{-5} cm^2s^{-1}. A model presented by Song *et al.* did not consider the holiday explicitly and used the assumption that the resistivity of the electrolyte in the disbondment was uniform and as such concentration gradients were negligible.[4,5] DISCOM is more sophisticated than the two other models for disbonded coating systems presented in literature. The development of DISCOM is presented in Chapter 4. The model accounted for the simultaneous treatment of electroneutrality and transport of species by diffusion and migration. The electrochemical reactions considered were corrosion, oxygen reduction, and hydrogen evolution. The influences of applied potential, bulk resistivity, gap size, and disbondment length on the system are presented in Chapter 5.

In addition to providing insight into the processes contributing to the disbonded-coating system, simulations can assist in determining the cathodic protection requirements for pipelines with disbonded coatings. A model is presented that accommodated disbonded coating systems with disbondment lengths greater than 3 cm. The results of this model were used to develop a design equation for the solution potential associated with a disbonded coating system under cathodic protection. The influence of species transport by migration and diffusion, electroneutrality, and the polarization kinetics of the metal surface was imbedded in the constants associated with the design equation. The model, simulations, and design equation are presented in Chapter 6.

The disbonded coating system belongs to a wider class of systems, referred to as occluded systems, that includes pits and crevices. There are numerous mathematical models of pits and crevices presented in literature. In the development of these models, assumptions were used to make the problem tractable. The applicability of several assumptions to the disbonded coating system, and occluded systems in general, is presented in Chapter 7.

A significant challenge involved in the development of DISCOM was the numerical difficulty encountered when homogeneous reactions were included. The quasipotential transformation method reported in literature was shown to accommodate several homogeneous reactions. The theoretical development of this method and the limitation of its applicability to the disbonded coating system are presented in Chapter 8.

Recent progress in the Scanning Kelvin probe experimental technique has made possible the measurement of the spatial-temporal distribution of potential at the buried metal-coating interface during the cathodic delamination of coated iron[6–8] and coated zinc.[9–11] These measurements substantiated a mechanistic model of

cathodic delamination. This mechanistic model is presented in Chapter 9. To date this model has remained qualitative and a research effort was made to develop a mathematical model of the cathodic delamination process. This research effort is presented in Chapters 9, 10, 11, and 12.

There is no mathematical model for the propagation of the front along the metal-coating interface during cathodic delamination presented in literature. CADEM simulated the propagation of the front associated with a cathodic delamination system at a zinc-coating interface. The key to the this model involved the hypotheses that the interfacial porosity and the interfacial polarization kinetics were pH dependent. The development of these hypotheses is presented in Chapter 10, and the model CADEM is presented in Chapter 11. The simulations presented in Chapter 12 provided qualitative agreement with published experimental results. This agreement supported the hypotheses that interfacial porosity and interfacial polarization contributed to the cathodic delamination system. The hypothesis that the interfacial porosity was pH dependent represented a novel approach at implicitly accounting for the bond breakage involved during cathodic delamination. This model is the first mathematical model for the propagation of the front during cathodic delamination and provides a foundation for more sophisticated models.

The mathematical models DISCOM and CADEM were applied to systems and the simulated results analyzed. The conclusions derived from these results are presented in the chapters where they are deduced and a summary of the conclusions is presented in Chapter 13. Recommendations for future work in modeling disbonded coating and cathodic delamination systems are presented in Chapter 13.

CHAPTER 2
BACKGROUND ELECTROCHEMISTRY

The fundamental electrochemistry relevant to the disbonded coating and cathodic delamination systems is presented in this chapter. A detailed treatment of electrochemistry from a mathematical perspective has been presented by Newman.[12]

2.1 Transport of Species

The conservation of mass restricts the governing equation for the concentration of a specie i in an electrochemical system to[12]

$$\frac{\partial c_i}{\partial t} = -\nabla \cdot \boldsymbol{N}_i + R_i \tag{2-1}$$

where the term on the left-hand-side represents the rate of change of concentration c_i with time t (accumulation) and the terms on the right-hand-side represent the net input due to the flux $\boldsymbol{N}_i$ and the net rate of production by homogeneous reactions R_i, respectively. In dilute electrochemical systems $\boldsymbol{N}_i$ is given by the Nernst-Planck equation[12]

$$\boldsymbol{N}_i = -z_i u_i c_i F \nabla \Phi - D_i \nabla c_i + c_i \boldsymbol{v} \tag{2-2}$$

where Φ is the local solution potential, u_i is the mobility, D_i is the diffusion coefficient, z_i is the charge number, $\boldsymbol{v}$ is the mass average velocity of the electrolyte, and F is Faraday's constant. The terms on the right-hand-side of equation (2-2) represent the contributions by migration, diffusion, and convection to the flux of a species, respectively.

Combination of equations (2-1) and (2-2), under the assumption that the electrolyte is incompressible ($\nabla \cdot \boldsymbol{v} = 0$), yields the governing equation for c_i in an

electrochemical system

$$\frac{\partial c_i}{\partial t} + \boldsymbol{v}_i c_i = z_i u_i F \nabla \cdot (c_i \nabla \Phi) + D_i \nabla^2 c_i + R_i \tag{2-3}$$

The governing equation for c_i is recast as

$$\frac{\partial c_i}{\partial t} = z_i u_i F \nabla \cdot (c_i \nabla \Phi) + D_i \nabla^2 c_i + R_i \tag{2-4}$$

for a stagnant system where convective contributions to the flux of a species are negligible.

Under the assumption of steady-state, mass-conservation restricts the governing equation for c_i to

$$0 = -\nabla \cdot \boldsymbol{N}_i + R_i \tag{2-5}$$

The governing equation for c_i is then given by

$$0 = z_i u_i F \nabla \cdot (c_i \nabla \Phi) + D_i \nabla^2 c_i + R_i \tag{2-6}$$

for a dilute, stagnant, electrochemical system at a steady-state condition.

The Nernst-Einstein equation, given by

$$u_i = \frac{D_i}{RT} \tag{2-7}$$

is applicable to dilute electrochemical systems, where R is the molar gas constant and T is the absolute temperature. The flux of a species was recast as

$$\boldsymbol{N}_i = -z_i D_i c_i F \nabla \phi - D_i \nabla c_i \tag{2-8}$$

by employing equation (2-7), the dimensionless potential ϕ

$$\phi = \frac{\Phi F}{RT} \tag{2-9}$$

and the assumption that the mass average velocity is equal zero. Equations (2-4) and (2-6) were recast in terms of ϕ as

$$\frac{\partial c_i}{\partial t} = D_i \left[z_i \nabla \cdot (c_i \nabla \phi) + \nabla^2 c_i \right] + R_i \tag{2-10}$$

and

$$0 = D_i \left[z_i \nabla \cdot (c_i \nabla \phi) + \nabla^2 c_i \right] + R_i \tag{2-11}$$

respectively.

2.2 Solution Potential

The governing equation for the solution potential in an electrochemical system is Poisson's equation[12]

$$\nabla^2 \Phi = -\frac{F}{\varepsilon} \sum_i z_i c_i \tag{2-12}$$

where ϵ is the permittivitty of the medium. This fundamental governing equation was used in a recent transient crevice model but is rarely used as the governing equation for Φ.[13]

A popular equation that has been used as the governing equation for Φ is the expression

$$\sum_i z_i c_i = 0 \tag{2-13}$$

based on the concept of electroneutrality at a point.[2,14–18] Newman has shown that outside the diffuse part of the double layer this equation is a very good approximation to Poisson's equation as any deviations from electrical neutrality are restored by large forces.[12]

Governing equations for Φ have also been derived by employing the electrochemical concepts of ionic current density $\boldsymbol{i}$

$$\boldsymbol{i} = F \sum_i z_i \boldsymbol{N}_i \tag{2-14}$$

and the conservation of charge[12]

$$\nabla \cdot \boldsymbol{i} = 0 \tag{2-15}$$

at a position in the electrolyte. Combination of equations (2-2) and (2-14), in the

absence of convection, yields

$$\boldsymbol{i} = -\kappa\nabla\Phi - F\sum_i z_i D_i \nabla c_i \tag{2-16}$$

where the conductivity κ is defined as

$$\kappa = \frac{F^2}{RT}\sum_i z_i^2 D_i c_i \tag{2-17}$$

The contributors to the ionic current density can be divided into migration current density $\boldsymbol{i}_\mathrm{m}$ and diffusion current density $\boldsymbol{i}_\mathrm{d}$[19]

$$\boldsymbol{i} = \boldsymbol{i}_\mathrm{m} + \boldsymbol{i}_\mathrm{d} \tag{2-18}$$

where

$$\boldsymbol{i}_\mathrm{m} = -\kappa\nabla\Phi \tag{2-19}$$

and

$$\boldsymbol{i}_\mathrm{d} = -F\sum_i z_i D_i \nabla c_i \tag{2-20}$$

The driving forces for the migration and diffusion current densities were solution potential and concentrations gradients, respectively.

Substitution of the current density given by equation (2-16) into the equation for the conservation of charge, given by equation (2-15), yields

$$\nabla\cdot(\kappa\nabla\Phi) + F\sum_i z_i D_i \nabla^2 c_i = 0 \tag{2-21}$$

Equation (2-21) can be used as a governing equation for Φ when concentrations gradients are known, *i.e.*, c_i as a function of position is known.

In the absence of concentration gradients, equation (2-16) reduces to an expression for Ohm's law

$$\boldsymbol{i} = -\kappa\nabla\Phi \tag{2-22}$$

which yields Laplace's equation for Φ

$$\nabla^2\Phi = 0 \tag{2-23}$$

with the application of the conservation of charge.

Poisson's equation, the equation for the condition of electroneutrality, and the equations based on the conservation of charge with or without concentration gradients, equations (2-12), (2-13), (2-21), and (2-23), respectively, have each been used as the governing equation for Φ in multi-dimensional domains. Walton *et al.* used an approach in which the value of Φ as a function of position in a 1-D domain was calculated when the current density due to electrochemical reactions and the concentration distributions were known.[20] This approach is described in section 10.6.

2.3 Electrode Kinetics

The distributions of solution potential and species concentrations in electrochemical systems are in response to electrochemical reactions on metal surfaces in the system. Consider the heterogeneous electrochemical reduction of ferricynadide to ferrocynanide on a nickel surface

$$\mathrm{Fe(CN)_6^{-3}} + \mathrm{e^-} \rightleftharpoons \mathrm{Fe(CN)_6^{-4}} \tag{2-24}$$

A reaction which involves the decrease in the oxidation number of a species is referred to as cathodic, whereas a reaction in which the oxidation number of a species is increased is referred to as anodic. For the reaction described by equation (2-24) the forward reaction, left to right, is cathodic and the backward reaction is anodic. The overall rate of the reaction r is given

$$r = r_f - r_b \tag{2-25}$$

where r_f and r_b are the forward and backward rates, respectively.

The forward and backward rates can be written in terms of a rate constant and a concentration term assuming that each reaction is first order. The overall rate is given by

$$r = k_f c_{\mathrm{Fe(CN)_6^{-3}}} - k_b c_{\mathrm{Fe(CN)_6^{-4}}} \tag{2-26}$$

From activated complex theory, equation (2-26) can be recast as

$$r = k_a \exp\left(\frac{(1-\beta)nF}{RT}V\right) c_{\mathrm{Fe(CN)_6^{-3}}} - k_c \exp\left(\frac{-\beta nF}{RT}V\right) c_{\mathrm{Fe(CN)_6^{-4}}} \tag{2-27}$$

where V is the potential at the metal-electrolyte interface, β is the fraction of the applied potential which favors the cathodic reaction (known as the symmetry factor) and n is the number of electrons transferred. Equation (2-27) can be written in terms of the normal current density i as

$$\frac{i}{nF} = k_a \exp\left(\frac{(1-\beta)nF}{RT}V\right) c_{\mathrm{Fe(CN)_6^{-3}}} - k_c \exp\left(\frac{-\beta nF}{RT}V\right) c_{\mathrm{Fe(CN)_6^{-4}}} \tag{2-28}$$

The potential at the metal-electrolyte interface, the interfacial potential, V is defined as

$$V = \Psi - \Phi \tag{2-29}$$

where Ψ is the potential of the metal and Φ is the potential of the solution at the inner limit of the diffusion layer in the electrolyte adjacent to the metal surface. The potential at $r_f = r_b$, *i.e.*, a zero overall rate, is termed the equilibrium potential V^o. At the equilibrium potential V^o, the net rate of the reaction is zero; however, the individual rates of the reactions are non-zero and equal. The current density at the equilibrium potential is termed the exchange current density i_o and is calculated using either

$$\frac{i_o}{nF} = k_a \exp\left(\frac{(1-\beta)nF}{RT}V^o\right) c_{\mathrm{Fe(CN)_6^{-3}}} \tag{2-30}$$

or

$$\frac{i_o}{nF} = k_c \exp\left(\frac{-\beta nF}{RT}V^o\right) c_{\mathrm{Fe(CN)_6^{-4}}} \tag{2-31}$$

Substitution of i_o into equation (2-28) results in the Butler-Volmer equation for the electrochemical reaction[12]

$$i = i_o \left(\exp\left(\frac{\alpha_a F}{RT} \eta_s \right) - \exp\left(\frac{-\alpha_c F}{RT} \eta_s \right) \right) \tag{2-32}$$

where the surface overpotential η_s is given by $\eta_s = V - V^o$, the anodic transfer coefficient α_a is given by $\alpha_a = (1 - \beta)n$, and the cathodic transfer coefficient is given by $\alpha_c = \beta n$.

The exponential behavior of the Butler-Volmer equation results in a characteristic feature of electrochemical reactions. At high overpotentials where $\alpha_a F \eta_s \gg RT$, equation (2-32) reduces to

$$i = i_o \exp\left(\frac{\alpha_a F}{RT} \eta_s \right) \tag{2-33}$$

Solving for η_s in equation (2-33) gives

$$\eta_s = \frac{RT}{\alpha_a F} \ln \left| \frac{i}{i_o} \right| \tag{2-34}$$

or

$$\eta_s = 2.303 \frac{RT}{\alpha_a F} \log_{10} \left| \frac{i}{i_o} \right| \tag{2-35}$$

The Tafel slope for the anodic reaction β_a is given by the expression in front of the log term in equation (2-35)

$$\beta_a = 2.303 \frac{RT}{\alpha_a F} \tag{2-36}$$

The corresponding Tafel slope for the cathodic reaction is given as

$$\beta_c = 2.303 \frac{RT}{\alpha_c F} \tag{2-37}$$

The Butler-Volmer equation, equation (2-32), can be recast using these Tafel slopes into

$$i = 10^{(V - E_a)/\beta_a} - 10^{(V - E_c)/\beta_c} \tag{2-38}$$

where E_a and E_c are termed the effective equilibrium potentials given by

$$E_a = V^o - \beta_a \log_{10} i_o \tag{2-39}$$

and

$$E_c = V^o - \beta_c \log_{10} i_o \tag{2-40}$$

respectively.[21]

2.4 Polarization Kinetics of Bare Steel

The electrochemical reactions of interest in the corrosion of steel include the corrosion reaction (or iron dissolution)

$$\mathrm{Fe} \rightarrow \mathrm{Fe}^{+2} + 2\mathrm{e}^- \tag{2-41}$$

the cathodic oxygen reduction reaction

$$\mathrm{O_2} + 2\mathrm{H_2O} + 4\mathrm{e}^- \rightarrow 4\mathrm{OH}^- \tag{2-42}$$

and the cathodic hydrogen evolution reaction

$$2\mathrm{H_2O} + 2\mathrm{e}^- \rightarrow \mathrm{H_2} + 2\mathrm{OH}^- \tag{2-43}$$

These reactions are considered to occur simultaneously on the steel surface. A premise of mixed potential theory is that electrochemical reactions can be treated independently.[22] Therefore, a Butler-Volmer equation such as equation (2-32) can be written for each of these reactions.

The current density due to the reversible corrosion reaction i_{Fe}

$$\mathrm{Fe} \Leftrightarrow \mathrm{Fe}^{+2} + 2\mathrm{e}^- \tag{2-44}$$

can then be obtained by

$$i_{\mathrm{Fe}} = 10^{(V - E_{\mathrm{a,Fe}})/\beta_{\mathrm{a,Fe}}} - 10^{(V - E_{\mathrm{c,Fe}})/\beta_{\mathrm{c,Fe}}} \tag{2-45}$$

where the first term on the right-hand-side of the equation represents the current density due to the forward, or anodic, reaction and the second term that due to the backward, or cathodic, reaction. In modeling the corrosion reaction, equation

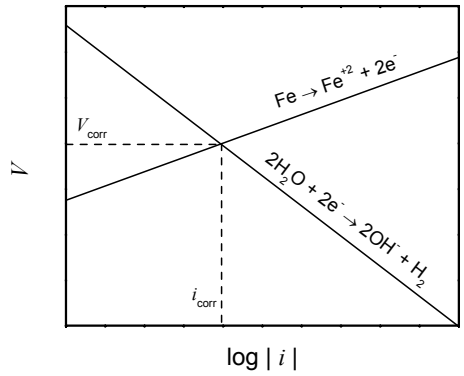

Figure 2-1: Polarization plots for corrosion and hydrogen evolution. The dashed lines indicate the corrosion potential V_{corr} and the corrosion current i_{corr}.

(2-41), only the current density due to the forward reaction was considered as it was assumed that this reaction was irreversible. The current density due to the corrosion reaction i_{Fe} is then given by

$$i_{\text{Fe}} = 10^{(V-E_{\text{Fe}})/\beta_{\text{Fe}}} \tag{2-46}$$

where $E_{\text{a,Fe}}$ and $\beta_{\text{a,Fe}}$ are replaced by E_{Fe} and β_{Fe}, respectively. Similarly, the current density i_{H_2} due to the irreversible hydrogen evolution reaction of equation (2-43) is given by

$$i_{\text{H}_2} = -10^{-(V-E_{\text{H}_2})/\beta_{\text{H}_2}} \tag{2-47}$$

under the assumption that the reaction is irreversible.

A plot of interfacial potential V as a function of the base ten logarithm of the current density due to an electrochemical reaction $\log_{10}|i|$ is termed a polarization plot. The polarization plots for the corrosion and hydrogen evolution reactions are shown on the same pair of axes in Figure 2-1. The point of intersection represents the condition at which the anodic i_{Fe} balances the cathodic i_{H_2}. The potential at this condition is termed the corrosion potential V_{corr}, and the current density is the corrosion current i_{corr}. Other terms for V_{corr} include the open circuit potential and the free corroding potential. The polarization behavior of the corrosion and

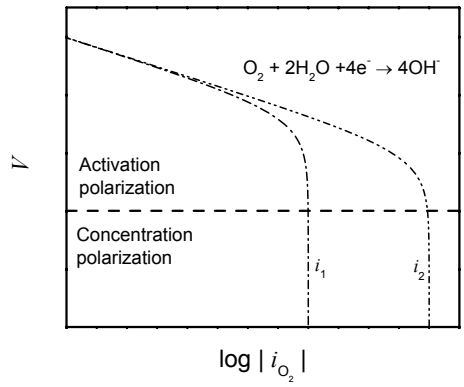

Figure 2-2: Polarization plots for oxygen reduction at two values of mass-transfer-limited current density designated as i_1 and i_2, such that $i_2 > i_1$. The plots superimpose for the part of the range of interfacial potential. The horizontal dashed line separates the activation potential and concentration polarization parts of the plots.

hydrogen evolution reactions are termed activation polarization as the rates of the electrochemical reactions are driven by the surface overpotential η_s.

The polarization plot for the cathodic oxygen reduction reaction is shown in Figure 2-2. The polarization behavior of this reaction is activation polarization for one part and concentration polarization for the other. The concentration polarization behavior is due to the limited rate at which oxygen can be transferred to the metal surface. The current density of the oxygen reduction reaction at which the mass-transfer of oxygen to the steel surface is a maximum is termed the mass-transfer-limited current density i_{lim,O_2}. The current density due to the oxygen reduction reaction i_{O_2} is given by the mathematical expression

$$i_{O_2} = -\left(\frac{1}{i_{\mathrm{lim},O_2}} - 10^{(V-E_{O_2})/\beta_{O_2}}\right)^{-1} \tag{2-48}$$

that accounts for both the activation and concentration polarization behavior.[23]

The net current density i_{net} for steel is given by the sum of the current densities due to the individual electrochemical reactions[21]

$$i_{\mathrm{net}} = i_{\mathrm{Fe}} + i_{O_2} + i_{H_2} \tag{2-49}$$

Table 2.1: Parameters used for the polarization behavior of bare steel.

Reaction	β, mV/decade	E, mV (SCE)
$Fe \rightarrow Fe^{+2} + 2e^-$	62.6	-475
$2H_2O + O_{2(aq)} + 4e^- \rightarrow 4OH^-$	66.5	-500
$2H_2O + 2e^- \rightarrow H_2 + 2OH^-$	132	-870

where

$$i_{Fe} = 10^{(\Psi-\Phi-E_{Fe})/\beta_{Fe}} \tag{2-50}$$

$$i_{O_2} = -\left(\frac{1}{i_{lim,O_2}} - 10^{(\Psi-\Phi-E_{O_2})/\beta_{O_2}}\right)^{-1} \tag{2-51}$$

and

$$i_{H_2} = -10^{-(\Psi-\Phi-E_{H_2})/\beta_{H_2}} \tag{2-52}$$

In these equations the interfacial potential V was replaced by the potential driving the electrochemical reaction $\Psi - \Phi$ where Φ is the solution potential of a reference electrode located adjacent to the metal surface and Ψ the potential of the metal, also referred to as the applied potential.

Polarization plots for steel showing the metal-electrolyte interfacial potential as functions of the values of corrosion, hydrogen evolution, oxygen reduction, and net current densities are shown in Figure 2-3.The parameters used in the polarization expressions for i_{Fe}, i_{O_2}, and i_{H_2} are given in Table 2.1. These parameters were obtained by fitting polarization curves to experimental data for a slit-holiday.[24] The corrosion potential of $V_{corr} \approx -0.475$ V_{SCE} represented the condition where the absolute value of i_{net} approached a zero value. The absolute value for i_{O_2} was 1 μA cm^2 and was unchanged with potential because the oxygen reduction reaction was mass-transfer-limited for the potential range shown in the figure.

For applied potentials more positive than V_{corr}, the net current density was anodic with the corrosion reaction dominating the cathodic oxygen reduction and hydrogen evolution reactions. The plots for i_{Fe} and i_{net} superimposed for $V >$

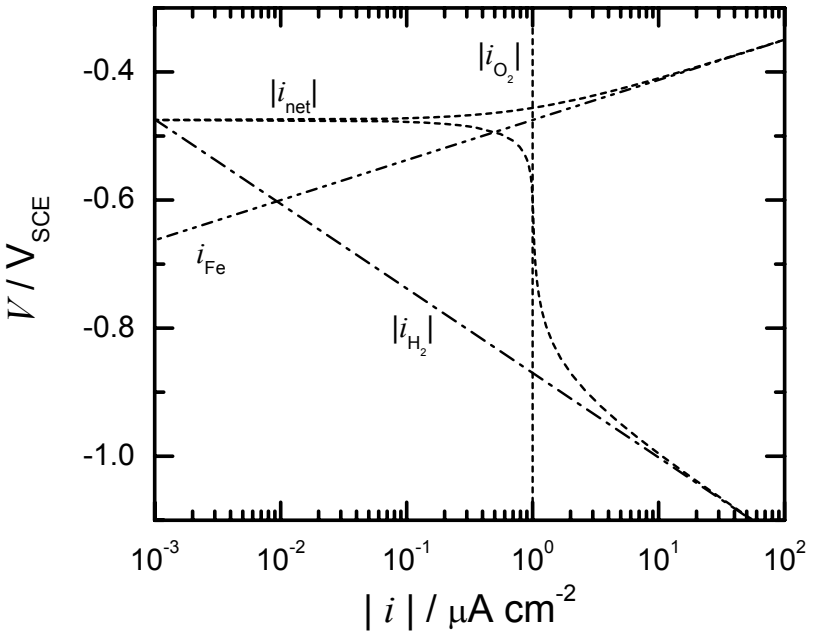

Figure 2-3: Polarization plot for steel showing the interfacial potential as functions of the absolute current densities for corrosion i_{Fe}, hydrogen evolution i_{H_2}, oxygen reduction i_{O_2}, and net current density i_{net}. The plots for corrosion and net current density superimposed for potentials more positive than -0.4 V_{SCE}. The plots for hydrogen evolution and net current density superimposed for potentials more negative than -1.05 V_{SCE}. The net current density approached a zero value at the potential -0.475 V_{SCE}.

-0.4 V_{SCE}. Applied potentials more negative than V_{corr} yielded a cathodic behavior of the metal, with the net current density being cathodic. In the potential range of $V_{corr} > V > -0.6$ there was a large change in the absolute value of i_{net} with applied potential. At $V \simeq -0.6$ V_{SCE} the change of current density with applied potential was significantly reduced as i_{lim,O_2} was reached. For $V < -0.75$ V_{SCE} the change in current density with applied potential was resumed as the hydrogen evolution reaction became more favorable. For $V < -1$ V_{SCE}, the plots for the absolute value of i_{H_2} and i_{net} superimposed.

2.5 Corrosion Control Methods

The corrosion control methods listed in Table 1.1 were recommended in a report sponsored by the Office of Infrastructure Research and Development in 2001.[1] Organic coatings represented the significant method of control against the corrosion of metal surfaces as indicated by the cost of this method compared to the others.

Metallic coatings involve the plating of a metal with another metal and the most common form is hot dipped galvanized steel. The metallic coating of zinc on galvanized steel acts as a barrier to the environment and as a sacrificial anode when the underlying steel surface is exposed. Corrosion resistant metals and alloys such as stainless steels, nickle-based alloys, and titanium alloys are used to replace the conventional carbon steel in applications where protective coatings are not feasible. Corrosion inhibitors such as chromium, phosphates, and zinc reduce the corrosion of an exposed metal surface when added in a small concentration to the metal environment. Polymers such as polyvinyl chloride, polyethylene, and fluropolymers are used for their anticorrosive properties.

2.5.1 Organic Coatings

Metal surfaces are protected from corrosion by a organic coatings that form a physical barrier between the metal and the atmosphere. The coatings are applied as micron thick layers. In the automotive and construction industries the organic coatings are also cosmetic. The inclusion of inhibitors as a constituent in organic coatings provides additional corrosion protection.[25,26]

In the pipeline industry the commonly used organic coatings include coal tar or asphalt enamels, polyethylene tapes, and fusion bonded epoxy. The properties required by pipeline coatings include strong adhesion to steel, resistance to flow at high temperature, flexibility at low temperatures, high impact resistance, resistance to cathodic disbonding, ease of application, and resistance to soil stress.[27]

The protection of pipelines is achieved by organic coatings together with anodic and cathodic protection methods. The anodic and cathodic protection methods address the defects that are associated with organic coatings.

2.5.2 Anodic and Cathodic Protection

The corrosion of metals involves the dissolution of the metal into the surrounding environment. When an additional metal is introduced that preferentially corrodes, the protection is anodic. When an electrical condition is used to make the metal dissolution reaction less favorable, the protection is cathodic.

Sacrificial anode. Protection of a metal can be provided by attaching a sacrificial anode which corrodes preferentially. A schematic diagram for a sacrificial anode system is shown in Figure 2-4. In this system an electrochemical cell is formed by the pipeline, the sacrificial anode, the soil, and an insulated wire connection. The anode material is selected such that a metal dissolution reaction occurs on the anode that is thermodynamically more favorable than the iron-dissolution reaction on the pipe surface. Magnesium metal is a common sacrificial anode ap-

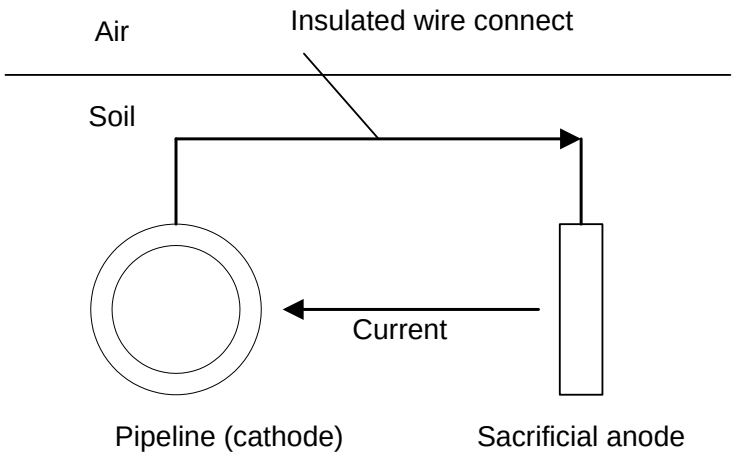

Figure 2-4: Schematic diagram of a sacrificial anode protection system for a pipeline.

plied in soil environments. The anodic metal dissolution reaction on the anode is balanced by cathodic reactions on the pipe surface *e.g.,* oxygen reduction and hydrogen evolution reactions.

Impressed current. The impressed-current cathodic protection system is based on lowering the potential of the pipe surface such that the corrosion reaction is less favorable. This is achieved by supplying a d.c. current to the pipe surface. In lowering the potential of the pipe surface, the cathodic reactions, oxygen reduction and hydrogen evolution, become more favorable (see Figure 2-3). A schematic diagram for an impressed current system is shown in Figure 2-5. Current is supplied to the pipe from the anode through the soil. The electrochemical reactions on the pipe are primarily cathodic with the anodic corrosion reaction being made negligible. The net cathodic reactivity on the pipe is balanced by anodic reactions on the anode that include water oxidation

$$2H_2O \rightarrow O_2 + 4H^+ + 4e^- \tag{2-53}$$

and chloride oxidation

$$2Cl^- \rightarrow Cl_2 + 2e^- \tag{2-54}$$

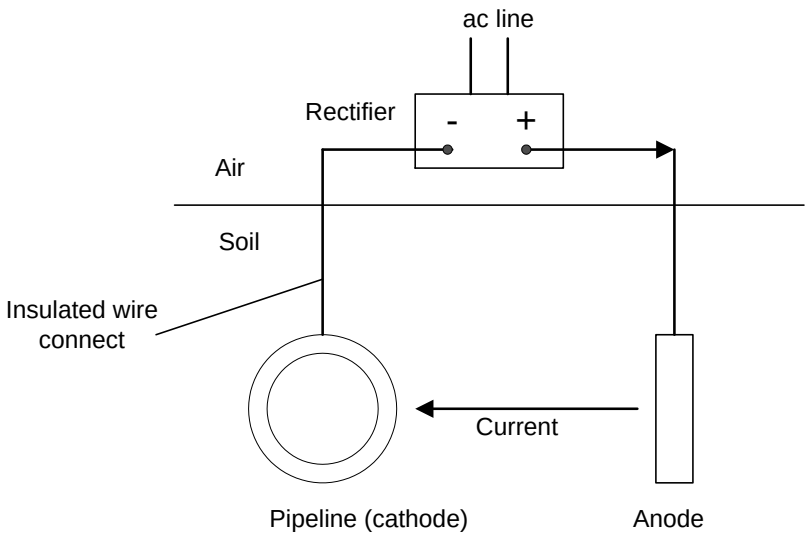

Figure 2-5: Schematic diagram of an impressed current cathodic protection system for a pipeline.

Impressed-current cathodic protection systems are generally used to mitigate corrosion at holidays. There are several criteria that are used to implement impressed-current cathodic protection.[22] One criterion involves the maintenance of the pipe surface at a potential more negative than -0.85 V relative to a copper-copper sulfate ($Cu/CuSO_4$) reference electrode or equivalently more negative than -0.773 V relative to a standard electrochemical electrode (SCE). Another criterion involves the maintenance of a minimum negative shift of 300 mV from the corrosion potential

Mathematical models have been presented in literature that assessed the cathodic protection requirements for a given pipeline with holidays.[21,28–33] In these models the potential and current distributions for a domain that included a pipeline were obtained by solving the Laplace equation for Φ. The boundary conditions at the holiday were governed by electrochemical reactions associated with steel. In these models, the conductivity of the medium was fixed with concentration gradients assumed to be negligible. The influence of any disbondment coating surrounding the holiday was not included. An approach can be developed where the model for disbonded coatings that is presented in Chapter 4, DISCOM, can

be coupled with a model for pipeline cathodic protection requirements. The former model would calculate the steady-state conditions in the disbonded coating system, where concentration gradients are applicable, and the latter model would calculate the potential and current density distributions in the bulk domain where the assumption of negligible concentration gradients is applicable. This approach has been reported for the parallel-sided crevice where the electrochemistry in the crevice region was coupled with the electrochemistry in the bulk.[34]

CHAPTER 3
LITERATURE REVIEW

The motivation for the research presented was to understand the phenomena that contribute to the disbonded coating and cathodic delamination systems. This motivation was achieved through the analysis of results simulated by mathematical models of these systems. Mathematical models were developed for these systems, DISCOM for the disbonded coating system and CADEM for the cathodic delamination system.

The disbonded coating system belonged to a wider class of systems termed occluded systems, that include pitting and crevice systems. In these systems the occluded environment is different from the bulk. There are simultaneous phenomena occurring that govern the occluded environment. The transport of species occurs by diffusion and migration with the contribution by convection being considered negligible. There are homogeneous reactions between aqueous species and there are electrochemical reactions at metal surfaces. The geometry of the occluded system also contribute to its environment. The phenomena that govern the cathodic delamination system were similar to those for the disbonded coating system and are presented in Chapter 9.

Mathematical models of occluded systems are used to calculate the conditions of the occluded domain. These conditions include the spatial distributions of c_i and Φ, and the current density distributions along any metal surface. There have been numerous mathematical models presented in literature for crevice and pitting systems, and detailed reviews have been presented by Sharland[35] and Turnbull.[36] Several pitting and crevice models are presented briefly in this chapter.

These models were relevant as they provided concepts that were used in the development of DISCOM and CADEM. Two models for the steady-state conditions in the disbonded coating system are presented by Chin and Sabde[2,3] and Song *et al.*[4,5] in literature. A model for the transient conditions in this system is presented by Sridhar *et al.*[37] These models are presented briefly in this chapter.

3.1 Disbonded Coating Models

Disbonded coating systems found on coated metals are approximated by longitudinal and radial geometries. A schematic diagram of the geometry of a longitudinal disbonded coating system is shown in Figure 3-1. The system consist of a region where the coating is disbonded, called the disbondment, adjacent to a holiday. The boundary located at the plane of symmetry can also represent an impermeable wall. The boundary with the bulk solution is called the mouth. The thickness of the disbondment, the gap, is uniform along its length. In longitudinal disbonded coating systems, the length of system in the direction normal to the page is assumed to be large as compared to the gap and the disbondment length. This facilitates the assumption that variations in a direction normal to the page are negligible. The geometry of the radial disbonded coating system is similar to that of the longitudinal system, except that there is an axis of symmetry instead of a plane of symmetry. The assumption of symmetry about this axis facilitates the assumption of an axisymmetric domain. The radial disbonded coating system is described in detail in section 4.1.

A model for a radial system was presented by Sabde in which the steady-state conditions of a disbonded coating system under cathodic protection were calculated.[2,3] In this model, only oxygen reduction was considered significant while corrosion and hydrogen evolution were considered insignificant. The ionic species Na^+, Cl^-, and OH^- were considered and the total ionic concentration c_T was given

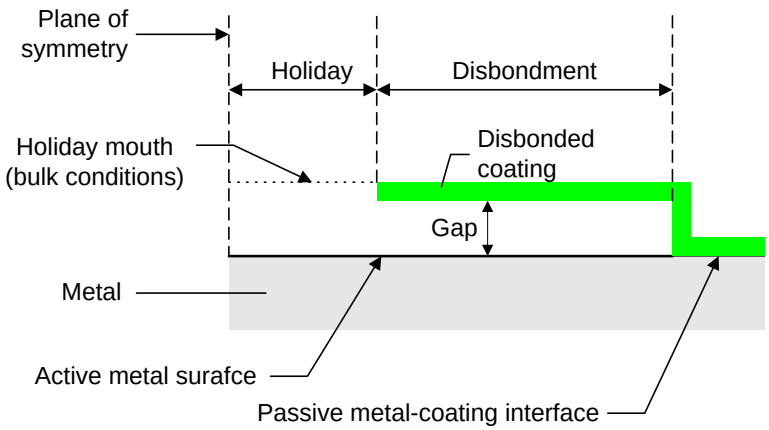

Figure 3-1: Schematic diagram of a longitudinal disbonded coating system (not drawn to scale).

by

$$c_T = c_{Na^+} + c_{Cl^-} + c_{OH^-} \tag{3-1}$$

The model used the assumption $D_i = 10^{-5}$ cm^{2}s^{-1} for the ionic species. This assumption resulted in a governing equation for c_T given by

$$\frac{\partial^2 c_T}{\partial r^2} + \frac{1}{r}\frac{\partial c_T}{\partial r} + \frac{\partial^2 c_T}{\partial z^2} = 0 \tag{3-2}$$

that was independent of Φ. Equation (3-2) together with boundary conditions, also independent of Φ, was solved to yield the distribution of c_T. The distribution of Φ was governed by

$$\frac{c_T}{r}\frac{\partial \Phi}{\partial r} + c_T\frac{\partial^2 \Phi}{\partial r^2} + \frac{\partial c_T}{\partial r}\frac{\partial \Phi}{\partial r} + c_T\frac{\partial^2 \Phi}{\partial z^2} + \frac{\partial c_T}{\partial z}\frac{\partial \Phi}{\partial z} = 0 \tag{3-3}$$

This equation was solved using the calculated distribution of c_T to yield the distribution of Φ. The distributions of c_i were calculated using the calculated distribution of Φ and the governing equation for c_i

$$z_i\frac{F}{RT}\nabla \cdot (c_i \nabla \Phi) + \nabla^2 c_i = 0 \tag{3-4}$$

in cylindrical coordinates. The method of solution of c_T, Φ, and c_i in the two-dimensional domain was a collocation finite-element numerical method.

The model DISCOM was developed to calculate the steady-state conditions of a disbonded coating system, similar to the model presented by Chin and Sabde.[2,3] In DISCOM the electrochemical reactions considered were corrosion, oxygen reduction, and hydrogen evolution whereas in Chin and Sabde's model only oxygen reduction was considered. The results presented in the chapter 5, obtained using DISCOM, demonstrated the importance of hydrogen evolution in disbonded coating systems.

The assumption used by Chin and Sabde where $D_i = 10^{-5}$ cm^{2}s^{-1} eliminated the coupling of the governing equations of c_i and Φ.[2,3] This assumption was not used in DISCOM. In DISCOM, the transport of species and the electroneutrality condition were satisfied simultaneously by the coupling of the governing equations for c_i and Φ.

The assumption that $D_i = 10^{-5}$ cm^{2}s^{-1} for the different species has been also been used in the development of a model for the growth of pits presented by Laycock.[38] The applicability of the assumption $D_i = 10^{-5}$ cm^{2}s^{-1} to disbonded coating systems is presented in section 7.2.

A transient model for a longitudinal disbonded coating system was presented by Sridhar *et al.*[37] in which the evolution of the disbonded coating environment was calculated. A method was used in this model where the species considered were separated into primary and secondary species. The concentration distributions of primary species were calculated using a given distribution for Φ and conservation relationships. The concentration distributions of secondary species were calculated using the concentration of primary species and equilibrium relationships associated with homogeneous reactions. Electroneutrality was not maintained explicitly but was satisfied by adjusting the concentration of a specie not involved in homogeneous reactions nor electrochemical reactions such as Na^+.

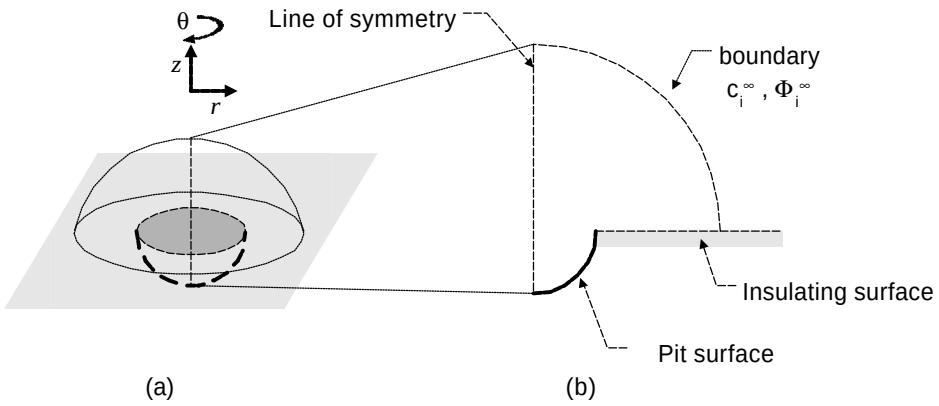

Figure 3-2: Schematic diagram of a hemispherical pit (not drawn to scale).

The method involving primary and secondary species employed by Sridhar *et al.*[37] decoupled the equilibrium relationships of the homogeneous relationships from the governing equations of the disbonded coating system. The computational requirement was significantly reduced by this decoupling. The applicability of this method to steady-state modeling of disbonded coating systems and more details of the separation procedure are presented in section 7.3.

3.2 Pit Models

The geometry of the pitting system is approximated by a hemispherical pit embedded in an insulating medium as shown in Figure 3-2(a). The dimensionality of the problem is simplified by assuming symmetry in the θ direction to recast the geometry into an axisymmetric region as shown in Figure 3-2(b). This axisymmetric region consist of a active pit surface surrounded by an insulating surface. The boundary with the bulk solution is located far from the pit and represents an equipotential line.

Pioneering work in steady-state modeling used assumptions to simplify the governing equations for the conditions in pits. Under the assumption that the conductivity of the electrolyte in the pit is uniform, concentration gradients are negligible, and the pit condition is represented by the spatial distribution of Φ.

The governing equation for Φ in this situation was given by Laplace's equation, equation (2-23). Newman *et al.*[39] reported the initial effort at pit modeling, which included the solution of Laplace's equation for Φ in the pit geometry. The boundary condition at the metal surface was a fixed current density and the calculated current distribution was the primary current distribution. A model for the secondary current distribution in a pit was reported by Verbrugge *et al.*[18] In this model the solution of Laplace's equation for Φ involved a boundary condition at the metal surface which was a function of Φ. This boundary condition was represented by the polarization kinetics of the metal dissolution reaction.

A steady-state model for a nickel pit environment has been reported by Harb[16] where the transport of species by migration and diffusion was considered explicitly. The governing equation for c_i was given by equation (2-6). The governing equation for Φ was the electroneutrality condition given by equation (2-13). In this model only nickel dissolution was considered at the pit surface. The species considered were Na^+, Cl^-, Ni^{+2}, $NiCl^+$, and $NiCl_2$. The homogeneous reactions

$$Ni^{+2} + Cl^- \rightleftharpoons NiCl^+ \tag{3-5}$$

and

$$NiCl^+ + Cl^- \rightleftharpoons NiCl_2 \tag{3-6}$$

were considered.

The method employed by Harb[16] involved eliminating the rate of homogeneous production R_i terms by combining the governing equations for c_i . The equilibrium relationships were included as governing equations. The governing equations consisted of a set of coupled partial, differential equations for c_i , non-linear equations for equilibrium relationships, and an algebraic expression for the electroneutrality condition. The steady-state governing equations were discretized using a finite-element formulation and the system of equations were solved us-

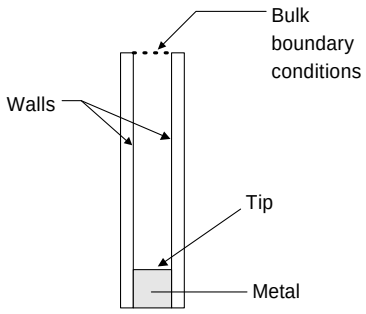

Figure 3-3: Schematic diagram of parallel-sided crevice (not drawn to scale).

ing an iterative numerical algorithm. The method used by Harb[16] to include the equilibrium relationships explicitly was also used in DISCOM.

A steady-state mathematical model for the aluminum pit environment has been reported by Verhoff.[14] In this model only aluminum dissolution was considered at the metal surface. Homogeneous reactions involving the hydrolysis of Al^{+3}, $Al(OH)^{+2}$, and $Al(OH)_2^{+}$ were considered. The solution method involved a variable transformation, the quasipotential transformation, and provided an accurate way to solve the governing equations. Systems which have been modeled using this transformation include the deposition of copper onto a disk electrode[40] and the dissolution of nickel in a pit system.[41] The details of the quasipotential transformation are presented in Chapter 8.

3.3 Crevice and Disbondment Models

The crevice system has been approximated by a geometry that consist of parallel walls, a tip, and a bulk boundary as shown in Figure 3-3. In these systems the assumption that variations in c_i and Φ perpendicular to the walls are negligible is used such that the variations parallel to the walls facilitate a one-dimensional solution. The parallel-sided crevice system has been modeled extensively in literature. Models have been reported where the tip was active and walls passive[17,42–47] Models where both tip and walls were active have also been reported.[13,17,47–52]

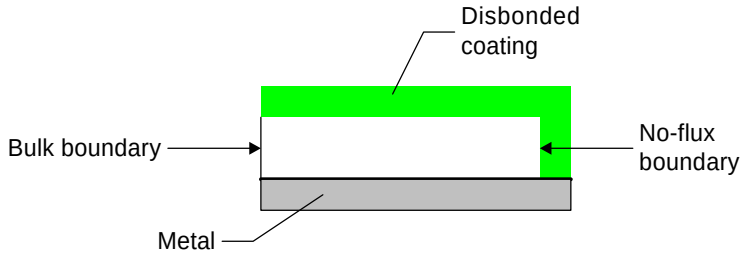

Figure 3-4: Schematic diagram of a disbonded coating crevice system (not drawn to scale).

Another type of crevice system involving a disbonded coating is shown in Figure 3-4. In this system, referred to as a disbondment system, the influence of a holiday is not considered. The electrochemical reactions are considered at the metal surface with the surface of the coating being passive. The large ratio of disbondment length to gap size facilitates the assumption that variations perpendicular to the metal surface are negligible such that the governing equations are one-dimensional in the direction parallel to the metal surface. The conditions at the bulk boundary are fixed while at the coating boundary a no-flux condition is used.

A method in which the distribution of Φ was calculated for a given distribution of c_i in a disbondment system was presented by Walton.[20] This method was used in the development of CADEM. Walton[20] used a method involving control volumes to develop a transient model for the conditions of the one-dimensional disbondment system. Equation (2-16) was used to relate the current density entering a control volume i_s to the solution potential drop in $\triangle\Phi$ across the control volume of length $\triangle x$

$$\triangle\Phi = \frac{\triangle x \left(-i_s - F \sum_i z_i D_i \nabla c_i \right)}{\kappa} \tag{3-7}$$

For the distributions of c_i and i_s at a given time, the distribution of Φ at a time one time-step forward was calculated. The calculated Φ distribution was then used in the governing equations for species conservation to calculate the distributions

of c_i . These distributions were adjusted such that equilibrium relationships were satisfied. After the equilibrium relationships were satisfied, electroneutrality was satisfied by adjusting the value of the concentration of a specie such as Na^+. More details of this method are given in section 10.6.

Recently, a model for the steady-state conditions in a disbondment system under cathodic protection has been reported by Song.[4,5] Concentration gradients were assumed negligible such that Laplace's equation governed the solution potential. The electrochemical reactions included were corrosion, oxygen reduction, and hydrogen evolution. The model essentially calculated the secondary current distribution in the disbondment by solving the Laplace equation for Φ with boundary conditions given by the polarization kinetics for the metal. The assumption of negligible concentration gradients neglected the contribution of current carried by diffusion transport in the electrolyte. The contribution of diffusion transport in the disbondment of a disbonded coating system is shown to be significant in this work and cannot be assumed negligible even for low conductivity environments.

CHAPTER 4
DISBONDED COATING MODEL

The mathematical model DISCOM calculated the steady-state conditions in a radial disbonded coating system under cathodic protection. This model was developed using concepts from the models reported in literature and presented briefly in the previous chapter. The development of DISCOM is presented in this chapter.

The homogeneous reaction of ferrous hydrolysis was included in the development of DISCOM using the approach employed by Harb[16] to account for the equilibrium relationship of the homogeneous reaction explicitly. It was assumed that the influence of H^+ was negligible as the system was under cathodic protection with OH^- being produced at the metal surface and alkaline conditions existing in the system. Therefore, the specie H^+ and the associated water dissociation homogeneous reaction were not considered in the development of DISCOM.

4.1 Disbonded Coating System

A schematic diagram of the cross-section of a radial disbonded coating system is shown in Figure 4-1. A line of symmetry OY is present in the geometry and the system is described for a symmetric cross-section. The domain of the disbonded coating system (OABCDEFK) is divided into the holiday (OADEF) and disbondment (ABCD) as shown in Figure 4-1. The boundaries of the disbonded coating system include the line of symmetry OF, metal surface OB, coating BC, CD, and DE and the mouth of the holiday FE.

The section of metal BG is covered by coating and is considered to be passive and does not contribute to the disbonded coating system. The coating was con-

sidered to be impermeable to the passage of current and oxygen. When the metal surface of the disbonded coating system is under cathodic protection, current is delivered to the metal surface of the holiday and disbondment through the electrolyte in the holiday and disbondment.

Mathematical models for occluded systems reported in literature used the assumption that concentration gradients were negligible at positions far from the metal surface. This assumption introduced a boundary, the bulk boundary, where c_i and Φ were fixed. The positioning of the bulk boundary where Φ is fixed corresponds to the placement of a reference electrode at any position on the bulk boundary. In DISCOM, the bulk boundary was positioned at the mouth of the holiday and exterior to this boundary was the bulk electrolyte.

The boundaries of the holiday include the line of symmetry OF, the metal surface OA, and the coating DE. The holiday shares boundaries FE and AD with the bulk and the disbondment, respectively. The boundary FE is referred to as the mouth of the holiday. Transport of species between the holiday and bulk is across the mouth and transport between the holiday and disbondment is across the entry of the disbondment AD.

The boundaries of the disbondment includes the metal surface AB, the coating BC and CD, and the boundary AD which was shared with the holiday. The metal surface AB was uncovered. The gap between the metal surface and the disbonded coating was uniform across the length of the disbondment AB.

DISCOM was developed to accommodate two systems comprising of different ionic species. In one system, which was without $Fe(OH)^+$, the conservation of the four species Na^+, Cl^-, OH^-, and Fe^{+2} were considered. In the other system, the system with $Fe(OH)^+$, the conservation of the five species Na^+, Cl^-, OH^-, Fe^{+2},

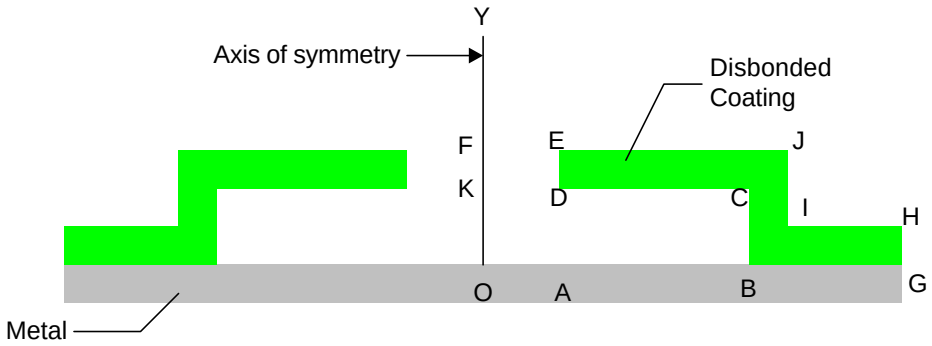

Figure 4-1: Schematic diagram of a radial disbonded coating system.

and $Fe(OH)^{+}$ were considered together with the homogeneous reaction

$$Fe^{+2} + OH^{-} \rightleftharpoons Fe(OH)^{+} \tag{4-1}$$

between Fe^{+2} and OH^{-}. In both systems, the electrochemical reactions at the metal surface along the holiday and disbondment included corrosion, oxygen reduction, and hydrogen evolution described by reactions given in equations (2-41), (2-42), and (2-43), respectively.

4.2 Mathematical Model

The development of the two-dimensional mathematical model DISCOM is presented in this section.

4.2.1 Governing Equations

The governing equation for c_i was given by steady-state mass-conservation, equation (2-5)

$$0 = -\nabla \cdot \boldsymbol{N}_i + R_i$$

In the absence of convection and for a dilute solution, the governing equation for c_i was given by equation (2-11)

$$0 = D_i \left[z_i \nabla \cdot (c_i \nabla \phi) + \nabla^2 c_i \right] + R_i$$

System without $Fe(OH)^{+}$. In the absence of homogeneous reactions when the specie $Fe(OH)^{+}$ was not considered the four species included were Na^{+}, Cl^{-},

$OH^-$and Fe^{+2} . The governing equations for this system comprised of five coupled equations.

The species $Na^+$and Cl^-, were referred to as chemically inert species as they did not participate in homogeneous nor electrochemical reactions. The governing equations for the chemically inert species were

$$0 = D_{Na^+}\left[z_{Na^+}\nabla\cdot(c_{Na^+}\nabla\phi) + \nabla^2 c_{Na^+}\right] \tag{4-2}$$

and

$$0 = D_{Cl^-}\left[z_{Cl^-}\nabla\cdot(c_{Cl^-}\nabla\phi) + \nabla^2 c_{Cl^-}\right] \tag{4-3}$$

for c_{Na^+} and c_{Cl^-} , respectively.

The governing equations for species involved in the electrochemical reactions were

$$0 = D_{OH^-}\left[z_{OH^-}\nabla\cdot(c_{OH^-}\nabla\phi) + \nabla^2 c_{OH^-}\right] + R_{OH^-} \tag{4-4}$$

and

$$0 = D_{Fe^{+2}}\left[z_{Fe^{+2}}\nabla\cdot(c_{Fe^{+2}}\nabla\phi) + \nabla^2 c_{Fe^{+2}}\right] + R_{Fe^{+2}} \tag{4-5}$$

for OH^- and Fe^{+2}, respectively. In equations (4-4) and (4-5) the conditions $R_{OH^-} = 0$ and $R_{Fe^{+2}} = 0$ were used because no homogeneous reactions were considered. The system of equations were completed using the equation

$$z_{Na^+}c_{Na^+} + z_{Cl^-}c_{Cl^-} + z_{OH^-}c_{OH^-} + z_{Fe^{+2}}c_{Fe^{+2}} = 0 \tag{4-6}$$

that satisfied the condition of electroneutrality.

System with $Fe(OH)^+$. When the specie $Fe(OH)^+$ was considered the homogeneous reaction described by equation (4-1) was included. The species considered were Na^+, Cl^-, OH^-, Fe^{+2} , and $Fe(OH)^+$. The governing equations for this system comprised of 6 coupled equations.

The governing equation for $c_{Fe(OH)^+}$ was

$$0 = D_{Fe(OH)^+}\left[z_{FeOH^+}\nabla\cdot(c_{Fe(OH)^+}\nabla\phi) + \nabla^2 c_{Fe(OH)^+}\right] + R_{Fe(OH)^+} \tag{4-7}$$

The homogeneous reaction was assumed to be at equilibrium such that the net production of OH^- by the homogeneous reaction at any position was equal to a zero value

$$R_{OH^-} + R_{Fe(OH)^+} = 0 \tag{4-8}$$

and the net rate of production of Fe^{+2} was also equal to a zero value

$$R_{Fe^{+2}} + R_{Fe(OH)^+} = 0 \tag{4-9}$$

Substitution of equations (4-4) and (4-7) into equation (4-8) yielded the governing equations for c_{OH^-}

$$\begin{aligned} 0 &= D_{OH^-}\left[z_{OH^-}\nabla\cdot(c_{OH^-}\nabla\phi) + \nabla^2 c_{OH^-}\right] \\ &+ D_{Fe(OH)^+}\left[z_{Fe(OH)^+}\nabla\cdot(c_{Fe(OH)^+}\nabla\phi) + \nabla^2 c_{Fe(OH)^+}\right] \end{aligned} \tag{4-10}$$

Substitution of equations (4-5) and (4-7) into equation (4-9) yielded the governing equations for $c_{Fe^{+2}}$

$$\begin{aligned} 0 &= D_{Fe^{+2}}\left[z_{Fe^{+2}}\nabla\cdot(c_{Fe^{+2}}\nabla\phi) + \nabla^2 c_{Fe^{+2}}\right] \\ &+ D_{Fe(OH)^+}\left[z_{Fe(OH)^+}\nabla\cdot(c_{Fe(OH)^+}\nabla\phi) + \nabla^2 c_{Fe(OH)^+}\right] \end{aligned} \tag{4-11}$$

The governing equations when $Fe(OH)^+$ was considered included conservation of species given by equations (4-2), (4-3), (4-10), and (4-11). The equilibrium relationship

$$\frac{c_{Fe(OH)^+}}{c_{OH^-}\cdot c_{Fe^{+2}}} = K_I \tag{4-12}$$

and the electroneutrality condition given by

$$z_{Na^+}c_{Na^+} + z_{Cl^-}c_{Cl^-} + z_{OH^-}c_{OH^-} + z_{Fe^{+2}}c_{Fe^{+2}} + z_{Fe(OH)^+}c_{Fe(OH)^+} = 0 \tag{4-13}$$

completed the set of 6 coupled equations at a given position in the domain of the system.

4.2.2 Boundary Conditions

The conditions of c_i and Φ were fixed at the mouth FE to the bulk conditions $c_{i,\infty}$ and Φ_∞, respectively. The solution potential $\Phi_\infty = 0$ was used such that the calculated values for Φ in the model were referenced to a zero value at the bulk boundary position. The condition for Φ at all boundaries was the electroneutrality condition.

Natural boundary conditions were used for c_{Na^+}, c_{Cl^-}, c_{OH^-}, and $c_{Fe^{+2}}$ at all the boundaries except the mouth. The condition at the boundaries with the coating, BC, CD, and DE and the line of symmetry OF was the the no-flux condition given by

$$\boldsymbol{N}_i \cdot \boldsymbol{n} = 0 \tag{4-14}$$

where $\boldsymbol{n}$ was the unit vector normal to the surface.

On the boundary of the metal surface OB the no-flux condition was used for the chemically inert species Na^+ and Cl^-. The boundary conditions at the metal surface OB for Fe^{+2} and OH^- were obtained by relating the fluxes of these species with the current densities due to the electrochemical reactions on the metal surface. The polarization kinetics of the irreversible electrochemical reactions were used to calculate the current densities of these reactions. The current densities for i_{Fe}, i_{O_2}, and i_{H_2}were given by equations (2-50),(2-51), and (2-52), respectively. The boundary conditions

$$-z_{Fe^{+2}} D_{Fe^{+2}} c_{Fe^{+2}} \frac{\partial \phi}{\partial z} - D_{Fe^{+2}} \frac{\partial c_{Fe^{+2}}}{\partial z} = \frac{i_{Fe}}{2F} \tag{4-15}$$

and

$$-z_{OH^-} D_{OH^-} c_{OH^-} \frac{\partial \phi}{\partial z} - D_{OH^-} \frac{\partial c_{OH^-}}{\partial z} = \frac{i_{O_2}}{F} + \frac{i_{H_2}}{F} \tag{4-16}$$

were used for $c_{Fe^{+2}}$ and c_{OH^-}, respectively, along the metal boundary OB.

When $Fe(OH)^{+}$ was included the homogeneous equilibrium relationship between Fe^{+2} and OH^{-} was used as the boundary condition for $Fe(OH)^{+}$ along the boundaries except the bulk boundary FE where $c_{Fe(OH)^{+}}$ was fixed.

4.2.3 Oxygen Distribution

The polarization expression for the current density due to oxygen reduction, equation (2-51), used the mass-transfer-limited current density i_{lim,O_2} at the metal surface as a parameter. Calculation of the value of i_{lim,O_2} as a function of position on the metal surface involved solving for the oxygen distribution in the domain of the disbonded coating system.

The governing equation for c_{O_2} was given by

$$\nabla^2 c_{O_2} = 0 \tag{4-17}$$

under the assumption that oxygen did not participate in homogeneous reactions. The boundary condition at the mouth FE was the bulk oxygen concentration

$$c_{O_2} = c_{O_2,\infty} \tag{4-18}$$

The boundary condition at the axis of symmetry OF and the coating boundaries BC, CD and DE was the no-flux condition

$$\boldsymbol{N}_{O_2} \cdot \boldsymbol{n} = 0 \tag{4-19}$$

The boundary condition at the metal surface OB was

$$c_{O_2} = 0 \tag{4-20}$$

such that any oxygen at the metal surface was reduced according to oxygen reduction described by equation (2-42).

In cylindrical coordinates the governing equation for c_{O_2} was given by

$$\frac{1}{r}\frac{\partial}{\partial r}\left(r\frac{\partial c_{O_2}}{\partial r}\right) + \frac{1}{r^2}\frac{\partial^2 c_{O_2}}{\partial \theta^2} + \frac{\partial^2 c_{O_2}}{\partial z^2} = 0 \tag{4-21}$$

The axis of symmetry permitted the assumption that there was no variation in the θ-direction and the governing equation for c_{O_2} was recast as

$$\frac{1}{r}\frac{\partial}{\partial r}\left(r\frac{\partial c_{O_2}}{\partial r}\right)+\frac{\partial^2 c_{O_2}}{\partial z^2}=0 \tag{4-22}$$

and expanded to yield

$$\frac{1}{r}\frac{\partial c_{O_2}}{\partial r}+\frac{\partial^2 c_{O_2}}{\partial r^2}+\frac{\partial^2 c_{O_2}}{\partial z^2}=0 \tag{4-23}$$

A finite difference method was employed to solve equation (4-23) with the boundary conditions given by equations (4-18), (4-19), and (4-20). The value of i_{lim,O_2} on the metal surface was calculated using

$$i_{\mathrm{lim},O_2}=nFD_{O_2}\frac{\partial c_{O_2}}{\partial z} \tag{4-24}$$

where $n=4$ was the number of electrons transferred in the electrochemical oxygen reduction reaction per one molecule of oxygen O_2 (see equation (2-42)).

4.3 Method of Solution

The general form of the governing equation for the mass-transfer of a species was given by equation (2-11) and expanded to yield

$$D_i z_i c_i \nabla^2\phi + D_i z_i \nabla c_i \cdot \nabla\phi + D_i \nabla^2 c_i + R_i = 0 \tag{4-25}$$

where the first two terms were related to transport due to migration and the third to diffusion. The migration terms were non-linear and the diffusion term was linear. The radial disbonded coating system was modeled using the cylindrical coordinate system. Symmetry in the θ-direction reduced the dimensionality to two dimensions in the z and r coordinates. Expansion of equation (4-25) in the z and r directions yields

$$\begin{aligned} 0 &= z_i D_i c_i\left[\frac{\partial^2\phi}{\partial r^2}+\frac{\partial^2\phi}{\partial z^2}\right]+z_i D_i\left[\frac{\partial c_i}{\partial r}\frac{\partial\phi}{\partial r}+\frac{\partial c_i}{\partial z}\frac{\partial\phi}{\partial z}\right] \\ &+ D_i\left[\frac{\partial^2 c_i}{\partial r^2}+\frac{\partial^2 c_i}{\partial z^2}\right]+z_i D_i c_i\frac{1}{r}\frac{\partial\phi}{\partial r}+D_i\frac{1}{r}\frac{\partial c_i}{\partial r}+R_i \end{aligned} \tag{4-26}$$

Equation (4-26) represents the general form for the governing equation of c_i . When no homogeneous reactions were considered the system of equations consisted of four equations of the form of equation (4-26), one for each specie, and an algebraic expression for the electroneutrality condition.

The system of equations was non-linear and an iterative method was required to converge on a solution starting from an initial guess. The domain of the disbonded coating system was discretized into a regular grid. The linearized governing equations for species mass-transfer and electroneutrality were discretized using the nodes of the regular grid. Details of the method of solution are given in Appendix A.

The governing equations and boundary conditions for c_i and ϕ were discretized and cast into the form

$$\boldsymbol{K}_D \cdot \boldsymbol{C}_D = \boldsymbol{R}_D \tag{4-27}$$

where $\boldsymbol{K}_D$ was the global coefficient matrix, $\boldsymbol{C}_D$ was the global solution vector of c_i and ϕ, and $\boldsymbol{R}_D$ the global load vector. The matrix $\boldsymbol{K}_D$ and vector $\boldsymbol{R}_D$ were functions of c_i and ϕ and an iterative algorithm was employed. The mathematical model was developed using *Compaq Visual Fortran, Version* 6.1® with double precision accuracy. The program listing for DISCOM is given in Appendix B.

The algorithm for the calculation of the steady-state values for c_i and ϕ by the mathematical model DISCOM is presented in Figure 4-2 and summarized below:

1. The input data required for the model was read from input files in this step. The input data included dimensions of the 2-D domain, grid spacings $\triangle r$ and $\triangle z$, the applied potential Ψ, the convergence criterion $\xi_{o,D}$, and the bulk values for c_i , ϕ, and c_{O_2}.

2. The domain was discretized into regularly spaced nodes using the values of $\triangle r$ and $\triangle z$.

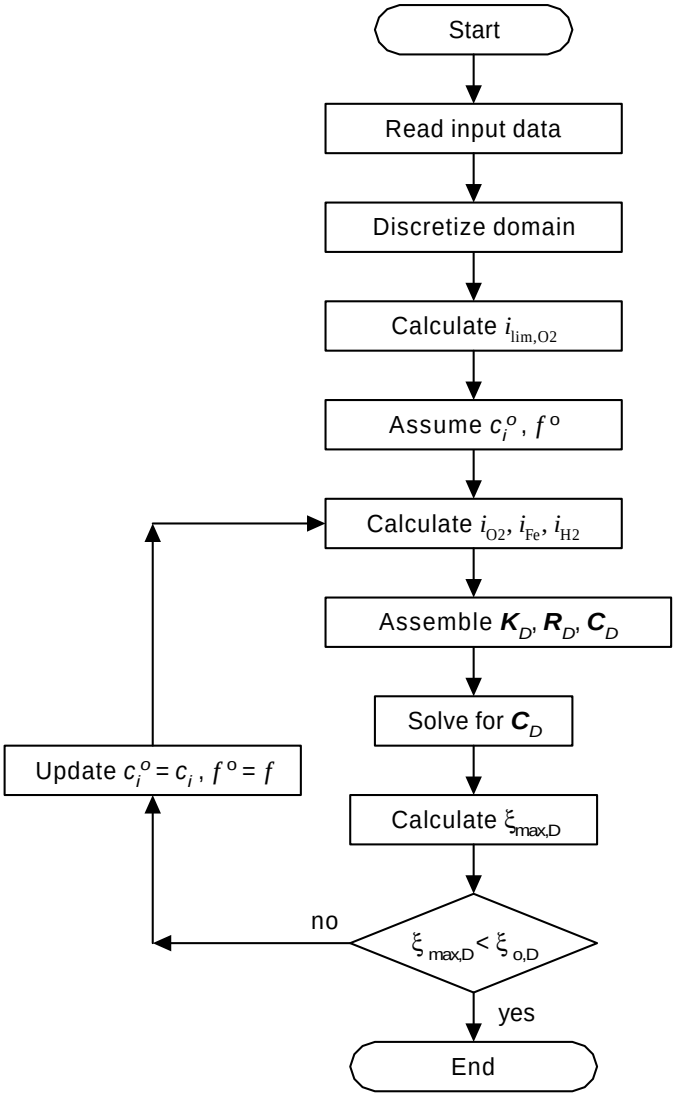

Figure 4-2: Algorithm for the mathematical model DISCOM.

3. The value of i_{lim,O_2} was calculated as a function of position along the metal surface. This involved solving Laplace's equation for c_{O_2}, equation (4-23), and using equation (4-24).

4. Values for c_i^o and ϕ^o were assumed in the domain using the bulk values $c_i^o = c_{i,\infty}$ and $\phi^o = \phi_\infty$.

5. The current densities i_{Fe}, i_{O_2}, and i_{H_2} were calculated as functions of position on the metal surface using the assumed values ϕ^o and the expressions for the polarization kinetics on the metal surface.

6. The global coefficient matrix $\boldsymbol{K}_D$ and global load vector $\boldsymbol{R}_D$ were assembled using the node values of c_i^o and ϕ^o, and the values of i_{lim,O_2}, i_{Fe}, i_{O_2}, and i_{H_2} at the nodes on the metal surface. The matrix $\boldsymbol{K}_D$ represents the linearized governing equations for species transport and electroneutrality.

7. The linear system of equations represented by equation (4-27) was solved using the LAPACK solver[53,54] to yield the calculated values c_i and ϕ. The LAPACK solver used LU decomposition with partial pivoting and row interchanges to solve the linear system of equations.

8. The percentage difference between the assumed values and the calculated values was given by ξ where

$$\xi = 100 \left| \frac{f - f^o}{f^o} \right| \tag{4-28}$$

and f was a generic variable representing the dependent variables c_i and ϕ. The value of ξ for each dependent variable at each node in the domain, except on the bulk boundary, was calculated and the maximum value of ξ, $\xi_{max,D}$, was determined.

9. The value of $\xi_{max,D}$ was compared with a convergence criterion $\xi_{o,D}$. For the condition $\xi_{max,D} > \xi_{o,D}$ the values of c_i^o and ϕ^o were updated with c_i and ϕ, respectively, and control returned to Step 5. For the condition $\xi_{max,D} < \xi_{o,D}$ control was passed to Step 10.

10. The calculated values of c_i and ϕ were written to files and the procedure was terminated.

4.4 Summary

A mathematical model DISCOM for the steady-state conditions in a radial disbonded coating system was developed. This model accounted for the transport of species and electroneutrality in the presence of multiple electrochemical reactions. The model also accommodated the homogeneous reaction between Fe^{+2} and OH^-. Cylindrical coordinates were used to discretize the governing equations. An iterative method of solution was used that involved linearization of the nonlinear governing equations.

CHAPTER 5
DISBONDED COATING ELECTROCHEMISTRY

The disbonded coating system consists of a holiday and a disbondment. The distributions of species concentrations and solution potential in the system are in response to the electrochemical reactions on the metal surfaces of the holiday and disbondment. The key electrochemical reactions are corrosion, oxygen reduction, and hydrogen evolution. The distributions are established by migration and diffusion transport of species driven by solution potential gradients and concentration gradients, respectively. The contribution by convection transport is considered negligible.

Chin and Sabde has presented the only mathematical model for the steady-state conditions in a disbonded coating system in literature.[2,3] The model was specific to systems under cathodic protection such that corrosion was neglected. Oxygen reduction was considered the significant electrochemical reaction with the contribution of hydrogen evolution being assumed negligible. The diffusion and migration of species were considered, however, the diffusion coefficients of the ionic species were assumed to be 10^{-5} cm^2s^{-1}.

A model for the steady-state solution potential distribution in a disbondment has been reported by Song *et al.* .[4,5] The holiday was not considered explicitly in this model as only the disbondment was modeled. All three key electrochemical reactions were considered on the metal surface of the disbondment. The resistivity of the electrolyte was assumed uniform with concentration gradients being neglected.

The mathematical model DISCOM was developed to calculate the steady-state conditions in a radial disbonded coating system. The three key electrochemical reactions were included. The transport of species by diffusion and migration were considered. The condition of electroneutrality was satisfied explicitly.

Simulated results of DISCOM showed that the assumptions used in the models presented by Chin and Sabde[2,3] and Song *et al.*[4,5] were inapplicable. The hydrogen evolution is a significant contributor to disbonded coating system especially in the disbondment where oxygen is depleted. Diffusion and migration of species both contribute to the transport of species. The assumption that the diffusion coefficients be equated to 10^{-5} cm^2s^{-1} eliminates any solution potential difference due to differences in mobility of species. The influence of this assumption is addressed in the following chapter.

The influences of several contributors to the disbonded coating system are shown in this chapter using simulated results of DISCOM. The contributions of applied potential, bulk electrolyte resistivity, disbondment gap size, and disbondment length were influential to the system. The criterion used for the cathodic protection of disbonded coating systems is shown to be applicable to the holiday but does not extend into the disbondment.

5.1 Model Parameters

The model parameters were associated with the geometry of the system, the composition of the bulk electrolyte, and the potential of the metal. The domain of the disbonded coating system is shown in Figure 5-1. The parameters associated with the geometry consisted of the holiday radius r_h (OA), the disbondment length r_d (AB), the disbondment gap g (AD), and the coating thickness a (DE). The parameters associated with the composition of the bulk electrolyte were the bulk concentration of ionic species $c_{i,\infty}$ and the bulk oxygen concentration $c_{O_2,\infty}$. The re-

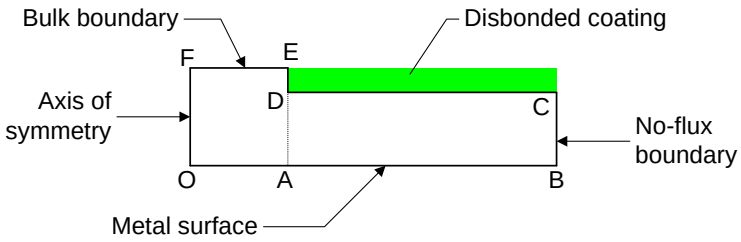

Figure 5-1: Schematic diagram of the domain of the radial disbonded coating system (not drawn to scale).

sistivity of the bulk electrolyte, bulk resistivity, was used to differentiate between different compositions of the bulk electrolyte. The bulk electrolyte consisted of dilute NaCl, which was assumed to be fully dissociated, a neutral pH, and a small concentration of Fe^{+2}. The ionic species considered were Na^{+},Cl^{-},OH^{-}, and Fe^{+2} in all the simulations. The ionic specie H^{+} was not considered under the assumption that the contribution of H^{+} was insignificant in the alkaline electrolyte of the disbonded coating system. The applied potential Ψ represents the potential of the metal such that the solution potential at the mouth of the holiday was a value of 0 V_{SCE} .

Input data for the model included values for D_i and parameters for the expressions used to calculate the polarization kinetics of the electrochemical reactions on the metal surface. The values of D_i for the ionic species were obtained from TEC-TRAN,[55] a transient model of the electrochemistry beneath disbonded coatings, and are given in Table 5.1. The value of $D_{O_2} = 2.92 \times 10^{-5}$ cm^2s^{-1} was used and corresponded to the diffusion coefficient in dilute NaCl solution.[56] The parameters used in the polarization expressions, equations (2-46), (2-47), and (2-48), are given in Table 2.1. The applied potential used in this expression was referenced to a standard calomel electrode (SCE) and the applied potentials reported here were similarly referenced.

The value of i_{lim,O_2} was used as an input parameter in the polarization expression for the current density i_{O_2} (see equation (2-48)). The distribution of i_{lim,O_2} on

Table 5.1: Diffusion coefficients in an aqueous medium D_i.

Specie i	$D_i \times 10^5$ ($cm^2 s^{-1}$)
Na^+	1.33410
Cl^-	2.03440
OH^-	5.24580
Fe^{+2}	0.71231
$Fe(OH)^+$	0.71172
Zn^{+2}	0.71231

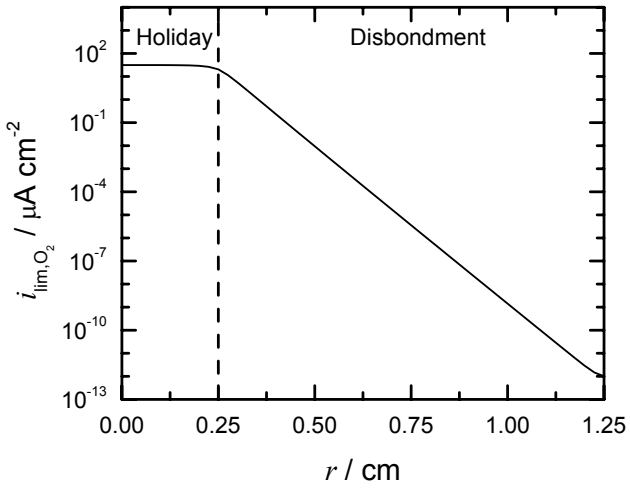

Figure 5-2: Calculated value of absolute value of oxygen reduction current density as a function of radial position on the metal surface. The dashed line at $r = 0.25$ cm indicates the boundary between the holiday and the disbondment.

the metal surface was obtained as a solution to Laplace's equation for c_{O_2} and is shown in Figure 5-2. The value of i_{lim,O_2} was approximately constant at 31 $\mu A/cm^2$ along the holiday metal surface and decreased exponentially along the disbondment metal surface such that at a position of 0.5 cm the value of i_{lim,O_2} was three orders of magnitude less than on the holiday surface. The distribution of i_{lim,O_2}used in the present work was consistent with the results of the mathematical model developed by Chin and Sabde.[2,3] The large exponential decrease in i_{lim,O_2} corresponded to an exponential decrease in the concentration of oxygen within the disbondment. Depletion of oxygen within the disbondment was observed in experimental studies[57] and also simulated in reported mathematical models.[4]

Table 5.2: Model parameters for System 1.

Parameter	Value
Disbondment length r_d	1.0 cm
Holiday radius r_h	0.25 cm
Gap size g	0.05 cm
Coating thickness a	0.05 cm
Bulk Na^+ concentration $c_{Na^+,\infty}$	10^{-3} M
Bulk Cl^- concentration $c_{Cl^-,\infty}$	10^{-3} M
Bulk OH^- concentration $c_{OH^-,\infty}$	10^{-7} M
Bulk Fe^{+2} concentration $c_{Fe^{+2}}$	10^{-15} M
Bulk resistivity ρ_∞	7.9 kΩ cm
Applied potential Ψ	-0.773 V_{SCE}

The model DISCOM was applied to several systems designated as Systems 1 through 12. In all these systems except for System 5, grid spacings of $\triangle r = 0.025$ cm and $\triangle z = 0.0125$ cm were used in the radial and axial directions, respectively. Grid spacings of $\triangle r = 0.025$ cm and $\triangle z = 0.00625$ cm were used in System 5. The convergence criterion for the iterative algorithm in DISCOM was $\xi_{o,D} = 0.01$.

The parameters for System 1 are given in Table 5.2. The bulk electrolyte was composed of 10^{-3} M NaCl, 10^{-7} MOH^-, and 10^{-15} MFe^{+2}. This bulk composition corresponded to a resistivity of 7.9 kΩ cm . Three electrochemical reactions were considered in System 1, oxygen reduction, hydrogen evolution, and corrosion. The applied potential for System 1 was the NACE recommended criterion for cathodic protection, *i.e.*, -0.773 V_{SCE}.

The model parameters for System 2 were the same as System 1. In System 2 the electrochemical reactions considered were oxygen reduction and corrosion. Hydrogen evolution was not considered as an electrochemical reaction in System 2 with the model parameters being the same for Systems 1 and 2. The results of Systems 1 and 2 were compared to demonstrate the importance of hydrogen evolution in disbonded coating systems.

Table 5.3: Model parameters for Systems 3 through 12.

System	Parameter	Value
3	Ψ	-0.823 V_{SCE}
4	Ψ	-0.723 V_{SCE}
5	g	0.025 cm
6	$c_{NaCl,\infty}$	10^{-2} M
7	$c_{NaCl,\infty}$	10^{-4} M
8	r_d	2.0 cm
9	r_d	3.0 cm
10	r_d and Ψ	3.0 cm and -0.529 V_{SCE}
11	r_d and Ψ	3.0 cm and -0.681 V_{SCE}
12	r_d and Ψ	3.0 cm and -0.818 V_{SCE}

System 1 was used as the control system and a parameter variation study was conducted by allowing the other systems, System 3 to 12, to be different from System 1 in specific parameters. The parameters for Systems 3 to 12 that are different from that used in System 1 are given in Table 5.3. The three key electrochemical reactions were considered in Systems 3 to 12, similar to System 1.

The influence of applied potential was investigated by comparing the results of Systems 1, 3, and 4. In System 3 the applied potential was -0.823 V_{SCE}, 50 mV more negative than -0.773 V_{SCE}. The applied potential in System 4 was -0.723 V_{SCE}, 50 mV more positive than -0.773 V_{SCE}. The influence of gap size was investigated by comparing the results of Systems 1 and 5. The value of g in System 5 was 0.025 cm , half of the gap used in System 1. The influence of the bulk resistivity was investigated by comparing the results of Systems 1, 6, and 7. The bulk value of $c_{NaCl,\infty}$was different for System 1, 6, and 7. The influence of the disbondment length was investigated by comparing the results for Systems 1, 8, and 9. The disbondment length of Systems 8 and 9 were 2 and 3 cm, respectively. The influence of cathodic protection criterion on a disbonded coating system is presented using the results from Systems 9, 10, 11, and 12.

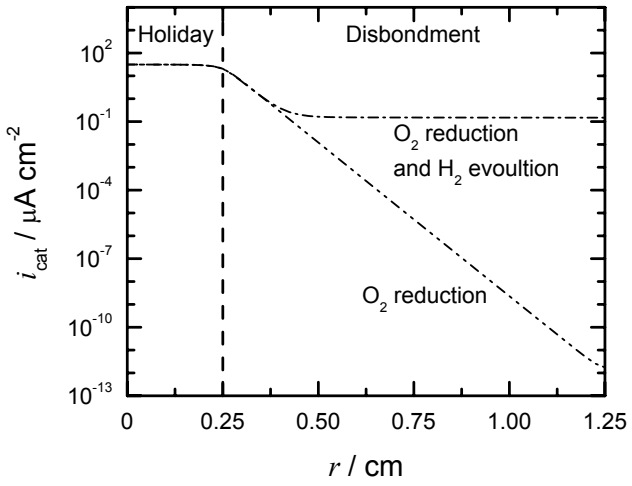

Figure 5-3: Calculated absolute value of cathodic current density as a function of radial position on the metal surface for the conditions when hydrogen evolution was included and when it was not included. The dashed line at $r = 0.25$ cm indicates the boundary between the holiday and the disbondment.

5.2 Importance of Hydrogen Evolution

The significant cathodic reactions in disbonded coating systems are oxygen reduction and hydrogen evolution. These reactions contribute to the disbonded coating system by producing OH^- ions on the metal surface. The importance of the hydrogen evolution in disbonded coating systems is presented in this section.

A measure of the rate of production of OH^- ions on the metal surface is given by the net cathodic current density i_{cat}. The distribution of the absolute value of i_{cat} on the metal surface is shown in Figure 5-3 for Systems 1 and 2. In System 1 both oxygen reduction and hydrogen evolution were considered, whereas in System 2 only oxygen reduction was considered.

The variations of i_{cat} with position on the metal surface for the systems were similar in the holiday and different in the disbondment. In the holiday, the absolute value of i_{cat} was constant at a value of 31 μA/cm^2 for both systems. For System 1, the absolute value of i_{cat} decreased with position exponentially up to $r = 0.38$ cm and then was approximately constant at 10^{-1} μA/cm^2 for the remain-

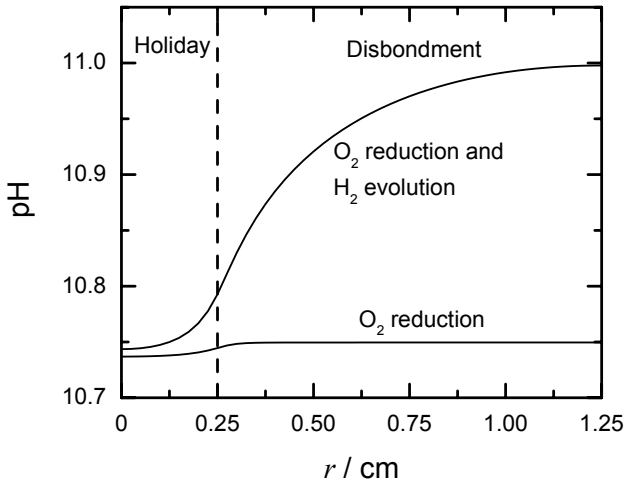

Figure 5-4: Calculated value of pH as functions of position on the metal surface for the conditions when hydrogen evolution was included and when it was not included. The dashed line at $r = 0.25$ cm indicates the boundary between the holiday and the disbondment.

der of the disbondment. For System 2, the absolute value of i_{cat} decreased exponentially in the disbondment. For positions $r < 0.38$ cm the distributions for the systems superimposed.

Comparison of Figures 5-2 and 5-3 shows that the distribution of i_{O_2} was the same as the distribution of i_{lim,O_2}. This was because oxygen reduction was mass-transfer-limited at the applied potential of -0.773 V_{SCE} used in these systems. In System 1, oxygen reduction was the significant cathodic electrochemical reaction for positions less than 0.38 cm , and hydrogen evolution was the significant cathodic electrochemical reaction for positions greater than 0.38 cm.

The influence of the hydrogen evolution reaction in terms of the production of OH^- ions can be seen in the distribution of pH on the metal surface that is shown in Figure 5-4 for Systems 1 and 2. The variations of pH with position on the metal surface in the disbondment were different for the two systems. When oxygen reduction was the only cathodic reaction, the value of pH increased slightly with position up to $r = 0.38$ cm and then was approximately constant. The radial gradient of pH was zero for $r > 0.38$ cm. When hydrogen evolution was included,

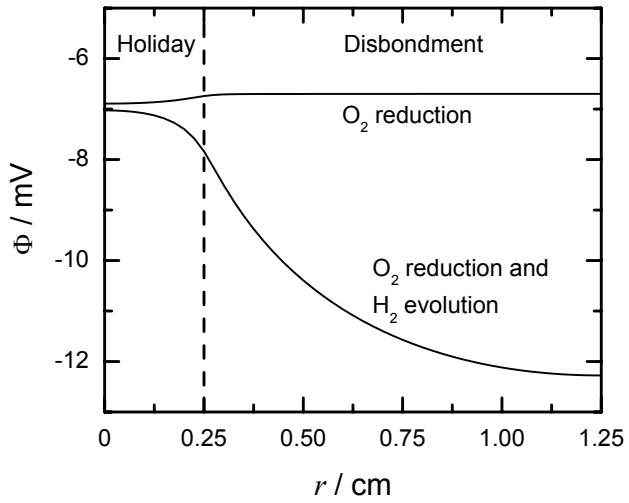

Figure 5-5: Calculated value of solution potential as a function of position on the metal surface for the conditions when hydrogen evolution was included and when it was not included. The dashed line at $r = 0.25$ cm indicates the boundary between the holiday and the disbondment.

the pH value increased with position in the disbondment with the radial gradient of pH approaching a zero value as the tip of the disbondment was approached.

For a given position in disbondment where $r > 0.38$ cm, a larger pH value was associated with the system that included hydrogen evolution. In System 2, the production of OH^- ions for $r > 0.38$ cm was by oxygen reduction which decreased exponentially with position. In System 1, the production of OH^- for positions in the disbondment was approximately 1000 times smaller than in the holiday but was still significant to contribute to the disbonded coating system.

The hydrogen evolution reaction on the metal surface contributed directly to the pH in the system as it produced OH^- ions. The distributions of the solution potential and other species concentrations were also influenced by hydrogen evolution as the phenomena that govern them were coupled. For example, the distribution of solution potential on the metal surface is shown in Figure 5-5 for Systems 1 and 2. For a given position in the disbondment, a more negative solution potential value was associated with the System that included hydrogen evolution.

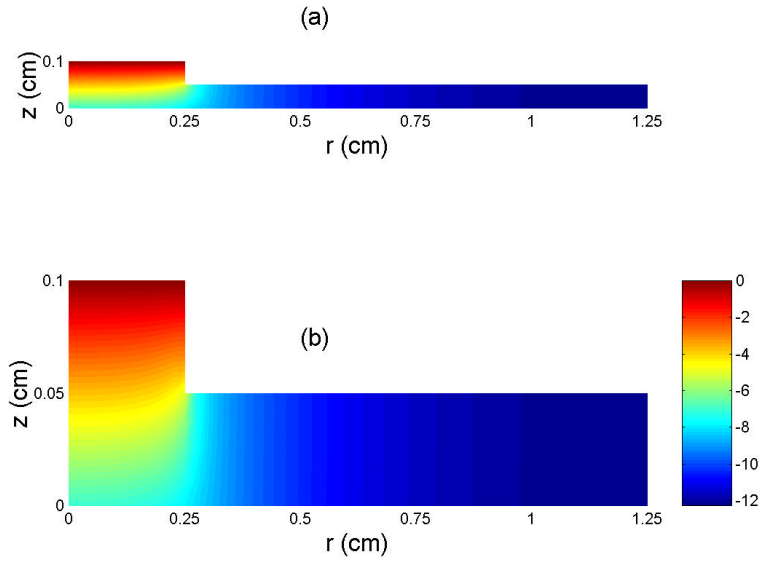

Figure 5-6: Calculated value of solution potential as a function of position in the two-dimensional domain for System 1. (a) drawn to scale and (b) expanded axial scale.

5.3 Influence of Applied Potential

The potential difference between the metal potential Ψ and the adjacent electrolyte solution potential Φ was the driving force for an electrochemical reaction on the metal surface. The applied potential therefore contributed to the production of species on the metal surface and the steady-state conditions in the disbonded coating system. The influence of the applied potential on the system is presented in this section.

5.3.1 Solution Potential

A plot of the solution potential Φ as a function of position in the two-dimensional domain is shown in Figure 5-6 for System 1 with an applied potential of $-0.773\ V_{SCE}$. The plot shown in Figure 5-6(a), which was drawn to scale, highlights the axial and radial dimensions of the system. There was a drop of approximately 7 mV between the mouth and metal surface of the holiday, a length of 0.1 cm. The solution potential drop across the 1 cm length disbondment was approximately 5 mV in the radial direction. The expanded axial scale used in Figure 5-6(b) shows that

the significant variation of Φ in the holiday was in the axial direction, whereas the significant variation of Φ in the disbondment was in the radial direction.

The negligible axial variation of Φ in the disbondment was consistent with experimental observations,[58] and supports the treatment of the disbondment as a one-dimensional domain with variation in the radial direction. This one-dimensional treatment of the disbondment was used in the development of a model for the cathodic delamination system, CADEM, presented in Chapter 11.

The gradient of Φ influenced the migration transport of species. The electric field is calculated as the negative gradient of Φ and represents the electromotive force on a positively charged particle. The electric field in the holiday was positive in the axial direction and in the disbondment was negative in the radial direction. Positive species migrated into the holiday from the bulk electrolyte, and into the disbondment from the holiday. Conversely, negative species migrated out of the disbondment and into the holiday, and out of the holiday and into the bulk electrolyte.

The distribution of solution potential on the metal surface is shown in Figure 5-7 with applied potential as a parameter. The variations of Φ with position were similar for the three applied potentials. The value of Φ decreased with position along the metal surfaces of the holiday and disbondment. For a given distribution, the radial gradient of Φ was the largest at the entry of the disbondment ($r = 0.25$ cm) and approached a value of zero as the tip of the disbondment was approached ($r = 1.25$ cm). For a given position on the metal surface, more negative values of Φ were associated with more negative applied potentials.

The values of the solution potential drop across the length of the disbondment were approximately 2 mV, 5 mV, and 10 mV for the applied potentials of -0.723 V_{SCE}, -0.773 V_{SCE}, and -0.823 V_{SCE}, respectively. For a given system, the

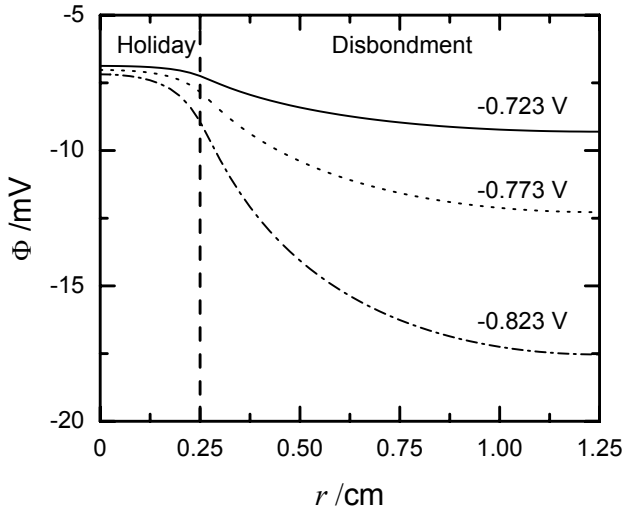

Figure 5-7: Calculated value of solution potential as a function of radial position on the metal surface with applied potential as a parameter. The dashed line at $r = 0.25$ cm indicates the boundary between the holiday and the disbondment.

solution potential drop in the disbondment was larger for more negative applied potentials. The largest difference in Φ between the distributions associated with the applied potentials of -0.723 and -0.823 V_{SCE} were 2 mV in the holiday and 9 mV in the disbondment. This indicated that the applied potential had a larger influence on the solution potential in the disbondment than in the holiday. These results are consistent with simulations of mathematical models reported in literature[5,37] and with experimental observations.[57–60]

5.3.2 Electrochemical Current Densities

The production of ionic species by surface electrochemical reactions provided significant changes to the electrolyte in the disbonded coating system as compared to the bulk electrolyte. A measure of a surface electrochemical reaction is given by the local current density of the reaction on the metal surface. A cathodic current density was represented by a negative value and an anodic current density by a positive value.

The cathodic current densities on the metal surface were due to oxygen reduction i_{O_2} and hydrogen evolution i_{H_2}. The absolute values of i_{O_2} and i_{H_2} as functions

of position on the metal surface are shown in Figure 5-8 with applied potential as a parameter. The distributions of i_{O_2} were independent of applied potential and in fact was equal to the distribution to i_{lim,O_2} (see Figure 5-2). This indicated that the value of $i_{O_2}$was mass-transfer-limited and independent of Φ for the range of applied potentials used in these simulations. The production of OH^- ions due to $i_{O_2}$was approximately constant along the holiday and decreased exponentially with position inside the disbondment.

The absolute value of i_{H_2} decreased with position for a given applied potential. The change in i_{H_2} across the disbondment was larger at a more negative applied potential. The values of i_{H_2} were on the order of of 10^{-1} $\mu A/cm^2$. This value was much smaller than the value of i_{O_2} in the holiday, but, in the disbondment where i_{O_2} was negligible, hydrogen evolution was the primary source of OH^-.

The anodic current density on the metal surface was due to corrosion i_{Fe}. The distribution of i_{Fe} on the metal surface is shown in Figure 5-9 with applied potential as a parameter. The value of i_{Fe} increased slightly with position, less than an order of magnitude, across the metal surface for the three applied potentials. The small changes in i_{Fe} with position for the three applied potentials were consistent with the small changes in Φ that were calculated.

The net current density i_{net} was given by the sum of the current densities of the oxygen reduction, hydrogen evolution, and corrosion electrochemical reactions. For a given applied potential, the value of i_{net} was negative along the metal surface which indicated that the cathodic current density was larger than the anodic current density. This demonstrated that the system was under cathodic protection for the applied potentials of -0.723, -0.773, and -0.823 V_{SCE} used in the simulations.

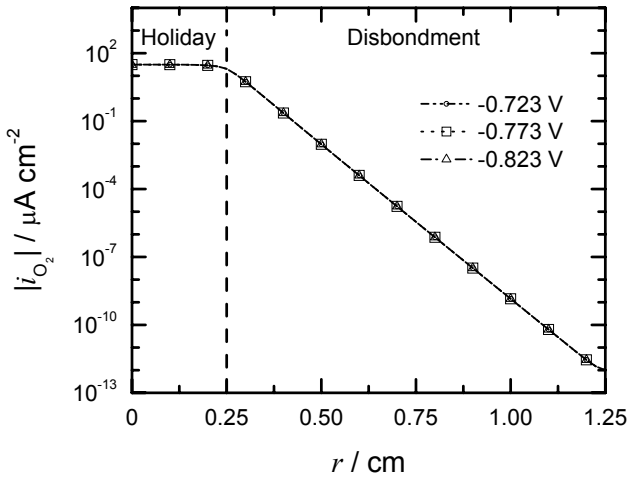

(a)

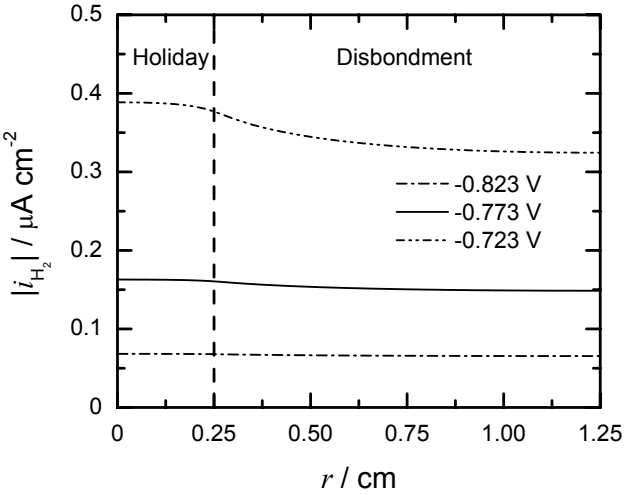

(b)

Figure 5-8: Calculated absolute value of the current density for the cathodic electrochemical reactions as a function of position on the metal surface with applied potential as a parameter. (a) oxygen reduction and (b) hydrogen evolution. The current density distributions for oxygen reduction are superimposed. The dashed line at $r = 0.25$ cm indicates the boundary between the holiday and the disbondment.

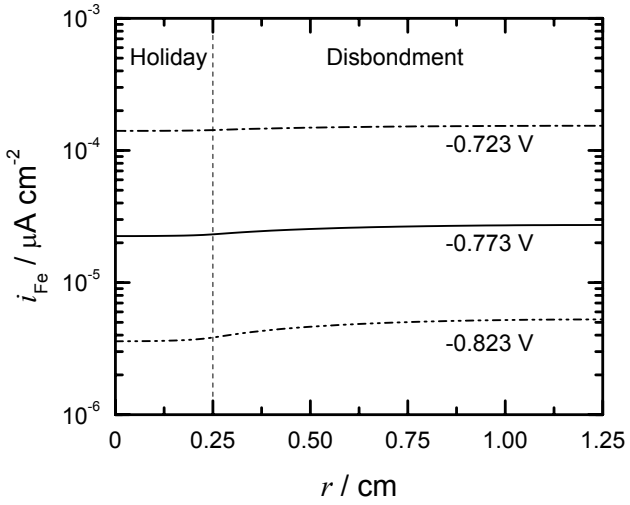

Figure 5-9: Calculated value of corrosion current density as a function of position on the metal surface with applied potential as a parameter. The dashed line at $r = 0.25$ cm indicates the boundary between the holiday and the disbondment.

The distribution of the absolute value of i_{net} is shown in Figure 5-10 with applied potential as a parameter. The variations of i_{net} with position were similar for the three applied potentials. Comparison of Figures 5-2 and 5-10 shows that for a given position in the holiday the value of i_{net} was equal to the value of i_{O_2}. Therefore, oxygen reduction was dominant in the holiday; whereas, hydrogen evolution and corrosion were negligible in the holiday. Along the disbondment surface the absolute value of i_{net} decreased up to a position of 0.5 cm and then remained approximately constant. For a given position in the disbondment greater than 0.5 cm, larger absolute values for the net current density were associated with more negative applied potentials. This result was expected as larger absolute values of i_{H_2} were associated with more negative applied potentials, as seen in Figure 5-8(b).

5.3.3 Ionic Current Density

The generation of current by the electrochemical reactions on the metal surface required the passage of current in the electrolyte. Current was carried by the transport of ionic species in the electrolyte. As seen in Figure 5-6, it can be assumed that the axial variation of Φ in the disbondment was negligible. The axial variation of c_i

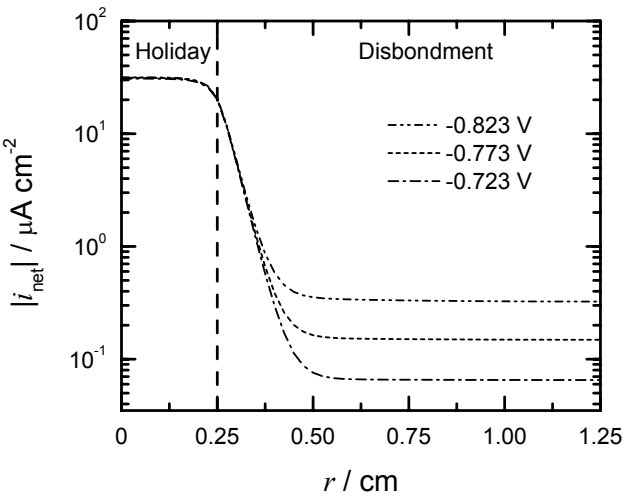

Figure 5-10: Calculated absolute value of net current density as a function of radial position on the metal surface with applied potential as a parameter. The dashed line at $r = 0.25$ cm indicates the boundary between the holiday and the disbondment.

was also negligible in the disbondment. It was therefore assumed that the significant current density distribution in the disbondment was in the radial direction.

The distribution of the radial current density i_r in the disbondment is shown in Figure 5-11 with applied potential as a parameter. The value of i_r was positive in the disbondment as current was supplied to the disbondment metal surface. The variations of i_r were similar for the three applied potentials. The value of i_r decreased with position approaching a zero-value as the disbondment tip was approached. For a given position in the disbondment, larger values of i_r were associated with more negative applied potentials. This was because hydrogen evolution became more significant with more negative applied potentials. Comparison of the distributions of Φ and i_r, given Figures 5-7 and 5-11, shows that larger values of i_r at the entry of the disbondment were associated with larger solution potential drops in the disbondment.

In the disbondment, the radial ionic current density was the sum of the radial migration current density $i_{r,m}$ and the radial diffusion current density $i_{r,d}$ (see equation 2-18). The values of $i_{r,m}$ and $i_{r,d}$ as functions of position are shown in Fig-

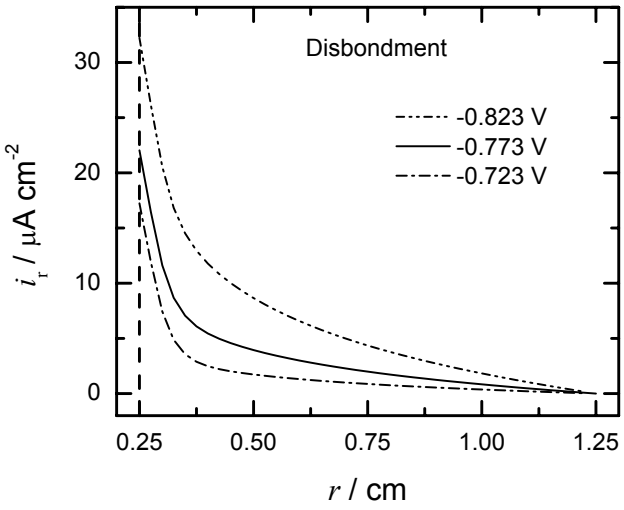

Figure 5-11: Calculated value of radial ionic current density in the disbondment as a function of position with applied potential as a parameter. The dashed line at $r = 0.25$ cm indicates the boundary between the holiday and the disbondment.

ure 5-12 with applied potential as a parameter. For a given applied potential, the variations of $i_{r,m}$ and $i_{r,d}$ with position were similar to that of i_r with position. The values of $i_{r,m}$ and $i_{r,d}$ decreased with position in the disbondment and approached a zero-value as the disbondment tip was approached. For a given position in the disbondment, larger values of $i_{r,m}$ and $i_{r,d}$ were associated with more negative applied potentials. This was consistent with the distributions of i_r seen in Figure 5-11. Therefore, for a given bulk electrolyte resistivity and at a given position in the disbondment, a change to a more negative applied potential resulted in increases in both $i_{r,m}$ and $i_{r,d}$.

The percentage contributions of $i_{r,m}$ and $i_{r,d}$ to the radial current density as functions of position is shown in Figure 5-13 with applied potential as a parameter. For $r > 1.125$ cm the $i_{r,m}$-contribution and $i_{r,d}$-contributions are not included as i_r approached a zero value due the no-flux condition for c_i at the coating boundary, $r = 1.25$ cm. The variations of the contributions of $i_{r,m}$ with position were similar for the three applied potentials; likewise, the variations of the $i_{r,d}$-contributions with position were similar for the three applied potentials. For a given applied

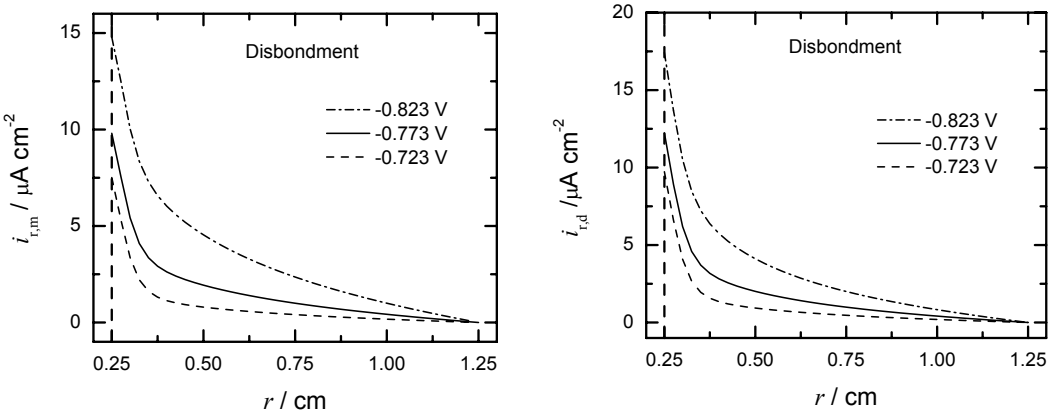

(a) (b)

Figure 5-12: Calculated values of radial ionic current density contributors in the disbondment as functions of position with applied potential as a parameter. (a) radial migration and (b) radial diffusion current densities. The dashed line at $r = 0.25$ cm indicates the boundary between the holiday and the disbondment.

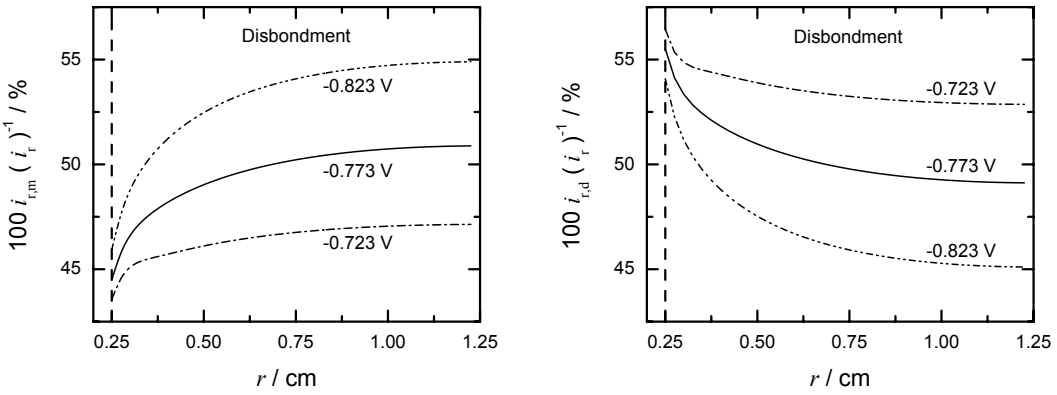

(a) (b)

Figure 5-13: Calculated values of relative contributions to radial ionic current density in the disbondment as a function of position with applied potential as a parameter. (a) radial migration current density and (b) radial diffusion current density. The dashed line at $r = 0.25$ cm indicates the boundary between the holiday and the disbondment.

potential, the value of the $i_{r,m}$-contribution increased with position in the disbondment. Conversely, for a given applied potential, the value of the $i_{r,d}$-contribution decreased with position in the disbondment.

The percentage contributions of $i_{r,d}$ and $i_{r,m}$ were on the same order of magnitude for the different applied potentials. The diffusion current density was driven by concentration gradients, therefore, the influence of concentration gradients on the conditions in the disbondment was significant. This result demonstrated that the assumption of negligible concentration gradients in the disbondment is invalid. This assumption was used in the model presented by Song *et al.* .[4,5] For a given position, smaller percentage contributions of $i_{r,d}$ and larger percentage contributions of $i_{r,m}$ were associated with more negative applied potentials. This was because larger solution potential drops in the disbondment were associated with more negative applied potentials, and $i_{r,m}$ was driven by solution potential gradients.

5.3.4 pH Distribution

A plot of pH as a function of position in the two-dimensional disbonded coating domain is shown in Figure 5-14 for System 1. The significant pH gradients were axial in the holiday and radial in disbondment. The pH difference of 3.7 units between the mouth and metal surface of the holiday represented a negative concentration gradient for OH^- in the axial direction in the holiday. Hydroxide ions were produced by the cathodic reactions on the metal surface, therefore, the net flux of OH^- was out of the domain through the mouth of the holiday. In the holiday, the positive electric field and the negative gradient of c_{OH^-} in the axial direction facilitated the migration and diffusion of OH^- out of the domain into the bulk electrolyte.

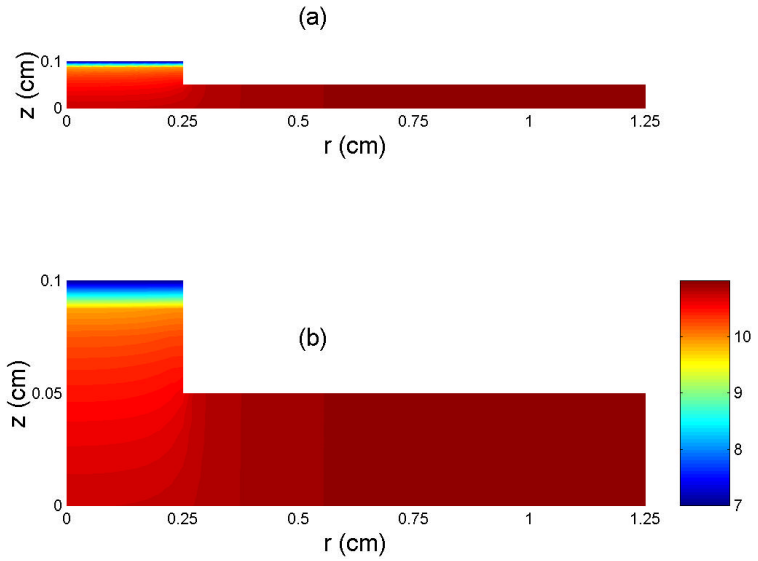

Figure 5-14: Calculated value of pH as a function of position in the two-dimensional domain for System 1. (a) drawn to scale and (b) expanded axial scale.

The distribution of pH on the metal surface is shown in Figure 5-15 with applied potential as a parameter. The variations of pH with position on the metal surface were similar for the three applied potentials. The pH increased with position and the radial gradient of pH approached a zero value as the disbondment tip was approached. The largest radial gradient of pH was located at the entry of the disbondment. For a given position on the metal surface, larger pH values were associated with more negative applied potentials. This was because the production of OH^- ions by hydrogen evolution increased with more negative applied potentials. This result was consistent with reported simulated[37] and experimental results.[58] Comparison of the distributions of pH and i_r, Figures 5-15 and 5-11, shows that at the entry of the disbondment, larger pH values were associated with larger values of i_r.

5.3.5 Ferrous Ion Distribution

A plot of the value of $c_{Fe^{+2}}$ as a function of position in the two-dimensional domain is shown in Figure 5-16 for System 1. The significant variations of $c_{Fe^{+2}}$ were axial in the holiday and radial in the disbondment. The axial gradients for

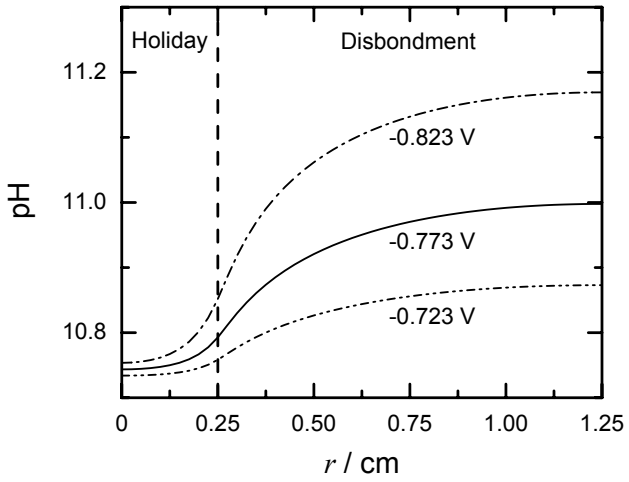

Figure 5-15: Calculated value of pH as a function of position on the metal surface with applied potential as a parameter. The dashed line at $r = 0.25$ cm indicates the boundary between the holiday and the disbondment.

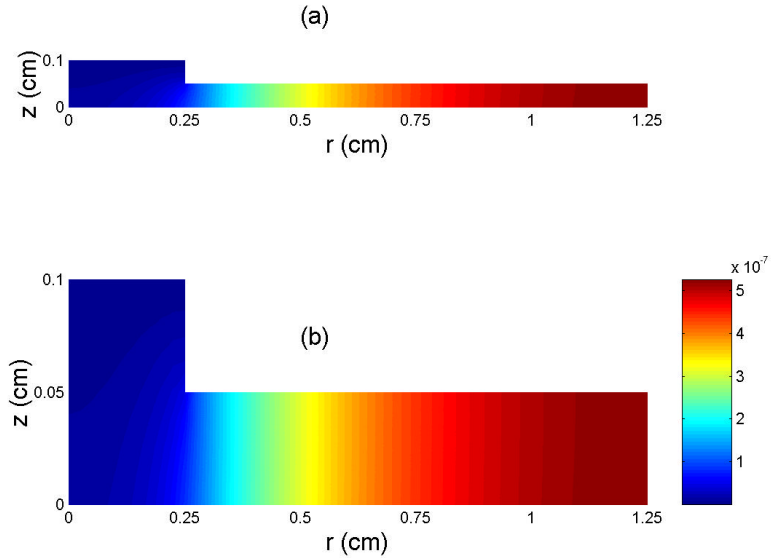

Figure 5-16: Calculated value of ferrous ion concentration as a function of position in the two-dimensional domain for System 1. (a) drawn to scale and (b) expanded axial scale.

$c_{Fe^{+2}}$ between the mouth and metal surface of the holiday was negative and drove Fe^{+2} ions out of the holiday and into the bulk electrolyte by diffusion. The radial gradient for $c_{Fe^{+2}}$ in the disbondment was negative and drove Fe^{+2} ions out of the disbondment and into the holiday.

The electric field in the system drove Fe^{+2} ions into the holiday from the bulk electrolyte and Fe^{+2} into the disbondment from the holiday. The Fe^{+2} species was produced along the metal surface by corrosion. The steady-state condition required no accumulation of species in the domain, therefore, there was a net flux of Fe^{+2} out of the domain. The net flux of Fe^{+2} out of the holiday into the bulk electrolyte was because the axial diffusion dominated the axial migration of Fe^{+2} in the holiday. Similarly, the net flux of Fe^{+2} out of the disbondment into the holiday was because the radial diffusion dominated the radial migration of Fe^{+2} in the disbondment.

Experiments conducted on disbonded coating systems are performed with a negligible concentration of ferrous ions in the bulk electrolyte. The value of $c_{Fe^{+2}}$ used in the simulations was negligible as compared to the other ionic species. The value of $c_{Fe^{+2}}$ in the bulk electrolyte was set at 10^{-15} M, eight orders of magnitude less than c_{OH^-} and twelve orders of magnitude less than c_{Na^+} and c_{Cl^-} . The value of $c_{Fe^{+2}}$ on the metal surface relative to $c_{Na^+,\infty}$ is shown in Figure 5-17 with applied potential as a parameter. The variation of $c_{Fe^{+2}}$ with position were similar for the three applied potentials. The value of $c_{Fe^{+2}}$ increased with position along the metal surface. The radial gradient of $c_{Fe^{+2}}$ approached a zero value as the tip of the disbondment was approached. The positive radial gradients of $c_{Fe^{+2}}$ in the disbondment, for a given applied potential, facilitated the diffusion of Fe^{+2} out of the disbondment and into the holiday.

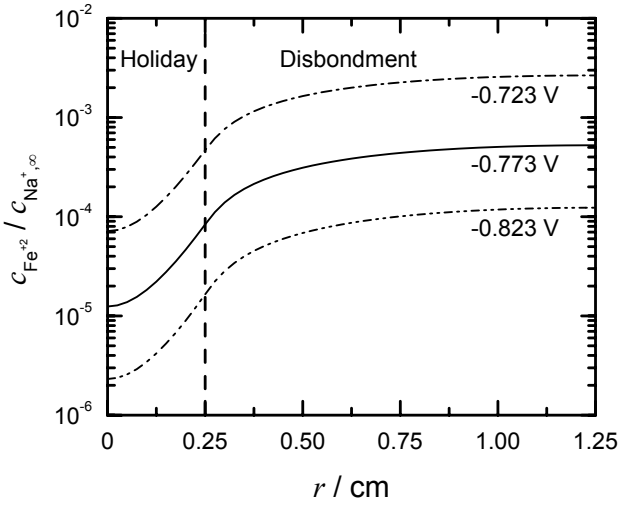

Figure 5-17: Calculated value of ferrous ion concentration as a function of position on the metal surface with applied potential as a parameter. The dashed line at $r = 0.25$ cm indicates the boundary between the holiday and the disbondment.

A measure of the electrochemical production of Fe^{+2} ions on the metal surface was given by the corrosion current density seen in Figure 5-9. For a given position on the metal surface, larger values of $c_{Fe^{+2}}$ were associated with more positive applied potentials. This was because the corrosion reaction increased with more positive applied potentials.

5.3.6 Chemically Inert Species

The bulk electrolyte used in the systems was dilute NaCl and contributed the ionic species Na^+ and Cl^- to the disbonded coating system. These species were considered inert as they did not participate in the electrochemical reactions on the metal surface, however, they contributed to the system by influencing the local electrolyte resistivity.

Plots of c_{Na^+} and c_{Cl^-} as functions of position in the two-dimensional domain are shown in Figures 5-18 and 5-19, respectively, for System 1. In the holiday, the axial variations of the inert species were significant; whereas, in the disbondment the radial variations were significant. The constraint of a zero-flux for these species required that there be no net transport of Na^+ and Cl^- at any position in the do-

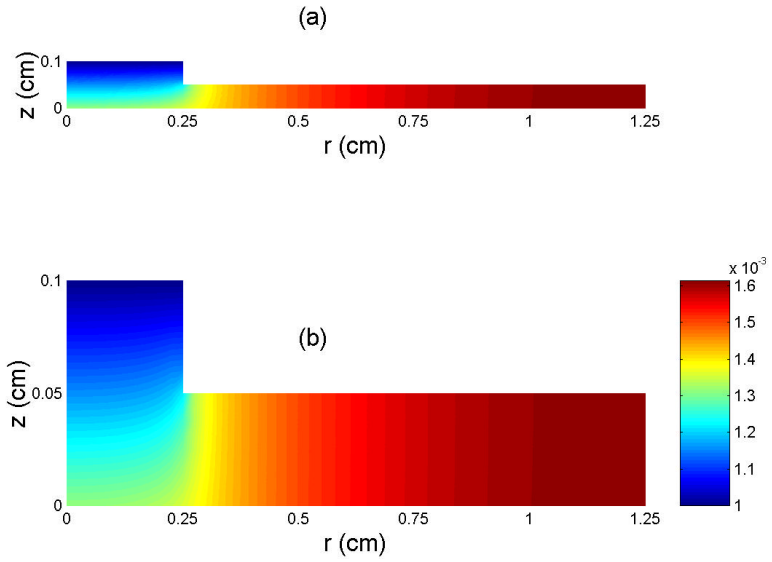

Figure 5-18: Calculated value of sodium ion concentration as a function of position in the two-dimensional domain for System 1 (a) drawn to scale and (b) expanded axial scale.

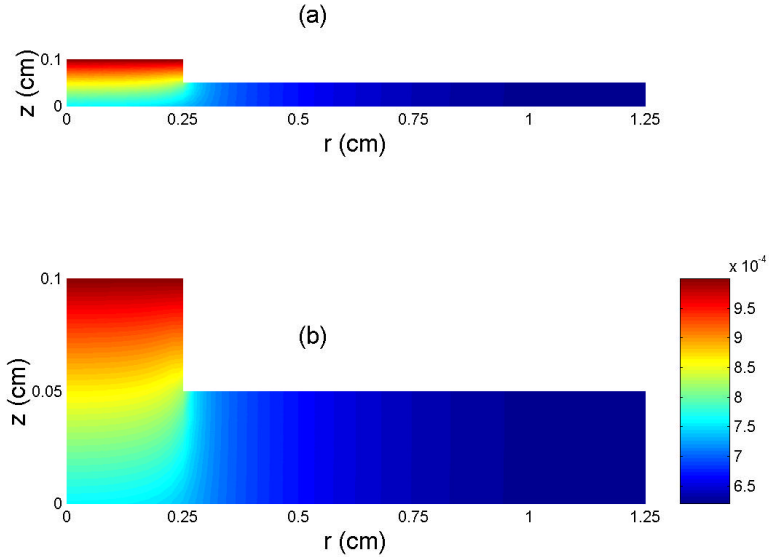

Figure 5-19: Calculated value of chloride ion concentration as a function of position in the two-dimensional domain for System 1. (a) drawn to scale and (b) expanded axial scale.

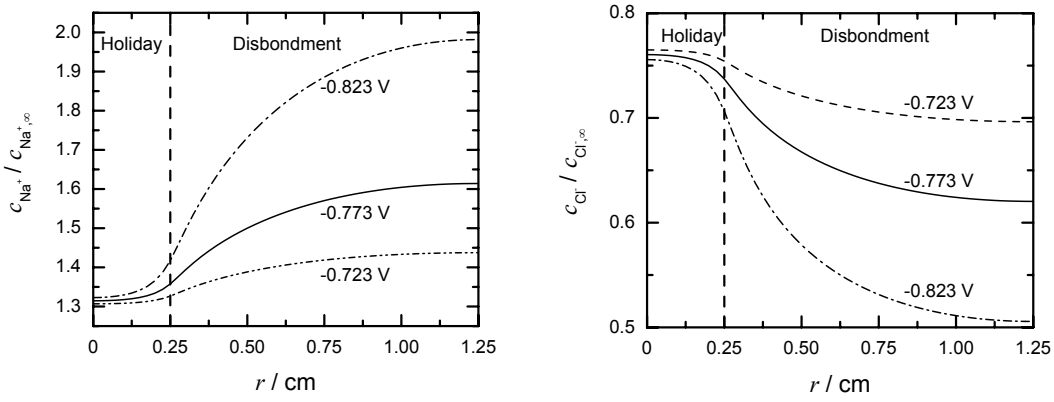

(a) (b)

Figure 5-20: Calculated value of concentration of chemically inert specie as a function of position on the metal surface with applied potential as a parameter. (a) sodium ion and (b) chloride ion. The dashed line at $r = 0.25$ cm indicates the boundary between the holiday and the disbondment.

main. The concentration gradients of Na^+ and Cl^- that existed in the holiday and disbondment drove transport by diffusion of these species. This diffusion transport was balanced by migration transport, that was driven by solution potential gradients.

The values of c_{Na^+} and c_{Cl^-} as functions of position on the metal surface are shown in Figure 5-20 with applied potential as a parameter. The distributions of c_{Na^+} and c_{Cl^-} were similar for the three applied potentials. The value of c_{Na^+} was approximately constant at 1.3 times the bulk value for positions on the holiday metal surface and increased with position along the metal surface of the disbondment. The value of c_{Cl^-} was approximately constant at a value 0.76 times the bulk value for positions on the holiday metal surface and decreased with position along the metal surface of the disbondment. The radial gradients of c_{Na^+} and c_{Cl^-} in the disbondment approached a zero value as the disbondment tip was approached. The calculated concentrations of Na^+ and Cl^- at the metal surface were in response to the generation of OH^- by electrochemical reactions and the constraint

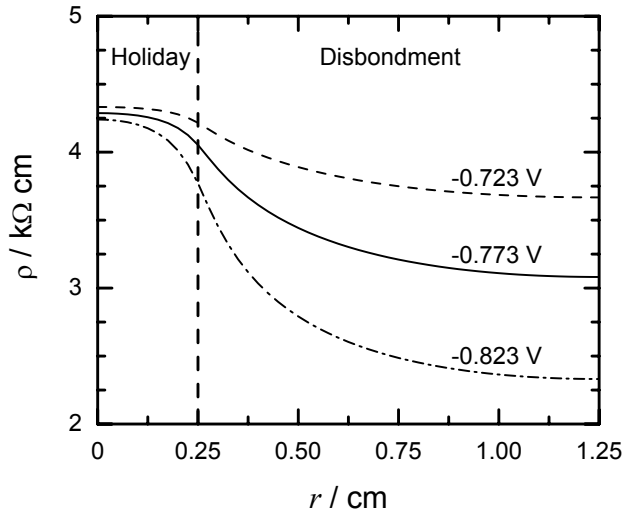

Figure 5-21: Calculated value of local electrolyte resistivity as a function of position on the metal surface with applied potential as a parameter. The dashed line at $r = 0.25$ cm indicates the boundary between the holiday and the disbondment.

of electroneutrality. For a given position in the disbondment, larger values of c_{Na^+} were associated with more negative applied potentials. For the negative Cl^- ion, smaller values of c_{Cl^-} were associated with more negative applied potentials for a given position in the disbondment.

The inert species Na^+ and Cl^- contributed to the disbonded coating system by influencing the distribution of the electrolyte resistivity. The local electrolyte resistivity is a measure of the electrolyte ability to pass current. The larger the resistivity, the less the ability of the electrolyte to pass current. The distributions of the electrolyte resistivity adjacent to the metal surface is shown in Figure 5-21 with applied potential as a parameter. The variations of resistivity with position were similar for the applied potentials. The resistivity decreased with position and approached a zero value as the tip was approached. For a given position, smaller values of resistivity were associated with more negative applied potentials. A decrease in local electrolyte resistivity in the disbondment enhanced the passage of current in the disbondment. At more negative applied potentials the cathodic current requirement of the disbondment increased as the hydrogen evolution re-

action became more significant. Therefore, the smaller values of resistivity at more negative applied potentials facilitated the larger current required by the hydrogen evolution reaction in the disbondment. Comparison of the distributions of local resistivity and ionic current density in the disbondment given in Figures 5-21 and 5-11, shows that for a given position in the disbondment, larger values of local resistivity were associated with smaller values of i_r.

5.4 Influence of Bulk Resistivity

The bulk electrolyte provided the boundary conditions for the composition at the mouth of the holiday. The composition of the bulk electrolyte was primarily Na^+ and Cl^-, and the resistivity of the bulk electrolyte provides a measure of its composition. The influence of the bulk resistivity on the disbonded coating system is presented in this section. The operator δ was defined to assist in the presentation of the results in this section. The value of $\delta\Phi$, for example, was

$$\delta\Phi = \Phi - \Phi|_{0.79} \tag{5-1}$$

and represented the difference between the value of Φ for a given bulk resistivity and the value of Φ corresponding to a bulk resistivity of 0.79 kΩ cm.

5.4.1 Solution Potential

The distribution of Φ on the metal surface is shown in Figure 5-22 with bulk resistivity as a parameter. The variations of Φ with position for the bulk resistivities of 0.79 and 79 kΩ cm were similar to the variation corresponding to the bulk resistivity of 7.9 kΩ cm, which was discussed. The solution potential drops between the mouth and metal surface of the holiday were 1, 7, and 36 mV for the bulk resistivities of 0.79, 7.9, and 79 kΩ cm, respectively. The solution potential drops across the disbondment corresponding to these resistivities were 1 mV, 5 mV, and 8 mV, respectively. Larger values of the solution potential drop between the mouth and

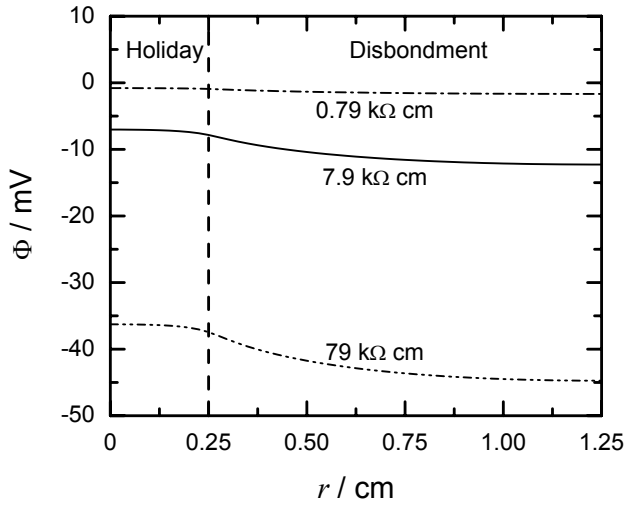

Figure 5-22: Calculated value of solution potential as a function of position on the metal surface with bulk resistivity as a parameter. The dashed line at $r = 0.25$ cm indicates the boundary between the holiday and the disbondment.

metal surface of the holiday were associated with larger bulk resistivities. Larger solution potential drops across the disbondment were associated with larger bulk resistivities.

The value of $\delta\Phi$ as a function of position on the metal surface is shown in Figure 5-23 with bulk resistivity as a parameter. For a given change in bulk resistivity, the relative change in solution potential was greater in the holiday than in the disbondment. These results indicated that the bulk resistivity influenced the solution potential in the holiday to a greater extent than in the disbondment.

5.4.2 Net Current Density

The distribution of the absolute value of the net current density on the metal surface is shown in Figure 5-24 with bulk resistivity as a parameter. The value of i_{net} was negative along the metal surface as oxygen reduction and hydrogen evolution dominated corrosion at the applied potential of -0.773 V_{SCE}. The variation of the absolute value of i_{net} with position for the bulk resistivities of 0.79 and 79 kΩ cm were similar to the corresponding variation for the bulk resistivity of 7.9 kΩ cm, which was discussed. For a given position in the holiday, the abso-

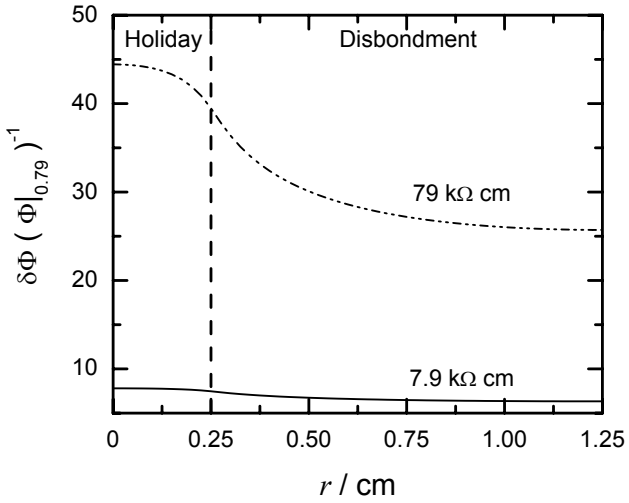

Figure 5-23: Calculated value of the difference in solution potential between a given bulk resistivity and the bulk resistivity of 0.79 kΩ cm as a function of position on the metal surface. The dashed line at $r = 0.25$ cm indicates the boundary between the holiday and the disbondment.

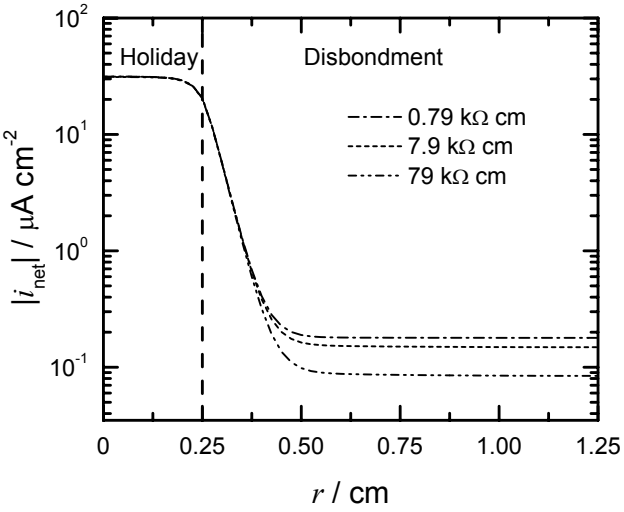

Figure 5-24: Calculated value of net current density as a function of position on the metal surface with bulk resistivity as a parameter.

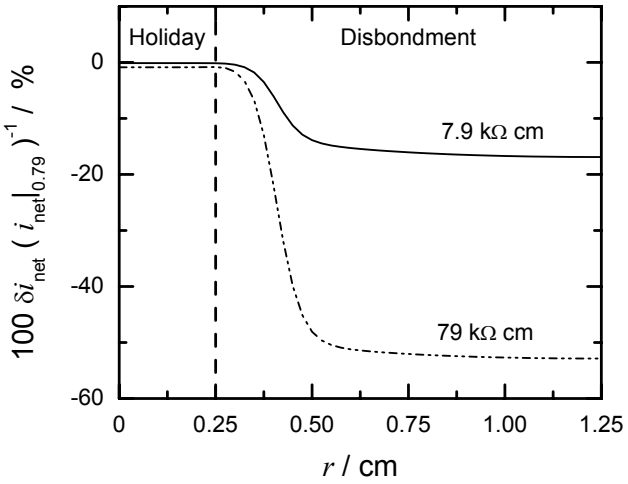

Figure 5-25: Calculated value of the difference in net current density between a given bulk resistivity and the bulk resistivity of 0.79 kΩ cm as a function of position on the metal surface. The dashed line at $r = 0.25$ cm indicates the boundary between the holiday and the disbondment.

lute value of i_{net} was approximately the same for the different bulk resistivities. This was because, the value of i_{net} in the holiday was primarily due to oxygen reduction, which was mass-transfer-limited and independent of the dependent variables of the system. For a given position in the disbondment, smaller absolute values of i_{net} were associated with larger bulk resistivities. This was because the value of i_{net} in the disbondment was primarily due to the potential dependent hydrogen evolution reaction. Smaller absolute values i_{H_2} were associated with more negative values of Φ, and therefore, with larger bulk resistivities.

The influence of the bulk resistivity on i_{net} in the holiday and disbondment can be seen in Figure 5-25. In this figure, the value of δi_{net} as a function of position is shown with bulk resistivity as a parameter. For a given change in resistivity, there was approximately no change in the value of i_{net} in the holiday; whereas, there was a larger change in the absolute value of i_{net} in the disbondment.

The current requirement of the holiday was the same for the different bulk resistivities. The migration current at a position was inversely proportional to the local resistivity and directly proportional to the local electric field. For a given

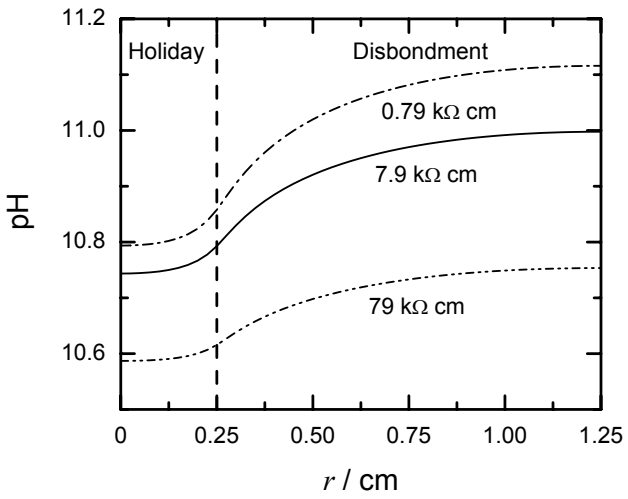

Figure 5-26: Calculated value of pH as a function of position on the metal surface with bulk resistivity as a parameter. The dashed line at $r = 0.25$ cm indicates the boundary between the holiday and the disbondment.

position in the holiday, larger values of the local resistivity were associated with larger values of the bulk resistivity. To maintain the migration current density, the electric field in the the holiday in the axial direction increased with larger values of solution potential drop between the mouth and metal surface of the holiday being associated with larger values of bulk resistivity (see Figure 5-22).

5.4.3 pH Distribution

The distribution of pH on the metal surface is shown in Figure 5-26 with bulk resistivity as a parameter. The variations of pH with position for the bulk resistivities of 0.79 and 79 kΩ cm were similar to that corresponding to a bulk resistivity of 7.9 kΩ cm, which was discussed. The bulk resistivity influenced the pH in the holiday and disbondment, with larger pH values associated with smaller values of bulk resistivity. This result was expected as larger values of bulk resistivity were associated with smaller absolute values of i_{H_2}, and therefore, smaller productions of OH^- in the disbondment.

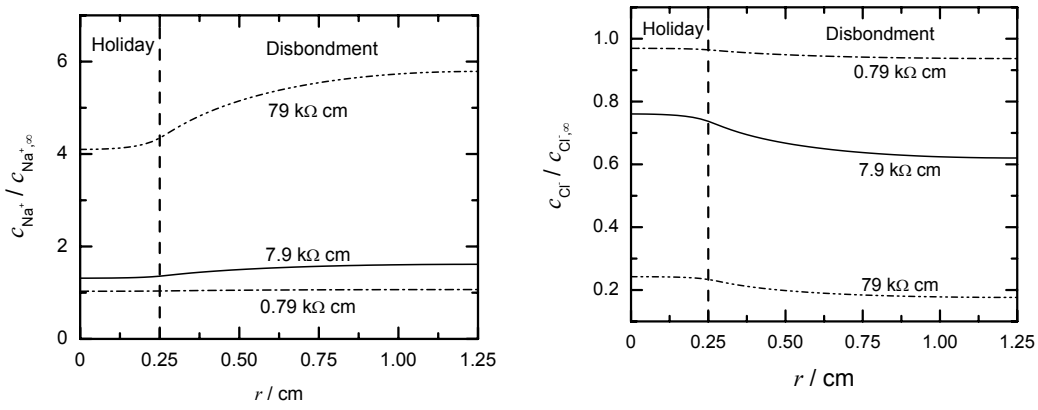

(a) (b)

Figure 5-27: Calculated value of concentrations of inert specie as a function of position on the metal surface with bulk resistivity as a parameter. (a) sodium ion and (b) chloride ion.

5.4.4 Chemically Inert species

The distributions of c_{Na^+} and c_{Cl^-} on the metal surface is shown in Figure 5-27 with bulk resistivity as a parameter. The variation of c_{Na^+} with position for the 7.9 kΩ cm bulk resistivity, which was discussed, was similar to the variations for the other two resistivities. Likewise, the variation for c_{Cl^-} with position for the for the 7.9 kΩ cm bulk resistivity, which was discussed, was similar to the variations for the other two resistivities. For a given value of bulk resistivity, the value of c_{Na^+} on the metal surface was greater than its bulk value and the value of c_{Cl^-} on the metal surface was less its the bulk value. These results were expected as a larger production of OH^- ions on the metal surface was associated with a smaller bulk resistivity, and the distributions of Na^+ and Cl^- responded to the production of the negatively charged OH^- on the metal surface.

5.4.5 Ionic Current Density

The current density on the metal surface in the disbondment was supported by current in the electrolyte. The distribution of the radial ionic current density in

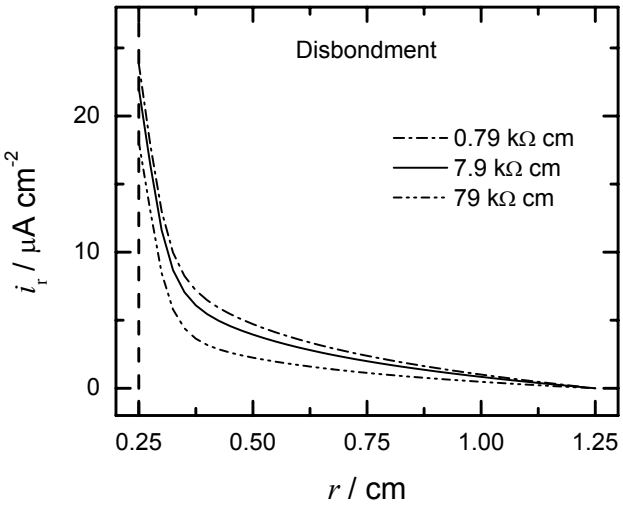

Figure 5-28: Calculated value of radial ionic current density as a function of position in the disbondment with bulk resistivity as a parameter. The dashed line at $r = 0.25$ cm indicates the boundary between the holiday and the disbondment.

the disbondment is shown in Figure 5-28 with bulk resistivity as a parameter. The distributions of i_r were similar for the different bulk resistivities; the distribution for the bulk resistivity of 7.9 kΩ cm was discussed. For a given position in the disbondment, larger values of i_r were associated with smaller resistivities. This was expected as smaller absolute values of i_{net} were associated with larger bulk resistivities.

The distributions of $i_{r,d}$ and $i_{r,m}$ are shown in Figure 5-29 with bulk resistivities as a parameter. The variations of $i_{r,d}$ with position for the bulk resistivities of 0.79 and 79 kΩ cm were similar to the variation for the bulk resistivity of 7.9 kΩ cm, which was discussed. For a given position in the disbondment, smaller values of $i_{r,d}$ were associated with larger bulk resistivities.

As seen in Figure 5-29(b), the variations of $i_{r,m}$ with position were similar for the different bulk resistivities. The value of $i_{r,m}$ relative to the value of $i_{r,m}$ corresponding to the bulk resistivity of 0.79 kΩ cm is shown in Figure 5-30 with bulk resistivity as a parameter. For a given position less than 0.29 cm in the disbondment, larger values of $i_{r,m}$ were associated with larger bulk resistivities. For po-

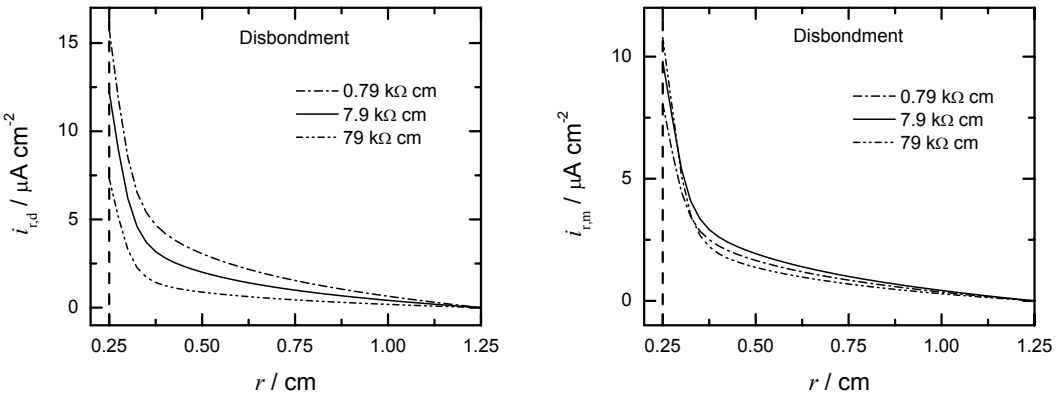

(a) (b)

Figure 5-29: Calculated value of contributors to the radial ionic current density as functions of position in the disbondment with bulk resistivity as a parameter. (a) radial diffusion current density and (b) radial migration current density. The dashed line at $r = 0.25$ cm indicates the boundary between the holiday and the disbondment.

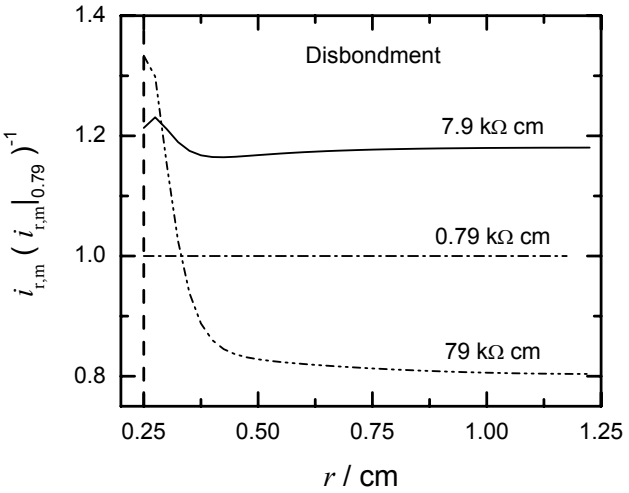

Figure 5-30: Calculated value of radial migration current density relative to the value associated with a bulk resistivity of 0.79 kΩ cm as a function of position in the disbondment with bulk resistivity as a parameter. The dashed line at $r = 0.25$ cm indicates the boundary between the holiday and the disbondment.

sitions greater than 0.29 cm the largest value of $i_{r,m}$ was associated with the bulk resistivity of 7.9 kΩ cm .

It was assumed that the axial variation of solution potential in the disbondment was negligible compared to the radial variation. The radial migration current density in the disbondment $i_{r,m}$ was given by the ratio of the local electric field in the radial direction E_r and the local electrolyte resistivity ρ. The distributions of the local electrolyte resistivity and local electric field adjacent to the metal surface in the disbondment are shown in Figure 5-31 with bulk resistivity as a parameter. For a given position in the disbondment, larger values of E_r and ρ were associated with larger bulk resistivities. The maximum value of $i_{r,m}$ for $r > 0.29$ cm that was associated with the bulk resistivity of 7.9 kΩ cm, seen in Figure 5-30, was attributed to the relative contributions of E_r and ρ in the disbondment.

The distributions of $\delta\rho$ and δE_r adjacent to the metal surface are shown in Figure 5-32 with bulk resistivities as a parameter. For a given increase in bulk resistivity, the value of E_r and ρ increased at any given position in the disbondment. The increase in E_r relative to the increase in ρ for a given change in bulk resistivity can be seen in Figure 5-33. In this figure, the ratio of the change in E_r relative to that with $\rho_\infty = 0.79$ kΩ cm to the change in ρ relative to that with $\rho_\infty = 0.79$ kΩ cm is shown with bulk resistivity as a parameter. A ratio greater than 1 represented the condition that the increase in E_r was larger than the corresponding increase in ρ for a given change in bulk resistivity. A ratio less than 1 represented the condition that the increase in E_r was less than the corresponding increase in ρ.

For positions less than 0.29 cm in the disbondment, an increase in E_r was larger than an increase in ρ that accompanied any increase in bulk resistivity. Therefore, the value of $i_{r,m}$ increased with bulk resistivities for $r < 0.29$ cm, as seen in Figure 5-30.

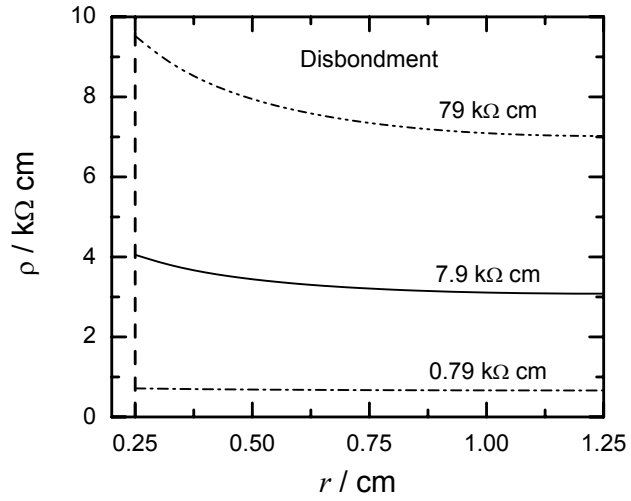

(a)

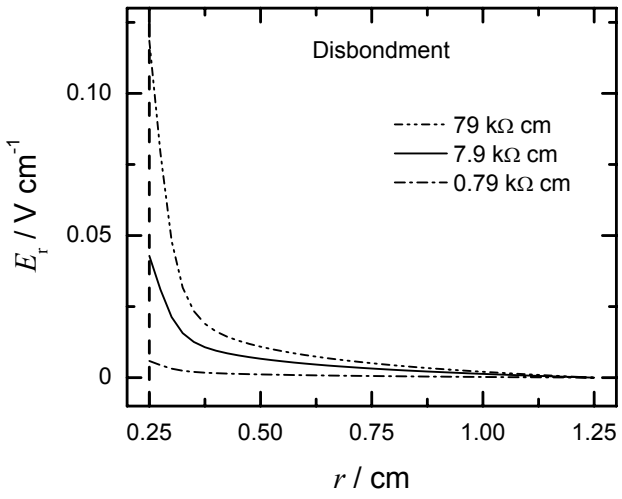

(b)

Figure 5-31: Calculated value of parameters associated with radial migration current density in the disbondment as a function of position in the disbondment with bulk resistivity as a parameter. (a)local electrolyte resistivity and (b)local electric field in the radial direction. The dashed line at $r = 0.25$ cm indicates the boundary between the holiday and the disbondment.

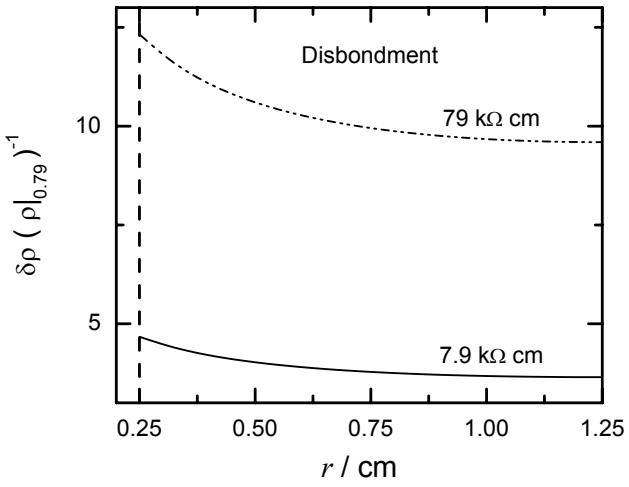

(a)

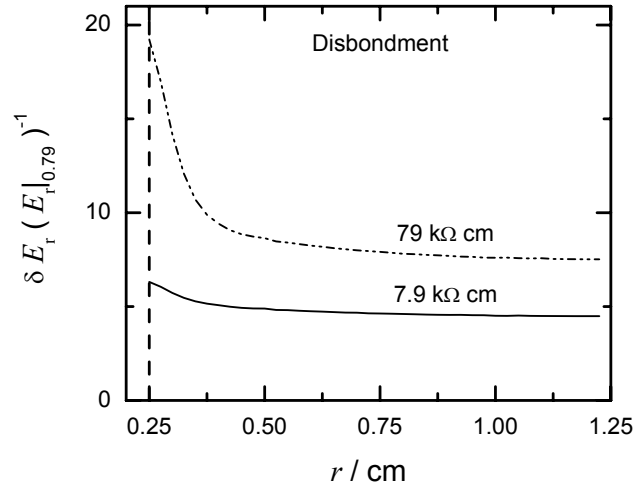

(b)

Figure 5-32: Calculated value of the difference between values associated with a given bulk resistivity and a bulk resistivity of 0.79 kΩ cm as a function of position in the disbondment. (a) local electrolyte resistivity and (b) local electric field in the radial direction. The dashed line at $r = 0.25$ cm indicates the boundary between the holiday and the disbondment.

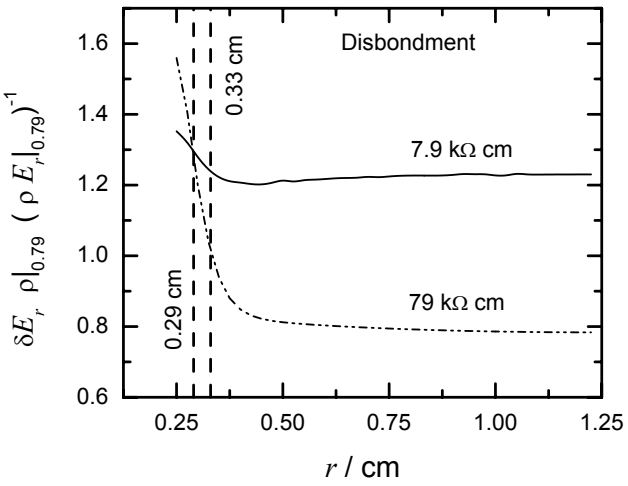

Figure 5-33: Calculated value of the increase in local electric field relative to the increase in local electrolyte resistivity as a function of position in the disbondment with bulk resistivity as a parameter.

For positions greater than 0.29 cm, when the bulk resistivity was increased from 0.79 to 7.9 kΩ cm, the ratio was greater than 1 such that the value of $i_{r,m}$ increased. When the the bulk resistivity increased from 0.79 to 79 kΩ cm, the ratio was greater than 1 up to a position of 0.33 cm and then was less than 1. Therefore, the value of $i_{r,m}$ increased for positions $0.29 < r < 0.33$ cm and decreased for position $r > 0.33$ cm. For positions $r > 0.29$ cm, the value of $i_{r,m}$ for the distribution associated with the bulk resistivity of 7.9 kΩ cm represented a maximum value because the relative contribution of the electric field to the radial migration current density balanced the contribution of the local electrolyte resistivity. For the increase in bulk resistivity beyond 7.9 kΩ cm, the increase in local electric field was smaller than the increase in local electrolyte resistivity such that the value of $i_{r,m}$ decreased.

The calculated values of the radial migration current density as a function of position in the disbondment for the applied potentials of -0.723 and -0.823 V_{SCE} are shown in Figure 5-34 with bulk resistivity as a parameter. The distribution of $i_{r,m}$ as a function of position in a 2 cm disbondment for the applied potential of

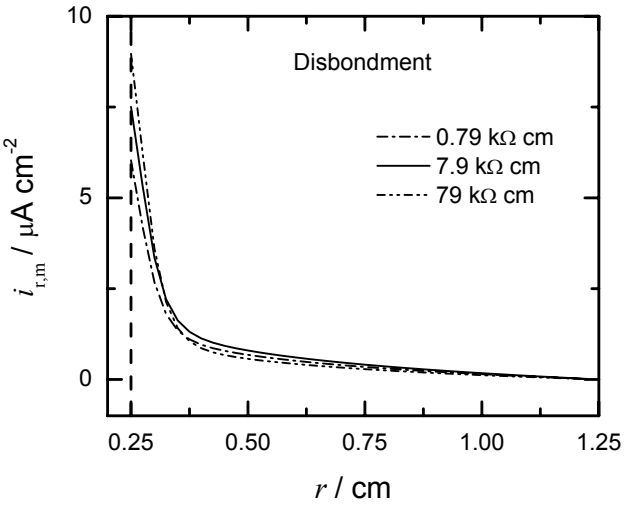

(a)

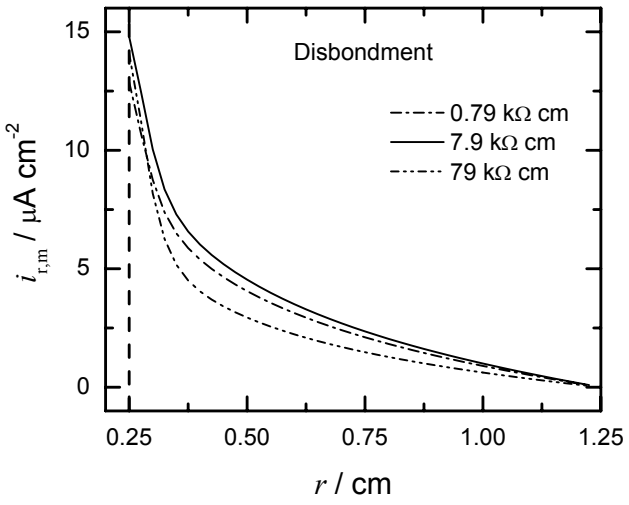

(b)

Figure 5-34: Calculated value of radial migration current density as a function of position in the disbondment with bulk resistivity as a parameter for given applied potentials. (a)-0.723 V_{SCE} and (b)-0.823 V_{SCE}. The dashed line at $r = 0.25$ cm indicates the boundary between the holiday and the disbondment.

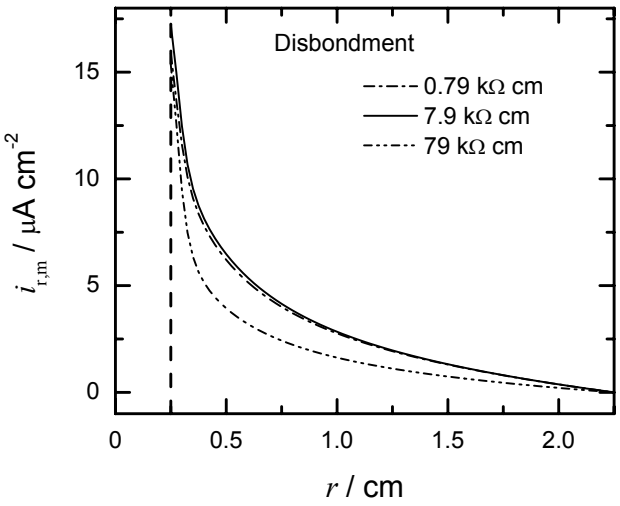

Figure 5-35: Calculated value of radial migration current density as a function of position in the disbondment with bulk resistivity as a parameter for a disbondment of length 2 cm. The dashed line at $r = 0.25$ cm indicates the boundary between the holiday and the disbondment.

-0.773 V_{SCE} is shown in Figure 5-35. As seen in Figures 5-34 and 5-35, the result that the value of $i_{r,m}$ was the largest for the all or the majority of the disbondment at the bulk resistivity of 7.9 kΩ cm was consistent for applied potentials other than -0.723 V_{SCE} and disbondments of lengths longer than 1 cm.

The percentage contributions of $i_{r,m}$ and $i_{r,d}$ to the radial current density as functions of position are shown in Figure 5-36 with bulk resistivity as a parameter. For the bulk resistivity of 7.9 kΩ cm, the $i_{r,m}$-contribution increased with position with the overall increase being approximately 5%. The $i_{r,d}$-contribution decreased with position with the overall decrease being approximately 5%. The $i_{r,m}$-contributions and $i_{r,d}$-contributions were uniform for the bulk resistivities of 0.79 and 79 kΩ cm for positions greater than 0.29 cm. For positions ranging from 0.25 cm to 0.29 cm, the value of the $i_{r,m}$-contribution increased by less than 2% while the $i_{r,d}$ decreased by less than 2%. Therefore, the relative contributions of migration and diffusion current densities to the ionic current density was approximately uniform except for a maximum change of 5% at a bulk resistivity of

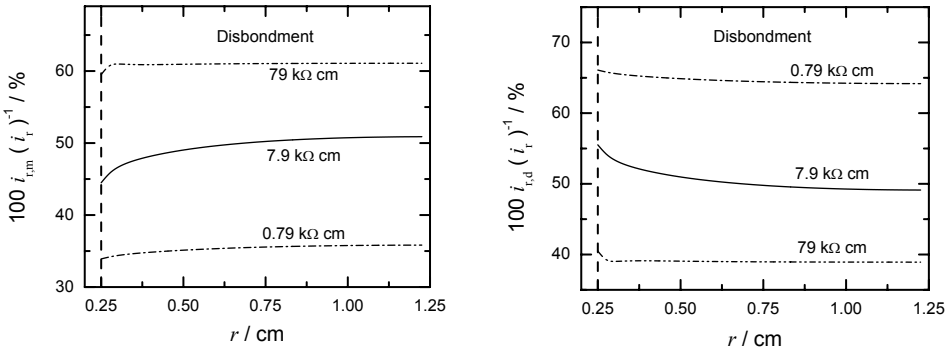

(a) (b)

Figure 5-36: Calculated value of relative contributions to radial ionic current density in the disbondment as a function of position with bulk resistivity as a parameter. (a) radial migration current density and (b) radial diffusion current density. The dashed line at $r = 0.25$ cm indicates the boundary between the holiday and the disbondment.

7.9 kΩ cm.

For a given position in the disbondment, smaller relative contributions of the migration current were associated with smaller bulk resistivities. This was consistent with the theory of supporting electrolytes, where the effect of migration was reduced with decreased resistivity.[12]

5.5 Influence of Gap Size

The gap size influenced the local electrolyte composition in the disbondment by restricting transport of species between the holiday and the disbondment. The smaller the gap size, the smaller the transport of ionic species between the holiday and the disbondment.

5.5.1 Electrochemical Current Densities

The distribution of the absolute net current density on the metal surface is shown in Figure 5-37(a) with gap size as a parameter. The value of i_{net} was negative along the metal surface for both gap sizes because the cathodic reactions, oxygen reduction and hydrogen evolution, dominated the anodic corrosion reac-

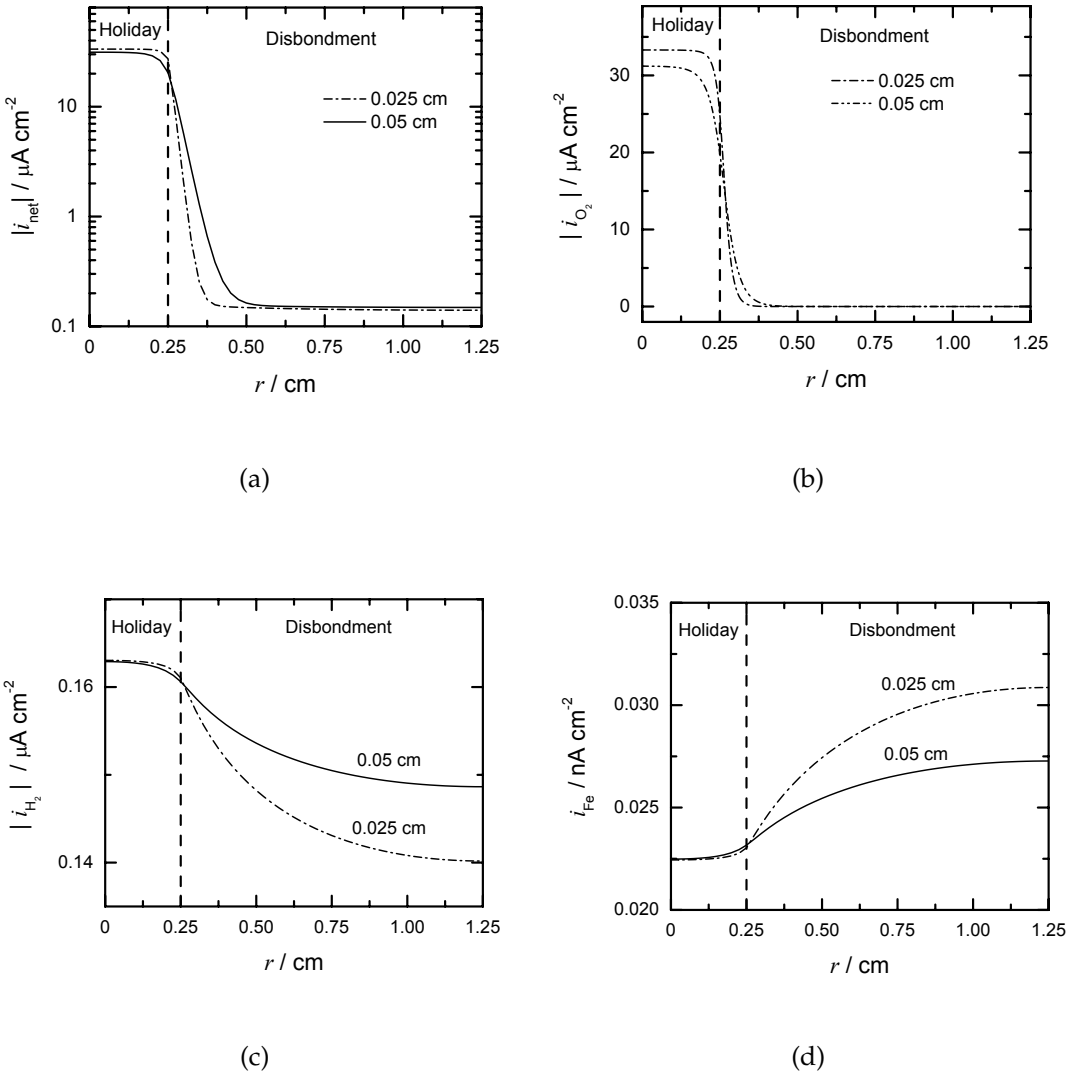

Figure 5-37: Calculated value of electrochemical current density as a function of position on the metal surface with the gap size as a parameter. (a) absolute net value, (b) oxygen reduction, (c) hydrogen evolution , and (d) corrosion. The dashed line at $r = 0.25$ cm indicates the boundary between the holiday and the disbondment.

tion at the applied potential of $-0.773\ V_{SCE}$. The variation of i_{net} with position for the gap of 0.025 cm was similar to that of gap 0.05 cm which was discussed.

For a given position in the holiday, the absolute value of i_{net} was larger for the smaller gap size. For a given position in the disbondment less than 0.5 cm, smaller absolute values of i_{net} were associated with the smaller gap size. These results were attributed to the oxygen reduction electrochemical reaction. The distribution of the absolute value of i_{O_2} on the metal surface is shown in Figure 5-37(b) with gap size as a parameter. Oxygen reduction was mass-transfer-limited for the applied potential of $-0.773\ V_{SCE}$. The smaller gap size restricted the passage of oxygen into the disbondment; therefore, for a given position in the disbondment the absolute value of i_{O_2} was smaller for the smaller gap size. By restricting the passage of oxygen into the disbondment, the smaller gap size increased the oxygen available for reduction in the holiday with the absolute value of i_{O_2} being larger for the smaller gap size.

In the disbondment, the primary cathodic reaction was hydrogen evolution as the oxygen concentration depleted exponentially with distance. For positions greater than 0.5 cm, the absolute value of i_{net} was smaller for the smaller gap because the value of absolute value of i_{H_2} was smaller. This can be seen in Figure 5-37(c), in which distribution of the absolute value of i_{H_2} on the metal surface is shown with gap size as a parameter.

The distribution of i_{Fe} on the metal surface is shown in Figure 5-37(d) with gap size as a parameter. For a given position in the holiday, the values of i_{Fe} were approximately equal. In the disbondment the variations of i_{Fe} with position were similar for both gap sizes. The value of i_{Fe} increased with position and the radial gradient of i_{Fe} approached a zero-value as the tip of the disbondment was approached. For a given position in the disbondment, a larger value of i_{Fe} was

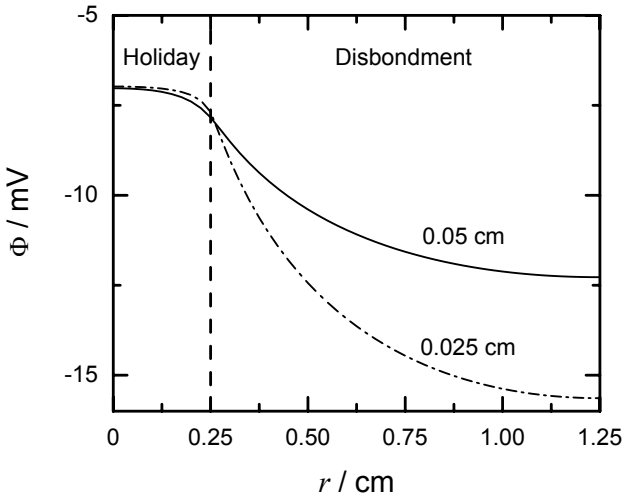

Figure 5-38: Calculated value of solution potential as a function of position on the metal surface with gap size as a parameter. The dashed line at $r = 0.25$ cm indicates the boundary between the holiday and the disbondment.

associated with the smaller gap size.

5.5.2 Solution Potential

The distribution of Φ on the metal surface is shown in Figure 5-38 with the gap size as a parameter. The variation of Φ with position for the 0.5 cm gap, which was discussed, was similar to the variation corresponding to the 0.025 cm gap. For a given position in the holiday, the values of Φ were approximately equal for the two gap sizes. The solution potential drop across the disbondment was 9 mV for the smaller gap as compared to 5 mV for the larger gap. For a given position in the disbondment, a more negative value of the solution potential was associated with the smaller gap size. This result is consistent with simulated[37] and experimental results[58,59] presented in literature. A more negative solution potential in the disbondment for the smaller gap resulted in an increased driving force for the corrosion reaction and a decreased driving force for hydrogen evolution. This was consistent with the relationships between i_{Fe} and gap size, and between i_{H_2} and gap size, as seen in Figures 5-37(c) and (d).

5.5.3 Concentrations

The distribution of c_i on the metal surface is shown in Figure 5-39 for the ionic species with gap size as a parameter. The variation of c_i with position for the 0.025 cm gap was similar to the corresponding variation for the 0.05 cm gap, which was discussed. On the metal surface of the holiday the pH, c_{Na^+}, and c_{Cl^-} were approximately equal for both gap sizes. For a given position in the holiday, smaller values of $c_{Fe^{+2}}$ were associated with the smaller gap. For a given position in the disbondment, larger values of pH, c_{Na^+}, and $c_{Fe^{+2}}$ were associated with the smaller gap size. For a given position in the disbondment, smaller values of c_{Cl^-} were associated with the smaller gap size. These results are consistent with reported simulations[37] and experimental results.[58]

In the disbondment, a smaller production of OH^- was associated with the smaller gap size. The larger value of pH at a given position in the disbondment was therefore due to to the increased restriction to transport between the holiday and disbondment that was associated with the smaller gap. In the disbondment, the larger value of $c_{Fe^{+2}}$ that was associated with the smaller gap size was attributed to the larger value of i_{Fe} and increased restriction associated with the smaller gap size.

5.5.4 Ionic Current Density

The distribution of the radial ionic current density in the disbondment is shown in Figure 5-40 with gap size as a parameter. The variation of i_r with position for the smaller pap was similar to the corresponding variation for the larger gap of 0.5 cm, which was discussed. For a given position in the disbondment, a larger value of i_r was associated with the smaller gap size. The larger values of i_r for the smaller gap were attributed to the smaller area normal to the radial direction in the disbondment as compared to the corresponding area of the larger gap.

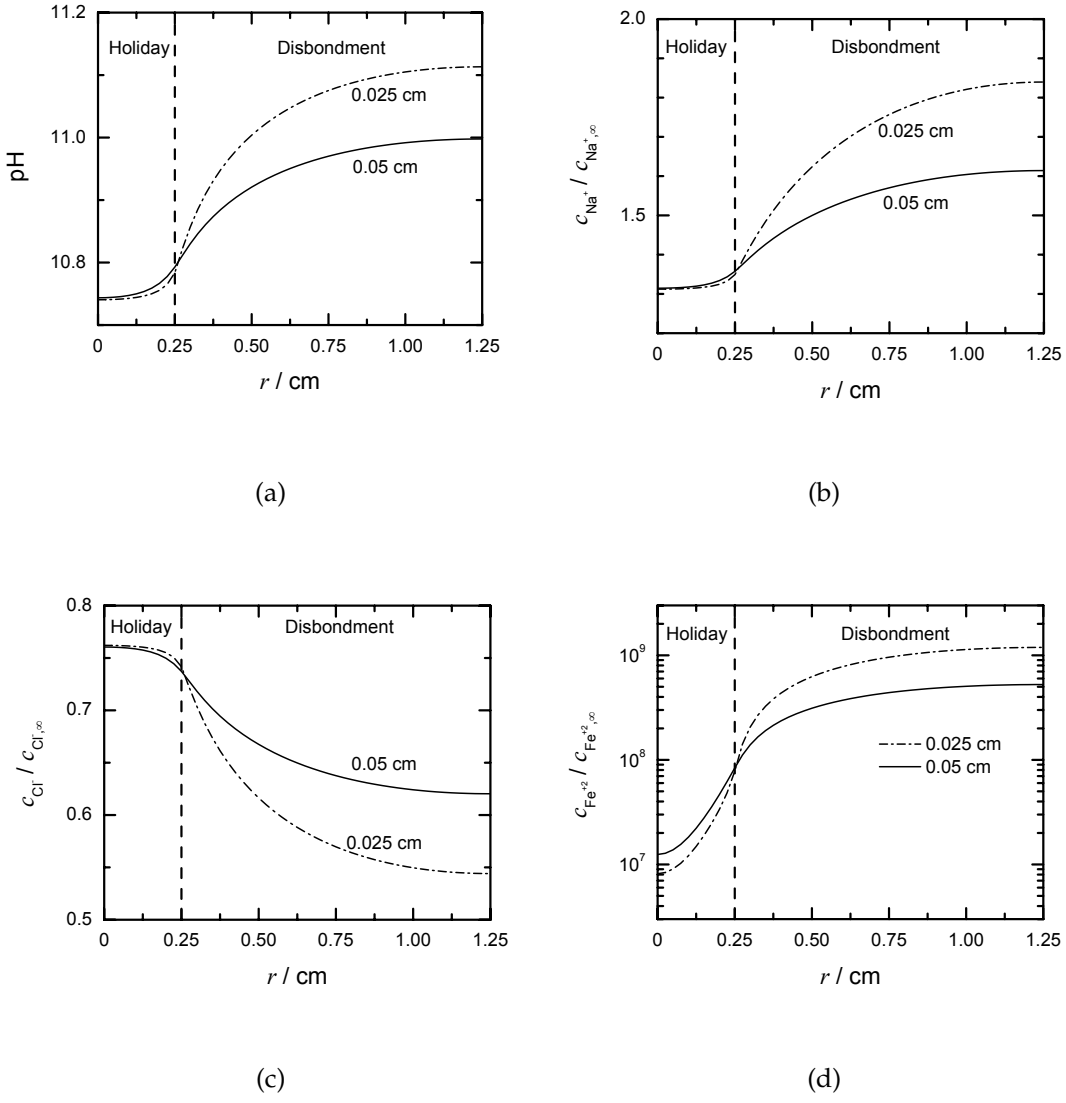

Figure 5-39: Calculated value of concentration as a function of position on the metal surface with the gap dimension as a parameter. (a) pH, (b) sodium ion (c) chloride ion, and (d) ferrous ion. The dashed line at $r = 0.25$ cm indicates the boundary between the holiday and the disbondment.

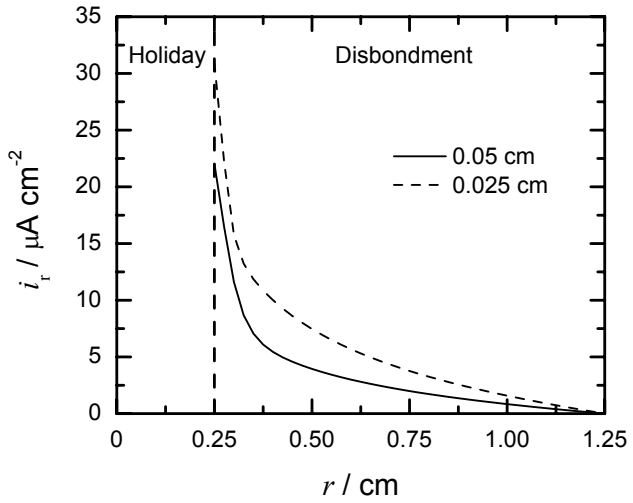

Figure 5-40: Calculated value of the radial ionic current density as a function of position in the disbondment with gap size as a parameter. The dashed line at $r = 0.25$ cm indicates the boundary between the holiday and the disbondment.

The radial migration and diffusion current densities were the contributors to the radial ionic current density. The distributions of $i_{r,m}$ and $i_{r,d}$ in the disbondment are shown in Figure 5-41 with gap size as a parameter. The variations of $i_{r,m}$ and $i_{r,d}$ with position in the disbondment were similar for both gap sizes. The variations of $i_{r,m}$ and $i_{r,d}$ for the gap size of 0.05 cm was discussed. For a given position in the disbondment, larger values of $i_{r,m}$ and $i_{r,d}$ were associated with the smaller gap size. This result was attributed to the smaller area normal to the metal surface in the disbondment that was associated with the smaller gap.

The relative contributions of $i_{r,m}$ and $i_{r,d}$ to the radial ionic current density were not equal, as can be seen in Figure 5-42. In this figure, the distributions of the relative contributions of $i_{r,m}$ and $i_{r,d}$ to i_r in the disbondment are shown with gap size as a parameter. For a given gap size, the relative contribution of $i_{r,m}$ increased with position and the relative contribution of $i_{r,d}$ decreased with position. For a given position in the disbondment, a larger relative contribution of migration was associated with the smaller gap size. This was attributed to the larger solution potential drop that was also associated with smaller gap size. For a given position

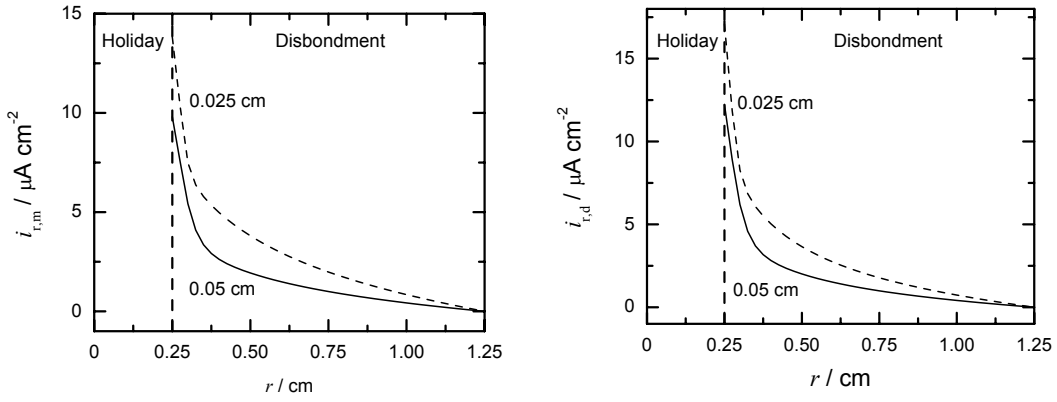

(a) (b)

Figure 5-41: Calculated value of the contribution to radial ionic current density as function of position in the disbondment with gap size as a parameter. (a) radial migration current density and (b) radial diffusion current density. The dashed line at $r = 0.25$ cm indicates the boundary between the holiday and the disbondment.

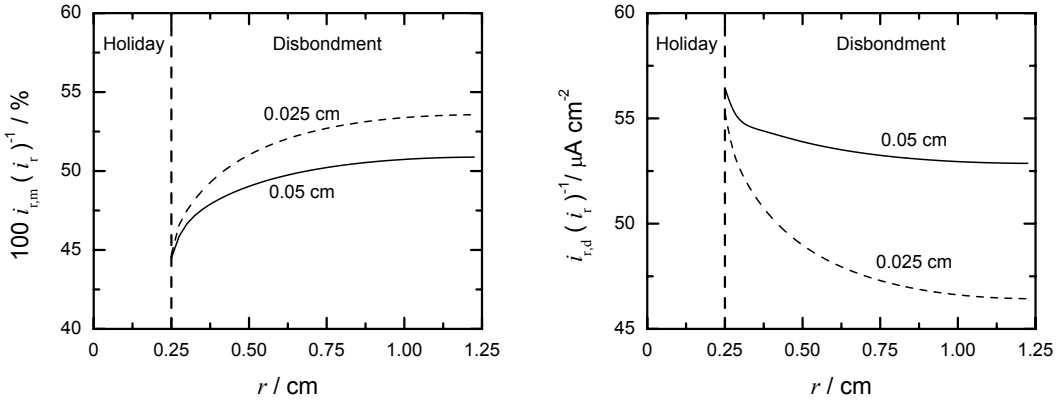

(a) $\boldsymbol{i}_{\mathrm{m}}$ (b) $\boldsymbol{i}_{\mathrm{d}}$

Figure 5-42: Calculated values of relative contribution to the radial ionic current density in the disbondment as a function of position with gap size as a parameter. (a) radial migration current density and (b) radial diffusion current density. The dashed line at $r = 0.25$ cm indicates the boundary between the holiday and the disbondment.

in the disbondment, the smaller relative contribution of diffusion associated with the smaller gap size was because the effect of migration current increased.

5.6 Influence of Disbondment Length

The electrochemical reactions on the metal surface of the disbondment contributed to the disbonded coating system by producing OH^- and Fe^{+2}. For a given gap size, larger production of these species were associated with longer disbondments. The influence of the disbonded length on the steady-state conditions in the disbonded coating system is presented in this section.

The aspect ratio r_g of the disbondment is given by the disbondment length divided by the gap size

$$r_g = \frac{r - r_h}{g} \tag{5-2}$$

It provides a measure by which disbonded coating systems of different disbonded lengths and gap sizes can be compared. The value of the aspect ratio is included as the top axis in the figures presented in this section.

5.6.1 Electrochemical Current Densities

The distribution of the absolute net current density on the metal surface is shown in Figure 5-43 with disbondment length as a parameter. The variations of the absolute value of i_{net} with position for the 2 and 3 cm lengths were similar to the variation for the 1 cm length that was discussed. For a given position on the metal surface, the value of i_{net} was negative which indicated that the cathodic reactions dominated the anodic reaction. This result was expected because the applied potential of $-0.773\ V_{SCE}$ favored the cathodic reactions and not the anodic corrosion reaction. The absolute values of i_{net} for the different lengths were approximately equal for positions up to 0.5 cm. This was because the mass-transfer-limited oxygen reduction reaction was dominant for these positions. For positions greater than 0.5 cm, smaller absolute values of i_{net} were associated with

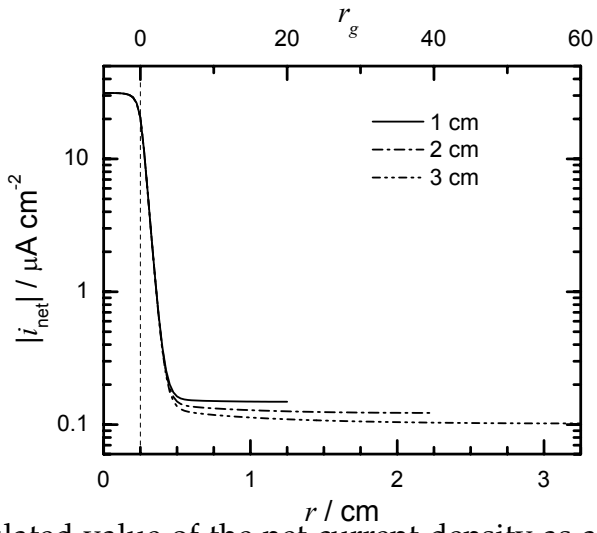

Figure 5-43: Calculated value of the net current density as a function of position on the metal surface with disbondment length as a parameter. The dashed line at $r = 0.25$ cm indicates the boundary between the holiday and the disbondment.

longer disbondments. This was attributed to the hydrogen evolution reaction. For a given position common between two distributions, a smaller absolute value of i_{H_2} was associated with the longer disbondment as seen in Figure 5-44. Although, smaller absolute values of i_{net} were associated with longer disbondments, the cathodic current generated by the disbondment increased with disbondment length because the metal surface area in the disbondment increased.

5.6.2 Ionic Current Density

The distribution of the radial ionic current density i_r in the disbondment is shown in Figure 5-45 with disbondment length as a parameter. The variations of i_r with position were similar for the different disbondment lengths. The value of i_r decreased with position and approached a zero value as the disbondment tip was approached. For a given position in the disbondment that was common between two distributions, a larger value of i_r was associated with the longer disbondment. This was because a larger cathodic current on the metal surface of the disbondment was associated with the longer disbondment.

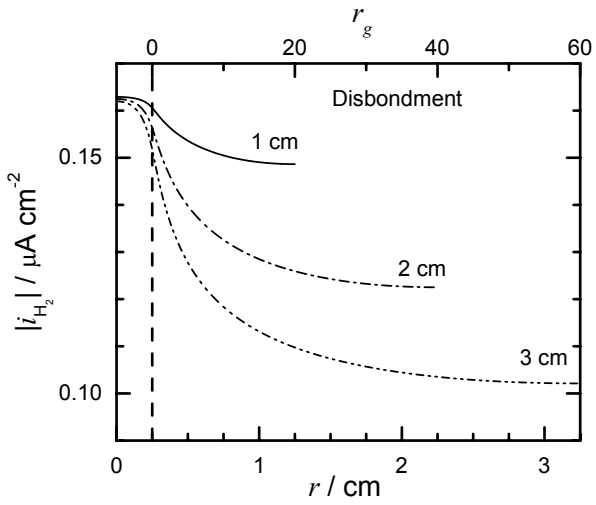

Figure 5-44: Calculated value of the absolute current density of the hydrogen evolution reaction as a function of position on the metal surface with disbondment length as a parameter. The dashed line at $r = 0.25$ cm indicates the boundary between the holiday and the disbondment.

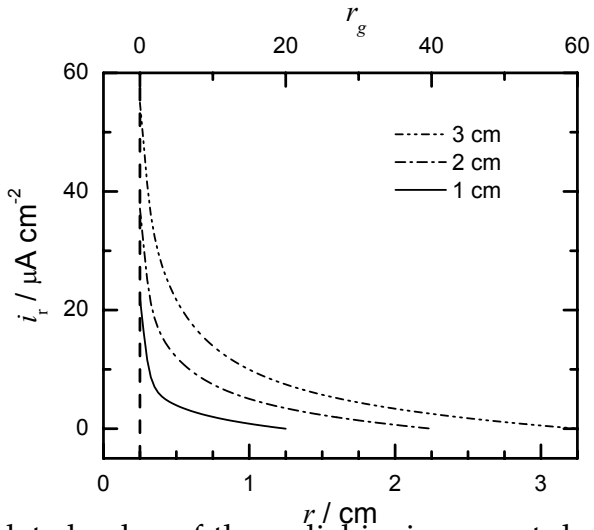

Figure 5-45: Calculated value of the radial ionic current density as a function of position in the disbondment with disbondment length as a parameter.

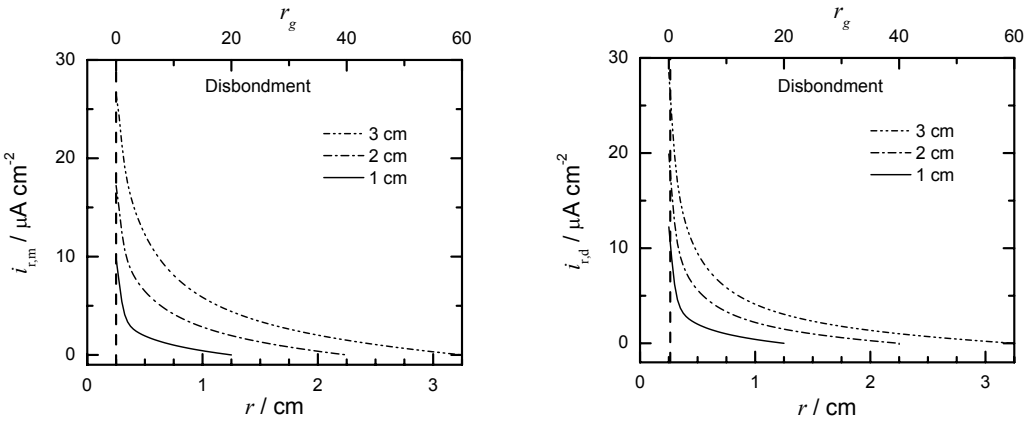

(a) (b)

Figure 5-46: Calculated value of the contribution to the radial ionic current density as function of position in the disbondment with disbondment length as a parameter. (a) radial migration current density and (b) radial diffusion current density. The dashed line at $r = 0.25$ cm indicates the boundary between the holiday and the disbondment.

The distributions of $i_{r,m}$ and $i_{r,d}$ in the disbondment are shown in Figure 5-46 with disbondment length as a parameter. The distributions of $i_{r,m}$ and $i_{r,d}$ for the 2 and 3 cm disbondment lengths were similar to the distribution for the 1 cm disbondment length, which were discussed. For a position common between two distributions, the values of $i_{r,m}$ and $i_{r,d}$ were larger for the longer disbondment. This was because a larger cathodic current was associated with the longer disbondment.

The relative contributions of $i_{r,m}$ and $i_{r,d}$ to the radial ionic current density in the disbondment are shown in Figure 5.6.2 with disbondment length as a parameter. The variations of the $i_{r,m}$ and $i_{r,d}$ contributions for the 2 and 3 cm disbondments were similar to the corresponding variations for the 1 cm disbondment that was discussed. For a position common between two distributions, a larger value of the $i_{r,m}$-contribution was associated with the longer disbondment. This demonstrated that the effect of migration in the disbondment increased with disbondment length. The effect of the radial diffusion current was smaller for longer

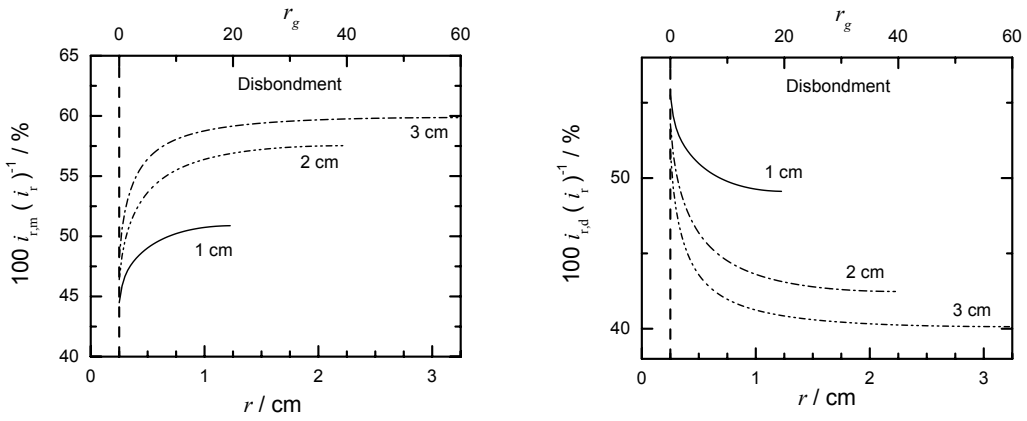

(a) (b)

Figure 5-47: Calculated value of the relative contribution to the radial ionic current density in the disbondment as a function of position with disbondment length as a parameter. (a) radial migration current density and (b) radial diffusion current density. The dashed line at $r = 0.25$ cm indicates the boundary between the holiday and the disbondment.

disbondment, but was still significant, especially over the first 1 cm into the disbondment.

5.6.3 Solution Potential

The distribution of the solution potential on the metal surface is shown in Figure 5-48 with disbondment length as a parameter. The variation of Φ with position for the 1 cm disbondment length, which was discussed, was similar to the corresponding variations for the 2 and 3 cm disbondment lengths. For a given position common between two distributions, a more negative solution potential was associated with the longer disbondment.

Comparison of Figures 5-45 and 5-48 shows the trend that at the entry of the disbondment, larger values of i_r were associated with larger solution potential drops in the disbondment. This trend was also seen in the distributions of solution potential and radial ionic current density when the applied potential was varied and the geometry and bulk composition were fixed (see Figures 5-11 and 5-7).

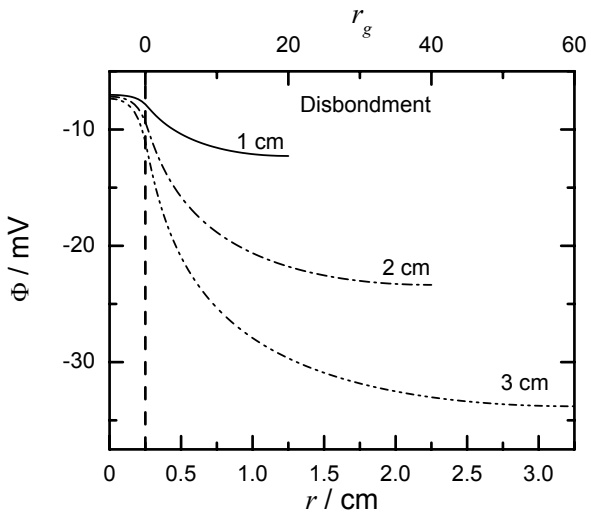

Figure 5-48: Calculated value of solution potential as a function of position in the disbondment with disbondment length as a parameter. The dashed line at $r = 0.25$ cm indicates the boundary between the holiday and the disbondment.

5.6.4 pH Distribution

The distribution of pH on the metal surface is shown in Figure 5-49 with disbondment length as a parameter. The variation of pH with position for the 1 cm length, which was discussed, was similar to the variations corresponding to the 2 and 3 cm lengths. For a given position common between two distributions, a larger pH was associated with the longer disbondment. This was attributed to the larger cathodic current, and therefore larger production of OH^-, in the disbondment associated with a longer disbondment.

Comparison of Figures 5-45 and 5-49 shows the trend that at the entry of the disbondment, a larger value of pH was associated with a larger value of i_r. This trend was also seen in the distributions of pH and radial ionic current density when the applied potential was varied and the geometry and bulk composition were fixed (see Figures 5-11 and 5-15).

5.6.5 Electrolyte Resistivity Distributions

The distribution of the local electrolyte resistivity on the metal surface is shown in Figure 5-50 with disbondment length as a parameter. The variation of the elec-

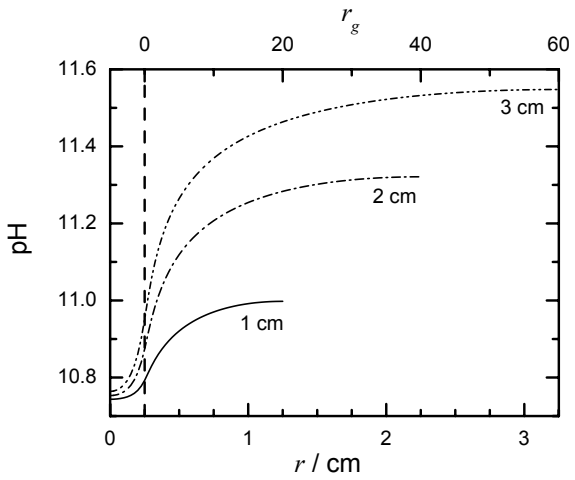

Figure 5-49: Calculated values of pH as a function of position in the disbondment with disbondment length as a parameter. The dashed line at $r = 0.25$ cm indicates the boundary between the holiday and the disbondment.

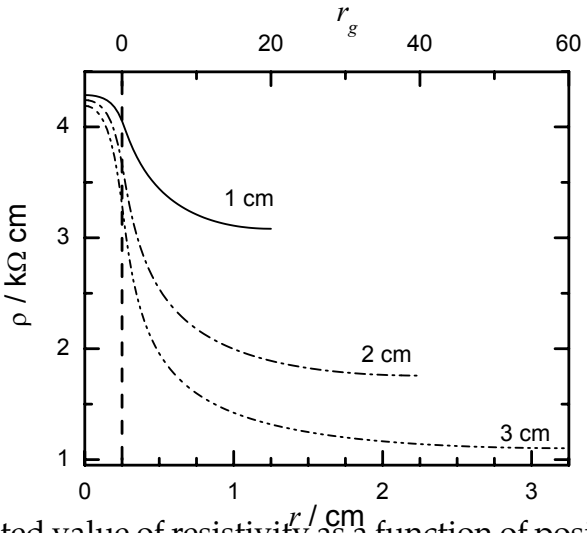

Figure 5-50: Calculated value of resistivity as a function of position in the disbondment with disbondment length as a parameter. The dashed line at $r = 0.25$ cm indicates the boundary between the holiday and the disbondment.

trolyte resistivity with position for the 1 cm disbondment, which was discussed, was similar to the corresponding distributions for the 2 and 3 cm disbondments. For a given position common between two distributions, a smaller local electrolyte resistivity was associated with the longer disbondment. The longer disbondments were associated with larger currents and smaller resistivities; the smaller resistivity enhancing the migration driven current.

Comparison of Figures 5-45 and 5-49 shows the trend that at the entry of the disbondment, a larger value of the local electrolyte resistivity was associated with a smaller value of i_r. This trend was also seen when the applied potential was varied and the geometry and bulk composition were fixed (see Figures 5-11 and 5-21).

5.7 Polarization Kinetics

Cathodic protection is used to mitigate the corrosion of the metal surface in disbonded coating systems. The influence of cathodic protection on the polarization kinetics of the metal surface of the disbonded coating system is presented in this section using the results of Systems 9, 10, 11, and 12.

5.7.1 Cathodic Protection Criteria

Two criteria used in the implementation of cathodic protection, given in section 2.5.2, are examined in this section. One criterion, Criterion 1, involves the maintenance of the pipe surface at a potential more negative than -0.773 V_{SCE}. The other, Criterion 2, involves the maintenance of a minimum negative shift of 0.3 V from the corrosion potential.

A schematic diagram of the criteria is shown in Figure 5-51. In this figure the metal-electrolyte interfacial potential V is given as a function of corrosion current density and as a function of absolute net current density for a position on the holiday metal surface. The distributions associated with i_{Fe} and the absolute i_{net}

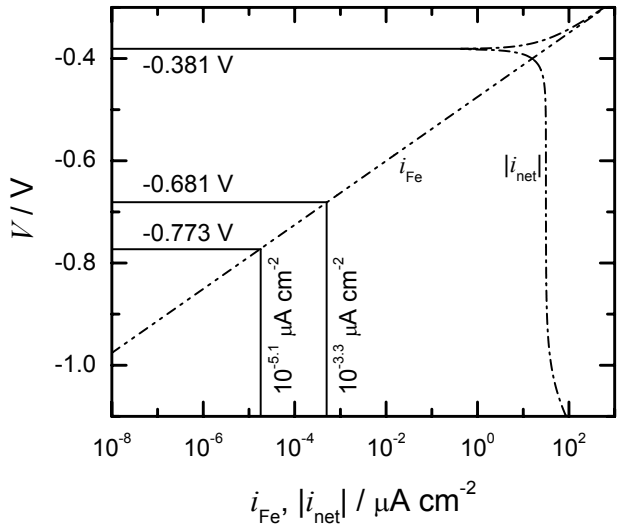

Figure 5-51: Calculated value of metal-electrolyte interfacial potential as functions of corrosion current density and absolute net current density.

superimposed for $V > -0.35$ V. The distributions associated with i_{Fe} and i_{net} were discussed in section 2.4.

As seen in Figure 5-51, a corrosion current density of $10^{-5.1}$ μA/cm^2 was associated with a value of $V = -0.773$ V_{SCE}. The corrosion potential on the metal surface of the holiday was -0.381 V_{SCE}. A shift of -0.3 V resulted in an interfacial potential of -0.681 V_{SCE} with a corresponding corrosion current density of $10^{-3.3}$ μA/cm^2. Criterion 1 is a more acceptable criterion as the value of i_{Fe} was approximately two orders of magnitude less than the value of i_{Fe} corresponding to Criterion 2.

5.7.2 Polarization Kinetics of Disbonded Coatings

The value of i_{lim,O_2} was an input parameter in the calculation of the polarization kinetics of the metal surface. Since i_{lim,O_2} was a function of position on the metal surface, the polarization kinetics was also a function of the position on the metal surface. The polarization kinetics on the metal surface is shown in Figure 5-52 with position on the metal surface as a parameter. The distribution of V with the absolute value of i_{net} was discussed before in section 2.4.

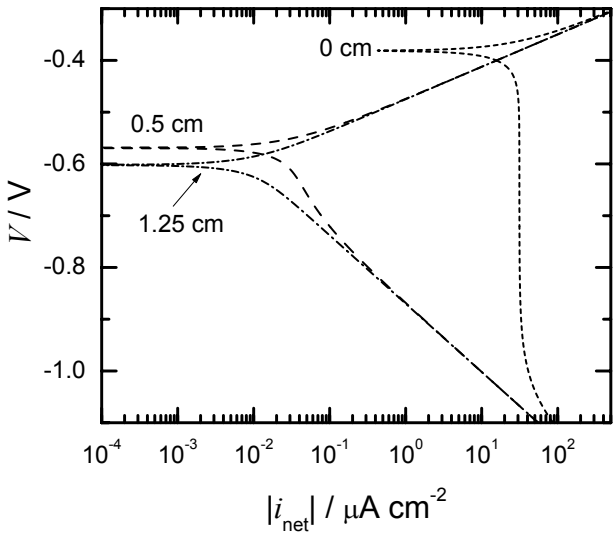

Figure 5-52: Metal-electrolyte interfacial potential as a function of absolute net current density with position on the metal surface as a parameter.

The position $r = 0$ cm represented a position on the holiday metal surface. The corrosion potential associated with this position was -0.381 V_{SCE}. The influence of oxygen reduction on the polarization kinetics of the holiday can be seen as the value of $i_{net} = 30$ $\mu A/cm^2$ was unchanged for the potential range $-0.5 < V < -1.0$. The position $r = 0.5$ cm represented a position in the disbondment where the value of i_{lim,O_2} was reduced by three orders of magnitude (see Figure 5-2). The corrosion potential associated with this position was -0.570 V_{SCE}, a drop of -0.195 V from the corrosion potential associated with the holiday. The position of 1.25 cm represented a position where the primary source of cathodic current was given by hydrogen evolution. The corrosion potential associated with this position was -0.6 V_{SCE}, a 0.225 V drop from the corrosion potential associated with the holiday. For disbondments longer than 1 cm, the polarization kinetics for positions $r > 1.25$ cm would be the same as that at $r = 1.25$ cm. This is because the influence of oxygen reduction is negligible compared with hydrogen evolution for $r > 1.25$ cm.

The distribution associated with the 1.25 cm position was designated the non-oxygenated polarization plot as the contribution of oxygen reduction to the ca-

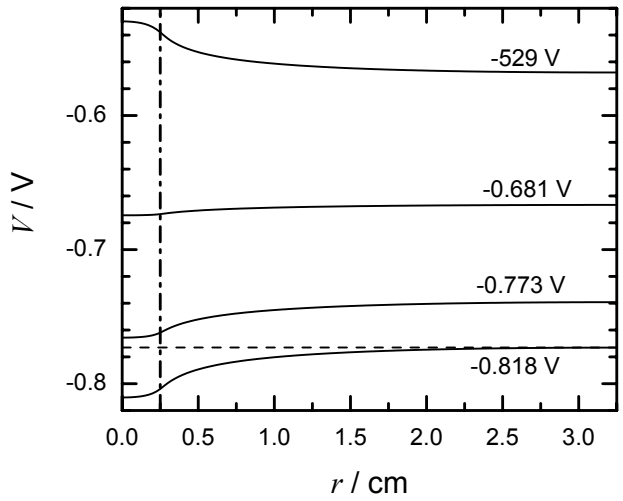

Figure 5-53: Calculated value of metal-electrolyte interfacial potential as a function of position on the metal surface with applied potential as a parameter.

thodic current density was negligible compared to that of hydrogen evolution. The distribution associated with the 0 cm position was designated the oxygenated polarization plot as the contribution of oxygen reduction to the cathodic current density was significant compared to that of hydrogen evolution.

For the non-oxygenated polarization plot, a metal-electrolyte interfacial potential of -0.6 V_{SCE} represented the condition where the local corrosion and hydrogen evolution current densities balanced. This interfacial potential divided the plot into the anodic and cathodic parts. The anodic part was for metal-electrolyte interfacial potentials more positive than -0.6 V_{SCE} such that the anodic corrosion reaction dominated the cathodic hydrogen evolution reaction. The cathodic part was for interfacial potentials more negative than -0.6 V_{SCE} where hydrogen evolution dominated corrosion.

5.7.3 Metal-Electrolyte Interfacial Potential

The distribution of the metal-electrolyte interfacial potential is shown in Figure 5-53 with applied potential as a parameter. The variations of V with position were different between the applied potential of -0.529 V_{SCE} and the other applied po-

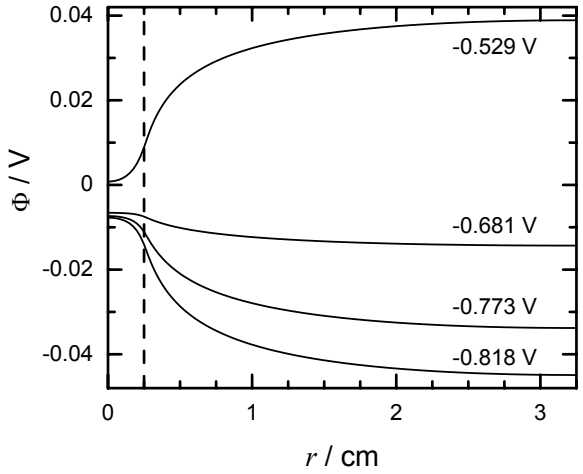

Figure 5-54: Calculated values of solution potential as a function of position on the metal surface with applied potential as a parameter. The dashed line at $r = 0.25$ cm indicates the boundary between the holiday and the disbondment.

tentials. This was because the variations of Φ were different (see Figure 5-54). The value of V decreased with position for the applied potential of -0.529 V_{SCE} and the value of V increased with position for the other applied potentials. The value of V for the applied potential of -0.818 V_{SCE} approached a value of -0.773 V_{SCE} as the tip of the disbondment was approached. Therefore, the applied potential of 0.818 V_{SCE} satisfied Criterion 1. The other applied potentials did not satisfy this criterion.

The distribution of i_{Fe} on the metal surface is shown in Figure 5-55 with applied potential as a parameter. Included in this figure is the corrosion current density of $10^{-5.1}$ $\mu A/cm^2$ that represented an acceptable level of corrosion for Criterion 1. For a given position smaller values of i_{Fe} were associated with more negative applied potentials. This indicated that there was increased cathodic protection with more negative applied potentials. Only the applied potential of -0.818 V_{SCE} satisfied the acceptable level of corrosion associated with Criterion 1 along the entire metal surface.

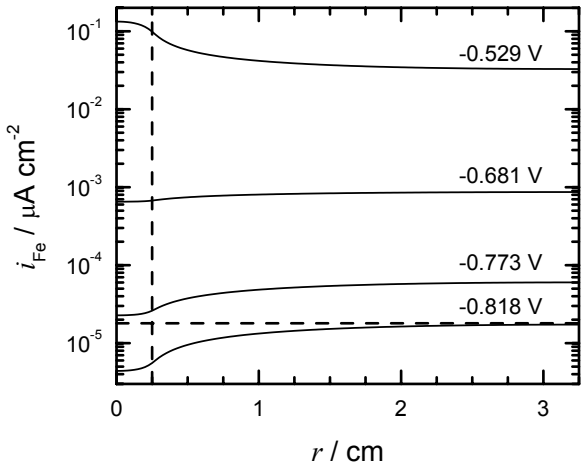

Figure 5-55: Calculated value of corrosion current density as a function of position with applied potential as a parameter. The corrosion current density of $10^{-5.1}$ μA/cm^2 that is shown by the dashed line represents an acceptable level of corrosion. The dashed line at $r = 0.25$ cm indicates the boundary between the holiday and the disbondment.

The distribution of the metal-electrolyte interfacial potential as a function of absolute net current density is shown in Figure 5-53 with applied potential as a parameter. Plots of interfacial potential as a function of absolute net current density for oxygenated and non-oxygenated conditions are included in this figure.

The values of V for the plot associated with the -0.529 V_{SCE} applied potential were more positive than -0.6 V_{SCE}. Part of this plot superimposed on the anodic part of the non-oxygenated polarization plot. This indicated that for part of the metal surface the influence of oxygen reduction was negligible, and in this part the anodic corrosion dominated the cathodic hydrogen evolution.

The values of V for the plots associated with applied potentials of -0.681, -0.773, and -0.818 V_{SCE} were more negative than -0.6 V_{SCE}. Part of each of these plots superimposed on the cathodic part of the non-oxygenated polarization plot. The superimposed part was associated with the condition that the oxygen reduction current density was negligible compared with the hydrogen evolution current density.

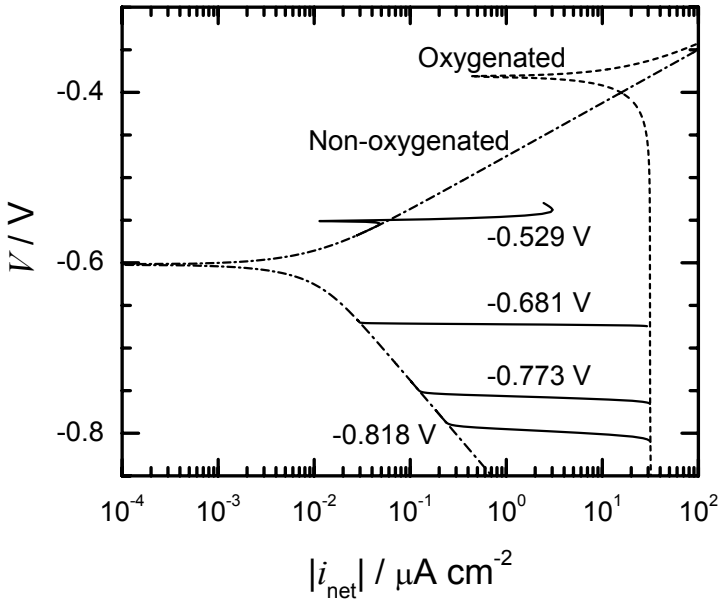

Figure 5-56: Calculated value of interfacial potential as a function of absolute net current density with applied potential as a parameter. Plots of interfacial potential as a function of absolute net current density for oxygenated and non-oxygenated conditions are included.

5.7.4 Open Circuit Potential

The applied potential of -0.529 V_{SCE} corresponded to the open circuit potential for the given geometry and bulk composition of System 9. The anodic current generated by corrosion was balanced by the cathodic current generated by oxygen reduction and hydrogen evolution at this applied potential. The absolute net, corrosion, and absolute cathodic current densities as functions of position on the metal surface are shown in Figure 5-57 for the applied potential of -0.529 V_{SCE}. For positions less than 0.425 cm, the value of i_{net} was negative with the cathodic oxygen reduction and hydrogen evolution reactions dominating the corrosion reaction. For positions greater than 0.425 cm, the corrosion reaction dominated the cathodic reactions and the value of i_{net} was positive.

The absolute net current density increased as a function of position in the holiday. This was because the value of i_{Fe} decreased with position and the absolute value of i_{cat} increased with position. For the positions ranging from 0.25 to 0.425 cm, the values of i_{Fe} and i_{cat} decreased with position. The absolute value of

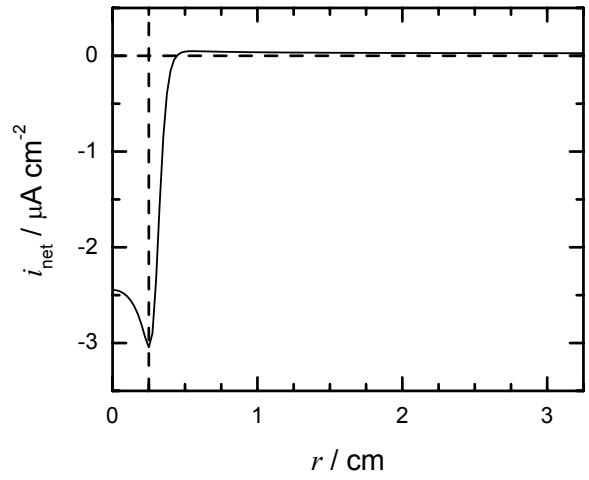

(a)

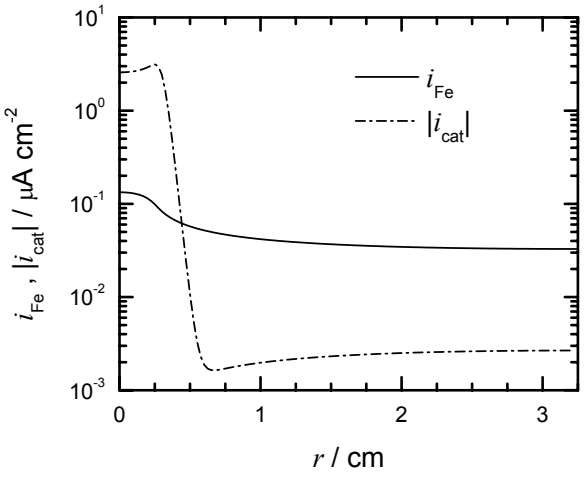

(b)

Figure 5-57: Calculated value of current density as a function of position at the open circuit potential. (a) net current density and (b) anodic and cathodic current densities.

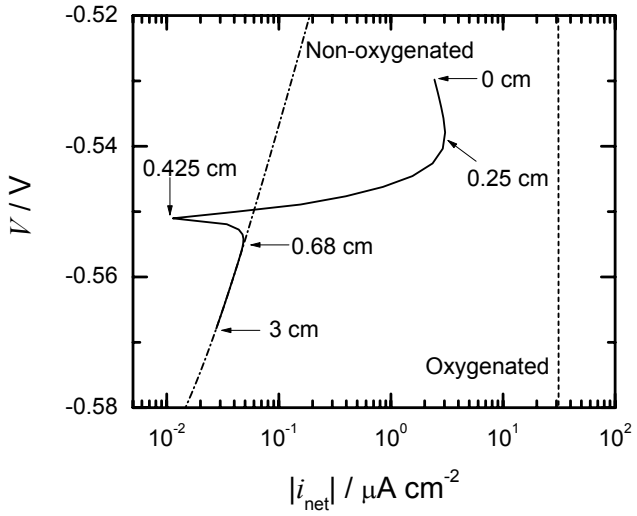

Figure 5-58: Calculated value of the metal-electrolyte interfacial potential as a function of absolute net current density for the open circuit condition. Plots of interfacial potential as a function of absolute net current density for oxygenated and non-oxygenated conditions are included.

i_{net} approached a zero value as the position 0.425 cm was approached because at this position i_{Fe} and i_{cat} were approximately equal.

For positions ranging from 0.425 to 0.68 cm, the values of i_{Fe} and i_{cat} continued to decrease with position. The decrease for i_{cat} was larger than i_{Fe}, such that the value of i_{net} approached a maximum value at the position of 0.68 cm. For positions greater than 0.68 cm, the value of i_{Fe} decreased with position and the value of i_{cat} increased with position such that the value of i_{net} decreased as a function of position for positions greater than 0.68 cm.

The metal-electrolyte interfacial potential as a function of the absolute value of the net current density is shown in Figure 5-58 for the applied potential of -0.529 V_{SCE}. The polarization plots for the non-oxygenated and oxygenated conditions are included. The positions on the metal surface corresponding to the polarization plot are shown. The cathodic reactions of oxygen reduction and hydrogen evolution dominated the anodic corrosion reaction for the positions ranging from 0 to 0.425 cm. The anodic reactions dominated the cathodic reactions for positions greater than 0.425 cm. The plot superimposed on the anodic part of the

non-oxygenated plot for the positions greater than 0.68 cm. For these positions the influence of oxygen reduction was negligible compared to hydrogen evolution, and corrosion dominated hydrogen evolution.

5.8 Summary

The model DISCOM was applied to several disbonded coating systems and the simulated results were used to determine the influences that applied potential, bulk resistivity, gap size, and disbondment length had on the system. The results were presented in terms of the calculated dependent variables c_i and Φ, the current densities of the electrochemical reactions on the metal surface, and the radial ionic, migration and diffusion current densities in the disbondment. The trends of the simulated results were in agreement with simulated and experimental trends reported in literature.

The contribution of the holiday was important as there were large changes in the dependent variables perpendicular to the holiday metal surface. Oxygen reduction was significant in the holiday, whereas hydrogen evolution was significant in the disbondment. The gap of the disbondment restricted the transport of species between the disbondment and the holiday.

The trends observed for the chemically inert species of Na^+ and Cl^- were in response to the electrochemical production of the negative OH^- on the metal surface. The distributions of these species established the electrolyte resistivity distribution that supported the current requirement of the metal surface.

The contributions of the radial migration and radial diffusion current densities to the radial ionic current density were comparable. The radial diffusion current density was driven by concentration gradients and therefore the assumption that concentration gradients are negligible in the disbondment is invalid.

Larger relative contributions of the radial migration current density to the radial ionic current density in the disbondment were associated with smaller bulk resistivities. This result was consistent with supporting electrolyte theory. However, a maximum value of the radial migration current density was associated with the bulk resistivity of 7.9 kΩ cm for all or the majority of positions in the disbondment. This feature associated with the 7.9 kΩ cm bulk resistivity was consistent for the different applied potentials and for disbondments of different lengths. This result has not been reported in literature.

The polarization kinetics of the disbonded coating system metal surface was function of the mass-transfer-limited current density of oxygen reduction for positions less than 1 cm into the disbondment. For positions beyond 1 cm into the disbondment, the influence of oxygen reduction was negligible.

DISCOM was used to calculate the applied potential necessary such that the NACE criterion was satisfied by the interfacial potential along the metal surface being more negative than -0.773 V_{SCE}. This application of DISCOM supports future work where DISCOM is combined with a model that calculates the current requirements for pipelines.

The open circuit potential and the zero-net-current density condition on the holiday were calculated for a given disbonded coating system. The large difference between these potentials demonstrated that although the holiday of a system is under cathodic protection, the disbondment may be insufficiently protected such that corrosion dominates. This result demonstrated that the open circuit potential of the system is a better benchmark for cathodic protection criterion compared to the zero net current density condition of the metal surface in the holiday.

CHAPTER 6
SOLUTION POTENTIAL DROP DESIGN EQUATION

The model developed in Chapter 4, DISCOM, calculated the steady-state distributions of species concentrations and solution potential in the system in response to the electrochemical reactions on the metal surface. In DISCOM, the system domain, which comprised of a holiday and a disbondment, was modeled as a two-dimensional domain. This model was used to investigate the phenomena and parameters that contribute to the disbonded coating system and simulations were presented for disbondments of lengths 3 cm and shorter.

Disbondments of lengths greater than 3 cm have been observed on coated pipelines that have been excavated. It was shown in the previous chapter that the significant variation of the dependent variables was in the radial direction for the disbondment and in the axial direction for the holiday. A disadvantage of DISCOM is that the disbondment is modeled as a two-dimensional domain while there is only significant variation in the radial direction. In this chapter a model is presented, DISCOX, where the disbondment, modeled as a one-dimensional domain, was coupled to the holiday, modeled as a two-dimensional domain. The motivation for this model was to calculate the steady-state distributions associated with disbondments of lengths up to 10 cm. Distributions of solution potential and local electrolyte resistivity adjacent to the metal surface are presented as functions of disbondment length and bulk electrolyte resistivity.

At present there is no design equation that can calculate the solution potential drop between the mouth of the holiday and the disbondment tip. An initial effort at developing a design equation that can calculate such a solution potential drop

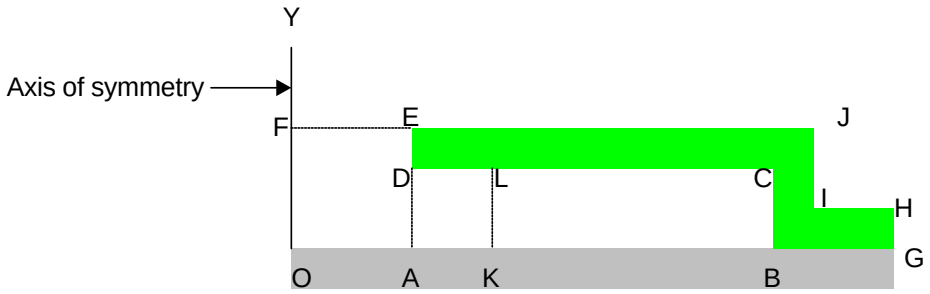

Figure 6-1: Schematic diagram of the radial disbonded coating system (not drawn to scale).

is presented. The influence of species transport by migration and diffusion, electroneutrality, and the polarization kinetics of the metal surface is imbedded in the constants associated with the design equation. The design equation for the solution potential drop can be used in cathodic protection models to implicitly account for disbonded coating systems.

6.1 Mathematical Model

The domain of the radial disbonded coating system consisted of a a holiday and disbondment as shown in Figure 4-1 and described in section 4.1. The domain of the disbonded coating system was divided into the holiday OADEF, adjacent region AKLD, and crevice KBCL, as shown in Figure 6-1. The holiday and adjacent region were modeled as a 2-D domain and the crevice as a 1-D domain. The models for the holiday-adjacent sub-domain OAKLDEF and the crevice sub-domain KBCL were coupled at the common boundary KL using continuity of species concentration, solution potential, and fluxes of species in the radial direction.

The four species were considered in the mathematical model were Na^{+}, Cl^{-}, OH^{-}, and Fe^{+2}. The nomenclature for the concentration of a specie i and dimensionless solution potential in the holiday-adjacent sub-domain were c_i and ϕ. The underlined variables $\underline{c_i}$ and $\underline{\phi}$ were used for the concentration of a specie i and the dimensionless solution potential in the crevice sub-domain. No homogeneous reactions were considered. The electrochemical reactions considered were iron dis-

solution, oxygen reduction, and hydrogen evolution, as described by equations (2-41), (2-42), and (2-43), respectively. The current densities for these reactions i_{Fe}, i_{O_2}, and i_{H_2}were given by equations (2-50),(2-51), and (2-52), respectively.

The value of i_{lim,O_2} was calculated as a function of position along OAK. In this calculation the governing equation for the mass-transfer of dissolved oxygen was solved in the 2-D sub-domain of OAKLDEF. The method was similar to that given in section 4.1. The contribution of oxygen reduction for positions along KB was assumed to be negligible when compared to the contribution of hydrogen evolution.

6.1.1 Holiday-Adjacent System

A mathematical model, HAM, was developed for the steady-state conditions of the 2-D holiday-adjacent system. This model was similar to DISCOM which was presented in Chapter 4. The sub-domain modeled by HAM was OAKLDEF. The geometry of this sub-domain included the holiday radius r_h (OA) , the length of the metal surface in the adjacent region r_a (AK), the thickness of the adjacent region g (KL), and the coating thickness a (DE).

The steady-state electrochemistry of the 2-D holiday-adjacent system was similar to that of the disbonded coating system presented in Chapter 4. The governing equations for the dependent variables at non-boundary nodes in the holiday-adjacent system were the same as those described for the disbonded coating system in section 4.2 when $Fe(OH)^+$ was not included. The governing equations for c_i and ϕ in the holiday-adjacent system were equations (4-2), (4-3), (4-5), and (4-4) for species mass-transfer, and equation (4-6) for the electroneutrality condition. In equations (4-4) and (4-5) the conditions $R_{OH^-} = 0$ and $R_{Fe^{+2}} = 0$ were used.

The boundary conditions at the metal surface boundary OAK was similar to that for the metal surface of the disbonded coating system. At the metal surface

boundary, the conditions for c_{Na^+} and c_{Cl^-} were the no-flux condition given by equation (4-14). The conditions for $c_{Fe^{+2}}$ and c_{OH^-} on the metal surface OAK were given by equations (4-15) and (4-16), respectively.

The conditions at the coating boundaries LD and DE were the no-flux condition for all the species. At the mouth FE the values of c_i and Φ were set to their bulk values.

The boundary condition on KL was a flux condition given by

$$-z_i D_i c_i \frac{\partial \phi}{\partial r} - D_i \frac{\partial c_i}{\partial r} = \underline{N_i^*} \tag{6-1}$$

where c_i and ϕ were the concentration of a species i and dimensionless solution potential in the holiday-adjacent sub-domain, and $\underline{N_i^*}$ was the flux in the r-direction at the boundary KL in the crevice sub-domain. The value of $\underline{N_i^*}$ was given by

$$\underline{N_i^*} = -z_i D_i \underline{c_i^*} \frac{\partial \underline{\phi^*}}{\partial r} - D_i \frac{\partial \underline{c_i^*}}{\partial r} \tag{6-2}$$

where $\underline{c_i^*}$ and $\underline{\phi^*}$ were the concentration of a species i and the dimensionless solution potential in the crevice on KL.

6.1.2 Crevice System

The sub-domain KBCL in Figure 6-1 was modeled as a 1-D crevice system. A mathematical model CREM was developed for the steady-state conditions in the 1-D crevice system and is presented in this subsection. The geometry of the crevice sub-domain included the crevice length r_c (KB) and the crevice thickness g (BC).

The governing equation for the mass-transfer of a species i in a dilute environment was equation (2-5)

$$0 = -\nabla \cdot \boldsymbol{N}_i + R_i$$

This equation was recast to a 1-D domain in cylindrical coordinates to give

$$0 = -\frac{1}{r}\left[\frac{d(r\underline{N_i})}{dr}\right] + \underline{S_i} \tag{6-3}$$

where $\underline{N}_i$ was the flux of a species i in the r-direction and $\underline{S}_i$ the production of species from electrochemical reactions. No homogeneous reactions were considered with $R_i = 0$. Expanding equation (6-3) yielded

$$0 = z_i D_i \underline{c}_i \frac{d^2\underline{\phi}}{dr^2} + D_i \frac{d^2\underline{c}_i}{dr^2} + z_i D_i \frac{d\underline{c}_i}{dr}\frac{d\underline{\phi}}{dr} + \frac{D_i}{r}\left[z_i \underline{c}_i \frac{d\underline{\phi}}{dr} + \frac{d\underline{c}_i}{dr}\right] + \underline{S}_i \tag{6-4}$$

The governing equations for the concentration of the species Na^+ and Cl^- that did not participate in electrochemical reactions were

$$\begin{aligned} 0 &= z_{Na^+} D_{Na^+}\left[\underline{c}_{Na^+}\frac{d^2\underline{\phi}}{dr^2} + \frac{d\underline{c}_{Na^+}}{dr}\frac{d\underline{\phi}}{dr}\right] + D_{Na^+}\frac{d^2\underline{c}_{Na^+}}{dr^2} \\ &+ \frac{D_{Na^+}}{r}\left[z_{Na^+}\underline{c}_{Na^+}\frac{d\underline{\phi}}{dr} + \frac{d\underline{c}_{Na^+}}{dr}\right] \end{aligned} \tag{6-5}$$

and

$$\begin{aligned} 0 &= z_{Cl^-} D_{Cl^-}\left[\underline{c}_{Cl^-}\frac{d^2\underline{\phi}}{dr^2} + \frac{d\underline{c}_{Cl^-}}{dr}\frac{d\underline{\phi}}{dr}\right] + D_{Cl^-}\frac{d^2\underline{c}_{Cl^-}}{dr^2} \\ &+ \frac{D_{Cl^-}}{r}\left[z_{Cl^-}\underline{c}_{Cl^-}\frac{d\underline{\phi}}{dr} + \frac{d\underline{c}_{Cl^-}}{dr}\right] \end{aligned} \tag{6-6}$$

respectively with $\underline{S}_{Na^+} = 0$ and $\underline{S}_{Cl^-} = 0$.

The governing equations for the mass-transfer of the species Fe^{+2} and OH^- were

$$\begin{aligned} 0 &= z_{Fe^{+2}} D_{Fe^{+2}}\left[\underline{c}_{Fe^{+2}}\frac{d^2\underline{\phi}}{dr^2} + \frac{d\underline{c}_{Fe^{+2}}}{dr}\frac{d\underline{\phi}}{dr}\right] + D_{Fe^{+2}}\frac{d^2\underline{c}_{Fe^{+2}}}{dr^2} \\ &+ \frac{D_{Fe^{+2}}}{r}\left[z_{Fe^{+2}}\underline{c}_{Fe^{+2}}\frac{d\underline{\phi}}{dr} + \frac{d\underline{c}_{Fe^{+2}}}{dr}\right] + \underline{S}_{Fe^{+2}} \end{aligned} \tag{6-7}$$

and

$$\begin{aligned} 0 &= z_{OH^-} D_{OH^-}\left[\underline{c}_{OH^-}\frac{d^2\underline{\phi}}{dr^2} + \frac{d\underline{c}_{OH^-}}{dr}\frac{d\underline{\phi}}{dr}\right] + D_{OH^-}\frac{d^2\underline{c}_{OH^-}}{dr^2} \\ &+ \frac{D_{OH^-}}{r}\left[z_{OH^-}\underline{c}_{OH^-}\frac{d\underline{\phi}}{dr} + \frac{d\underline{c}_{OH^-}}{dr}\right] + \underline{S}_{OH^-} \end{aligned} \tag{6-8}$$

respectively, where

$$\underline{S}_{Fe^{+2}} = \frac{i_{Fe}}{2F} \tag{6-9}$$

and

$$\underline{S}_{OH^-} = \frac{i_{H_2}}{-F} \tag{6-10}$$

The governing equation for the dimensionless solution potential $\underline{\phi}$ was

$$z_{Na^+}\underline{c}_{Na^+} + z_{Cl^-}\underline{c}_{Cl^-} + z_{OH^-}\underline{c}_{OH^-} + z_{Fe^{+2}}\underline{c}_{Fe^{+2}} = 0 \tag{6-11}$$

This equation was based on the condition of electroneutrality at any position in the domain given by equation (2-13).

The system of equations for the steady-state conditions in the 1-D crevice system were the mass-transfer governing equations (6-5), (6-6), (6-7), and (6-8), and the equation for the electroneutrality condition (2-13).

The two boundaries for the 1-D crevice domain were located at KL and BC (see Figure 6-1). The conditions for $\underline{c}_i^*$ and $\underline{\phi}^*$ at the boundary KL were fixed to the conditions at the position located midway along KL in the holiday-adjacent domain c_i^* and ϕ^*. The boundary condition for the species at BC was a no-flux condition given by

$$-z_i D_i \underline{c}_i \frac{\partial \underline{\phi}}{\partial r} - D_i \frac{\partial \underline{c}_i}{\partial r} = 0 \tag{6-12}$$

The electroneutrality condition equation (6-11) was applicable as the boundary condition for $\underline{\phi}$ at BC.

6.2 Method of Solution

The model DISCOX calculated the steady-state conditions in the holiday-adjacent system coupled with the crevice system. This model was constructed using the models HAM and CREM.

The model HAM was used to calculate the steady-state conditions in the holiday-adjacent system given the boundary condition at the common boundary KL. The details of this model were similar to DISCOM that was presented in Chapter 4.

In HAM, the linearized governing equations were discretized using second order difference approximations to yield

$$\boldsymbol{K}_{HA} \cdot \boldsymbol{C}_{HA} = \boldsymbol{R}_{HA} \tag{6-13}$$

where $\boldsymbol{K}_{HA}$, $\boldsymbol{C}_{HA}$, and $\boldsymbol{R}_{HA}$ were the global coefficient matrix, the global solution vector, and the global load vector for the holiday-adjacent system.

A method of solution similar to that used for the holiday-adjacent system was used for the crevice system. The linearized governing equations for $\underline{c_i}$ and $\underline{\phi}$ in the crevice system were discretized using a second order difference approximations to yield

$$\boldsymbol{K}_{C} \cdot \boldsymbol{C}_{C} = \boldsymbol{R}_{C} \tag{6-14}$$

where $\boldsymbol{K}_{C}$,$\boldsymbol{C}_{C}$, and $\boldsymbol{R}_{C}$ were the global coefficient matrix, the global solution vector, and the global load vector for the crevice system.

The global coefficient matrices $\boldsymbol{K}_{HA}$ and $\boldsymbol{K}_{C}$, and the global load vectors $\boldsymbol{R}_{HA}$ and $\boldsymbol{R}_{C}$ were functions of c_i ϕ, $\underline{c_i}$, and $\underline{\phi}$ and an iterative algorithm for DISCOX was developed involving HAM and CREM. The mathematical models DISCOX, HAM and CREM were developed using *Compaq Visual Fortran, Version* 6.1® with double precision accuracy.

Algorithm for DISCOX

The algorithm for the calculation of the steady-state values for c_i , ϕ, c_i^*, and ϕ^* used in DISCOX is presented in Figure 6-2 and summarized below:

1. The input data required for DISCOX was read from input files.
2. The 2-D holiday-adjacent and the 1-D crevice sub-domains were discretized.
3. The value of i_{lim,O_2} as a function of position on the metal surface of the holiday-adjacent sub-domain was calculated.

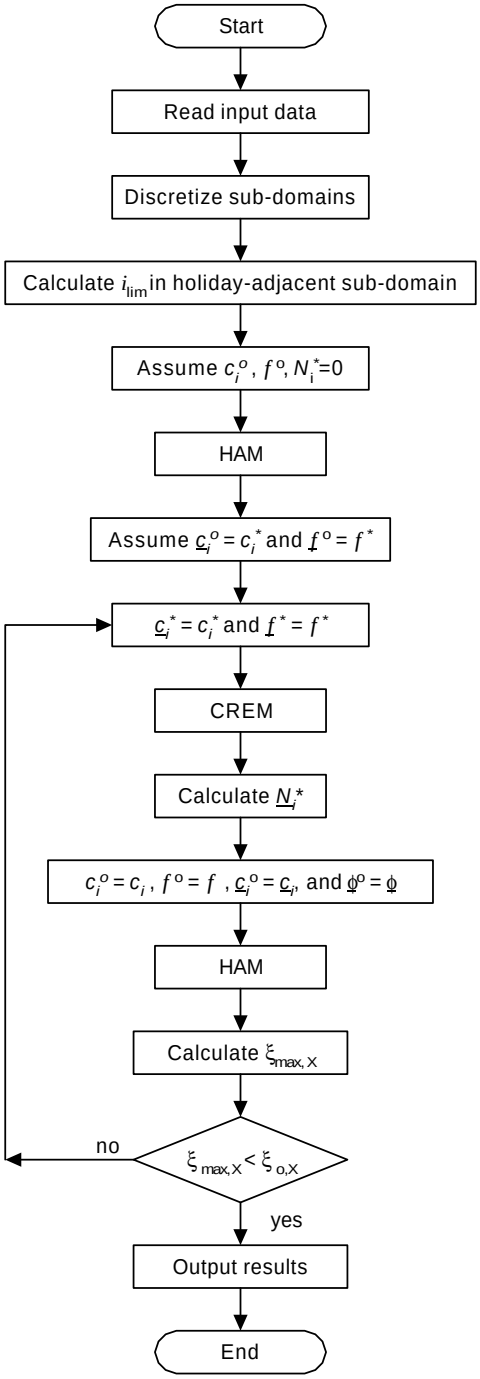

Figure 6-2: The algorithm for the mathematical model DISCOX.

4. The values c_i^o and ϕ^o were assumed for c_i and ϕ, respectively, in the holiday-adjacent system. The flux at the common boundary was set to a zero value, $\underline{N_i^*} = 0$.

5. The vector $\boldsymbol{C}_{HA}$ was calculated using HAM.

6. The values for $\underline{c_i^o}$ and $\underline{\phi^o}$ in the crevice were assumed as conditions at the common boundary KL with $\underline{c_i^o} = c_i^*$ and $\underline{\phi^o} = \phi^*$.

7. The values for $\underline{c_i^*}$ and $\underline{\phi^*}$ at the common boundary KL were fixed with $\underline{c_i^*} = c_i^*$ and $\underline{\phi^*} = \phi^*$.

8. The vector $\boldsymbol{C}_C$ was calculated using CREM.

9. The flux at the common boundary between sub-domains $\underline{N_i^*}$ was calculated.

10. The assumed values c_i^o, ϕ^o,$\underline{c_i^o}$, $\underline{\phi^o}$ were updated with calculated values c_i , ϕ, $\underline{c_i}$, and $\underline{\phi}$, respectively.

11. The vector $\boldsymbol{C}_{HA}$ was calculated using HAM.

12. The percentage difference between the assumed values and the calculated values was given by ξ where

$$\xi = 100 \left| \frac{f - f^o}{f^o} \right| \tag{6-15}$$

and f was a generic variable representing the dependent variables c_i and ϕ. The value of ξ for each dependent variable at each node in the domain, except on the bulk boundary, was calculated and the maximum value of ξ, $\xi_{max,X}$, was determined.

13. The value of $\xi_{max,X}$ was compared with a convergence criterion $\xi_{o,X}$. For the condition $\xi_{max,X} > \xi_{o,X}$ the values of c_i^o and ϕ^o were updated with c_i and ϕ,

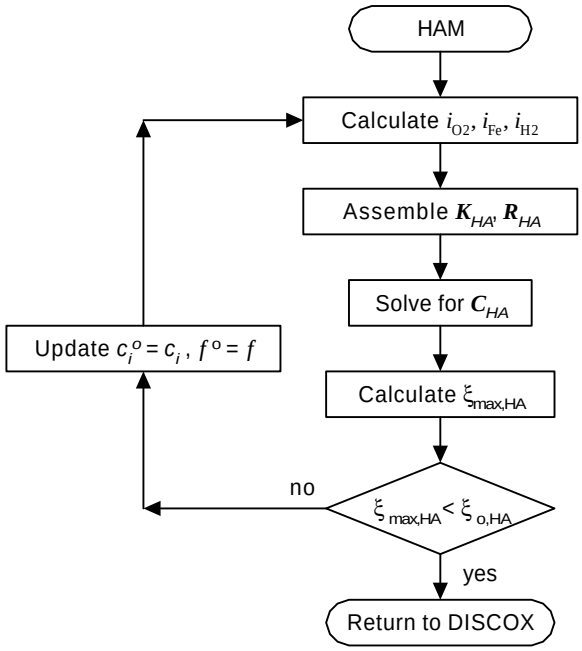

Figure 6-3: The algorithm for the mathematical model HAM.

respectively, and control returned to Step 7. For the condition $\xi_{max,X} < \xi_{o,X}$ control was passed to Step 14.

14. The calculated results were output to files and the procedure terminated.

Holiday-Adjacent Algorithm

The algorithm for the calculation of the steady-state values for c_i and ϕ used in HAM is presented in Figure 6-3 and summarized below:

1. The values of i_{Fe}, i_{O_2}, and i_{H_2} were calculated as functions of position on the metal surface using ϕ^o.

2. The matrix $\boldsymbol{K}_{HA}$ and vector $\boldsymbol{R}_{HA}$ were assembled using c_i^o and ϕ^o.

3. Equation (6-13) was solved to yield the vector $\boldsymbol{C}_{HA}$ which contained the calculated values c_i and ϕ.

4. The percentage difference between the assumed values and the calculated

values was given by ξ where

$$\xi = 100 \left| \frac{f - f^o}{f^o} \right| \tag{6-16}$$

and f was a generic variable representing the dependent variables c_i and ϕ. The value of ξ for each dependent variable at each node in the holiday-adjacent sub-domain, except on the bulk boundary, was calculated and the maximum value of ξ, $\xi_{max,HA}$, was determined.

5. The value of $\xi_{max,HA}$ was compared with a convergence criterion $\xi_{o,HA}$. For the condition $\xi_{max,HA} > \xi_{o,HA}$ the values of c_i^o and ϕ^o were updated with c_i and ϕ, respectively, and control returned to Step 1. For the condition $\xi_{max,HA} < \xi_{o,HA}$ control was passed to Step 6.

6. Control was returned to DISCOX.

Crevice Algorithm

The algorithm for the calculation of the steady-state values for $\underline{c_i}$, and $\underline{\phi}$ used in CREM is presented in Figure 6-4 and summarized below:

1. The values i_{Fe} and $i_{\mathrm{H_2}}$ as functions of position on the metal surface of the crevice were calculated.

2. The matrix $\boldsymbol{K}_C$ and vector $\boldsymbol{R}_C$ were assembled using $\underline{c_i^o}$ and $\underline{\phi^o}$.

3. Equation (6-14) was solved to yield $\boldsymbol{C}_C$ which contained the calculated values $\underline{c_i}$ and $\underline{\phi}$.

4. The percentage difference between the assumed values and the calculated values was given by ξ where

$$\xi = 100 \left| \frac{f - f^o}{f^o} \right| \tag{6-17}$$

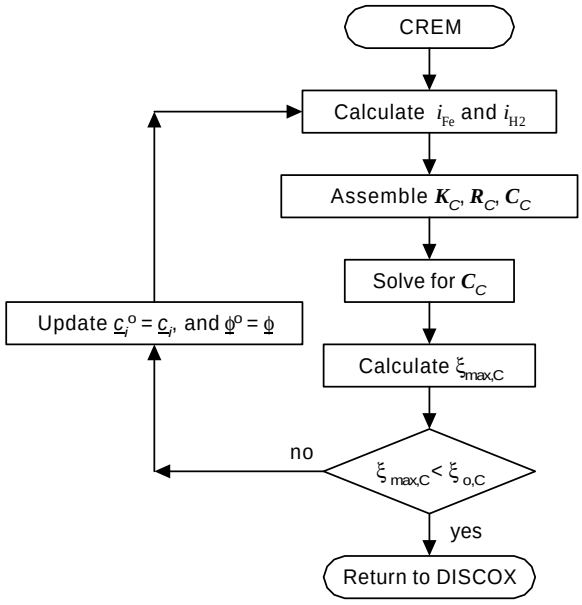

Figure 6-4: The algorithm for the mathematical model CREM.

and f was a generic variable representing the dependent variables $\underline{c}_i$, and $\underline{\phi}$. The value of ξ for each dependent variable at each node in the crevice sub-domain, except on the common boundary between the sub-domains, was calculated and the maximum value of ξ, $\xi_{max,C}$, was determined.

5. The value of $\xi_{max,C}$ was compared with a convergence criterion $\xi_{o,C}$. For the condition $\xi_{max,C} > \xi_{o,C}$ the assumed values were updated with $\underline{c}_i^o = \underline{c}_i$ and $\underline{\phi}^o = \underline{\phi}$, and control returned to Step 1. For the condition $\xi_{max,C} < \xi_{o,C}$ control was passed to Step 6.

6. Control was returned to DISCOX.

6.3 Results

The model that was developed in this chapter was used to simulate the steady-state conditions for disbonded coating systems with long disbondments. The general trends associated with the conditions of disbonded coating systems were presented in Chapter 5.

6.3.1 Model Parameters

The model parameters were associated with the geometry of the system, the composition of the bulk electrolyte, and potential of the metal. The domain of the disbonded coating system is shown in Figure 6-1. The parameters associated with the geometry consisted of the holiday radius r_h (OA), the adjacent length r_a (AK), the crevice length r_c (KB), the gap size g (AD), and the coating thickness a (DE). The disbondment length r_d was given by the sum of r_a and r_c. The parameters associated with the composition of the bulk electrolyte were the bulk concentration of ionic species $c_{i,\infty}$ and the bulk oxygen concentration $c_{O_2,\infty}$. The resistivity of the bulk electrolyte, bulk resistivity, was used to differentiate between different compositions of the bulk electrolyte. The bulk electrolyte consisted of dilute NaCl, which was assumed to be fully dissociated, a neutral pH, and a small concentration of Fe^{+2}. The ionic species considered were Na^+,Cl^-,OH^-, and Fe^{+2} in all the simulations. The ionic specie H^+ was not considered under the assumption that the contribution of H^+ was insignificant in the alkaline electrolyte of the disbonded coating system. The metal potential Ψ represents the potential of the metal such that the solution potential at the mouth of the holiday was a value of 0 V_{SCE} . The metal potential used in the simulations presented was -0.773 V_{SCE}.

The model DISCOX was applied to several systems. In all the systems the grid spacings of $\triangle r = 0.025$ cm and $\triangle z = 0.0125$ cm were used in the radial and axial directions, respectively, for the holiday-adjacent sub-domain. A grid spacing of $\triangle r = 0.025$ cm was used in radial direction for the crevice sub-domain. The convergence criteria for the iterative algorithms used in DISCOX were $\xi_{o,X} = 0.1$ and $\xi_{o,HA} = \xi_{o,C} = 0.01$.

The model parameters common to all the systems modeled were r_h, g, a, $c_{OH^-,\infty}$, and $c_{Fe^{+2},\infty}$. The values for these parameter are given in Table 6.1. The designation

Table 6.1: Model parameters common to disbonded coating systems modeled.

Parameter	Value
r_h	0.5 cm
g	0.05 cm
a	0.05 cm
$c_{OH^-,\infty}$	10^{-7} M
$c_{Fe^{+2},\infty}$	10^{-15} M

of the modeled systems and the associated parameters are given in Table 6.2.

6.3.2 Calculated Distributions

Presented in this section are the solution potential and local electrolyte distributions along the metal surface for systems where the bulk electrolyte resistivity and disbondment length were varied. The parameters of the holiday radius, the gap size, and the metal potential were all fixed for the systems. The parameters used for the systems are given in the previous section.

The distributions of solution potential are shown in Figure 6-5 with disbondment length as a parameter for bulk electrolyte resistivities of 0.79, 7.9 and 79 kΩ cm. The distributions of solution potential were similar for the three bulk electrolyte resistivities. Comparison of these figures shows that for a given disbondment length, more negative values of Φ were associated with bulk electrolytes of larger resistivities.

The distributions of the local electrolyte resistivity are shown in Figure 6-6 with disbondment length as a parameter for bulk electrolyte resistivities of 0.79, 7.9 and and 79 kΩ cm. The variation of local electrolyte resistivity with position were similar for the three bulk electrolyte resistivities and was discussed. Comparison of the figure associated the different bulk resistivities shows that for a given disbondment length, more negative values of Φ were associated with bulk electrolytes of larger resistivities.

Table 6.2: Model parameters used in the simulations of DISCOX.

System	r_d/cm	r_c/cm	r_a/cm	$c_{\mathrm{NaCl},\infty}$ /M	ρ_∞ /kΩcm
A0	0	0	0	0.01	0.79
A1	1	0	1		
A3	3	2			
A5	5	4			
A8	8	7			
A100	10	9			
B0	0	0	0	0.001	7.9
B1	1	0	1		
B3	3	2			
B5	5	4			
B8	8	7			
B100	10	9			
C0	0	0	0	0.0001	79
C1	1	0	1		
C3	3	2			
C5	5	4			
C8	8	7			
C100	10	9			
D0	0	0	0	0.005	1.58
D1	1	0	1		
D3	3	2			
D5	5	4			
D8	8	7			
D100	10	9			
E0	0	0	0	0.0005	15.8
E1	1	0	1		
E3	3	2			
E5	5	4			
E8	8	7			
E100	10	9			
F0	0	0	0	0.0002	39.5
F1	1	0	1		
F3	3	2			
F5	5	4			
F8	8	7			
F100	10	9			

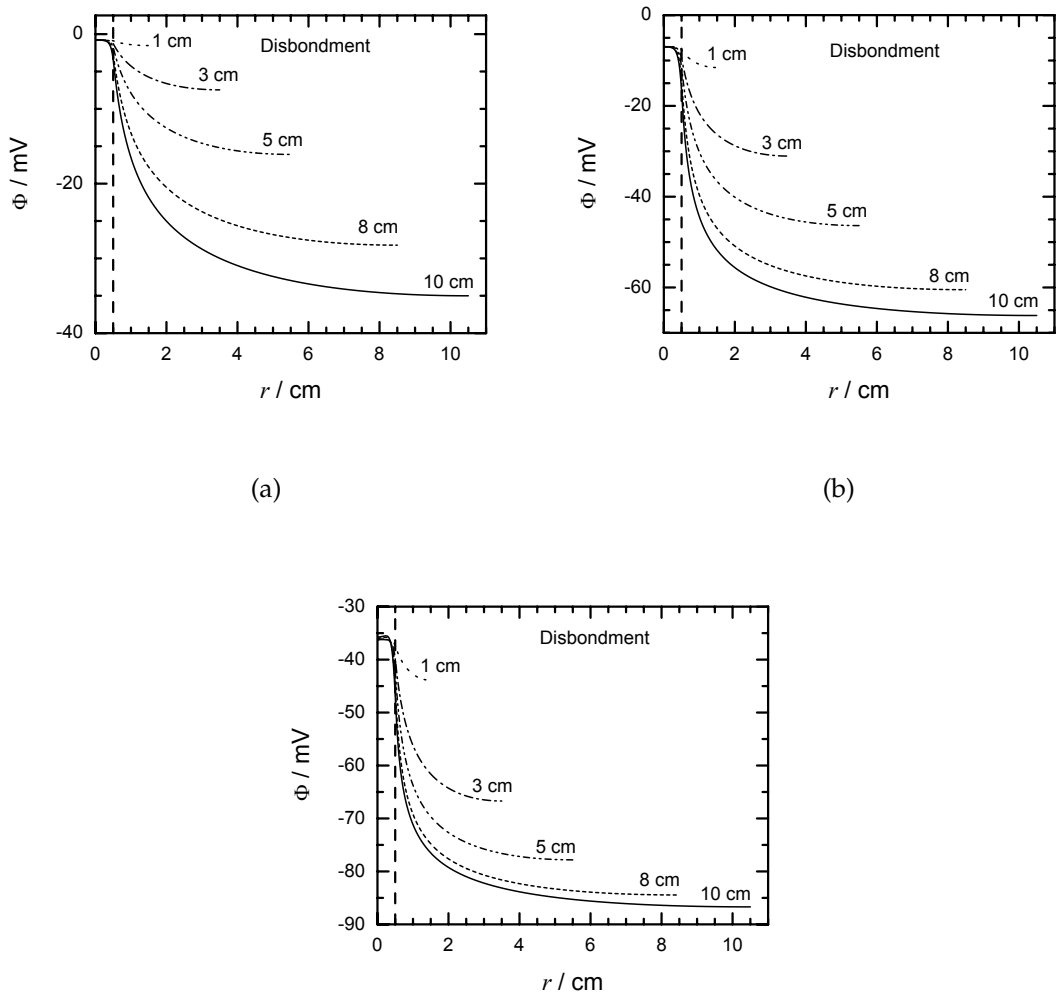

Figure 6-5: Calculated solution potential as a function of position on the metal surface with disbondment length as a parameter for given bulk resistivity. (a) 0.79 kΩ cm, (b) 7.9 kΩ cm and (c) 79 kΩ cm. The dashed line at $r = 0.5$ cm separates the holiday and disbondment.

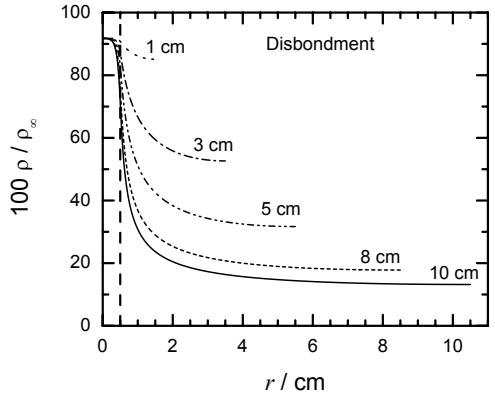

(a)

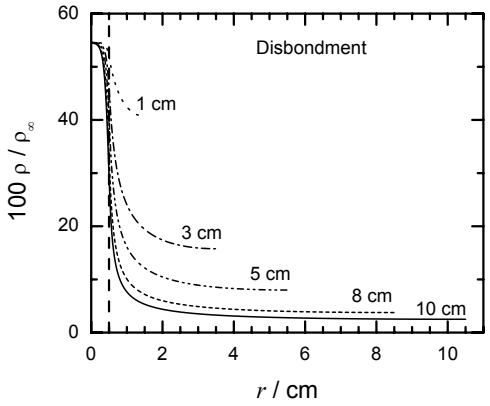

(b)

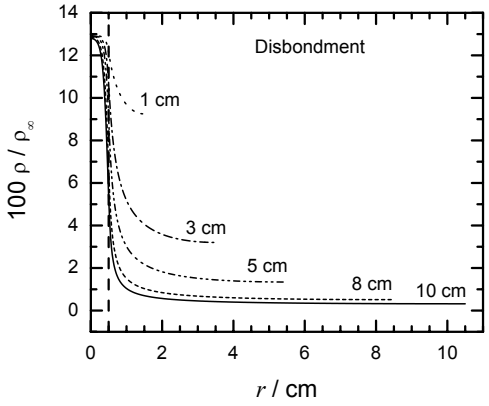

(c)

Figure 6-6: Calculated local electrolyte resistivity as a function of position on the metal surface with disbondment length as a parameter for given bulk resistivity. (a) 0.79 kΩ cm, (b) 7.9 kΩ cm and (c) 79 kΩ cm. The dashed line at $r = 0.5$ cm separates the holiday and disbondment.

Table 6.3: Calculated solution potential in mV at tip of disbondment for given disbondment length and bulk resistivity.

Disbondment length / cm	Bulk Resistivity / kΩ cm					
	0.79	1.58	7.9	15.8	39.5	79
0	−0.785	-1.55	−6.94	-12.54	-24.1	−36.2
1	−1.53	-2.94	−11.5	-18.7	-31.8	−43.9
3	−7.46	-12.5	−31.0	-41.3	-5.7	−66.7
5	−16.1	-23.9	−46.4	-56.6	-69.3	−77.8
8	−28.2	-37.8	−60.5	-68.9	-78.3	−84.5
10	−36.6	-44.9	−62.9	-73.4	-81.4	−85.7

Table 6.4: Calculated electrolyte resistivity at the tip of the disbondment as a percentage of the bulk resistivity for given disbondment length and bulk resistivity.

Disbondment length / cm	Bulk Resistivity / kΩ cm		
	0.79	7.9	79
0	91.8	54.6	12.9
1	85.1	40.7	9.25
3	52.6	15.8	3.20
5	31.7	8.00	1.34
8	17.8	3.77	0.513
10	13.2	2.50	0.318

6.3.3 Tip Values

The values of the solution potential at the tip of the disbondment for a given disbondment length and bulk resistivity are given in Tables 6.3. The value of the local electrolyte resistivity expressed as a percentage of the bulk resistivity is shown in Table 6.4 for a given disbondment length and bulk resistivity. The values associated with a disbondment length of 0 cm in Tables 6.3 and 6.4 is the value at the holiday surface in the absence of a disbondment.

The value of the solution potential at the tip of the disbondment represented the solution potential drop $\triangle\Phi$ from the mouth of the holiday to the tip of the disbondment because the value of Φ at the mouth was set at a zero value. The value associated with the local electrolyte resistivity represented the change in resistivity as compared to the bulk electrolyte.

The values given in Tables 6.3 and 6.4 were used to construct Figure 6-7. In this figure, the calculated value of the solution potential drop and local electrolyte resistivity are shown as functions of disbondment length with bulk resistivity as a parameter. For a given bulk electrolyte resistivity, larger solution potential drops and smaller local electrolyte resistivities were associated with longer disbondments. For a given disbondment length, larger solution potential drops were associated with larger bulk electrolyte resistivities. The change in the local electrolyte resistivity was larger for larger bulk electrolyte resistivities for a given disbondment length.

6.4 Design Equation

The value of the solution potential drop for disbondment lengths of 0, 1, 3, 5, and 8 cm are shown in Figure 6-7 as a function of disbondment length for three bulk electrolyte resistivities of 0.79, 7.9 and 79 kΩ cm. The development of a design equation is presented in this section where the value of the solution potential drop was a function of the disbondment length and bulk electrolyte resistivity. The design equation was developed for conditions of a 0.5 cm holiday radius, 0.05 cm gap size, 0.05 cm coating thickness, and a metal potential of -0.773 V_{SCE} relative to a zero value of solution potential at the mouth of the holiday.

The DISCOX-calculated values of $\triangle\Phi$ are shown in Figure 6-8 for disbondment lengths and bulk electrolyte resistivities. Distributions of $\triangle\Phi$ are shown in Figure 6-8 for a given bulk resistivity. The equation of a distribution was of the form

$$\triangle\Phi = a_1 + \frac{a_2}{1 + \exp((a_3 - r_d)/a_4)} \tag{6-18}$$

where a_1, a_2, a_3, and a_4 were design parameters. The values of these design parameters were obtained by fitting by inspection the distribution to the DISCOX-calculated values. The values of the design parameters associated with the bulk resistivities are given in Table 6.5.

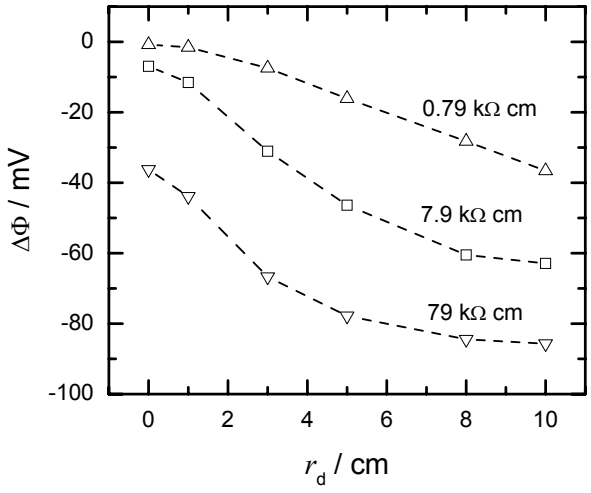

(a)

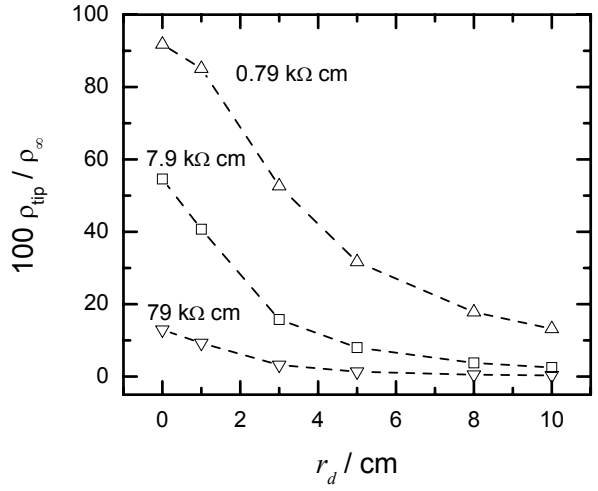

(b)

Figure 6-7: Calculated value of at the disbondment tip as a function of disbondment length with bulk resistivity as a parameter. (a) solution potential drop and (b) local electrolyte resistivity. The value associated with a disbondment length of 0 cm is the value at the holiday surface in the absence of a disbondment.

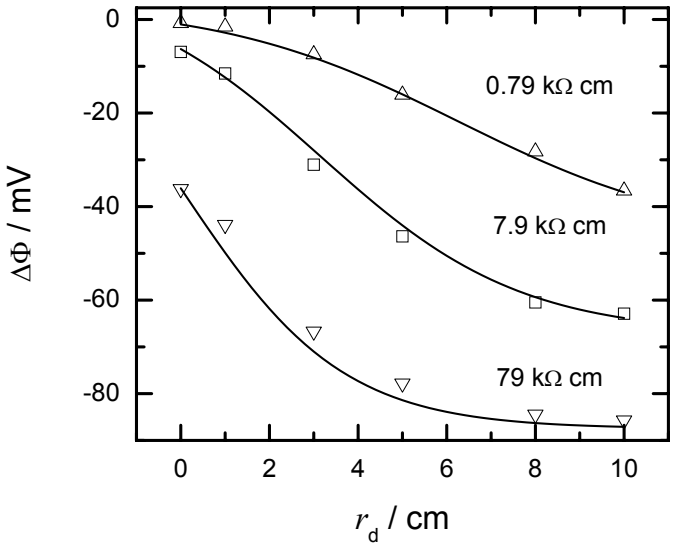

Figure 6-8: Calculated solution potential drop as a function of disbondment length with bulk resistivity as a parameter. The values calculated using the mathematical model are indicated with symbols where 0.79 kΩ cm:△, 7.9 kΩ cm:□ and 79 kΩ cm:▽.

Table 6.5: Design parameter values associated with design equation for the solution potential drop.

Bulk resistivity / kΩ cm	Design parameters			
	a_1 / mV	a_2 / mV	a_3 / cm	a_4 / cm
0.79	4	−50	6.2	2.8
7.9	8	−75	3	2.1
79	14	−100	0.1	1.9

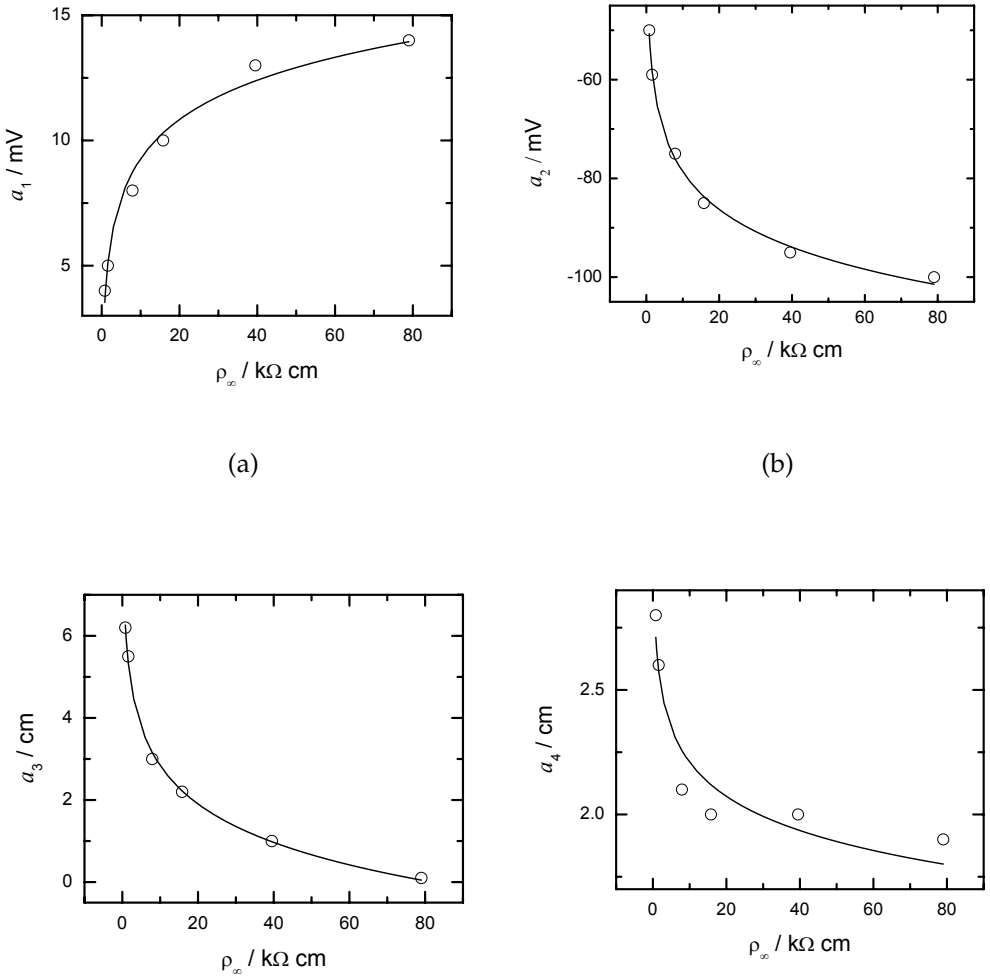

Figure 6-9: Parameters for solution potential drop equation as functions of bulk electrolyte resistivity. (a) a_1, (b) a_2, (c) a_3, and (d) a_4.

The design parameters are shown as functions of the bulk resistivity in Figure 6-9. The distributions of a given design parameter as a function of bulk electrolyte resistivity is shown in Figure 6-9. The expression for the distributions were of the form

$$a_k = p_k \ln(\rho_\infty) + q_k \tag{6-19}$$

where $k = 1, 2, 3, 4$ and p_k and q_k were design expression parameters. The values of these parameters were obtained using *Microsoft EXCEL®* and are given in Table 6.6.

Table 6.6: Parameters associated with the expressions for the design parameters used in the calculated of the solution potential drop in a disbonded coating system.

k	p_k	q_k
1	2.1715 mV	4.1785 mV
2	−10.857 mV	−52.559 mV
3	−1.3246 cm	5.8378 cm
4	−0.1954 cm	2.6706 cm

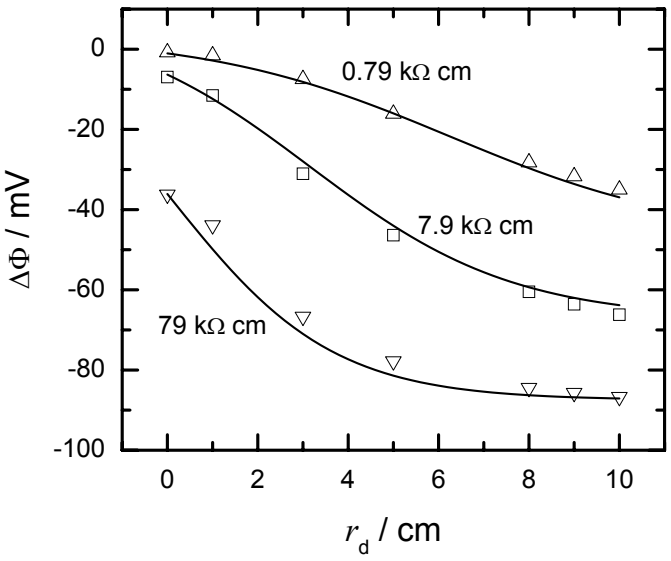

Figure 6-10: The solution potential drop as a function of disbondment length with bulk resistivity as a parameter calculated using the design equation. The values calculated using the mathematical model DISCOX are indicated with symbols where △:0.79 kΩ cm, □:7.9 kΩ cm, and ▽:79 kΩ cm.

The design equation for the solution potential at the tip of the disbondment was

$$\triangle\Phi(r_d, \rho_\infty) = a_1(\rho_\infty) + \frac{a_2(\rho_\infty)}{1 + \exp((a_3(\rho_\infty) - r_d)/a_4(\rho_\infty)} \tag{6-20}$$

where the design parameters were functions of bulk resistivity in kΩ cm given by equation (6-19). The value of the solution potential drop as a function of disbondment length is shown in Figure 6-10 with bulk electrolyte resistivity as a parameter. Values of $\triangle\Phi$ calculated using DISCOX are shown. For a given disbondment length and bulk electrolyte resistivity, there was agreement between the values of $\triangle\Phi$ calculated using the design equation and calculated using DISCOX.

6.5 Summary

A mathematical model DISCOX for the steady-state conditions in a radial disbonded coating system was developed. In this model the holiday and a section of the disbondment was modeled as a two-dimensional domain and the remainder of the disbondment as a one-dimensional domain. This model accounted for the transport of species and electroneutrality in the presence of multiple electrochemical reactions. Cylindrical coordinates were used to discretize the governing equations. An iterative method of solution was used that involved linearization of the nonlinear governing equations. The results presented were used to construct a design equation for the solution potential drop between the mouth of the holiday and the disbondment tip. The solution potential drop was a function of bulk electrolyte resistivity and disbondment length where the parameters for the holiday radius, the gap size, the coating thickness, and metal potential were fixed.

CHAPTER 7
EXAMINATION OF MODEL ASSUMPTIONS

The mathematical models presented in literature for the disbonded coating system employed assumptions. These assumptions reduced the complexity of the governing equations of the system. In the model presented by Chin and Sabde[2,3] the assumption that the diffusion coefficients of ionic species be equated to 10^{-5} cm^2s^{-1} was used. In the model presented by Sridhar *et al.*[37] the equilibrium relationships were decoupled from the governing equations of the species considered. The applicability of these assumptions was investigated to determine whether or not to include them in DISCOM. The findings of this investigation are presented in this chapter.

The assumption that is commonly used in modeling pit systems is the placement of the bulk boundary far from the metal surface of the pit (see Figure 3-2). In the development of DISCOM the bulk boundary was arbitrarily placed at the mouth of the holiday. The assumption that supported this was that concentration gradients exterior to the holiday were negligible. An investigation into the influence of bulk boundary location and the validity of the associated assumption is presented in this chapter.

7.1 Influence of Bulk Boundary Location

The influence of the bulk boundary location for disbonded coating systems was investigated by simulating the steady-state conditions for two systems. In one system, called the Inner System, the bulk boundary was positioned at the mouth of the holiday as shown in Figure 7-1(a). In the other system, called the Extended System, the bulk boundary was position in the bulk electrolyte as shown in Figure

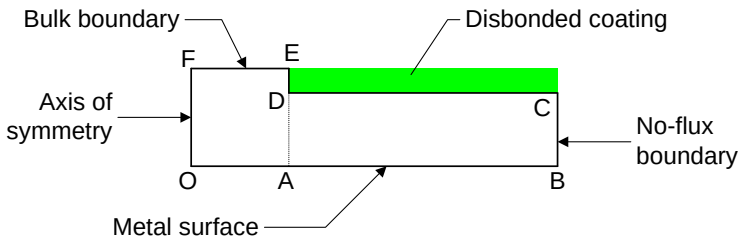

(a)

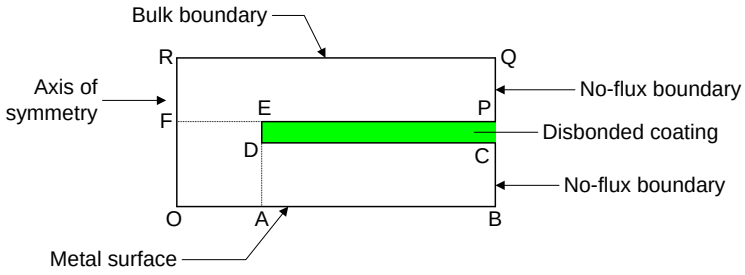

(b)

Figure 7-1: Schematic diagrams for the (a) Inner System and (b) Extended System.

7-1(b).

The model DISCOM was used to simulate the electrochemistry of the Inner System. This model was extended to accommodate the domain of the Extended System and used to calculate the steady-state conditions of the Extended System.

7.1.1 Model Parameters

The geometry of the Inner System consisted of a holiday radius $r_h = 0.25$ cm, a disbondment length $r_d = 1.0$ cm, a gap $g = 0.05$ cm, and a coating thickness $a = 0.05$ cm. In the Extended System the dimensions for r_h, r_d, g, and a were the same as the Inner System and the bulk boundary was positioned such that it was parallel to the metal surface. The perpendicular distance between the mouth and the bulk boundary FR (see Figure 7-1(b)) was $l_{up} = 0.05$ cm . In the simulations of both systems a grid spacing of $\triangle r = 0.0125$ cm and $\triangle z = 0.0125$ cm was used. The convergence criterion for the iterative algorithm was $\xi_{o,D} = 0.01$.

In both systems the ionic species considered were Na^{+}, Cl^{-}, OH^{-}, and Fe^{+2}, and no homogeneous reactions were included. The bulk solution comprised of 10^{-3} M NaCl, 10^{-15} M Fe^{+2}, and 10^{-7} M OH^{-}. The electrochemical reactions considered were oxygen reduction, hydrogen evolution, and corrosion. The bulk oxygen concentration was 2.78×10^{-4} M. The metal potential was $\Psi = -0.773$ V_{SCE} such that the current density due to the oxygen reduction reaction was mass-transfer-limited along the metal surface of the domain. The model parameters for the Inner System and System 1 were the same.

7.1.2 Mass-Transfer-Limited Current Density

The value of i_{lim,O_2} as a function of position on the metal surface is shown in Figure 7-2 for the two systems. For a given position, the value of i_{lim,O_2} was less for the Extended System as compared with the Inner System. This result was expected as the further away the bulk boundary was from the metal surface the less the value of the normal concentration gradient for oxygen at the metal surface. Included in Figure 7-2 is the percentage difference as a function of position between the values of i_{lim,O_2} for the two systems relative to value of the Inner system. The percentage difference was approximately 32.5% along the metal surface.

7.1.3 Solution Potential Distribution

The value of Φ as a function of position is shown in Figure 7-3 for the Inner and Extended Systems. The variation of Φ in the radial direction was negligible in the holiday of the Inner System. The variation of Φ was significant in the axial direction in the holiday with the value of Φ dropping from the bulk value of 0 mV at the mouth to -7 mV at the metal surface. The variation of Φ in the disbondment was significant in the radial direction with negligible variation in the axial direction. These variations were discussed in section 5.3.

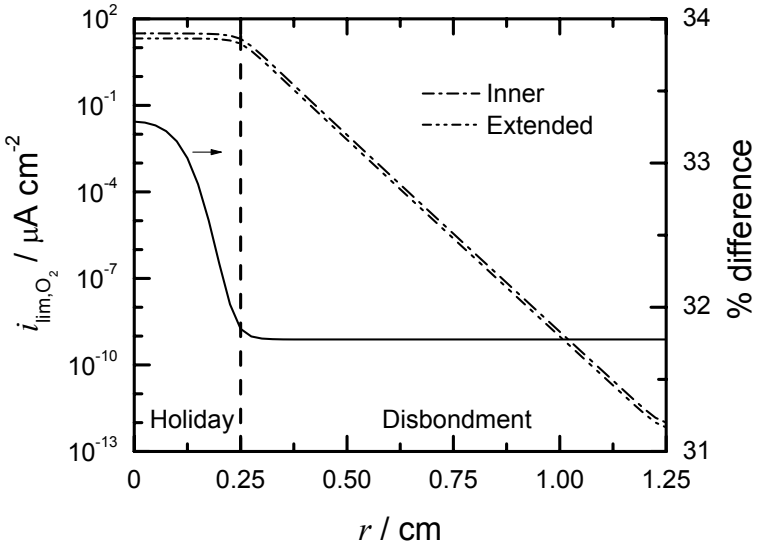

Figure 7-2: Calculated value of mass-transfer-limited current density for oxygen reduction as a function of position on the metal surface for the Inner and Extended Systems. The percentage difference between the values for the Inner and Extended Systems relative to the Inner System value is shown. The dashed line at $r = 0.25$ cm indicates the boundary between the holiday and the disbondment.

The domain of the Extended System was divided into the holiday, the disbondment, and the outer region FEPQR (see Figure 7-1(b)). In the outer region there was little variation in Φ for positions where $r > 0.25$ cm. For positions $r < 0.25$ cm the value of Φ dropped approximately 3 mV from the bulk boundary to the mouth of the holiday (see Figure 7-3(b)). In the holiday, the variation in the axial direction was significant and this included a drop in Φ from -3 mV at the mouth to -7 mV at the metal surface. The drop of 7 mV in Φ between the bulk boundary and the metal surface of the holiday for the Extended System was approximately equal to that observed for the Inner System.

The value of Φ as functions of position on the metal surface for the Inner and Extended Systems are shown in Figure 7-4. In the Inner System, Φ was approximately constant along the holiday and decreased montonically along the disbondment. The variation of Φ for the Inner System was discussed in section 5.3. The variation of Φ with position for the Extended System was similar to that of the Inner System.

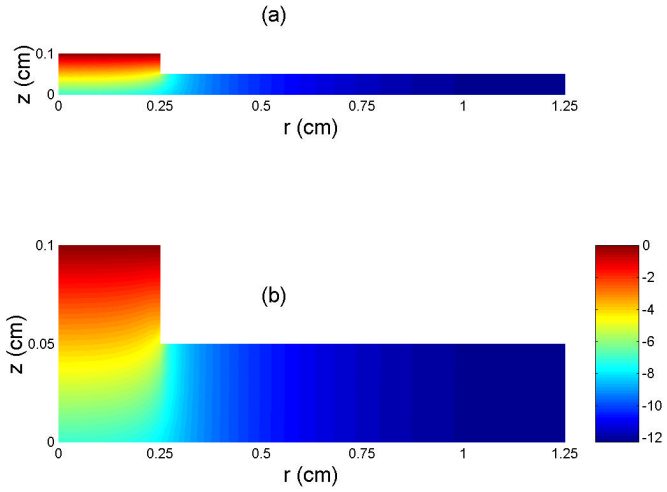

(a)

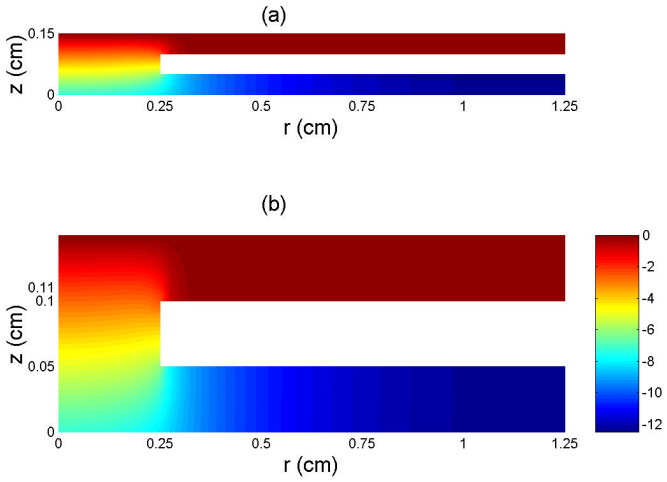

(b)

Figure 7-3: Calculated value of solution potential as a function of position in the two-dimensional domain. (a) Inner System and (b) Extended System.

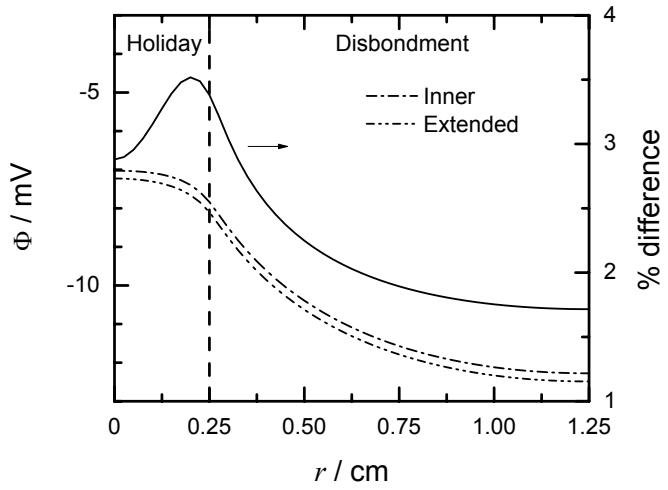

Figure 7-4: Calculated value for solution potential as a function of position on the metal surface for Inner and Extended Systems. The percentage difference between the values for the Inner and Extended Systems relative to the Inner System value is shown. The dashed line at $r = 0.25$ cm indicates the boundary between the holiday and the disbondment.

The value of Φ at a given position on the metal surface for the Inner System was more positive as compared to the value of the Extended System. Included in Figure 7-4 is the percentage difference as a function of position between the values of Φ relative to the Inner System value. The percentage difference increased from 3 percent to 3.75 percent across the holiday and then decreased from 3.5 to 1.75 percent with position in the disbondment.

7.1.4 pH Distribution

The value of pH as a function of position is shown in Figures 7-5 for the Inner and Extended Systems. The pH variation in the axial direction in the holiday was significant, increasing from the bulk value of 7 at the mouth to 10.75 at the metal surface, whereas the pH variation in the radial direction was negligible. The pH variation in the disbondment was significant in the radial direction and negligible in the axial direction.

There was little variation of pH in the outer region of the Extended System for positions $r > 0.25$ cm . The value of pH for positions $r < 0.25$ cm dropped

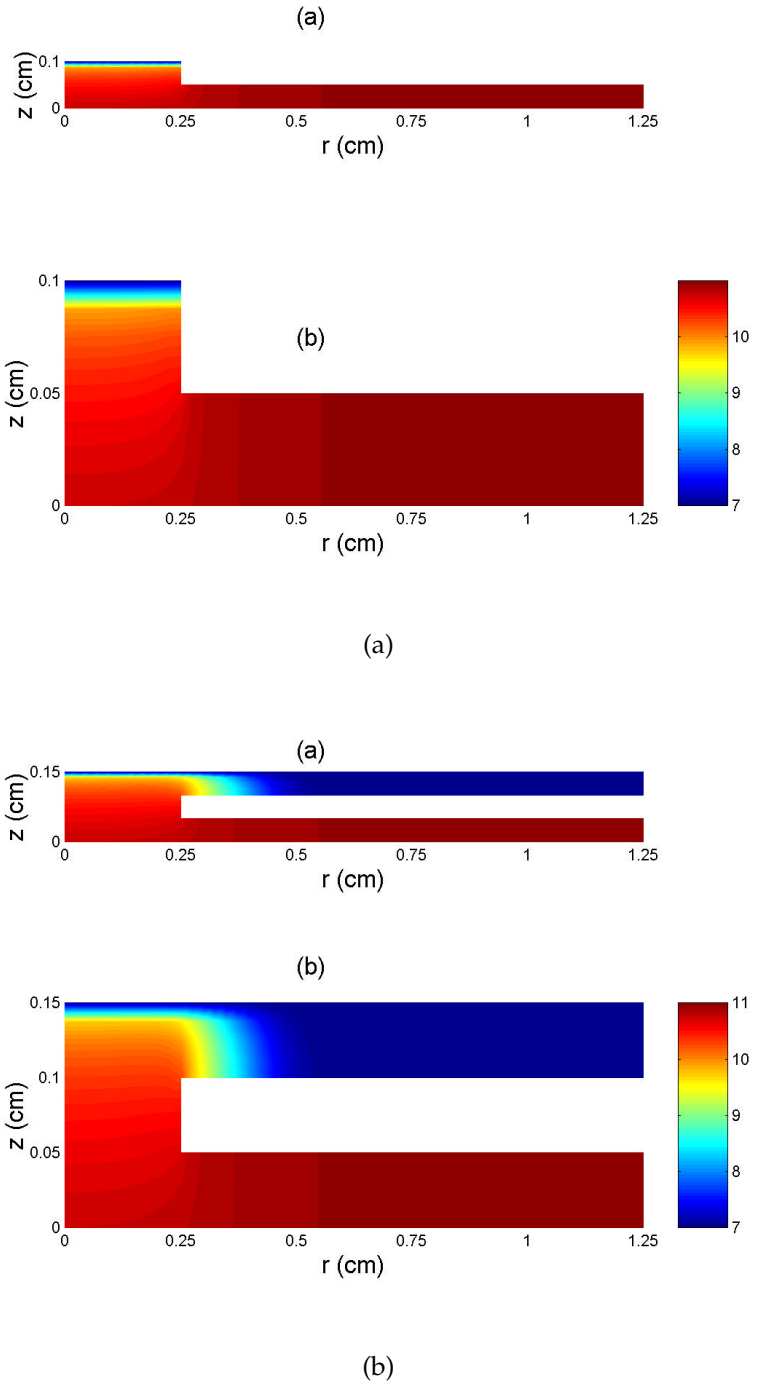

(a)

(b)

Figure 7-5: Calculated value of pH as a function of position. (a) Inner System and (b) Extended System.

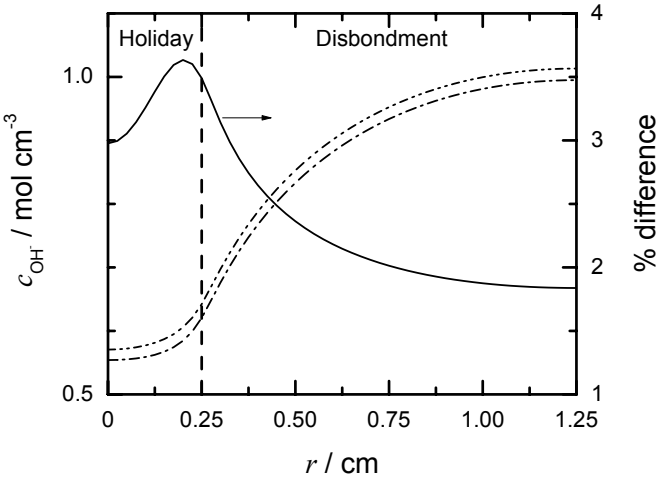

Figure 7-6: Calculated values of the hydroxide ion concentration as a function of position on the metal surface for Inner and Extended Systems. The percentage difference between the values of the Inner and Extended Systems relative to the Inner System value is shown. The dashed line at $r = 0.25$ cm indicates the boundary between the holiday and the disbondment.

approximately 3.5 units from the bulk boundary to the mouth of the holiday. The pH variation in the holiday perpendicular to the metal surface was significant and this included a drop of 0.25 units between the mouth and the metal surface. The pH drop between the bulk boundary and the metal surface of the holiday was approximately equal for the Extended and Inner Systems.

The value of c_{OH^-} as a function of position on the metal surface is shown in Figure 7-6 for the Inner and Extended Systems. The distribution of c_{OH^-} in the Inner System consisted of a montonically increasing value along the metal surfaces of the holiday and disbondment. The variation of pH for the Inner System was discussed in section 5.3.4. The variation of c_{OH^-} with position for the Extended System was similar to that of the Inner System. For a given position, the value of c_{OH^-} for the Inner System was less than that of the Extended System. Included in Figure 7-6 is the percentage difference as a function of position between the c_{OH^-} values of the systems relative to the Inner System. The percentage difference was less than 3.75% for positions on the metal surface.

7.1.5 Discussion

The positioning of the bulk boundary at the holiday mouth was under the assumption that the concentration gradients outside of the holiday were negligible. It was shown that there was a region immediately outside of the holiday, the outer region, where the gradient of c_{OH^-} was significant (see Figure 7-5(b)). Therefore, the assumption of negligible concentration gradients that supported the positioning of the bulk boundary at the holiday mouth was not applicable.

There was a 33% difference for the value of i_{lim,O_2} on the holiday metal surface between the systems. It would be expected that the large percentage difference in i_{lim,O_2} be accompanied by large percentage differences in Φ, c_{OH^-}, and other dependent variables. This large percentage difference in i_{lim,O_2} only translated into a percentage differences less than 4% for Φ and less than 3.75% for c_{OH^-} along the metal surface for the systems. This small percentage difference for Φ and pH was counterintuitive compared to the large 33% difference associated with i_{lim,O_2}. There were large changes in the conditions of the outer region for the Extended System. These changes established conditions at the mouth such that the values of c_i and Φ along the metal surface for the Inner and Extended Systems were approximately equal.

The development of DISCOM in Chapter 4 included the assumption that the contribution of convection to mass-transfer was negligible. This assumption is reasonable in the restricted geometry of the disbondment and holiday. In experimental and real systems the region external to the disbonded coating system may be influenced by convective transport. The small error associated with placing the bulk boundary at the mouth as opposed to in the bulk would be reduced as the concentration gradients in the outer region would be reduced with increased mass-transfer.

7.2 Diffusion Coefficients

Mathematical models for occluded systems have been presented in literature in which the diffusion coefficients of species have been approximated to simplify model development. The assumption that the diffusion coefficients of all the species was equal to 10^{-5} cm^2/s has been used for pit and disbonded coating systems.[2,38] The assumption that the diffusion coefficient of all species other than OH^- and H^+ was equal to 10^{-5} cm^2/s has also been used.[50] DISCOM was used to investigate the applicability of these assumptions to the disbonded coating system.

7.2.1 Model Parameters

Several systems were modeled with System 1, given in Chapter 5, being the control system. The parameter data for System 1 is given in Table 5.2. In System 1 the values of D_i used were literature values and no assumptions regarding the value of D_i were applied. Systems designated 1.1, 1.2, and 1.3 were modeled using the same model parameters as System 1. In these systems various assumed values of the diffusion coefficients of species were used. Table 7.1 lists the values of D_i used for Systems 1, 1.1, 1.2, and 1.3. The assumption that all the diffusion coefficients was equal to 10^{-5} cm^2/s was applied in System 1.1. This assumption has previously been used in literature.[2,38] In System 1.2 the diffusion coefficients of Na^+, Cl^-, and Fe^{+2} were set at 10^{-5} cm^2/s and that of OH^- was unaltered. This was similar to the assumption used by Sharland.[50] In System 1.3 the diffusion coefficients of Na^+, Cl^-, and Fe^{+2} were set at 10^{-5} cm^2/s and that of OH^- was set at $0.5 \times 5.24580 \times 10^{-5}$ cm^{2}s^{-1}.

7.2.2 Results and Discussion

The variation of the dependent variables Φ, pH, c_{Na^+}, c_{Cl^-}, and $c_{Fe^{+2}}$ are shown as functions of position on the metal surface in Figures 7-7, 7-8, 7-9, 7-10, and 7-11,

Table 7.1: Assumed diffusion coefficients for species.

Parameter i	System 1	System 1.1	System 1.2	System 1.3
$D_{Na^+} \times 10^5$ cm^2/s	1.33410	1	1	1
$D_{Cl^-} \times 10^5$ cm^2/s	2.03440	1	1	1
$D_{OH^-} \times 10^5$ cm^2/s	5.24580	1	5.24580	2.62290
$D_{Fe^{+2}} \times 10^5$ cm^2/s	0.71231	1	1	1

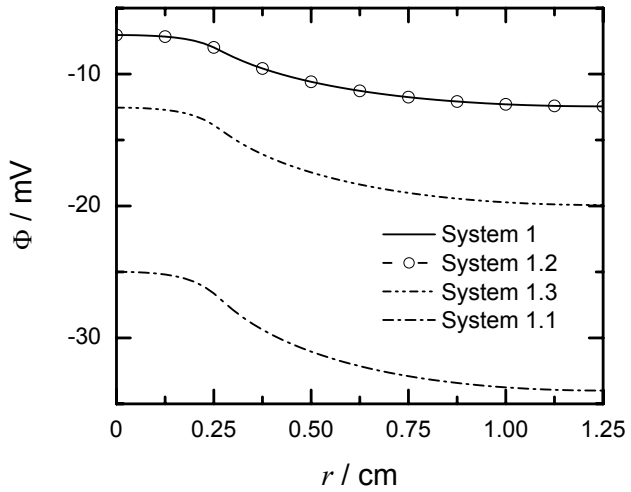

Figure 7-7: Calculated value of solution potential as a function of position on the metal surface with system as a parameter. The distributions for Systems 1 and 1.2 superimposed.

respectively. The variation of the dependent variables with position for System 1 was discussed in Chapter 5. The variation of the system variables with position for Systems 1.1, 1.2, and 1.3 were similar to that of System 1.

The results for Systems 1 and 1.2 were approximately equal with the distributions superimposing for variables Φ, pH, c_{Na^+}, and c_{Cl^-}. For a given position, smaller values of $c_{Fe^{+2}}$ was associated with System 1.2 compared to the corresponding values of System 1. In the disbonded coating system that was investigated the electrochemical production of OH^- was significant as compared to that for Fe^{+2}. Therefore, the equating of diffusion coefficients of all species other than the specie under significant electrochemical production was reasonable.

Comparison of the distributions for the Systems 1 and 1.1 indicated that the assumption that $D_i = 10^{-5}$ cm^{2}s^{-1} for all the species was not applicable to the dis-

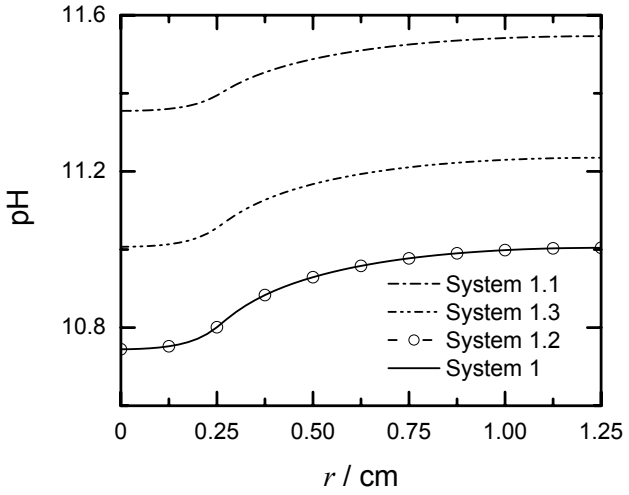

Figure 7-8: Calculated value of pH as a function of position on the metal surface with system as a parameter. The distributions for Systems 1 and 1.2 superimposed.

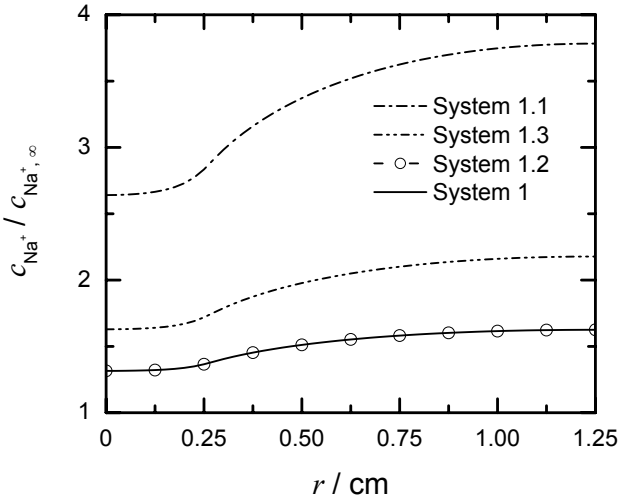

Figure 7-9: Calculated value of the sodium ion concentration as a function of position on the metal surface with system as a parameter. The distributions for Systems 1 and 1.2 superimposed.

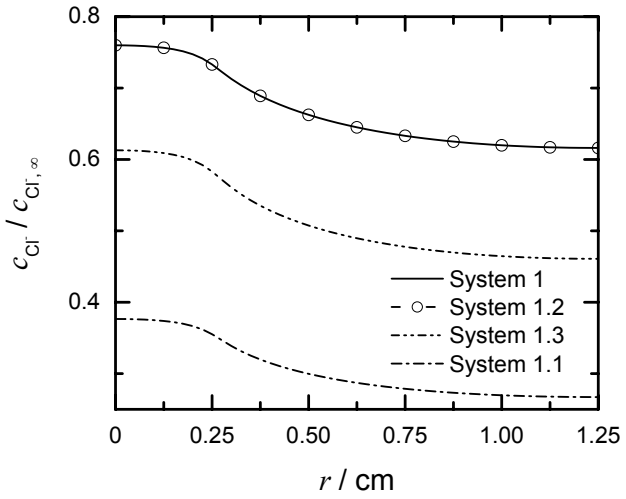

Figure 7-10: Calculated value of the chloride ion concentration as a function of position on the metal surface with system as a parameter. The distributions for Systems 1 and 1.2 superimposed.

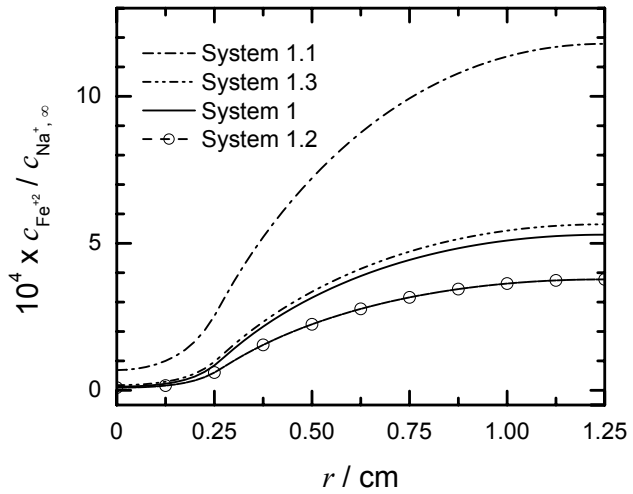

Figure 7-11: Calculated value of the ferrous ion concentration as a function of position on the metal surface with system as a parameter.

bonded coating system. The results for System 1.3 were an improvement when compared with System 1.1. The simplification of model development by equating diffusion coefficients to 10^{-5} cm^2s^{-1} is not recommended for occluded systems. The equating of the diffusion coefficients to 10^{-5} cm^2s^{-1} of minor species not participating in electrochemical reactions is a reasonable assumption.

7.3 Decoupling Homogeneous Reactions

The inclusion of homogeneous reactions explicitly as governing equations has been a numerical challenge in model development for occluded systems. A transient model reported in literature employed a method that decoupled the homogeneous reactions from the governing equations.[37,55] In this method the species were separated into primary and secondary species. The separation was such that the concentrations of secondary species were derived from the primary species, conservation equations, and chemical equilibrium relationships for homogeneous reactions. This method is termed the primary-secondary species method in this work with an abbreviation of PS method.

DISCOM, presented in Chapter 4, was developed to accommodate the homogeneous reaction between Fe^{+2} and OH^- as described by equation (4-1). The method employed in this model accounted for the equilibrium relationship of the homogeneous reaction explicitly. This method is referred to as the Coupled method here.

A model PS-DISCOM was developed to include the reaction between Fe^{+2} and OH^- as described by equation (4-1) using the PS method. In this section the development of PS-DISCOM is presented. Results are presented for a disbonded coating system which was modeled using DISCOM and PS-DISCOM.

7.3.1 Electrochemical System

The domain of the disbonded coating system used to investigate the PS method was similar to that used for System 1 of Chapter 5 and is shown in Figure 4-1. The electrochemical reactions considered were corrosion and hydrogen evolution.

The five species Na^+, Cl^-, OH^-, Fe^{+2}, and $Fe(OH)^+$ were considered with the homogeneous reaction described by equation (4-1)

$$Fe^{+2} + OH^- \rightleftharpoons Fe(OH)^+$$

The equilibrium constant for the relationship given by equation (4-12)

$$\frac{c_{Fe(OH)^+}}{c_{OH^-} \cdot c_{Fe^{+2}}} = K_I$$

was $K_I = 10^{5.7}$.[55]

7.3.2 Primary-Secondary Species Method

The PS method involved separating the species into primary and secondary species. The dependent variables in the system were c_{Na^+}, c_{Cl^-}, c_{OH^-}, $c_{Fe^{+2}}$ and ϕ. A sub-system was used in the development of the method. This system comprised the primary species Na^+, Cl^-,OH^-, and Fe^{+2} and ϕ and was designated the primary sub-system. The dependent variables in the primary sub-system were $\tilde{c}_{Na^+}$, $\tilde{c}_{Cl^-}$, $\tilde{c}_{OH^-}$, $\tilde{c}_{Fe^{+2}}$, and ϕ. The calculated values for $\tilde{c}_i$ were used to calculate c_{OH^-}, $c_{Fe^{+2}}$, and $c_{Fe(OH)^+}$ in a correction procedure.

Primary Sub-System Governing Equations

The governing equations for the primary species c_{Na^+} and c_{Cl^-} in the primary sub-system were

$$0 = D_{Na^+}\left[z_{Na^+}\nabla \cdot (\tilde{c}_{Na^+}\nabla\phi) + \nabla^2\tilde{c}_{Na^+}\right] \tag{7-1}$$

and

$$0 = D_{Cl^-}\left[z_{Cl^-}\nabla \cdot (\tilde{c}_{Cl^-}\nabla\phi) + \nabla^2\tilde{c}_{Cl^-}\right] \tag{7-2}$$

respectively. The governing equations for c_{OH^-} and $c_{Fe^{+2}}$ were

$$0 = D_{OH^-}\left[z_{OH^-}\nabla\cdot(\tilde{c}_{OH^-}\nabla\phi)+\nabla^2\tilde{c}_{OH^-}\right]+S_{Fe(OH)^+} \tag{7-3}$$

$$0 = D_{Fe^{+2}}\left[z_{Fe^{+2}}\nabla\cdot(\tilde{c}_{Fe^{+2}}\nabla\phi)+\nabla^2\tilde{c}_{Fe^{+2}}\right]+S_{Fe(OH)^+} \tag{7-4}$$

where

$$S_{Fe(OH)^+} = D_{Fe(OH)^+}\left[z_{Fe(OH)^+}\nabla\cdot(c^o_{Fe(OH)^+}\nabla\phi)+\nabla^2 c^o_{Fe(OH)^+}\right] \tag{7-5}$$

with $c^o_{Fe(OH)^+}$ being an assumed value for $c_{Fe(OH)^+}$. The governing equation for ϕ was

$$z_{Na^+}\tilde{c}_{Na^+}+z_{Cl^-}\tilde{c}_{Cl^-}+z_{OH^-}\tilde{c}_{OH^-}+z_{Fe^{+2}}\tilde{c}_{Fe^{+2}} = -z_{Fe(OH)^+}c^o_{Fe(OH)^+} \tag{7-6}$$

and represented the condition of electroneutrality.

Primary System Boundary Conditions

The conditions of $\tilde{c}_i$ and Φ were fixed at the mouth FE to the bulk conditions $c_{i,\infty}$ and Φ_∞, respectively. The solution potential $\Phi_\infty = 0$ was used such that the calculated values for Φ in the model were referenced to a zero value at the bulk boundary position.

The boundary condition for the chemically inert species at all boundaries except the mouth was the the no-flux condition given by

$$\tilde{\boldsymbol{N}}_i\cdot\boldsymbol{n} = 0 \tag{7-7}$$

where $\boldsymbol{n}$ was the unit vector normal to the surface and $\tilde{\boldsymbol{N}}_i$ the flux of a species in the primary sub-system.

The boundary conditions for Fe^{+2} and OH^- on the all boundaries except the mouth and metal surface was

$$\tilde{\boldsymbol{N}}_i\cdot\boldsymbol{n}+\boldsymbol{N}_{Fe(OH)^+}\cdot\boldsymbol{n} = 0 \tag{7-8}$$

where

$$\boldsymbol{N}_{\mathrm{Fe(OH)^+}} = -z_{\mathrm{Fe(OH)^+}} D_{\mathrm{Fe(OH)^+}} c^o_{\mathrm{Fe(OH)^+}} \nabla\phi - D_{\mathrm{Fe(OH)^+}} \nabla c^o_{\mathrm{Fe(OH)^+}} \tag{7-9}$$

The boundary conditions at the metal surface OB for Fe^{+2} and OH^- were obtained by relating the fluxes of these species with the current densities due to the electrochemical reactions on the metal surface. The polarization kinetics of the irreversible electrochemical reactions were used to calculate the current densities of these reactions. The current densities for i_{Fe} and $i_{\mathrm{H_2}}$were given by equations (2-50) and (2-52), respectively. The boundary conditions

$$-z_{\mathrm{Fe^{+2}}} D_{\mathrm{Fe^{+2}}} \tilde{c}_{\mathrm{Fe^{+2}}} \frac{\partial\phi}{\partial z} - D_{\mathrm{Fe^{+2}}} \frac{\partial \tilde{c}_{\mathrm{Fe^{+2}}}}{\partial z} + N_{\mathrm{Fe(OH)^+}} = \frac{i_{\mathrm{Fe}}}{2F} \tag{7-10}$$

and

$$-z_{\mathrm{OH^-}} D_{\mathrm{OH^-}} \tilde{c}_{\mathrm{OH^-}} \frac{\partial\phi}{\partial z} - D_{\mathrm{OH^-}} \frac{\partial \tilde{c}_{\mathrm{OH^-}}}{\partial z} + N_{\mathrm{Fe(OH)^+}} = \frac{i_{\mathrm{H_2}}}{-F} \tag{7-11}$$

were used for Fe^{+2} and OH^-, respectively, along the metal boundary OB where

$$N_{\mathrm{Fe(OH)^+}} = -z_{\mathrm{Fe(OH)^+}} D_{\mathrm{Fe(OH)^+}} c^o_{\mathrm{Fe(OH)^+}} \frac{\partial\phi}{\partial z} - D_{\mathrm{Fe(OH)^+}} \frac{\partial c^o_{\mathrm{Fe(OH)^+}}}{\partial z} \tag{7-12}$$

The boundary condition for ϕ was the electroneutrality condition that was applicable at all boundaries.

Correction procedure

The correction procedure was used to calculate the values of $c_{\mathrm{OH^-}}$, $c_{\mathrm{Fe^{+2}}}$, and $c_{\mathrm{Fe(OH)^+}}$ given the values of $\tilde{c}_i$. This procedure involved solving the simultaneous equations given by the conservation of the ferrous ion

$$c_{\mathrm{Fe^{+2}}} + c_{\mathrm{Fe(OH)^+}} = \tilde{c}_{\mathrm{Fe^{+2}}} + c^o_{\mathrm{Fe(OH)^+}} \tag{7-13}$$

the conservation of the hydroxide ion

$$c_{\mathrm{OH^-}} + c_{\mathrm{Fe(OH)^+}} = \tilde{c}_{\mathrm{OH^-}} + c^o_{\mathrm{Fe(OH)^+}} \tag{7-14}$$

and the equilibrium relationship

$$\frac{c_{Fe(OH)^+}}{c_{OH^-} \cdot c_{Fe^{+2}}} = K_I \tag{7-15}$$

The value of c_{Cl^-} was equated to the value of $\tilde{c}_{Cl^-}$. The electroneutrality condition was satisfied by adjusting the value of c_{Na^+} using

$$z_{Na^+} c_{Na^+} = -\left(z_{Cl^-} c_{Cl^-} + z_{OH^-} c_{OH^-} + z_{Fe^{+2}} c_{Fe^{+2}} + z_{Fe(OH)^+} c_{Fe(OH)^+}\right) \tag{7-16}$$

7.3.3 Method of Solution

The governing equations and boundary conditions of the primary sub-system were discretized and cast into the form

$$\boldsymbol{K}_{PS} \cdot \boldsymbol{C}_{PS} = \boldsymbol{R}_{PS} \tag{7-17}$$

where $\boldsymbol{K}_{PS}$ was the global coefficient matrix, $\boldsymbol{C}_{PS}$ was the global solution vector, and $\boldsymbol{R}_{PS}$ the global load vector for the primary sub-system. The matrix $\boldsymbol{K}_{PS}$ and vector $\boldsymbol{R}_{PS}$ were functions of $\tilde{c}_i$ and ϕ and an iterative algorithm was employed. The Newton-Rhapson method was used in the solution of the simultaneous equations of the correction procedure.[61]

The mathematical model PS-DISCOM was developed using *Compaq Visual Fortran, Version* 6.1® with double precision accuracy to solve the governing equations for the primary sub-system and the simultaneous equations of the correction procedure. The algorithm for PS-DISCOM is presented in Figure 7-12 and summarized below:

1. The necessary input data was read from files.

2. The domain was discretized using the spacings in the radial and axial directions.

3. The values for the dependent variables c_i^o, and ϕ^o, where $\tilde{c}_i^o = c_i^o$, were assumed.

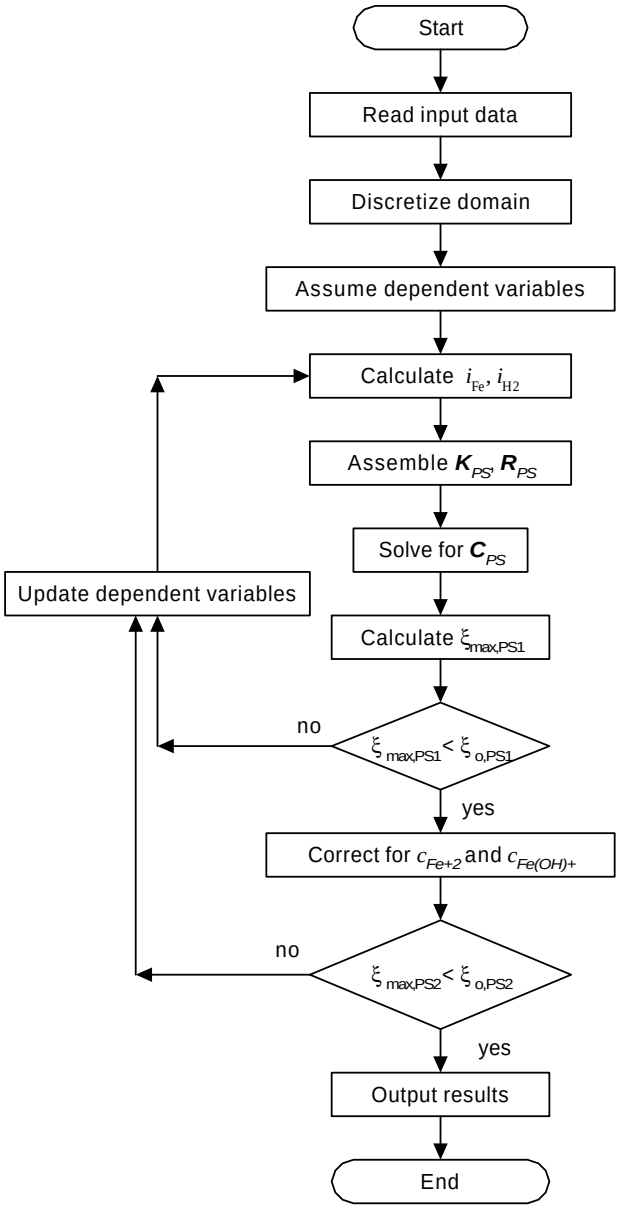

Figure 7-12: The algorithm for the primary-secondary species method implemented into DISCOM.

4. The current densities i_{Fe} and i_{H_2} as functions of position on the metal surface were calculated using ϕ^o.

5. The matrix $\boldsymbol{K}_{PS}$ and vector $\boldsymbol{R}_{PS}$ were assembled using $\tilde{c}_i^o$ and ϕ^o.

6. The equation (7-17) was solved to yield the calculated values $\tilde{c}_i$ and ϕ.

7. The value of $\xi_{max,PS1}$ was calculated where $\xi_{max,PS1}$ is the maximum of ξ_{PS1} which was given by

$$\xi_{PS1} = \left| \frac{f - f^o}{f^o} \right| \tag{7-18}$$

where f was a generic variable for $\tilde{c}_i$ and ϕ.

8. The value of $\xi_{max,PS1}$ was compared with a preset convergence criterion $\xi_{o,PS1}$. If $\xi_{max,PS1} > \xi_{o,PS1}$ then the assumed values were updated $\tilde{c}_i^o = \tilde{c}_i$ and $\phi^o = \phi$ and control returned to Step 4.

9. The values of c_{OH^-}, $c_{Fe^{+2}}$, and $c_{Fe(OH)^+}$ were corrected using the correction procedure.

10. The value $\xi_{max,PS2}$ was calculated, where $\xi_{max,PS2}$ was the maximum of ξ_{PS2} which was given by

$$\xi_{PS2} = \left| \frac{c_{Fe(OH)^+} - c^o_{Fe(OH)^+}}{c^o_{Fe(OH)^+}} \right| \tag{7-19}$$

11. The value of $\xi_{max,PS2}$ was compared with a preset convergence criterion $\xi_{o,PS2}$. If $\xi_{max,PS2} > \xi_{o,PS2}$ then assumed values were updated $\tilde{c}_i^o = c_i$, $c^o_{Fe(OH)^+} = c_{Fe(OH)^+}$, and $\phi^o = \phi$ and control returned to Step 4. If $\xi_{max,PS2} < \xi_{o,PS2}$ then control was passed to the next step.

12. The calculated results were output to files and the procedure terminated.

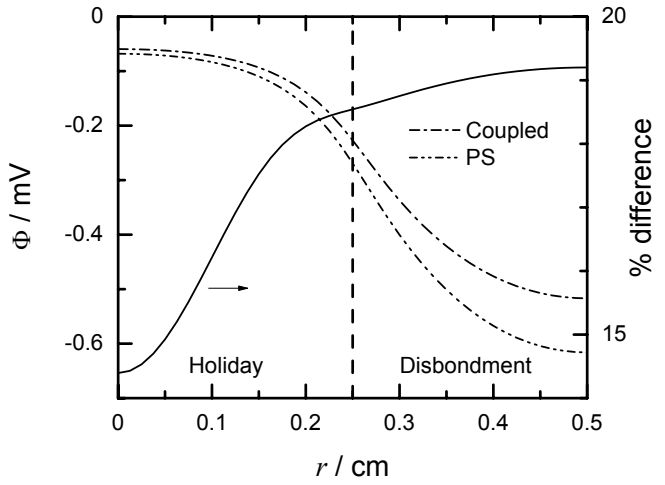

Figure 7-13: Calculated value of solution potential as a function of position on the metal surface with numerical method used as a parameter. The percentage difference between the values for the methods relative to the Coupled method value is shown. The dashed line at $r = 0.25$ cm indicates the boundary between the holiday and the disbondment.

7.3.4 Results and Discussion

The applicability of the PS method was accessed by comparing the results of the models PS-DISCOM and DISCOM for a given electrochemical system. The geometric dimensions of this disbonded coating system were $r_h = 0.25$ cm, $r_d = 0.25$ cm, $g = 0.05$ cm, and $a = 0.05$ cm. In the simulations grid spacings of $\triangle r = 0.0125$ cm and $\triangle z = 0.00625$ cm were used. The convergence criteria used in the iterative procedures were $\xi_{o,PS1} = \xi_{o,PS2} = 0.01$.

The bulk electrolyte of the system included 10^{-3} M NaCl, 10^{-7} M OH^-, and 10^{-10} M Fe^{+2}. The values for D_i were the same as literature values and are given in Table 5.1. The parameters used in the polarization expressions, equations (2-46) and (2-47), are given in Table 2.1. The applied potential used was $\Psi = -0.773$ V_{SCE}.

The calculated values of Φ as a function of position on the metal surface is shown in Figure 7-13 with the method employed as a parameter. The percentage difference between the methods relative to the Coupled method as a function of position is included in this figure. The variations of Φ with position were simi-

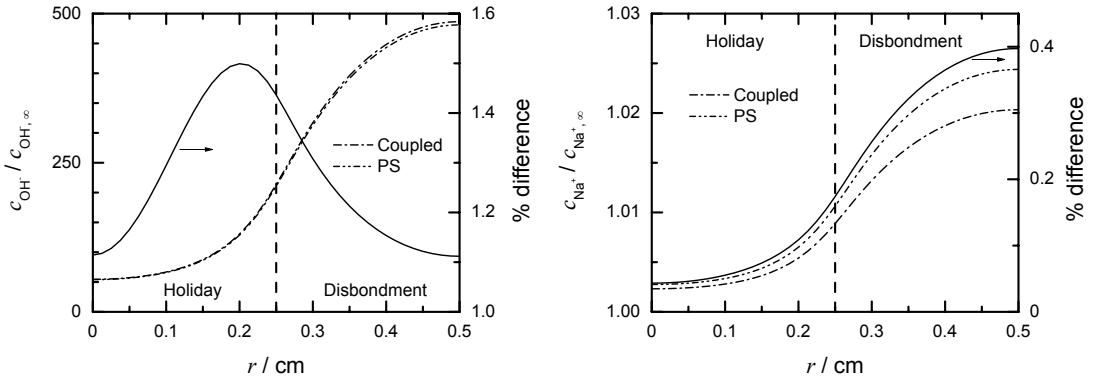

(a)

(b)

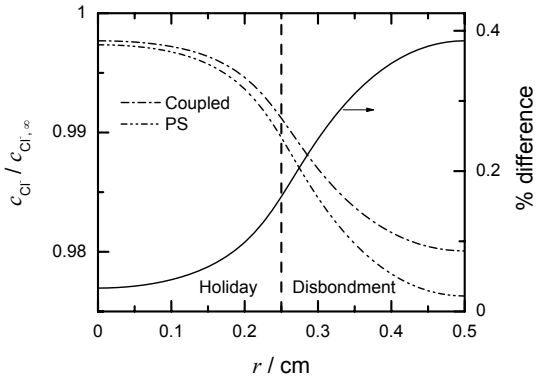

(c)

Figure 7-14: Calculated values of concentrations as functions of position on the metal surface with method used as a parameter. (a) hydroxide ion, (b) sodium ion, and (c) chloride ion. The percentage difference between the values for the methods relative to the Coupled method value is shown. The dashed line at $r = 0.25$ cm indicates the boundary between the holiday and the disbondment.

lar for both methods. The value of Φ at a given position was more negative for the PS method as compared with the Coupled method. The percentage difference increased with position, increasing from 14% to 20% over the holiday and disbondment.

The calculated values of c_{OH^-}, c_{Na^+}, and c_{Cl^-} as functions of position on the metal surface are shown in Figure 7-14 with the method employed as a parameter. The variations of c_{OH^-}, c_{Na^+}, and c_{Cl^-} with position were similar for both meth-

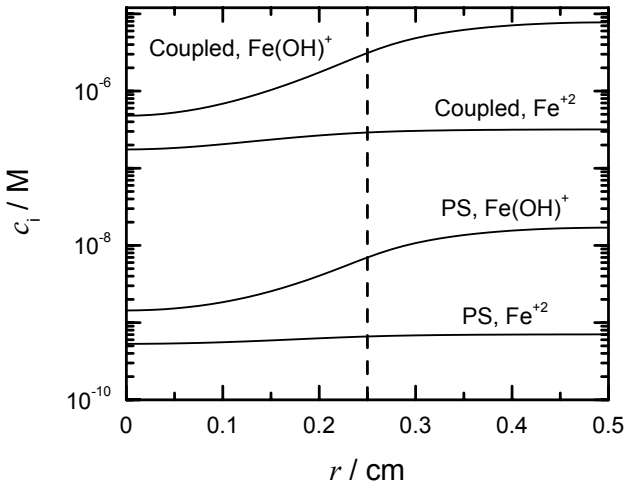

Figure 7-15: Calculated values of concentrations of ferrous ion and ferrous hydroxide ion as functions of position on the metal surface with method used as a parameter. The dashed line at $r = 0.25$ cm indicates the boundary between the holiday and the disbondment.

ods. The percentage difference between the calculated values for c_{OH^-} relative to the Coupled method was observed to have a maximum of 1.5%. The percentage differences for c_{Na^+} and c_{Cl^-} were observed to increase with position. The percentage difference at the tip of the disbondment was 0.4% and 0.8% for c_{Na^+} and c_{Cl^-}, respectively.

The calculated values of $c_{Fe^{+2}}$ and $c_{Fe(OH)^+}$ as functions of position on the metal surface are shown in Figure 7-15 with method used as a parameter. For a given position, the calculated values of $c_{Fe^{+2}}$ and $c_{Fe(OH)^+}$ for the PS method were between two and three orders of magnitude less than the Coupled method . Therefore, the decoupling of the homogeneous relationships from the governing equations for the species is not applicable to the calculation of the steady-state conditions of the disbonded coating system. This result is also applicable to steady-state models of occluded systems such as pits and crevices.

The governing equations for c_i in transient models is given by equation (2-1)

$$\frac{\partial c_i}{\partial t} = -\nabla \cdot \boldsymbol{N}_i + R_i$$

In the application of transient models a pseudo steady-state is assumed to be achieved after a long simulation time. This assumption is based on the idea that the rate of change of concentrations with time is negligible after a sufficiently long simulation time *i.e.,*

$$\frac{\partial c_i}{\partial t} \approx 0 \tag{7-20}$$

The governing equations at the pseudo steady-state reduce to equation (2-5)

$$0 = -\nabla \cdot \boldsymbol{N}_i + R_i$$

therefore the conditions at the pseudo steady-state satisfy the steady-state conditions. The assumption of decoupling homogeneous reactions was shown to be inapplicable to the calculation of the steady-state conditions of occluded systems. It follows that this assumption may also be inapplicable in the calculation of pseudo steady-state conditions by transient models. The applicability of the PS method for transient models can be the basis of future work.

7.4 Summary

The location of the bulk boundary at the mouth of the holiday was shown to be an acceptable location for the calculation of the steady-state conditions on the metal surface of a radial disbonded coating system. There were significant concentration gradients in the region exterior to the mouth of the holiday when the bulk boundary was located further into the bulk electrolyte. These gradients had little influence on the distributions of c_i and Φ on the metal surface. The assumption that the diffusion coefficients of the species be equated to 10^{-5} cm^2s^{-1} was shown to be an unreasonable assumption. The method involving the separation of species into primary and secondary species to reduce computational difficulty was shown to be an inapplicable approach to model the steady-state conditions of disbonded coating systems. This result indicated that this method may also

be inapplicable to models that calculate the evolution of conditions in disbonded coating systems.

CHAPTER 8
QUASIPOTENTIAL TRANSFORMATION

The steady-state distributions of concentration and solution potential of occluded systems are governed by coupled equations. The equations includes partial differential equations for the conservation of species, an algebraic equation for electroneutrality, and non-linear expressions when homogeneous reactions are considered. Solution methods reported in literature for the coupled equations involved discretizing the partial differential equations using finite-difference and finite-element techniques. These techniques transform the governing equations into a system of linear equations that is solved iteratively. The inclusion of non-linear expressions for homogeneous reactions dramatically increases the condition number of the matrix representing the coefficients of the system of equations. Thus, inclusion of homogeneous reactions is accompanied by numerical difficulty.

The quasipotential transformation method was introduced recently and applied to a pitting system.[41] The application of this transformation converted the partial differential equations for c_i into ordinary differential equations. Advantages of this method were increased accuracy and the inclusion of homogeneous reactions. The limitation of the method is that it can accommodate only the production or consumption of one specie by electrochemical reactions. Systems where only one specie is produced or consumed by electrochemical reactions were referred to as single-source systems. Two-source systems were those that involved the production or consumption of two species by electrochemical reactions.

Verification of the quasipotential transformation has not been presented in literature except for a qualitative agreement between the results for two pitting

systems.[18] A quantitative verification of the quasipotential transformation is presented for a two-dimensional, single-source system. The applicability of the transformation to a one-dimensional, two-source system and the inapplicability of the transformation to two-dimensional, two-source system are demonstrated. The abbreviations of 2-D and 1-D for two-dimensional and one-dimensional, respectively, are used in this chapter.

8.1 Theoretical Development

The initial formulation of the quasipotential transformation was introduced in 1991 by Baker *et al.*.[62] The transformation was applicable to steady-state, dilute, stagnant electrochemical systems where activity coefficient corrections and convective transport could be neglected. In this introduction, the transformation was applied to both a 2-D, single-source system and a 2-D, two-source system. The formulation of the transformation presented essentially included writing c_i and Φ as single-valued functions of the quasipotential, Q.[63] In this way, the spatial dependencies of c_i and Φ were transferred to Q. This formulation has since been used in literature.[14,40,41,64–66] Pillay presented a more rigorous development of the definition of Q and its properties, and an outline of Pillay's development is reproduced here.[65]

From the Nernst-Planck equation, equation (2-2), the flux of a species $\boldsymbol{N}_i$ in dilute electrochemical systems where convection is negligible is given by

$$\boldsymbol{N}_i = -z_i u_i c_i F \nabla \Phi - D_i \nabla c_i$$

Under the assumption that c_i was a single-valued function of Φ, $\boldsymbol{N}_i$ was recast as

$$\boldsymbol{N}_i = f_i(\Phi) \nabla \Phi \tag{8-1}$$

where

$$f_i(\Phi) = -z_i u_i F c_i - D_i \frac{dc_i}{d\Phi} \tag{8-2}$$

The assumption that c_i was a single-valued function of Φ is the fundamental assumption of the transformation.

The current density $\boldsymbol{i}$ at a position in the electrolyte is expressed as equation (2-14)

$$\boldsymbol{i} = F\sum_i z_i \boldsymbol{N}_i$$

Taking the curl of both sides of this equation yielded

$$\nabla \times \boldsymbol{i} = \nabla \times \left(F\sum_i z_i \boldsymbol{N}_i \right) \tag{8-3}$$

$$= F\sum_i z_i \left(\nabla \times \boldsymbol{N}_i\right) \tag{8-4}$$

The term in brackets in equation (8-4) was evaluated as

$$\nabla \times \boldsymbol{N}_i = \nabla \times \left(f_i \nabla\Phi\right) \tag{8-5}$$

$$= f_i\left(\nabla \times \nabla\Phi\right) + \left(\nabla f_i \times \nabla\Phi\right) \tag{8-6}$$

using equation (8-1). The two terms in brackets in equation (8-6) were both individually equal to zero as the curl of a gradient is equal to zero

$$\nabla \times \nabla\Phi = 0 \tag{8-7}$$

and the cross product of parallel vectors is equal to zero

$$\left(\nabla f_i\right) \times \nabla\Phi = \frac{df_i}{d\Phi}\nabla\Phi \times \nabla\Phi \tag{8-8}$$

$$= 0 \tag{8-9}$$

Substitution of the result

$$\nabla \times \boldsymbol{N}_i = 0 \tag{8-10}$$

into equation (8-4) yielded

$$\nabla \times \boldsymbol{i} = 0 \tag{8-11}$$

From Stoke's theorem,[67] since $\nabla \times \boldsymbol{i} = 0$, then

$$\oint \boldsymbol{i} \cdot d\boldsymbol{x} = 0 \tag{8-12}$$

As shown by Pillay,[65] for two different points in a 2-D domain O and P

$$\int_{C_1} \boldsymbol{i} \cdot d\boldsymbol{x} = \int_{C_2} \boldsymbol{i} \cdot d\boldsymbol{x} \tag{8-13}$$

where C_1 and C_2 were two different paths joining O and P. The line integral of $\boldsymbol{i}$ over any curve joining O to P depends on the position vectors of O and P. Pillay[65] defined the function $Q(\boldsymbol{x})$ where

$$-Q(\boldsymbol{x}) \quad = \quad -Q(\boldsymbol{x}_o) + \int_O^P \boldsymbol{i} \cdot d\boldsymbol{x} \tag{8-14}$$

such that

$$\boldsymbol{i} = -\nabla Q \tag{8-15}$$

where $\boldsymbol{x}_o$ was an arbitrary position with the value $Q(\boldsymbol{x}_o)$ an arbitrary value. A property of Q was that it satisfied Laplace equation

$$\nabla^2 Q = 0 \tag{8-16}$$

due to the conservation of charge (equation (2-15)).

8.2 Validation of Fundamental Assumption

The validation of the fundamental assumption used in the development of transformation is presented in this section for a 2-D, single, source system.

8.2.1 2-D, Single-Source System

A rectangular 2-D, single-source system is shown in Figure 8-1. The boundary CD was the bulk boundary. The boundaries OD, AB, and BC were passive. The boundary OA was active with hydrogen evolution as the electrochemical reaction.

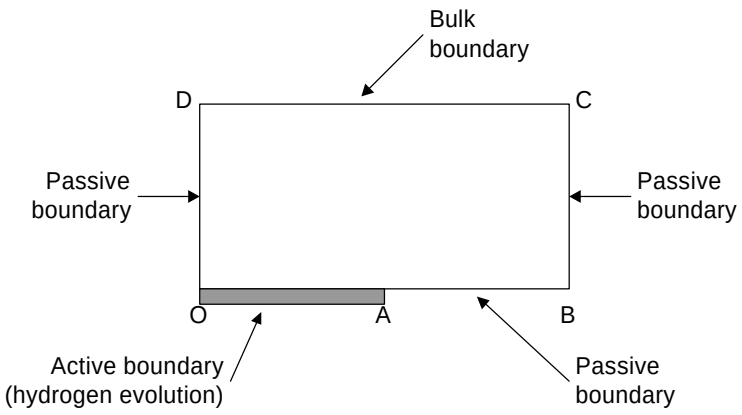

Figure 8-1: Schematic diagram of the two-dimensional domain used for the single-source system.

The dimensions of the domain consisted of OA $= 0.1$ cm, AB $= 0.1$ cm, and OD $=$ 0.1 cm.

The chemical species considered in the system included Na^+, Cl^-, OH^-, and Fe^{+2}. No homogeneous reactions were considered. The bulk solution consisted of 10^{-4} M NaCl, 10^{-7} M OH^-, and 10^{-10} M Fe^{+2}. The values of $c_{Na^+,\infty}$ and $c_{Cl^-,\infty}$ were set equal to that of $c_{NaCl,\infty}$ under the assumption that NaCl was fully dissociated. The values for D_i and equilibrium constants were obtained from TECTRAN[55] and are given in Table 5.1. The applied potential was -0.55 V_{SCE}.

The boundary conditions at DC were $c_i = c_{i,\infty}$ and $\Phi = 0$. The calculated values for Φ were therefore referenced to a zero value at the mouth. For all species, the boundary conditions at the passive boundaries OD, AB, and BC were zero-flux conditions

$$\boldsymbol{N}_i \cdot \boldsymbol{n} = 0 \tag{8-17}$$

where $\boldsymbol{n}$ was the unit normal vector. The condition at the active boundary OA for species not participating in the electrochemical reaction, Na^+, Cl^-, and Fe^{+2}, was also the zero-flux condition.

The electrochemical reaction at the active boundary OA was hydrogen evolution with a polarization expression given by equation (2-52). The boundary con-

dition at the active surface for OH^- that was produced by hydrogen evolution was obtained by relating the flux of the species with the rate of electrochemical production

$$\boldsymbol{N}_{OH^-} \cdot \boldsymbol{n} = \frac{i_{H_2}}{-F} \tag{8-18}$$

The electroneutrality condition, equation (2-13), was applicable throughout the domain.

8.2.2 Results

A finite-difference model FDM2D was developed to solve the governing equations for the 2-D, single-source system described in section 8.2.1. The mathematical model was developed using *Compaq Visual Fortran, Version* 6.1® with double precision accuracy. A convergence criterion of 0.01 percent was used for convergence of the iterative procedure employed. The rectangular grid used a spacing of 0.0125 cm in the x and y directions.

The calculated value of c_{OH^-} and Φ as functions of position in the domain are shown in Figure 8-2. The software *Matlab* version 5.3® was used to draw these figures. The command *griddata* was used to generate a surface that was superimposed on the data points. The surface points were obtained by interpolating the values at the calculated data points given. The spatial dependencies of c_{OH^-} and Φ were observed in Figures 8-2(a) and (b), respectively. The spatial dependencies of c_{Na^+}, c_{Cl^-}, and $c_{Fe^{+2}}$ were also observed by constructing figures for these species similar to that of Figure 8-2(a). These figures are not reported in this work.

The initial assumption of the quasipotential transformation was that c_i can be written as a single-valued function of Φ. The calculated values of c_{Na^+}, c_{Cl^-}, c_{OH^-}, and $c_{Fe^{+2}}$ were each paired with the value of Φ at a given node position in the 2-D domain. These pairs were used to construct the plots of c_i as functions of Φ shown in Figure 8-3. As seen in this figure, c_i was a function of Φ. Therefore, the

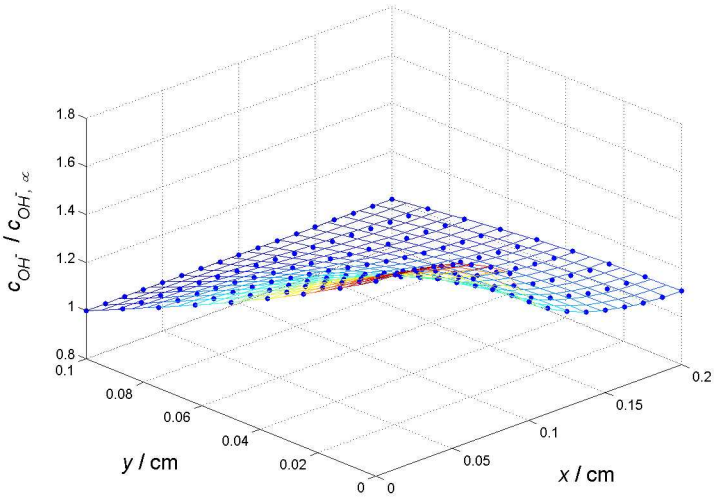

(a)

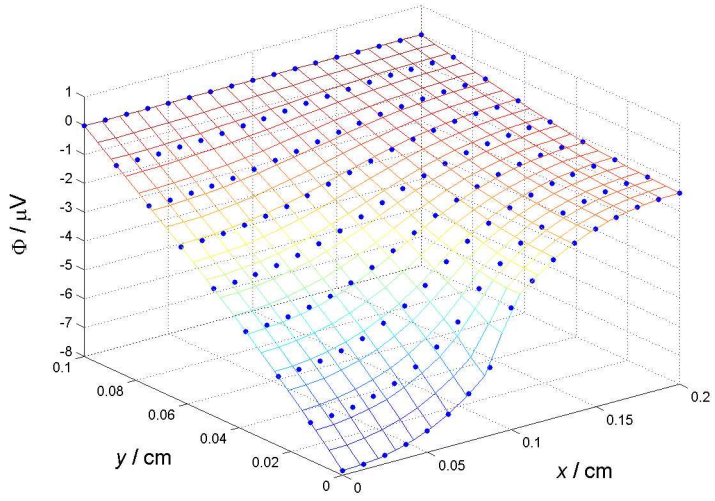

(b)

Figure 8-2: Calculated values of dependent variables as functions of position in the 2-D domain of the single-source system. (a) hydroxide ion concentration and (b) solution potential.

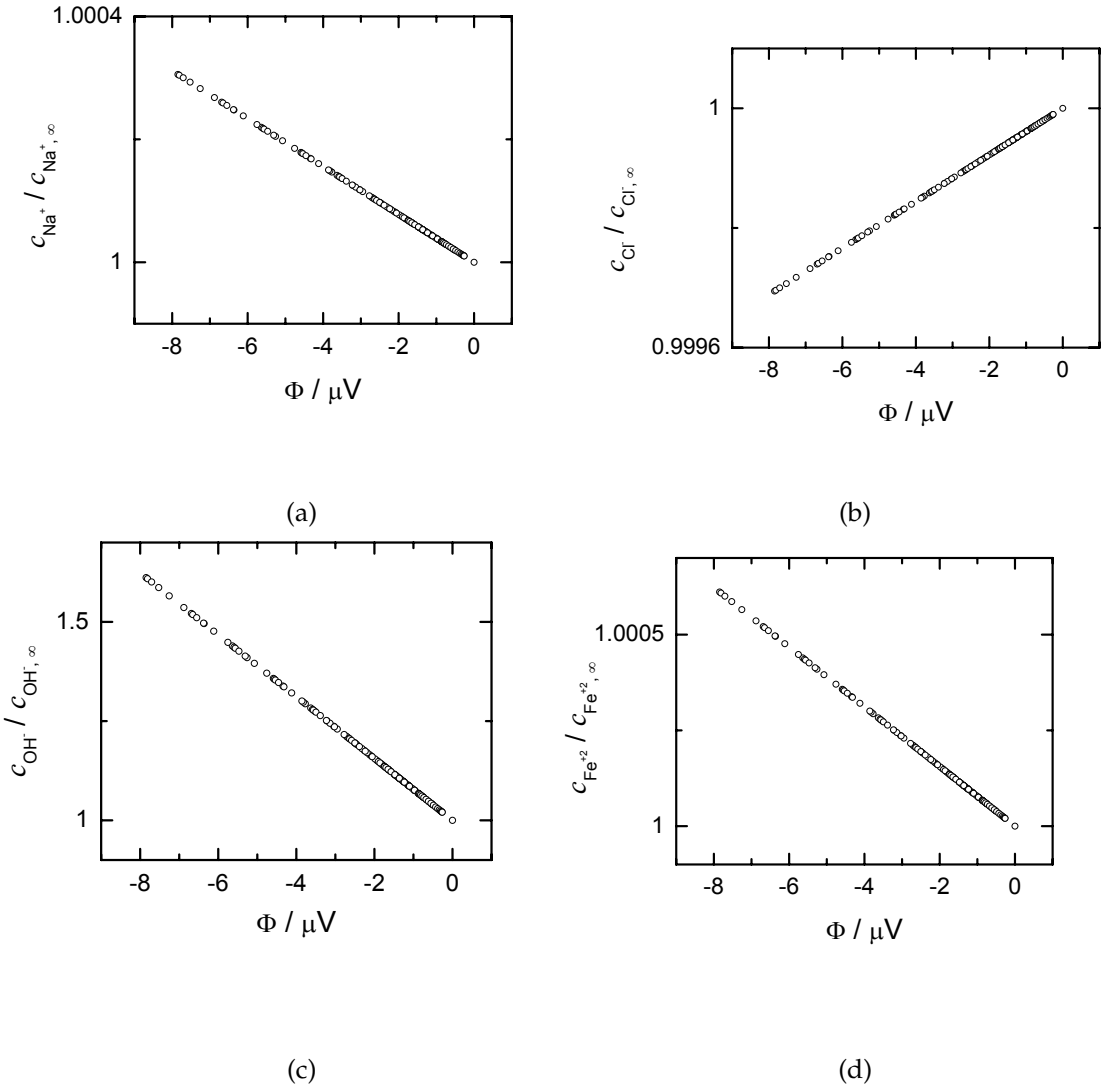

Figure 8-3: Calculated values of concentrations as functions of solution potential for the 2-D, single-source system. (a) sodium ion, (b) chloride ion, (c) hydroxide ion, and (d) ferrous ion.

assumption that c_i was a single-valued function of Φ was valid for the 2-D, single source system. This assumption was therefore, also valid for 1-D, single-source systems.

The value of Q as a function of position in the 2-D domain was calculated for the single-source system by solving the Laplace equation for Q, equation (8-16). The condition

$$Q = 0 \tag{8-19}$$

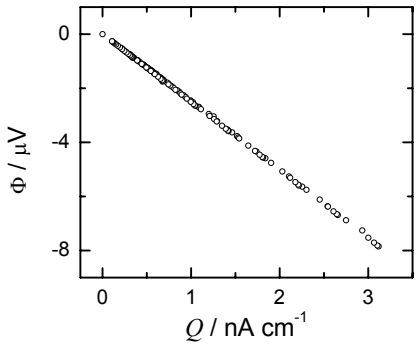

Figure 8-4: Calculated values of solution potential as a function of quasipotential for the 2-D, single-source system.

was used at the bulk boundary CD. At the passive boundaries, a no-flux condition was used

$$\nabla Q \cdot \boldsymbol{n} = 0 \tag{8-20}$$

At the active boundary OA the condition

$$-\nabla Q \cdot \boldsymbol{n} = i_{\mathrm{H_2}} \tag{8-21}$$

was used where $i_{\mathrm{H_2}}$ was calculated using the values for Φ obtained from the FDM2D model and the polarization expression given by equation (2-52).

The calculated values of c_i and Φ were each paired with the value of Q at a given node position in the 2-D domain. These pairs were used to construct the plots of Φ and c_i as functions of Q as shown in Figures 8-4 and 8-5. As seen in these figures, c_i and Φ were single-valued functions of Q. Therefore, c_i and Φ were in fact single-valued functions of Q in 2-D, single-source system and likewise 1-D, single-source systems, and not an assumption.

8.3 Quantitative Verification of Transformation

The quasipotential transformation method was based on the assumption that c_i can be written as a single-valued function of Φ. The method was applied to the 2-D, single-source system described in section 8.2.1 and is presented in this section. In this application the governing equations for species mass-transfer and

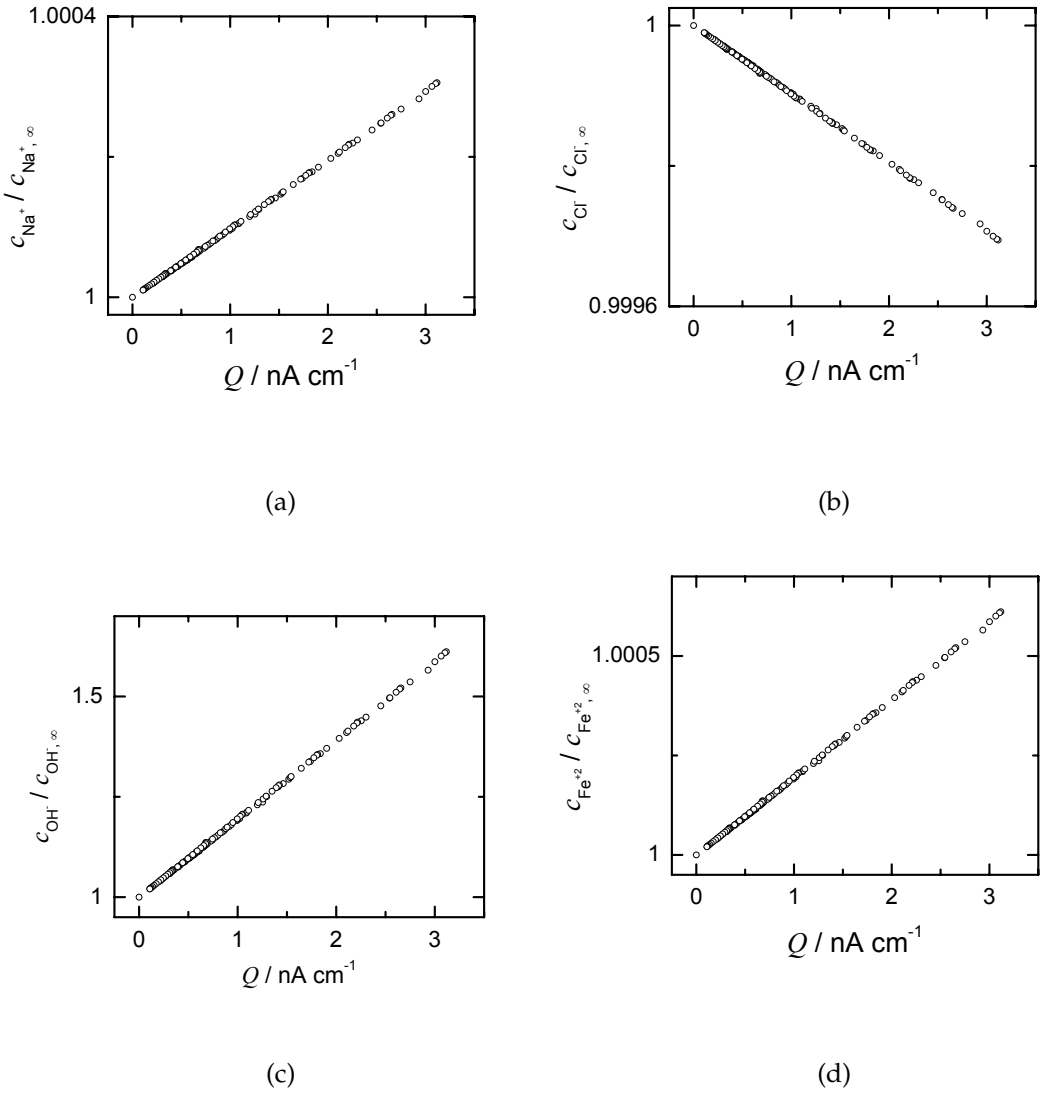

Figure 8-5: Calculated values of concentrations as functions of quasipotential for the 2-D, single-source system. (a) sodium ion, (b) chloride ion, (c) hydroxide ion, and (d) ferrous ion.

electroneutrality were decoupled into geometry-specific and system-specific parts. The nomenclature used for these parts was introduced by Pillay and Newman.[40] Combination of the results from both parts yielded $c_i(\boldsymbol{x})$ and $\Phi(\boldsymbol{x})$.

8.3.1 Geometry-Specific Part

The geometry-specific part involved solving Laplace's equation for Q, equation (8-16), to obtain Q as a function of position. At the boundary CD, the condition $Q = 0$ was used. The passive surfaces acted as insulators therefore, a zero-flux boundary condition, equation (8-20), was used. The boundary condition used at OA was given by equation (8-21), where i_{H_2} was obtained from the polarization expression, given by equation (2-52). This boundary condition was obtained using the definition of the quasipotential, equation (8-15).

8.3.2 System-Specific Part

The system-specific part involved deriving sufficient ordinary differential equations such that c_i and Φ can be obtained as functions of Q, *i.e.*, $c_i(Q)$ and $\Phi(Q)$, respectively. These equations were derived using expressions applicable to the species in the electrolyte.

The flux of a species was given by equation (2-8)

$$\boldsymbol{N}_i = -z_i D_i c_i F \nabla\phi - D_i \nabla c_i$$

where $\phi = (\Phi F)/(RT)$. This equation was recast in terms of Q as

$$\boldsymbol{N}_i = -D_i \left(z_i c_i \frac{d\phi}{dQ} + \frac{dc_i}{dQ} \right) \nabla Q \tag{8-22}$$

using the assumptions that c_i and ϕ were single-valued functions of Q and the chain rule.

The algebraic expression for the electroneutrality condition (equation (2-13)) was differentiated with respect to Q to obtain

$$z_{\mathrm{Na}^+} \frac{dc_{\mathrm{Na}^+}}{dQ} + z_{\mathrm{Cl}^-} \frac{dc_{\mathrm{Cl}^-}}{dQ} + z_{\mathrm{OH}^-} \frac{dc_{\mathrm{OH}^-}}{dQ} + z_{\mathrm{Fe}^{+2}} \frac{dc_{\mathrm{Fe}^{+2}}}{dQ} = 0 \tag{8-23}$$

This equation represented the governing equation for the solution potential in the system specific part.

The species that did not participate in homogeneous nor heterogeneous reactions were considered to be a stagnant specie.[68] The flux of a stagnant specie was set to zero in the domain

$$\boldsymbol{N}_i = 0 \tag{8-24}$$

Combination of equations (8-24) and (8-22), yielded

$$z_i c_i \frac{d\phi}{dQ} + \frac{dc_i}{dQ} = 0 \tag{8-25}$$

as the governing equation for the concentration of a stagnant specie. The equations

$$z_{Na^+} c_{Na^+} \frac{d\phi}{dQ} + \frac{dc_{Na^+}}{dQ} = 0 \tag{8-26}$$

$$z_{Cl^-} c_{Cl^-} \frac{d\phi}{dQ} + \frac{dc_{Cl^-}}{dQ} = 0 \tag{8-27}$$

and

$$z_{Fe^{+2}} c_{Fe^{+2}} \frac{d\phi}{dQ} + \frac{dc_{Fe^{+2}}}{dQ} = 0 \tag{8-28}$$

were derived for the concentrations c_{Na^+}, c_{Cl^-}, and $c_{Fe^{+2}}$, respectively.

The current density at any point in the domain $\boldsymbol{i}$ was given by equation (2-14). The fluxes of the stagnant species Na^+, $Cl^-$and Fe^{+2} were zero, therefore the current density was given by the flux of hydroxide ion

$$\boldsymbol{i} = F z_{OH^-} \boldsymbol{N}_{OH^-} \tag{8-29}$$

Substitution of equations (8-15) and (8-22) into equation (8-29) yielded

$$-\nabla Q = -F z_{OH^-} D_{OH^-} (z_{OH^-} c_{OH^-} \frac{d\phi}{dQ} + \frac{dc_{OH^-}}{dQ}) \nabla Q \tag{8-30}$$

which reduced to

$$z_{OH^-} c_{OH^-} \frac{d\phi}{dQ} + \frac{dc_{OH^-}}{dQ} = \frac{1}{F z_{OH^-} D_{OH^-}} \tag{8-31}$$

Equation (8-31) was the governing equation for c_{OH^-}.

The system-specific part consisted of equations (8-23), (8-26), (8-27), (8-28), and (8-31), and comprised a system of five, coupled, nonlinear, ordinary differential equations. This set of equations was applicable at any position in the domain as there was no spatial dependence. The initial conditions at $Q = 0$ for this ordinary differential equation problem corresponded to the bulk conditions at CD where

$$c_i(Q = 0) = c_{i,\infty} \tag{8-32}$$

and

$$\Phi(Q = 0) = 0 \tag{8-33}$$

8.3.3 Method of solution

A fourth-order Runge-Kutta algorithm was used to solve the system-specific set of equations in previous applications of the quasipotential transformation.[14,40,41] The semi-implicit extrapolation method[61] was found to provide a more accurate calculation of the concentrations of the minor species as compared with the Runge-Kutta algorithm. This method accommodated the stiffness of the ordinary differential equations.

The method of solution was iterative as the boundary condition on the metal surface for the geometry-specific part was a function of Φ which was calculated from the system-specific part. The algorithm used is outlined as follows:

1. The domain was discretized into nodes forming a regular grid.

2. Values $c^o_{i(j)}$ and $\phi^o_{(j)}$ were assumed for nodes on the active boundary OA where the subscript j indicates a node position on the surface OA.

3. The values of $\phi^o_{(j)}$ were used in the mathematical expression for the polarization kinetics to calculate the normal current density i_{H_2} as a function of position on OA.

4. The geometry-specific part was solved using a finite-difference method to obtain the values of Q at the nodes on the metal surface, $Q_{(j)}$.

5. The values of Q on OA were used in the semi-implicit extrapolation method[61] to calculate the values of $\phi_{(j)}$ and $c_{i(j)}$ at the nodes on the boundary OA.

6. A convergence criterion ξ_Q was calculated for each dependent variable, c_i and ϕ, at each node along OA using an equation of the form

$$\xi_Q = \left| \frac{f - f^o}{f^o} \right| \tag{8-34}$$

where f was a generic variable for c_i and ϕ. When the maximum value of ξ_Q, $\xi_{max,Q}$, exceeded a preset convergence criterion $\xi_{o,Q}$, the assumed values were updated with the calculated values at each node, and control returned to Step 2. The procedure was exited when $\xi_{max,Q} < \xi_{o,Q}$.

A computer model QPM2D was developed using the algorithm to solve the governing equations for the 2-D, single-source system described in section 8.2.1. The mathematical model was developed using *Compaq Visual Fortran, Version* 6.1® with double precision accuracy. A convergence criterion of 0.01 percent was used. A rectangular grid with spacings of 0.0125 cm in the x and y directions was used for the solution of the geometry-specific part.

8.3.4 Results

The distributions of c_i and Φ on the metal surface were calculated using the two methods of solution, the quasipotential method and a finite-difference method. The calculated values of Φ and c_i as functions of position on the metal surface OA

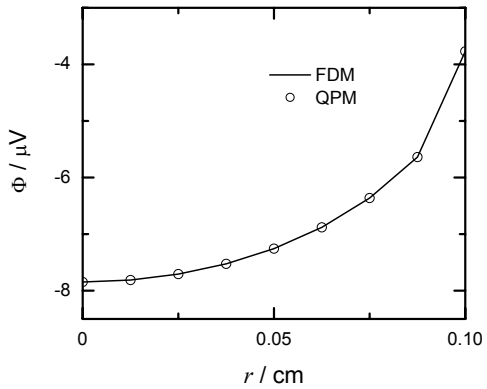

Figure 8-6: Calculated value of solution potential as a function of position along the metal boundary. QPM: quasipotential transformation method; FDM: finite-difference method.

are shown in Figures 8-6 and 8-7, respectively. with the method of solution as a parameter. The positions 0 cm and 0.1 cm corresponded to locations O and A, respectively. The results for the both methods were in excellent agreement. This provided quantitative verification of the quasipotential transformation applicability to 2-D, single-source systems.

8.4 Crevice System Application

The quasipotential transformation was shown to be applicable to 2-D, single-source systems. The transformation was therefore applicable to 1-D, single-source systems. The applicability of the transformation to a 1-D, two-source system is presented in this section. This application has not been presented in literature to date.

Models for the steady-state conditions in the 1-D crevice were developed using the quasipotential transformation QPM1D and using a finite-difference approach FDM1D. The development of QPM1D and the results from these models are presented in this section.

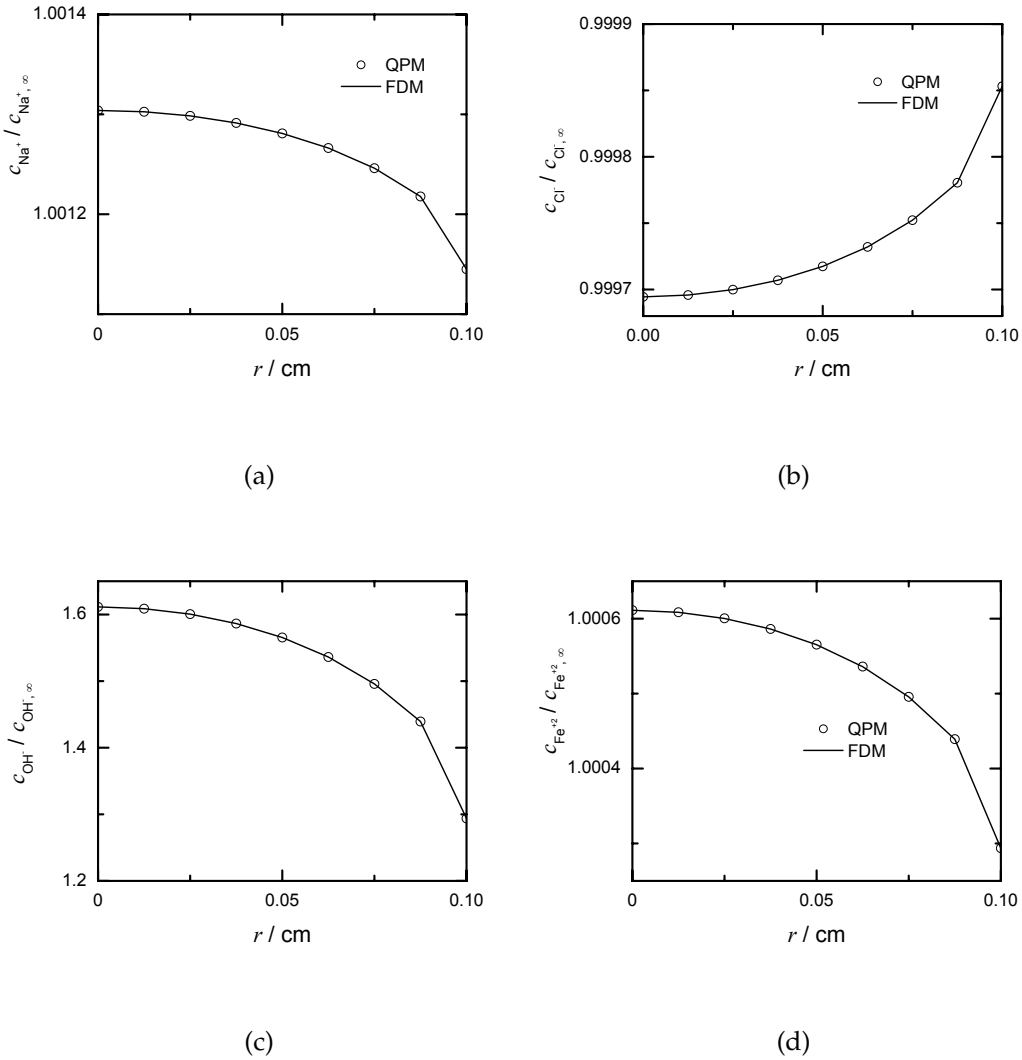

Figure 8-7: Calculated values of concentrations as functions of position on the metal boundary with solution method as a parameter. (a) sodium ion, (b) chloride ion, (c) hydroxide ion, and (d) ferrous ion. QPM: quasipotential transformation method; FDM: finite-difference method.

8.4.1 Crevice System

A 1-D crevice system is shown in Figure 3-3. The length of the crevice was l_c with the tip located at the position $x = 0$ and the bulk boundary at $x = l_c$. The ratio of crevice length to crevice width was assumed to be sufficiently large such that variations in c_i and Φ were normal to the tip and negligible normal to the walls. The variation in the direction normal to the walls and tip was assumed to be negligible. These two assumptions are used in modeling 1-D crevices.[17,44–47]

The tip of the crevice was active with corrosion and hydrogen evolution. The walls were passive. The bulk solution was a neutral, sodium chloride electrolyte with a very small ferrous composition. The chemical species considered in the system were Na^+, Cl^-, OH^-, and Fe^{+2}. No homogeneous reactions were considered.

8.4.2 Mathematical Model

The assumption that c_i was a single-valued function of Φ was applicable to 1-D, two-source systems. The assumptions that c_i and Φ were functions of Q were used to develop the system-specific part of QPM1D.

The flux of a specie was given by equation (8-22). The equations for the stagnant species were

$$z_{Na^+} c_{Na^+} \frac{d\phi}{dQ} + \frac{dc_{Na^+}}{dQ} = 0 \tag{8-35}$$

and

$$z_{Cl^-} c_{Cl^-} \frac{d\phi}{dQ} + \frac{dc_{Cl^-}}{dQ} = 0 \tag{8-36}$$

for Na^+ and Cl^-, respectively. The fluxes of the species produced by electrochemical reactions were

$$\left(z_{Fe^{+2}} c_{Fe^{+2}} \frac{d\phi}{dQ} + \frac{dc_{Fe^{+2}}}{dQ} \right) \frac{dQ}{dx} = \frac{i_{Fe}}{2F} \tag{8-37}$$

and

$$\left(z_{OH^-}c_{OH^-}\frac{d\phi}{dQ}+\frac{dc_{OH^-}}{dQ}\right)\frac{dQ}{dx}=\frac{i_{H_2}}{-F} \tag{8-38}$$

for Fe^{+2} and OH^-, respectively, where $i_{Fe}$and i_{H_2}were given by equations (2-50) and (2-52), respectively.

The property of Q given by equation (8-15) yielded

$$-\frac{dQ}{dx}=i_{net} \tag{8-39}$$

where

$$i_{net}=i_{Fe}+i_{H_2} \tag{8-40}$$

for the 1-D domain. Substitution of equation (8-39) into equations (8-37) and (8-38) yielded

$$z_{Fe^{+2}}c_{Fe^{+2}}\frac{d\phi}{dQ}+\frac{dc_{Fe^{+2}}}{dQ}=\frac{i_{Fe}}{-2Fi_{net}} \tag{8-41}$$

and

$$z_{OH^-}c_{OH^-}\frac{d\phi}{dQ}+\frac{dc_{OH^-}}{dQ}=\frac{i_{H_2}}{Fi_{net}} \tag{8-42}$$

respectively. The system-specific part consisted of equations (8-35), (8-36), (8-41), (8-42), and the electroneutrality condition differentiated with respect to Q

$$\frac{dc_{Na^+}}{dQ}+\frac{dc_{Cl^-}}{dQ}+\frac{dc_{OH^-}}{dQ}+\frac{dc_{Fe^{+2}}}{dQ}=0 \tag{8-43}$$

The geometry-specific part involved solving

$$\frac{d^2Q}{dx^2}=0 \tag{8-44}$$

with the boundary conditions of

$$Q=0 \tag{8-45}$$

and

$$\frac{dQ}{dx}=-i_{net} \tag{8-46}$$

at the bulk boundary $x = l_c$ and the metal boundary $x = 0$, respectively. The solution for the distribution of Q was

$$Q = -(l_c - x)i_{net} \tag{8-47}$$

where l_c was the crevice length in cm.

An algorithm similar to that given in subsection 8.3.3 was used to develop a computer program for QPM1D. The semi-implicit extrapolation method[61] was used for the solution of the system-specific part while the geometry-specific part was solved analytically using equation (8-47).

8.4.3 Results

The length of the crevice was $l_c = 1$ cm. The bulk solution was a 10^{-3} M NaCl, neutral medium. The values of $c_{Na^+,\infty}$ and $c_{Cl^-,\infty}$ were set equal to that of $c_{NaCl,\infty}$ under the assumption that NaCl was fully dissociated. The total elemental concentration of iron was set to 10^{-10} M. The values for D_i and equilibrium constants were obtained from TECTRAN[55] and are listed in Table 5.1. The parameters used for the calculation of $i_{H_2}$and i_{Fe}were obtained from Table 2.1. A convergence criterion of 0.01 percent was used in the models.

The results for three applied potentials are presented below. The value of $\Psi = -0.5$ V_{SCE} and $\Psi = -0.75$ V_{SCE} were selected such that the anodic corrosion reaction was dominant and the hydrogen evolution reaction was dominant, respectively. The value of $\Psi = -0.6$ V_{SCE} was selected such that the anodic and cathodic current densities were approximately equal.

The results for the values of i_{Fe}, i_{H_2}, and i_{net} for the three applied potentials are listed in Table 8.1. When Ψ was -0.5 V_{SCE} the tip was dominated by corrosion with $i_{net} \approx 193$ nA/cm^2. When Ψ was -0.75 V_{SCE} the tip was dominated by hydrogen evolution with $i_{net} \approx -117$ nA/cm^2. And when Ψ was -0.6 V_{SCE} the anodic and cathodic current densities at the tip were approximately equal. The models

Table 8.1: Calculated current density values for crevice system.

Ψ (V_{SCE})	Model	i_{Fe} (nA/cm^2)	i_{H_2} (nA/cm^2)	i_{net} (nA/cm^2)
-0.5	QPM1D	196.86	-2.2048	193.65
	FDM1D	195.87	-2.2048	193.66
-0.6	QPM1D	9.5516	-9.2365	0.31511
	FDM1D	9.5519	-9.2364	0.31546
-0.75	QPM1D	4.4861×10^{-3}	-117.39	-117.35
	FDM1D	4.4859×10^{-3}	-117.40	-117.35

QPM1D and FDM1D yielded results for i_{Fe} and i_{H_2} that were equal for three significant digits. This result supported the validity of the quasipotential transformation for 1-D two-source systems.

The calculated values of c_i and Φ as functions of position along the length of the crevice are presented in Figures 8-8, 8-9, and 8-10 for the conditions of $\Psi = -0.5$ V_{SCE} , $\Psi = -0.6$ V_{SCE} , and $\Psi = -0.75$ V_{SCE} , respectively. The calculated results from QPM1D and FDM1D superimposed. These results demonstrated the applicability of the quasipotential transformation to 1-D, two-source systems.

8.5 Transformation Limitation

The disbonded coating system involves the electrochemical production of ferrous and hydroxide ions on the metal surface in a 2-D domain. The disbonded coating system is therefore a 2-D, two source system. A 2-D, two-source system was modeled using the method of finite-difference for the discretization of the governing equations. The results from this model demonstrated that the fundamental assumption of the transformation was invalid in 2-D, two-source systems. As such, the quasipotential transformation is inapplicable to disbonded coating systems.

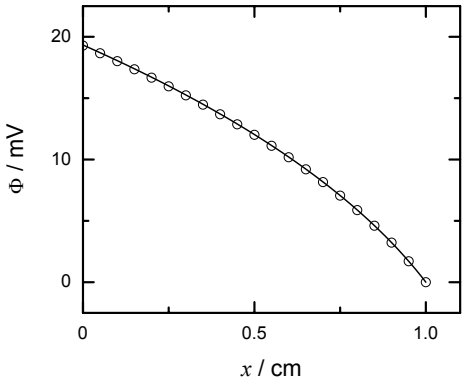

(a)

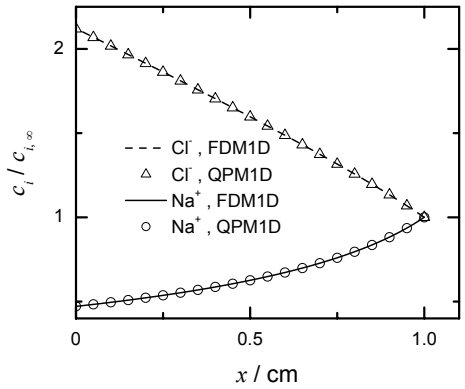

(b)

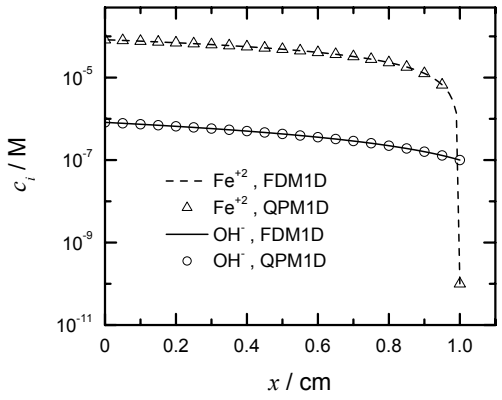

(c)

Figure 8-8: Calculated values dependent variables as functions of position in the crevice with solution method as a parameter. (a) solution potential and (b) sodium and chloride ions concentrations, and (c) hydroxide and ferrous ions concentrations.

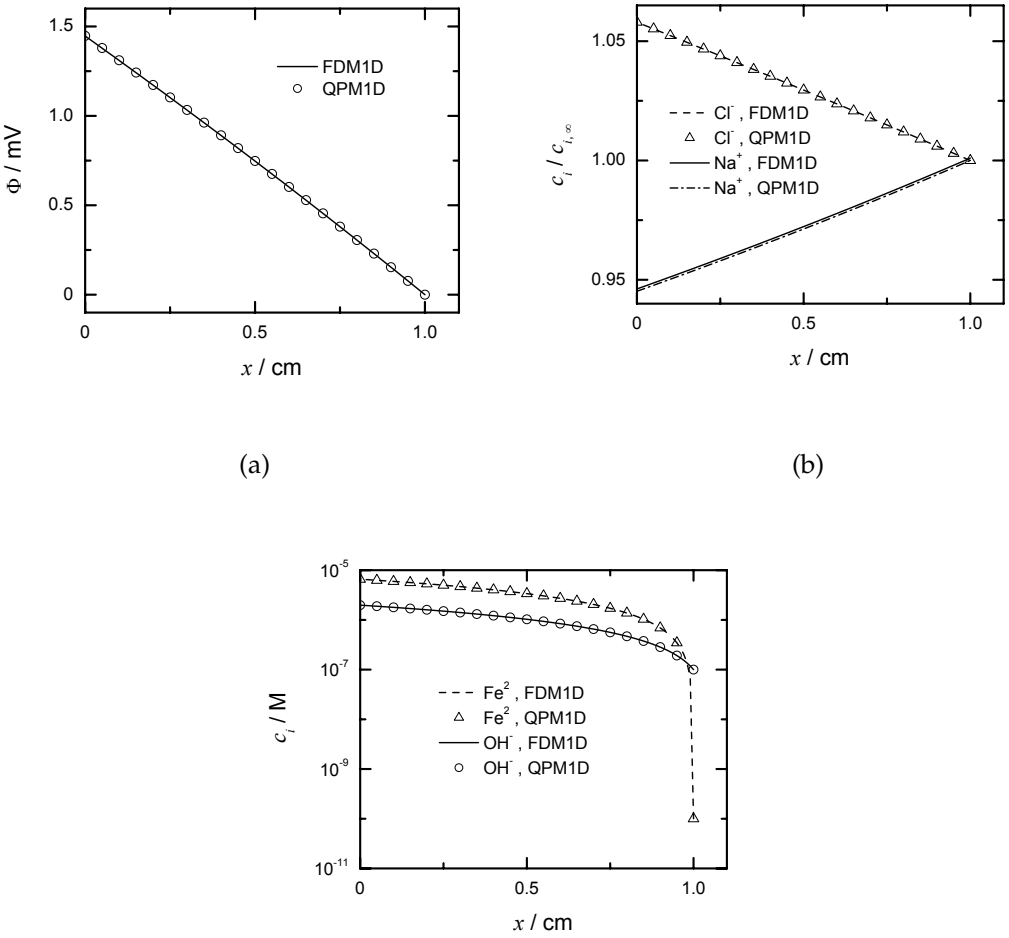

Figure 8-9: Calculated values dependent variables as functions of position in the crevice with solution method as a parameter. (a) solution potential and (b) sodium and chloride ions concentrations, and (c) hydroxide and ferrous ions concentrations.

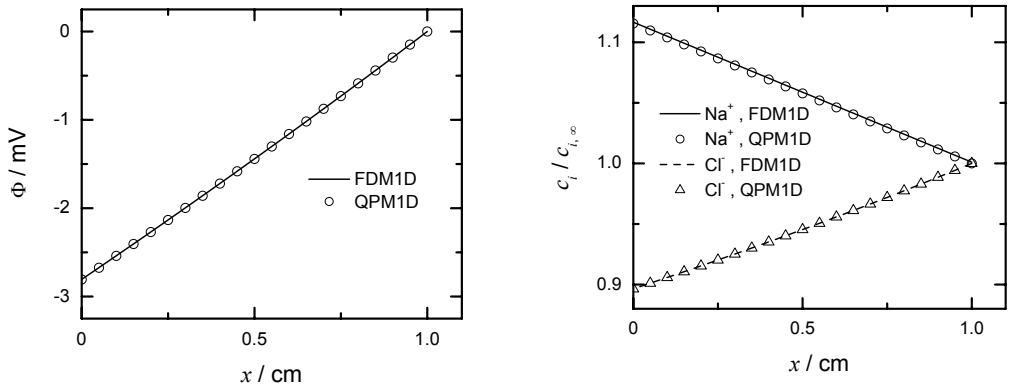

(a)

(b)

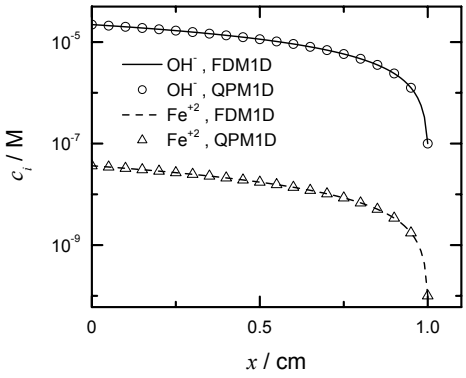

(c)

Figure 8-10: Calculated values dependent variables as functions of position in a crevice dominated by cathodic current. (a) solution potential and (b) sodium and chloride ions concentrations, and (c) hydroxide and ferrous ions concentrations.

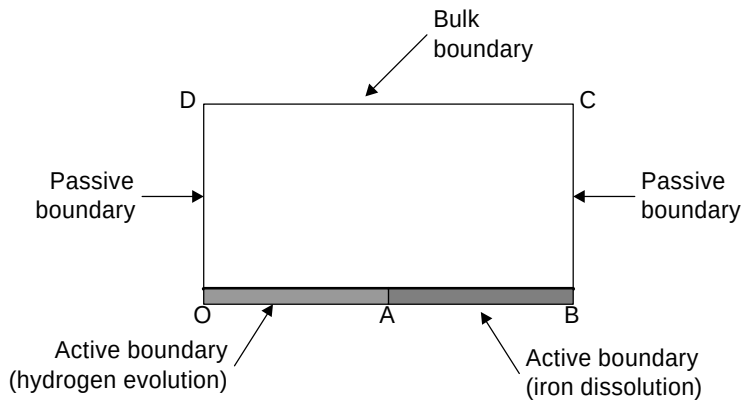

Figure 8-11: Schematic diagram of the two-dimensional domain used for two-electrochemical reaction system.

8.5.1 Electrochemical System

The electrochemical system used to investigate the two-source system is shown in Figure 8-11. The boundary CD was the bulk boundary. The boundaries OD and BC were passive. The boundaries OA and AB were active with hydrogen evolution and corrosion, respectively. The dimensions of the domain consisted of OA $= 0.1$ cm, AB $= 0.1$ cm, OD $= 0.1$ cm.

The chemical species considered in the system were Na^{+}, Cl^{-}, OH^{-}, and Fe^{+2}. No homogeneous reactions were considered. The bulk solution was a 10^{-4} M NaCl, neutral medium. The values of $c_{Na^{+},\infty}$ and $c_{Cl^{-},\infty}$ were set equal to that of $c_{NaCl,\infty}$ under the assumption that NaCl was fully dissociated. The elemental concentration of iron was set to 10^{-10} M. The values for D_i and equilibrium constants were obtained from TECTRAN[55] and are listed in Table 5.1. The applied potential was -0.55 V_{SCE}.

The electrochemical reaction at the active boundary OA was hydrogen evolution with a polarization expression given by equation (2-52). At the active boundary AB the electrochemical reaction was corrosion with i_{Fe} given by equation (2-50).

The boundary conditions for the concentrations at the mouth were the bulk concentrations $c_i = c_{i,\infty}$. The solution potential at this boundary was set to $\Phi = 0$. The calculated values for Φ were therefore referenced to a zero value at the mouth. For all species the boundary condition at the passive boundaries BC and OD was a no-flux condition

$$\boldsymbol{N}_i \cdot \boldsymbol{n} = 0 \tag{8-48}$$

where $\boldsymbol{n}$ was the unit normal vector. The condition at the active boundary for species not participating in the heterogeneous reaction was also a no-flux condition. The boundary condition at the active surface OA for OH^- that did participate in hydrogen evolution was obtained by relating the flux of the species with i_{H_2}

$$\boldsymbol{N}_{OH^-} \cdot \boldsymbol{n} = \frac{i_{H_2}}{-F} \tag{8-49}$$

The condition for Fe^{+2} at the boundary AB was obtained similarly as

$$\boldsymbol{N}_{Fe^{+2}} \cdot \boldsymbol{n} = \frac{i_{Fe}}{2F} \tag{8-50}$$

The electroneutrality condition, equation (2-13), was applicable throughout the domain.

8.5.2 Results

A finite-difference model was developed to solve the governing equations for the electrochemical system described in section 8.5.1. The mathematical model was developed using *Compaq Visual Fortran, Version* 6.1® with double precision accuracy. A convergence criterion of 0.01 percent was used for convergence of the iterative procedure employed. The rectangular grid used a spacing of 0.0125 cm in the x and y directions.

The fundamental assumption of the quasipotential development was that c_i can be written as a single-valued function of Φ. This assumption was shown to be

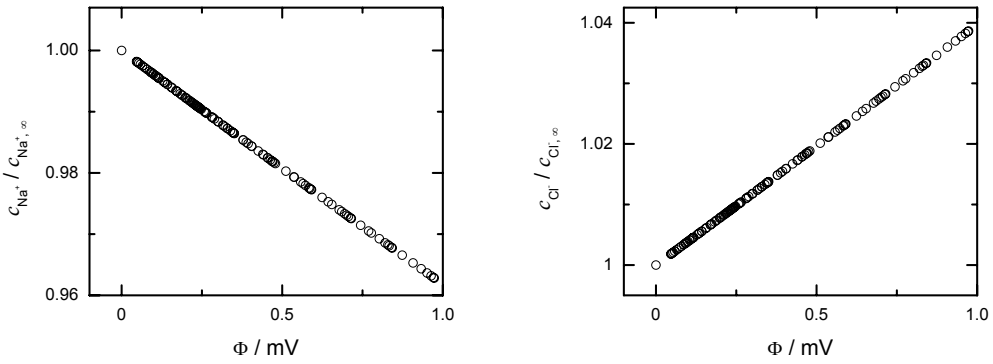

(a) (b)

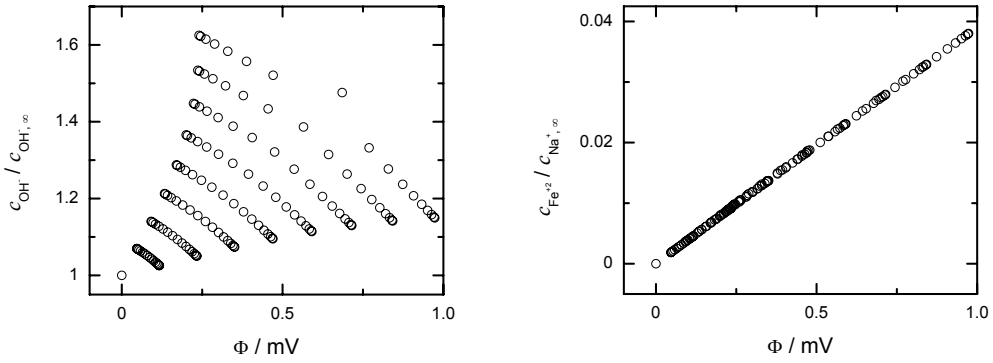

(c) (d)

Figure 8-12: Calculated values of concentrations as functions of solution potential for the 2-D, two-source system. (a) sodium ion, (b) chloride ion, (c) hydroxide ion, and (d) ferrous ion.

valid for 2-D, single-source systems in section 8.2.2. The calculated values of c_{Na^+}, c_{Cl^-}, c_{OH^-}, and $c_{Fe^{+2}}$ were each paired with the value of Φ at a given node position in the 2-D domain for the system described. These pairs were used to construct the plots of c_i as functions of Φ as shown in Figure 8-12. As seen in this figure, c_{OH^-} was clearly not a single-valued function of Φ. The figures for c_{Na^+}, c_{Cl^-}, and $c_{Fe^{+2}}$ indicated that these variables were approximately single-valued functions of Φ in this application, but this is not a general approximation. The assumption that c_i is a single-valued function of Φ is invalid for the two-source systems. Therefore, in

two-dimensional domains the quasipotential transformation is limited to single-source systems.

8.6 Summary

The fundamental assumption of the quasipotential transformation involves writing the concentration of a specie as a single-valued function of the solution potential. This assumption was validated and the quasipotential transformation method was quantitatively verified for a single-source system in a 2-D domain. The applicability of the transformation to two-source systems was limited to the 1-D domain; this applicability was quantitatively verified. The fundamental assumption of the transformation was shown to be invalid in a 2-D, two-source system. As such, the quasipotential transformation was inapplicable for the disbonded coating system which involves the electrochemical production of ferrous and hydroxide ions on the metal surface.

CHAPTER 9
CATHODIC DELAMINATION SYSTEM

Phenomena involved in the cathodic delamination system have been identified in experimental investigations reported in literature.[6–11,69–73] These phenomena have been used to propose a mechanistic model for the delamination process under open circuit conditions.[7,9] In this chapter the proposed mechanistic model of cathodic delamination is briefly described and the experimental results reported for coated zinc presented.

9.1 Mechanistic Model

The model described here was based on the qualitative mechanistic models for the cathodic delamination process presented in literature for coated iron[7] and zinc.[9] The cathodic delamination process involves several phenomena that interact simultaneously such that a delamination front propagates along the metal-coating interface.[74] A schematic diagram of a cathodic delamination system on a coated metal is shown in Figure 9-1. The system includes an electrolyte and a metal that is partially covered by a coating. A section of metal surface OA is exposed to the electrolyte. The degraded coating ABCD is a micron-thick region in which the matrix of the polymer is transformed to a gelatinous medium.[6,75,76] The adhesive bond at the metal-coating interface is weakened along AB and unaltered along BE. The delamination process is transient and the schematic diagram shown in Figure 9-1 represent the system at a given time during the propagation stage of the process. The delamination process propagates with the degraded region growing in length parallel to the metal surface from ABCD to AB'C'D.

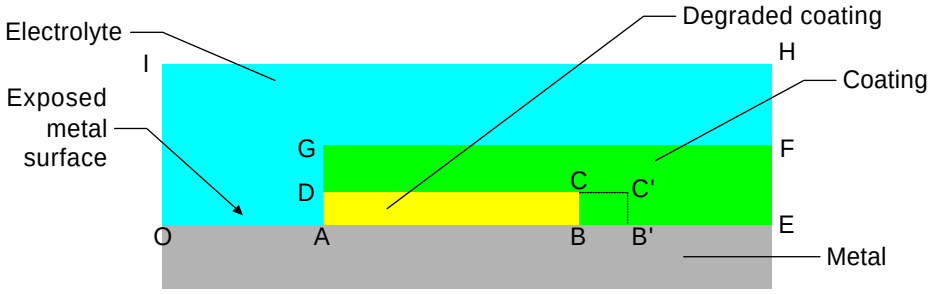

Figure 9-1: Schematic diagram of the cathodic delamination system.

An important requirement for the delamination process is that the coating is permeable, allowing transport of oxygen through the coating to the metal surface. Experimental results for coated zinc[9] and iron[7] indicated that in the absence of oxygen the delamination front cannot propagate. The reduction of oxygen results in the production of OH^-, which has been linked to the degradation of the coating material.[76] This degradation included the weakening or breaking of the adhesive metal-coating bond. The mechanism by which the dissolved oxygen is reduced to hydroxide ions involves the formation of free radicals. The free-radicals have also been linked to the degradation of the metal-coating bond.

The oxygen that is transported by diffusion to the metal-coating interface is susceptible to being reduced through oxygen reduction. Along the metal-coating interface BE oxygen reduction is limited by the metal dissolution reaction which is inhibited.[7,9] Further beyond the delamination front, the local current density is equal to zero, and the oxygen reduction reaction is balanced by the anodic metal dissolution reaction.

Along the metal-coating interface AB the metal dissolution reaction is said to be inhibited, and the oxygen reduction reaction proceeds at the mass-transfer-limited rate. The oxygen reduction reaction on AB is supported by a metal dissolution reaction taking place at the exposed metal surface OA. The delamination process can be described, therefore, as being driven by a galvanic couple between the metal-

electrolyte interface OA and the metal-coating interface AB. Under open circuit conditions when no current is supplied to the system the cathodic oxygen reduction reaction on AB is balanced by an anodic reaction on the exposed metal surface OA, with a galvanic couple being developed between the surfaces OA and AB. When an external current source is imposed on the system the cathodic oxygen reduction reaction on AB is balanced by an anodic reaction on a counter electrode located in the electrolyte.

The phenomena involved in the delamination process interact such that the delamination process propagates along to the metal surface with the degraded coating region growing in length. This is represented by the change of the boundary BC to B'C' as shown in Figure 9-1. This boundary change occurs by the simultaneous breakage of adhesive bonds, the degradation of the coating, the reduction of oxygen at the metal-coating interface, and the transport of positively charged ions into BB'C'C from ABCD as well as the transport of negatively charged ions from BB'C'C to ABCD.

9.2 Coated-Zinc Experimental Results

Extensive experimental investigations of the cathodic delamination process have recently been reported for coated zinc[9−11,25,26] and coated iron.[6−8] Previous experimental efforts interpreted the results of chemical analysis of the degraded coating for insight into potential distributions.[74,76,77] The more recent experimental investigations employed the Scanning Kelvinprobe to measure the potential distribution at the buried metal-coating interface. These measurements were taken in-situ during the delamination process. Other tests performed yielded intensities of Na^+ and Cl^-, pH, and the adhesion between the metal and coating as functions of position. The results reported by Furbeth and Stratmann for coated zinc are presented in this section.[9−11]

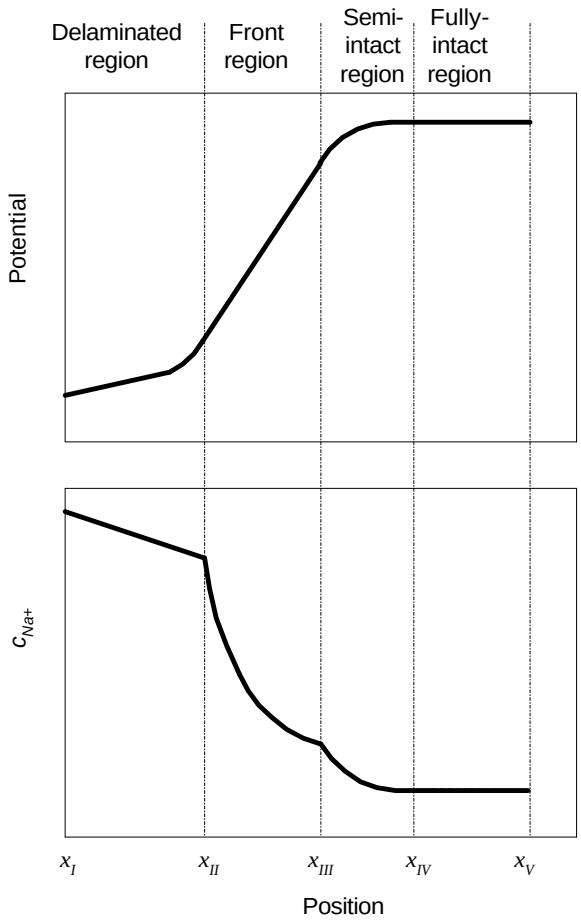

Figure 9-2: Schematic diagram of experimental interfacial potential and sodium ion concentration as functions of position in the delamination zone.

9.2.1 Potential and Concentration

Experimental results of potential of the metal-coating interface as a function of position (distance from defect) were reported by Furbeth and Stratmann.[9] The corresponding result of a small-spot XPS analysis of the metal surface after removal of the delaminated polymer coat was also reported with the intensities of the Na^+ and Cl^- species as functions of position. A schematic diagram of the experimental distributions of the interfacial potential and sodium ion concentration are shown in Figure 9-2. The position x_I in this figure was referenced to the defect-delamination boundary (position A in Figure 9-1).

The pH distribution in the delamination zone was investigated using phenolphathalein pigments and microscopic photography. Furbeth and Stratmann ob-

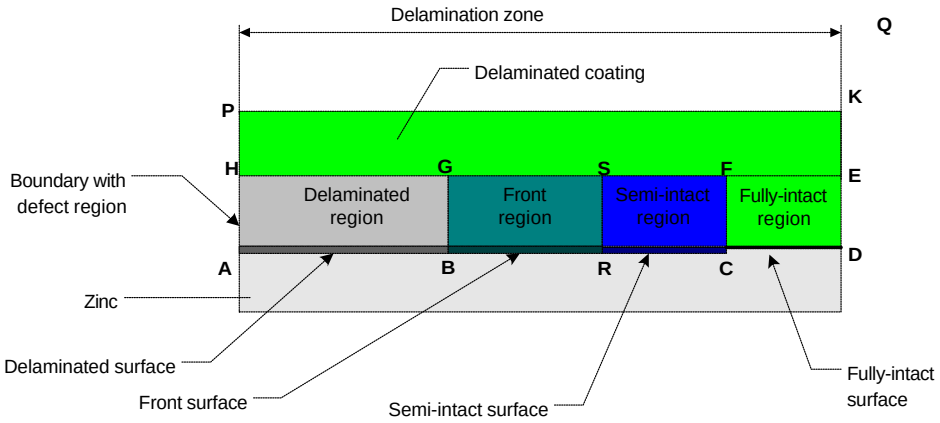

Figure 9-3: Schematic diagram of the delamination zone at a given time divided into regions.

served from a microscopic photograph that a pH greater than 10 was present along the delaminated and front regions.[9] This observation was consistent with results for the pH in the delamination zone during the delamination of coated zinc reported by Williams and McMurray.[25]

Four regions were identified in Figure 9-2. The position ranging from x_I to x_{II}, x_{II} to x_{III}, x_{III} to x_{IV}, and x_{IV} to x_V were designated the delaminated region, front region, semi-intact region, and fully-intact region, respectively. A schematic diagram of the different regions in the delamination zone at a given time is shown in Figure 9-3. The delaminated, front, and semi-intact regions were characterized by the presence of degraded coating and reduced adhesive strength between metal and coating. The fully-intact region represented a region where the destruction of the bonding between the coating and metal substrate was absent and the coating was in its original form *i.e.*, un-degraded.

In the delaminated region c_{Na^+} and V changed linearly and non-linearly, respectively, with position. In the front region c_{Na^+} had a non-linear change with position and V an approximately linear change with position. The conditions at the delaminated/front boundary and front/semi-intact boundary were non-zero flux conditions as experimental observations indicated that there was transport of

species between the delaminated region and semi-intact region through the front region.

The semi-intact region represented a transition region between the coating undergoing delamination in the front region and the coating where delamination was absent, the fully-intact region. The semi-intact region had non-linear changes in c_{Na^+} and V with position. The gradient of c_{Na^+} decreased with position and the gradient of V increased with position. The gradients of both c_{Na^+} and V approached a zero value as the fully-intact region was approached. This decrease in gradients translated into a decreasing flux for Na^+ as the fully-intact region was approached.

The fully-intact region represented the region where the delamination process was negligible at the interface between the coating and the metal. The region therefore shared the same porosity as the coating. At the metal-coating interface the local current density was a zero value as the anodic current density of the zinc dissolution reaction was balanced by the cathodic current density of the oxygen reduction reaction. The distributions of c_{Na^+} and V in the fully-intact region were represented by the line segments corresponding to the position range x_{IV} to x_V in Figure 9-2.

9.2.2 De-adhesion Test

A de-adhesion test was used to investigate the strength of adhesion between the coating and the metal after the coating was allowed to undergo delamination. The results for such a test included the distribution of the tensile force required to remove the coating and the metal-coating interface potential distribution obtained immediately before the de-adhesion test was undertaken. Furbeth and Stratmann[9] reported the results for a de-adhesion test that are shown in a schematic diagram in Figure 9-4.

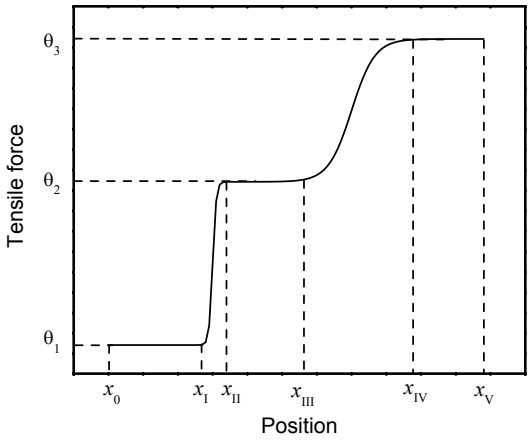

Figure 9-4: Schematic diagram of tensile force required to remove coating as a function of position in the delamination zone.

There were several regions observed from the the tensile force distribution shown in Figure 9-4. In the region corresponding to positions ranging from x_0 to x_I, the tensile force had at a constant value of θ_1. There was a non-linear increase in the tensile force from θ_2 to θ_3 for the positions ranging from x_{III} to x_{IV}. For the positions ranging from x_{III} to x_{IV}, the tensile force increased non-linearly from θ_2 and approached the value of θ_3. The tensile force was θ_3 for the positions ranging from x_{IV} to x_V. The tensile force of θ_3 required to remove the coating in this position range represented the adhesion strength between the coating and the metal that is unaffected by the delamination process.

Furbeth and Stratmann reported potential distributions as a function of time for a defect-delamination system that was de-oxygenated after an extended delamination time period.[9] The potential distributions as functions of time for the same system was reported when oxygen was re-introduced into the system. After analysis of these results together with other reported experimental results,[70] the tensile force distribution shown in Figure 9-4 was divided into different regions. The positions ranging from x_0 to x_I represented a region of coating where there was almost complete loss of adhesion between the gel-medium and the metal.

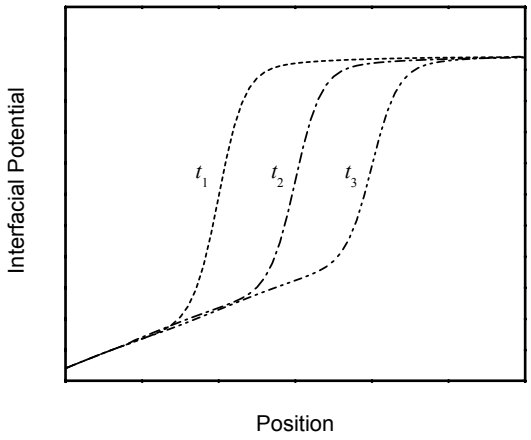

Figure 9-5: Schematic diagram of interfacial potential as a function of position in the delamination zone for elapsed times t_1, t_2 and t_3, where $t_3 > t_2 > t_1$.

This region only appears in the delamination zone after the coating has undergone delamination for an extended period of time and was designated the extended region. The positions ranging from x_{II} to x_{III}, from x_{III} to x_{IV}, and from x_{IV} to x_V corresponded to the delaminated, front and semi-intact, and fully-intact regions, respectively. This division of the tensile distribution into the extended, delaminated, front and semi-intact, and fully-intact regions has not been presented in literature before.

9.2.3 Delamination Potential

Furbeth and Stratmann reported experimental results of the potential at a zinc-coating interface V as a function of position with elapsed time as a parameter.[10] Similar results have also been reported by Williams and McMurray[25]and Williams *et al.*.[26] A schematic diagram of the experimental interfacial potential results on coated zinc is shown in Figure 9-5. The delaminated, front and semi-intact, and fully-intact regions were identifiable for a given distribution of V. The shape or profile of the distribution of V was approximately maintained with the delaminated region increasing in length and the fully-intact region decreasing in length with time.

Three features were identified from the distributions in Figure 9-5. One feature was that for a given elapsed time the delaminated region, the front and semi-intact regions, and the fully-intact regions were distinct. The second feature was that the gradients of potential remained approximately unchanged in the delaminated and front regions. The third feature was that the value of the interfacial potential in the fully-intact region was unchanged with time.

Furbeth and Stratmann analyzed the experimental interfacial potential distributions and showed that the power law

$$x_{del} = k_{del} t_{del}^{a_{del}} \tag{9-1}$$

could fit the data where x_{del} was the point of inflection on the part of the plot corresponding to the front region of the potential profile, k_{del} was a rate constant, t_{del} was the delamination time, and a_{del} was an exponent.[10] The calculated value of $a_{del} = 0.55$ was used by Furbeth and Stratmann to conclude that the mechanism for the delamination process was mass-transfer controlled and not kinetic controlled.[10] This conclusion supported the development of the quantitative mathematical model based on fundamental electrochemical concepts that is presented in this work.

9.3 Objective

A quantitative mathematical model does not exist for the propagation of front along the metal-coating interface during cathodic delamination of a coated metal. A model has been developed that accounted for the transport of water and oxygen normal to the metal surface.[78] This model was used to demonstrate that the thickness of the coating influenced the propagation rate of the front.

The experimental results presented in literature for coated zinc demonstrated that the cathodic delamination process involved coupling of mass-transfer of Na^+, electrochemical production of OH^-, loss of adhesion at the metal-coating interface,

and propagation of a front along the interface. The experiments also indicated that a micron-thick section of coating was degraded into a gel-like medium. This was supported by the calculated diffusion coefficients for ionic species in the delamination zone, which was two orders of magnitude smaller than that associated with an aqueous medium.[6]

The experimental observations were not sufficient to identify all of the phenomena that contribute to the delamination process. The objective of the present work was to develop a mathematical model for the propagation of the delamination front on coated zinc that can be used to identify phenomena that may contribute to the delamination process.

The mathematical model CADEM was developed to simulate the propagation of the front along the metal-coating interface in a delamination zone where the extended region was absent. The model considered the four species Na^{+}, Cl^{-}, OH^{-}, and Zn^{+2}. No homogeneous reactions were included. The electrochemical reactions at the metal coating interface were zinc dissolution and oxygen reduction. The hypotheses that the interfacial porosity and interfacial polarization kinetics were pH dependent were used in the development of CADEM.

9.3.1 pH-Dependent Polarization Kinetics

A hypothesis that the polarization kinetics of the metal-coating interface was pH-dependent was included in the development of CADEM. The dependence of the polarization kinetics of a metal surface on the pH of the adjacent electrolyte in an aqueous medium is well known in electrochemistry literature. Pourbaix diagrams relate the equilibrium potential of a metal surface as a function of pH.[79]

It has been observed that the presence of films or deposits at a metal surface influence the polarization kinetics when oxygen reduction is involved.[80] The deposit reduces the transport of oxygen to the metal surface and also reduce the surface

area available for electrochemical reactions. Experimental observations have indicated that the anodic metal dissolution reaction at a metal-coating interface is inhibited or poisoned.[7,9]

9.3.2 pH-Dependent Interfacial Porosity

The adhesive strength between the coating and the metal was measured as a function of position by the de-adhesion test.[9] The OH^- ion has been implicated in coating degradation and the loss of adhesive strength.[76] Therefore, the extent of coating degradation to a gel-medium and adhesive strength were related by the OH^- ion.

In the delaminated and front regions the concentrations of the two major species, Na^+ and OH^-, were approximately equal. Therefore, the distribution of c_{OH^-} was similar to that observed for c_{Na^+}. Comparison of experimental pH and adhesive strength distributions, indicated that at a high pH the adhesive strength was low and that at a low pH the adhesive strength was high. This supported the experimental observation that the OH^- ion was linked to the degradation of the coating and the weakening of the adhesion between the metal and the coating.

The degradation of a given section of coating to a gel-medium results in the increase in the transport of species through that section of coating. The increase in transport is due to the increase in the porosity of the coating section. Therefore, it was assumed that the porosity of the gel-medium was related to the coating degradation.

The relationships of coating degradation and pH and coating degradation and porosity were coupled to yield the hypothesis that the porosity of the gel-medium at the metal-coating interface was pH dependent. This porosity was referred to as the interfacial porosity.

A transient model for disbonded coating systems reported in literature considered the porosity of the electrolyte in the disbondment as a function of solid species deposited.[37,55] In the modeling of batteries and fuel cells the porosity of the medium is included as a parameter.[81–83] Unlike the transient model and the models for fuel cells and batteries, in CADEM the interfacial porosity was considered as a spatial variable and modeled explicitly. The inclusion of porosity in the modeling of the propagation front represented a novel approach which implicitly accounts for the phenomena of bond breakage and coating degradation during cathodic delamination.

CHAPTER 10
PROPAGATION MODEL DEVELOPMENT

The phenomena of interfacial porosity and interfacial polarization kinetics were hypothesized to be involved in the propagation of the front along the metal-coating interface during cathodic delamination. Mathematical expressions for these phenomena as functions of local pH are presented in this chapter.

The propagation model represented the evolution of the delamination process given initial conditions of dependent variables and other contributing pH dependent phenomena. Expressions used to construct distributions for these initial conditions are presented in this chapter.

10.1 Mass Transfer

The medium of the delamination zone was considered to be porous. The extension of the governing equations for species mass-transfer in an aqueous medium to a porous medium is presented in this section. The governing equation for c_i in a non-porous medium is expressed as equation (2-1)[12]

$$\frac{\partial c_i}{\partial t} = -\nabla \cdot \boldsymbol{N}_i + R_i$$

The flux of a species in a dilute, aqueous electrochemical system was given by equation (2-8)

$$\boldsymbol{N}_i = -z_i D_i c_i F \nabla \phi - D_i \nabla c_i$$

where convective contributions were assumed to be negligible.

In a porous environment the diffusion coefficient of a species D_i^* was related to the porosity of the domain ϵ and D_i by[64]

$$D_i^* = \epsilon^{1.5} D_i \tag{10-1}$$

The flux of species in a dilute, porous environment $\boldsymbol{N}_i^*$ was given by

$$\boldsymbol{N}_i^* = -z_i D_i^* c_i \nabla\phi - D_i^* \nabla c_i \tag{10-2}$$

where c_i was the solution-phase concentration averaged over the pores. Equation (10-2) was recast in terms of D_i using equation (10-1) as

$$\boldsymbol{N}_i^* = \epsilon^{1.5}\left(-z_i D_i c_i \nabla\phi - D_i \nabla c_i\right) \tag{10-3}$$

In this equation the porosity of the environment ϵ is included explicitly.

The conservation of a species i in a porous medium was expressed as

$$\frac{(\partial \epsilon c_i)}{\partial t} = -\nabla \cdot \boldsymbol{N}_i^* + \epsilon R_i \tag{10-4}$$

and recast in terms of $\boldsymbol{N}_i$ as

$$\frac{\partial\left(\epsilon c_i\right)}{\partial t} = -\nabla \cdot \left(\epsilon^{1.5}\boldsymbol{N}_i\right) + \epsilon R_i \tag{10-5}$$

where $\boldsymbol{N}_i$ was the solution-phase flux averaged over the pores.

10.2 Polarization Kinetics

The electrochemical reactions of interest involved zinc dissolution and oxygen reduction. The expressions for the polarization kinetics at the metal-coating interface were developed starting from the expressions applicable to a bare metal surface. This development is presented in this section.

10.2.1 Zinc dissolution

The behavior of the reversible reaction involving zinc

$$\mathrm{Zn} \rightleftharpoons \mathrm{Zn}^{+2} + 2\mathrm{e}^- \tag{10-6}$$

is described by activation polarization. Only the forward zinc dissolution reaction

$$\mathrm{Zn} \rightarrow \mathrm{Zn}^{+2} + 2\mathrm{e}^- \tag{10-7}$$

was considered because the backward reaction involves the deposition of zinc which is negligible. In an aqueous medium with a bare metal surface the current density due to this reaction i_{Zn} was calculated using the expression

$$i_{\mathrm{Zn}} = i_{o,Zn} 10^{\left(V - E^{o}_{\mathrm{Zn}}\right)/\beta_{\mathrm{Zn}}} \tag{10-8}$$

where β_{Zn} was the Tafel slope, E^{o}_{Zn} was the equilibrium potential, and $i_{o,Zn}$ was the exchange current density for the zinc dissolution reaction. The current density due to zinc dissolution reaction at the zinc-coating interface $i^{\mathrm{coat}}_{\mathrm{Zn}}$ was calculated using

$$i^{\mathrm{coat}}_{\mathrm{Zn}} = \omega \zeta i_{o,\mathrm{Zn}} 10^{\left(V - E^{o}_{\mathrm{Zn}}\right)/\beta_{\mathrm{Zn}}} \tag{10-9}$$

In this expression the surface area available for the reaction was considered by including the parameter ω which represented the ratio

$$\omega = \frac{\text{available area for electrochemical reaction}}{\text{area of surface}} \tag{10-10}$$

The exchange current density for an electrochemical reaction is dependent on the nature of the surface of the metal. The exchange current density $i_{o,Zn}$ corresponded to a clean, polished metal surface in an aqueous medium. At a metal-coating interface the exchange current would be very different from that of an electrolyte-metal interface. The effect of this difference in exchange current density was considered by including a poisoning parameter ζ defined as

$$\zeta = \frac{i^{\mathrm{coat}}_{o,\mathrm{Zn}}}{i_{o,\mathrm{Zn}}} \tag{10-11}$$

where $i^{\mathrm{coat}}_{o,\mathrm{Zn}}$ was the exchange current density for zinc dissolution at a metal-coating interface. This parameter also accounted for the presence of any salt films on the metal surface which would poison the metal surface.

10.2.2 Oxygen Reduction

The polarization kinetics of the oxygen reduction reaction given by equation (2-42)

$$O_2 + 2H_2O + 4e^- \rightarrow 4OH^-$$

is described by activation polarization for one part and concentration polarization for another part (see Section 2.4).

The assumption that the oxygen reduction reaction was mass-transfer-limited at the metal-coating interface was used. The current density due to oxygen reduction on the metal-coating interface $i_{O_2}^{coat}$was calculated using

$$i_{O_2}^{coat} = -\omega \alpha_{O_2} i_{lim,O_2}^{coat} \tag{10-12}$$

where i_{lim,O_2}^{coat} was the mass-transfer-limited current density for oxygen reduction at the metal-coating interface. In equation (10-12) a blocking factor α_{O_2} was included to consider the reduction in the transport of oxygen due to the presence of a porous salt film.

A schematic diagram of the delamination zone is shown in Figure 9-3. The value of i_{lim,O_2}^{coat} at any given position along AC was calculated using

$$i_{lim,O_2}^{coat} = -nFD_{O_2}c_{O_2,\infty}\frac{\epsilon_g^{1.5}\epsilon_c^{1.5}}{\epsilon_g^{1.5}(a_c) + \epsilon_c^{1.5}g_m} \tag{10-13}$$

where g_m and a_c were the thickness of the gel-medium and coating, respectively, ϵ_c was the porosity of the un-degraded coating, and ϵ_m was the local porosity of the gel-medium.

10.3 Initial Concentration Distributions

The mathematical model CADEM was developed to simulate the evolution of the conditions in the delamination zone starting with a developed delamination zone. A developed delamination zone consisted of distinct delaminated, front,

semi-intact, and fully-intact regions. The formulation of equations to describe the concentration distributions at the initial time t_o is presented in this section.

The initial distribution for c_{Na^+} was formulated using experimental results reported by Furbeth and Stratmann and shown in Figure 9-2.[9] Separate equations were formulated for the initial Na^+ distribution in each of the regions of the delamination zone. The experimental distribution of the Cl^- intensity reported by Furbeth and Stratmann did not permit much insight into its distribution except its magnitude as compared to c_{Na^+}.[9] The trend in the c_{Cl^-} distribution was assumed to follow the same trend as the distribution for c_{Na^+}. The initial distribution for c_{OH^-} was constructed similar to the construction for c_{Na^+}. The initial distribution for $c_{Zn^{+2}}$ was calculated using the condition of electroneutrality.

The delamination zone was divided into the regions shown in Figure 9-2. The lengths of the delaminated, front, semi-intact, and fully-intact regions at the initial time were designated as l_{del}, l_{fro}, l_{sem}, and l_{int}, respectively. The concentrations c_i at positions x_I, x_{II}, x_{III}, x_{IV}, and x_V were designated by $c_{i,I}$, $c_{i,II}$, $c_{i,III}$, $c_{i,IV}$, and $c_{i,V}$, respectively. The species considered in the model were Na^+, Cl^-, OH^- and Zn^{+2}.

In the delaminated region c_i , excluding $c_{Zn^{+2}}$, was formulated as a linear function of position. For a position x in the delaminated region c_i at t_o was given by

$$c_i(x, t_o) = c_{i,I} + \chi_i(x - x_I) \tag{10-14}$$

where χ_i was given by

$$\chi_i = \frac{c_{i,x_{II}} - c_{i,I}}{l_{del}} \tag{10-15}$$

and represented the gradient of c_i in the delaminated region.

The initial distribution in the front region for c_i , excluding $c_{Zn^{+2}}$, was non-linear and was formulated using the exponential expression

$$c_i(x, t_o) = c_{i,II} \exp\left(\lambda_{i,fro}(x - x_{II})\right) \tag{10-16}$$

where $\lambda_{i,fro}$ was given by

$$\lambda_{i,fro} = \frac{1}{l_{fro}} \ln\left(\frac{c_{i,III}}{c_{i,II}}\right) \tag{10-17}$$

and represented the parameter used to describe the non-linear change of c_i in the front region.

The initial distribution for c_i , excluding $c_{Zn^{+2}}$, in the semi-intact region was non-linear and was formulated similarly to the distribution in the front region. The equation

$$c_i(x, t_o) = c_{i,III} \exp\left(\lambda_{i,sem}(x - x_{III})\right) \tag{10-18}$$

was used where $\lambda_{i,sem}$ was given by

$$\lambda_{i,sem} = \frac{1}{l_{sem}} \ln\left(\frac{c_{i,IV}}{c_{i,III}}\right) \tag{10-19}$$

and represented the parameter to describe the non-linear change in c_i with position in the semi-intact region.

The fully-intact region corresponded to a coating region with the absence of delamination. The distribution of c_i was assumed uniform in this region and was given by

$$c_i(x, t_o) = c_{i,IV} \tag{10-20}$$

where x was a position in the fully-intact region.

10.4 pH-Porosity Dependence

The hypothesis that the interfacial porosity was pH dependent was introduced in section 9.3. An expression for the relationship between interfacial porosity and pH is presented in this section.

The adhesive strength between the coating and the metal was measured as a function of position by the de-adhesion test.[9] The adhesive strength increased

monotonically with position. Therefore, it was assumed that the interfacial porosity also changed monotonically with position except that it decreased with position. This was consistent with the reasoning that at high strengths the coating degradation was low with the porosity low, and at low strength the coating degradation was high and the porosity likewise high.

An assumed distribution for ϵ is given in Figure 10-1(a). In the delaminated region ϵ was assumed to vary linearly with position with ϵ decreasing from ϵ_1 to ϵ_2. The ϵ-distribution in the front and semi-intact regions were non-linear with ϵ decreasing from ϵ_2 to ϵ_3 and ϵ_3 to ϵ_4, respectively. The fully-intact region corresponded to a coating region with the absence of delamination and ϵ was assumed to be unchanged at ϵ_4 in this region.

An assumed pH-distribution is shown in Figure 10-1(b). The relationship between ϵ and pH was constructed by coupling the distributions shown in Figures 10-1 (a) and (b) to yield the ϵ-pH distribution shown in Figure 10-2. A formulation for this plot was obtained by fitting by inspection an equation of the form

$$\epsilon = \frac{b_{\epsilon,1}}{1+\exp(b_{\epsilon,2}(pH - b_{\epsilon,3}))} + \frac{b_{\epsilon,4}}{1+\exp(b_{\epsilon,5}(pH - b_{\epsilon,6}))} + b_{\epsilon,7} \tag{10-21}$$

to the plot where $b_{\epsilon,1}$ to $b_{\epsilon,7}$ were fitting parameters.

10.5 pH-Polarization Dependence

The polarization parameters α_{O_2}, ω, and ζ were used in the calculation of the current densities due to zinc dissolution i_{Zn}^{coat} and oxygen reduction $i_{O_2}^{coat}$, equations (10-9) and (10-12), respectively. These parameters were assumed to be functions of pH and expressions were developed for these functions.

10.5.1 Blocking Parameter

The presence of the deposits at the metal-coating interface was not modeled explicitly. Instead the effect of the deposits on the transport of oxygen was included

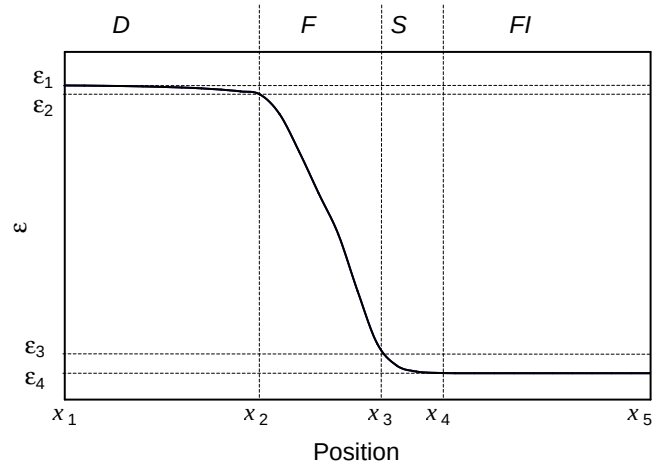

(a)

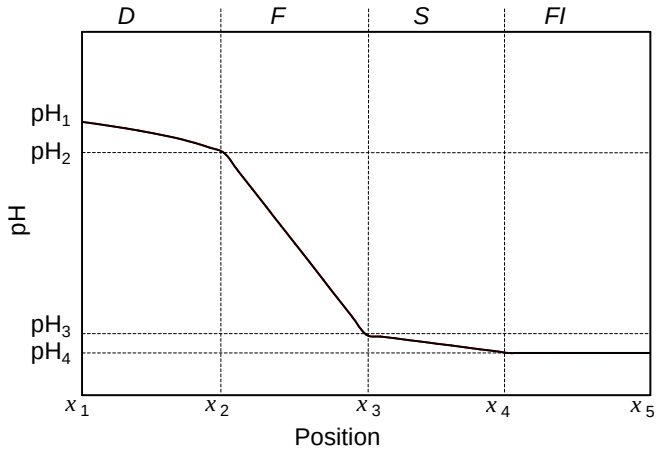

(b)

Figure 10-1: Schematic diagrams for interfacial porosity and pH as functions of position in the delamination zone at the initial time. (a) interfacial porosity and (b) pH. The dashed lines separate the delamination zone into the delaminated region *D*, the front region *F*, the semi-intact region *S* and the fully-intact region *FI*.

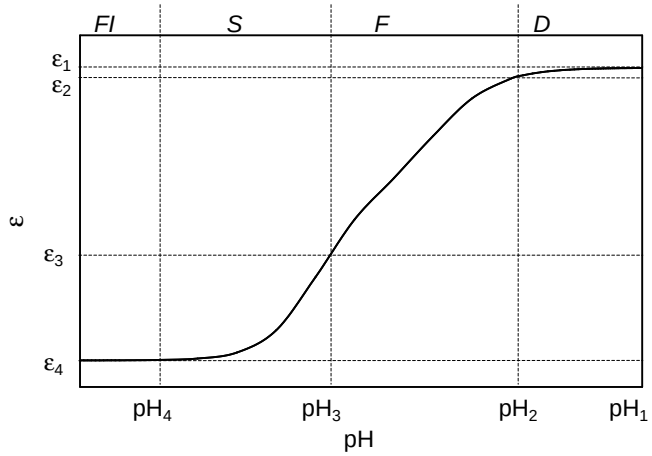

Figure 10-2: Schematic diagram for interfacial porosity as a function of pH. The dashed lines separate the delamination zone into the delaminated region *D*, the front region *F*, the semi-intact region *S* and the fully-intact region *FI*.

by using a blocking parameter α_{O_2}. The blocking parameter α_{O_2} was used in the calculation of $i_{O_2}^{coat}$ at the metal-coating interface, equation(10-12).

An assumed distribution for α_{O_2} as a function of position along the metal-coating interface is shown in Figure 10-3(a). In the delaminated region the value of α_{O_2} was constant at $\alpha_{O_2,1}$. A value of $\alpha_{O_2,1} \leq 1$ was selected as the transport of oxygen to the delaminated region interface was assumed to be hindered by the presence of deposits. In the front region it was assumed that the effect of deposits on the transport of oxygen to the interface was less and an increase in α_{O_2} from $\alpha_{O_2,1}$ to $\alpha_{O_2,2}$ was assumed across the front region. The semi-intact region represented a transition region between the front and fully-intact regions. The value of α_{O_2} was assumed to decrease from $\alpha_{O_2,2}$ to $\alpha_{O_2,3}$ in the semi-intact region. The value of α_{O_2} was assumed to be constant at $\alpha_{O_2,3}$ in the fully-intact region.

The relationship between α_{O_2} and pH was constructed by coupling the distributions shown in Figures 10-3(a) and 10-1(b). The resulting distribution for the α_{O_2}-pH relationship is shown in Figure 10-3(b). A formulation for this distribution

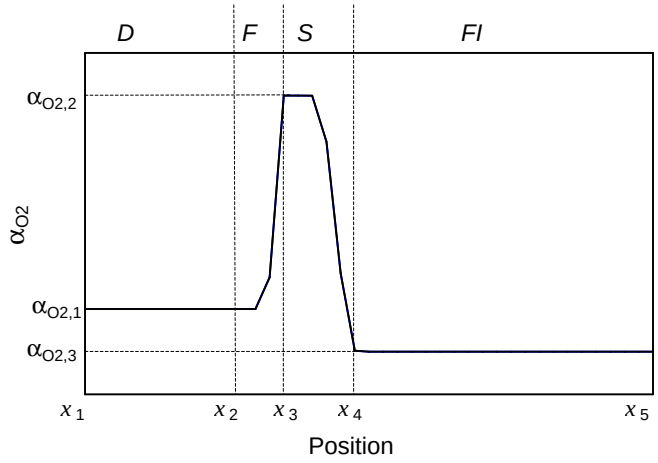

(a)

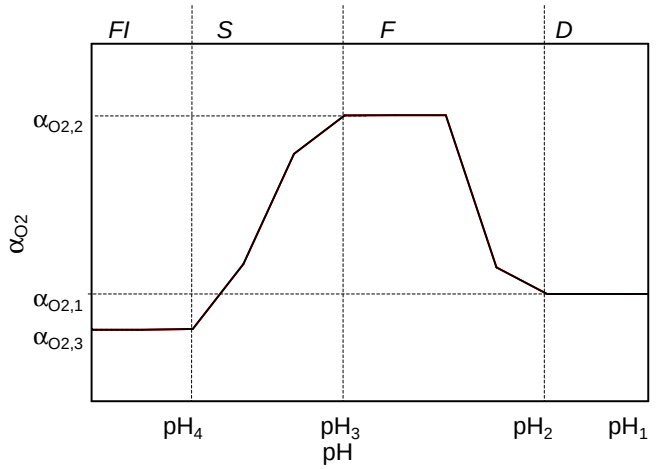

(b)

Figure 10-3: Schematic diagram for blocking polarization parameter (a) as a function of position in the delamination zone at the initial time and (b) as a function of pH. The dashed lines separate the delamination zone into the delaminated region *D*, the front region *F*, the semi-intact region *S* and the fully-intact region *FI*.

was obtained by fitting by inspection an equation of the form

$$\alpha_{O_2} = \left(\frac{b_{\alpha,1}\exp(-b_{\alpha,2}(pH - b_{\alpha,3}))}{1 + b_{\alpha,1}\exp(-b_{\alpha,2}(pH - b_{\alpha,3}))} + b_{\alpha,7}\right) \cdot \left(\frac{1}{1/b_{\alpha,4} + \exp(-b_{\alpha,5}(pH - b_{\alpha,6}))} + b_{\alpha,8}\right) \quad (10\text{-}22)$$

where $b_{\alpha,1}$ through $b_{\alpha,8}$ were fitting parameters.

10.5.2 Surface Coverage Parameter

The surface coverage parameter ω was used to express the surface area available for an electrochemical reaction at the metal-coating interface. An assumed distribution of ω as a function of position is shown in Figure 10-4(a). In the delaminated region ω was assumed to decrease linearly from ω_1 to ω_2. In the front and semi-intact regions ω was assumed to decrease exponentially from ω_2 to ω_3 and from ω_3 to ω_4, respectively. The value of ω was assumed to be constant at ω_4 in the fully-intact region.

The relationship between ω and pH was constructed by coupling the distributions shown in Figures 10-4(a) and 10-1(b). The resulting distribution for the ω-pH relationship is shown in Figure 10-4(b). A formulation for this distribution was obtained by fitting by inspection an equation of the form

$$\omega = \frac{b_{\omega,1}}{1 + \exp(b_{\omega,2}(pH - b_{\omega,3}))} + \frac{b_{\omega,4}}{1 + \exp(b_{\omega,5}(pH - b_{\omega,6}))} + b_{\omega,7} \quad (10\text{-}23)$$

where $b_{\omega,1}$ through $b_{\omega,7}$ were fitting parameters.

10.5.3 Poisoning Parameter

The poisoning parameter ζ was used to consider the effect of the nature of interface on the zinc dissolution reaction. The zinc dissolution reaction was assumed to be unfavorable in the delamination zone with the assumption $\zeta << 1$. An assumed distribution for ζ as a function of position is shown in Figure 10-5(a). In the delaminated region ζ was assumed to be constant at ζ_1. In the front and

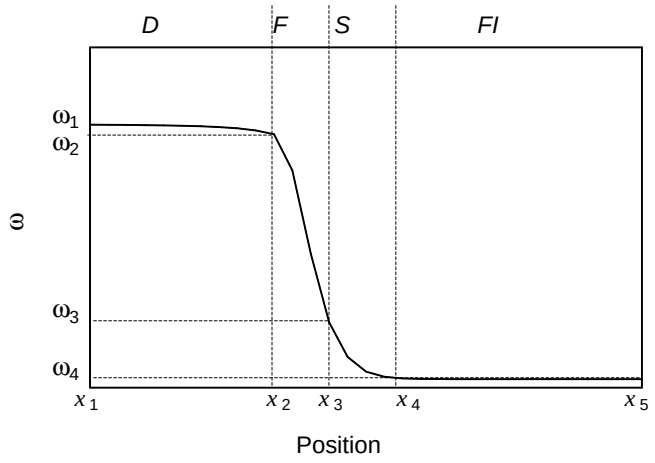

(a)

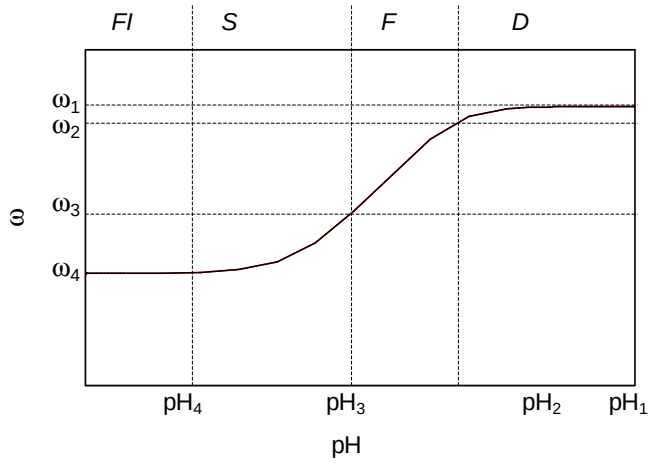

(b)

Figure 10-4: Schematic diagram for surface coverage polarization parameter (a) as a function of position in the delamination zone at the initial time and (b) as a function of pH. The dashed lines separate the delamination zone into the delaminated region *D*, the front region *F*, the semi-intact region *S* and the fully-intact region *FI*.

semi-intact regions ζ was assumed to decrease exponentially from ζ_1 to ζ_2 and from ζ_2 to ζ_3, respectively. The value of ζ was assumed to be constant at ζ_3 in the fully-intact region.

The relationship between ζ and pH was constructed by coupling the distributions shown in Figures 10-5(a) and 10-1(b). The resulting distribution for the ζ-pH distribution is shown in Figure 10-5(b). A formulation for this distribution was obtained by fitting by inspection an equation of the form

$$\zeta = \frac{b_{\zeta,1}}{1+\exp(b_{\zeta,2}(pH - b_{\zeta,3}))} + \frac{b_{\zeta,4}}{1+\exp(b_{\zeta,5}(pH - b_{\zeta,6}))} + b_{\zeta,7} \tag{10-24}$$

where $b_{\zeta,1}$ through $b_{\zeta,7}$ were fitting parameters.

10.6 Initial Solution Potential Distribution

The initial solution potential distribution $\Phi(x, t_o)$ was calculated using the initial distributions for c_i , ϵ, α_{O_2}, ω, and ζ. The method used for the calculation was similar to that used by Walton *et al.*[20] This method employed a decoupling of the governing equation for c_i from that of Φ.

In the mathematical model CADEM four species were considered Na^+, Cl^-, OH^-, and Zn^{+2}, and no homogeneous reactions were included. The electrochemical reactions included zinc dissolution, equation (10-7), and oxygen reduction, equation (2-42).

The delamination zone ADEH shown in Figure 9-3 was divided into control volumes v with nodes m at the control volume center as shown in Figure 10-6. The nodes and control volumes were designated m_1 to m_{max} and v_1 to v_{max}, respectively. The conditions at m_1 were given and a no-flux boundary condition was used at m_{max}. The surface area of each control volume A_s (except v_1 and v_{max}), the cross-sectional area shared by volumes A_C, and the gap of the gel-medium g_m were uniform across the length of the zone.

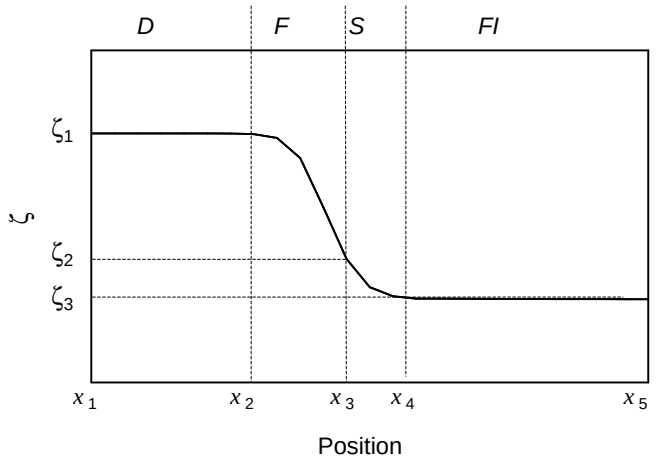

(a)

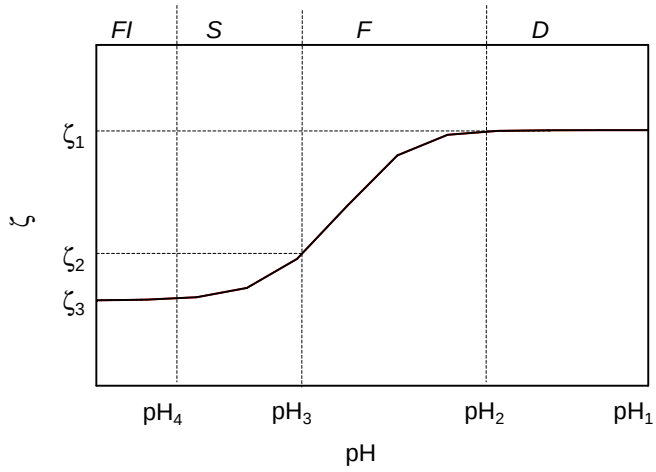

(b)

Figure 10-5: Schematic diagram for poisoning polarization parameter (a) as a function of position in the delamination zone at the initial time and (b) as a function of pH. The dashed lines separate the delamination zone into the delaminated region *D*, the front region *F*, the semi-intact region *S* and the fully-intact region *FI*.

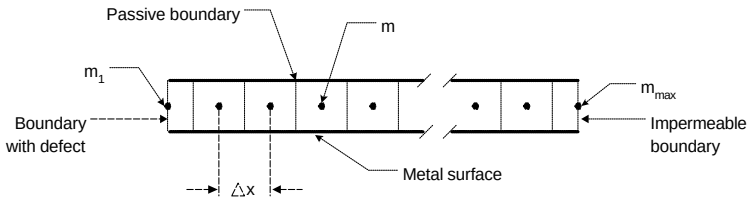

Figure 10-6: Schematic diagram of delamination zone discretized into control volumes.

At a position m in the delamination zone, the current density $i_{s(m)}$ entering a control volume v_m with node m was given by

$$i_{s(m)} = -\kappa_{(m)} \nabla \Phi_{(m)} + i_{d(m)} \tag{10-25}$$

where the diffusion current $i_{d(m)}$ was

$$i_{d(m)} = -F \sum z_i D_i \epsilon_{(m)}^{1.5} \nabla c_{i(m)} \tag{10-26}$$

and the conductivity $\kappa_{(m)}$ was

$$\kappa_{(m)} = \frac{F^2}{RT} \sum_i z_i^2 D_i \epsilon_{(m)}^{1.5} c_i \tag{10-27}$$

In these equations for $i_{d(m)}$ and $\kappa_{(m)}$, the porosity of the delamination zone is considered explicitly.

The current density $i_{s(m)}$ was given by

$$i_{s(m)} = \frac{-A_{s(m)}}{A_{c(m)}} \sum_{k=m}^{k=m_{max}} i_{e(k)} \tag{10-28}$$

$$= \frac{1}{g_m} \sum_{k=m}^{k=m_{max}} i_{e(k)} \tag{10-29}$$

where $i_{e(k)}$ was the net current density due to electrochemical reactions in a control volume v_k. The value of $i_{e(k)}$ was given by the net current density due to the electrochemical reactions

$$i_{e(k)} = i_{\mathrm{Zn(k)}}^{\mathrm{coat}} + i_{\mathrm{O_2(k)}}^{\mathrm{coat}} \tag{10-30}$$

where $i_{\mathrm{Zn(k)}}^{\mathrm{coat}}$ and $i_{\mathrm{O_2(k)}}^{\mathrm{coat}}$ were the current densities due to zinc dissolution and oxygen reduction at the node k, respectively. These were calculated using equations (10-9) and (10-12), respectively.

From equation (10-25) the gradient of Φ at a position m was

$$\nabla \Phi_{(m)} = \frac{i_{s(m)} - i_{d(m)}}{-\kappa_{(m)}} \tag{10-31}$$

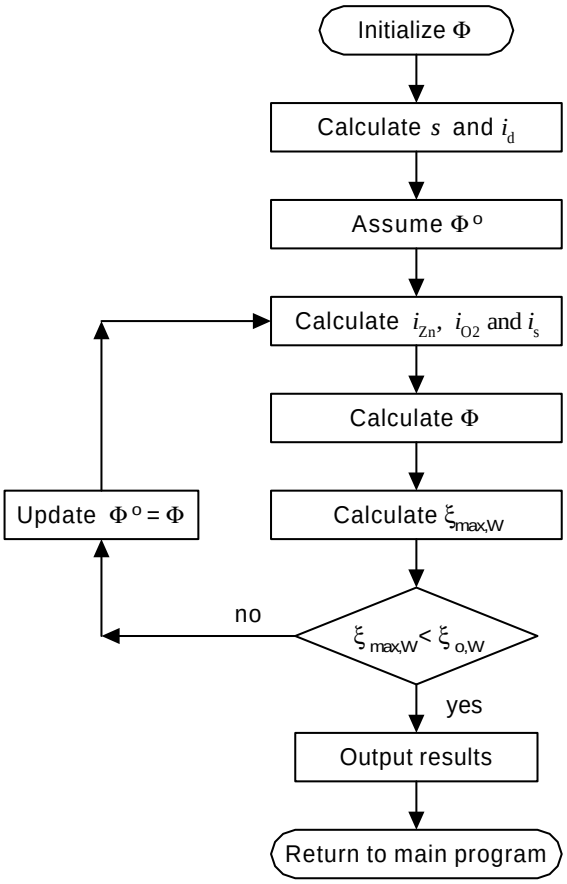

Figure 10-7: Algorithm for the calculation of the initial distribution of the solution potential.

A Taylor series expansion for $\Phi_{(m+1)}$ about $\Phi_{(m)}$

$$\Phi_{(m+1)} = \Phi_{(m)} + \nabla\Phi_{(m)}\triangle x \tag{10-32}$$

was used to calculate Φ at a node $m+1$ using the value of Φ at the node m, $\nabla\Phi_{(m)}$, and the spacing between the nodes $\triangle x$.

The algorithm used for the calculation of $\Phi(x, t_o)$ is presented in Figure 10-7 and summarized below:

1. The values for κ and i_d at the control volume nodes were calculated for the given distributions of c_i and ϵ.

2. The distribution of solution potential was assumed as Φ^o.

3. The current densities i_{Zn}^{coat}, $i_{O_2}^{coat}$, and i_s were calculated at the nodes.

4. The value of Φ was calculated at the nodes using equation (10-32).

5. The maximum percentage difference $\xi_{max,W}$ between Φ and Φ^o was calculated where the percentage difference ξ_W was given by

$$\xi_W = 100 \left| \frac{\Phi - \Phi^o}{\Phi} \right| \tag{10-33}$$

6. The value of $\xi_{max,W}$ was compared with a convergence criterion $\xi_{o,W}$. If $\xi_{max,W} < \xi_{o,W}$ then control was returned to the main program. If $\xi_{max,W} > \xi_{o,W}$ then the value of Φ^o was updated with Φ and control was returned to Step 3.

10.7 Summary

The governing equation for c_i in a porous medium was developed in terms of the porosity, and the concentrations and fluxes averaged over the pores per unit volume. The polarization expressions for zinc dissolution and oxygen reduction were adjusted to be applicable to the metal-coating interface. Polarization parameters were included in this adjustment that accounted for the reduction in oxygen transport to the interface, the reduction in the surface area available for electrochemical reactions at the interface, and the poisoning of the zinc dissolution reaction at the interface. Expressions for the pH dependence of porosity and the polarization parameters were developed. The method of solution of calculating the initial distribution for Φ starting from the initial distributions for c_i , ϵ, ω, α_{O_2}, and ζ was described.

CHAPTER 11
PROPAGATION MODEL

The development of the mathematical model CADEM is presented in this chapter. The model simulated the propagation of the front along the metal-coating interface during the cathodic delamination of a coated metal.

11.1 Delamination Zone

The delamination zone ADEH shown in Figure 9-3 was discretized into nodes m as shown in Figure 11-1. The nodes were designated m_1 to m_{max}. The conditions at m_1 were given as the conditions at the boundary AH that was shared with the defect. A no-flux boundary condition was used at the external boundary node m_{max}. The gap of the zone g_m was uniform across the length of the zone. The four species considered were Na^+, Cl^-, OH^-, and Zn^{+2}, and no homogeneous reactions were included. The electrochemical reactions included zinc dissolution, equation (10-7), and oxygen reduction, equation (2-42).

11.2 Governing Equations

The governing equations for the conditions in the delamination zone included equations for electroneutrality, species mass-transfer, and the relationship between pH and interfacial porosity.

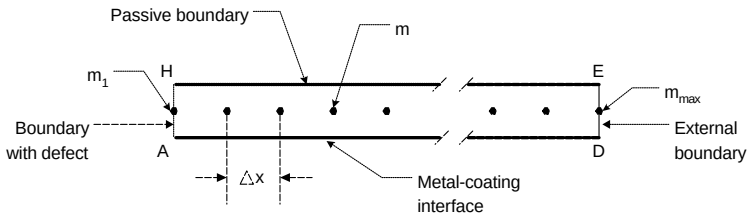

Figure 11-1: Schematic diagram of the delamination zone discretized into nodes.

The variables φ and ϕ were used in the development where

$$\varphi = \epsilon^{1.5} \tag{11-1}$$

and ϕ was a dimensionless variable given by equation (2-9)

$$\phi = \frac{\Phi F}{RT}$$

The dependent variables c_{Na^+}, c_{Cl^-}, c_{OH^-}, $c_{Zn^{+2}}$, ϕ, and φ were assigned indices 1 to 6, respectively. The independent variables were time t and position x.

11.2.1 Electroneutrality

The governing equation for the solution potential

$$\sum_{i=1}^{i=4} z_i c_i = 0 \tag{11-2}$$

was derived from the condition of electroneutrality, equation (2-13).

11.2.2 Mass-transfer

The governing equation for c_i in a 1-D domain as shown in Figure 11-1 was

$$\frac{\partial (\epsilon c_i)}{\partial t} = -\frac{\partial \left(\epsilon^{1.5} N_i\right)}{\partial x} + \epsilon R_i + S_i \tag{11-3}$$

where S_i was the rate of production per unit volume by electrochemical reactions. Expansion of equation (11-3) and substitution of ϵ with φ yielded

$$\frac{\partial \left(\varphi^{2/3} c_i\right)}{\partial t} = -\varphi \frac{\partial N_i}{\partial x} - N_i \frac{\partial \varphi}{\partial x} + S_i \tag{11-4}$$

as the governing equation for c_i when homogeneous reactions were not considered.

The chemically inert species Na^+ and Cl^- did not participate in electrochemical reactions. The governing equations for c_{Na^+} and c_{Cl^-} were

$$\frac{\partial \left(\varphi^{2/3} c_{Na^+}\right)}{\partial t} = -\varphi \frac{\partial N_{Na^+}}{\partial x} - N_{Na^+} \frac{d\varphi}{dx} \tag{11-5}$$

and

$$\frac{\partial\left(\varphi^{2/3}c_{Cl^-}\right)}{\partial t} = -\varphi\frac{\partial N_{Cl^-}}{\partial x} - N_{Cl^-}\frac{\partial\varphi}{dx} \tag{11-6}$$

respectively, with $S_{Na^+} = 0$ and $S_{Cl^-} = 0$. The governing equation for $c_{Zn^{+2}}$ was

$$\frac{\partial\left(\varphi^{2/3}c_{Zn^{+2}}\right)}{\partial t} = -\varphi\frac{\partial N_{Zn^{+2}}}{\partial x} - N_{Zn^{+2}}\frac{\partial\varphi}{dx} + S_{Zn^{+2}} \tag{11-7}$$

where

$$S_{Zn^{+2}} = \frac{i_{Zn}^{coat}}{2F} \tag{11-8}$$

with i_{Zn}^{coat} given by equation (10-9). The governing equation for $c_{OH^-}$was

$$\frac{\partial\left(\varphi^{2/3}c_{OH^-}\right)}{\partial t} = -\varphi\frac{\partial N_{OH^-}}{\partial x} - N_{OH^-}\frac{\partial\varphi}{dx} + S_{OH^-} \tag{11-9}$$

where

$$S_{OH} = \frac{i_{O_2}^{coat}}{-F} \tag{11-10}$$

with $i_{O_2}^{coat}$ given by equation (10-12).

11.2.3 pH-Porosity

A hypothesis was introduced that the interfacial porosity in the delamination zone was a function of pH (see section 9.3). This hypothesis accounted implicitly for the bond-breakage and coating degradation that accompanied the propagation of the front along the metal-coating interface during cathodic delamination. The hypothesis for the ϵ-pH relationship was included in CADEM for the conditions when the ϵ-pH relationship was equilibrated and not equilibrated.

Equilibrium Relationship

The time constants for the bond-breakage and coating degradation phenomena are not reported, but, under the assumption that they are sufficiently small, for a given change in pH, an equilibrium value of ϵ can be attained instantaneously.

The equation that governed the equilibrium relationship between porosity ϵ and pH was equation (10-21)

$$\epsilon = \frac{b_{\epsilon,1}}{1+\exp(b_{\epsilon,2}(pH - b_{\epsilon,3}))} + \frac{b_{\epsilon,4}}{1+\exp(b_{\epsilon,5}(pH - b_{\epsilon,6}))} + b_{\epsilon,7}$$

The formulation of this equation was given in section 10.4. Equation (10-21) was recast in terms of φ and c_{OH^-} as

$$\varphi^{2/3} = \frac{b_{\epsilon,1}}{1+b_{\epsilon,8}c_{OH^-}^{-b_{\epsilon,2}}} + \frac{b_{\epsilon,4}}{1+b_{\epsilon,9}c_{OH^-}^{-b_{\epsilon,5}}} + b_{\epsilon,7} \tag{11-11}$$

where

$$b_{\epsilon,8} = 10^{b_{\epsilon,2}}\exp(b_{\epsilon,2}(14 - b_{\epsilon,3})) \tag{11-12}$$

and

$$b_{\epsilon,9} = 10^{b_{\epsilon,5}}\exp(b_{\epsilon,5}(14 - b_{\epsilon,6})) \tag{11-13}$$

Non-equilibrium Relationship

The phenomena of bond-breakage and coating degradation involved chemical reactions. When the time constants for these phenomena are large compared to the time constants for the processes of diffusion and migration, the assumption that the equilibrium value of ϵ is attained instantaneously is invalid. A non-equilibrium relationship between ϵ and pH was considered given by

$$\frac{\partial \epsilon}{\partial t} = -k_{neq}\left(\epsilon - \epsilon_{eq}\right) \tag{11-14}$$

where the equilibrium porosity ϵ_{eq} was

$$\epsilon_{eq} = \frac{b_{\epsilon,1}}{1+\exp(b_{\epsilon,2}(pH - b_{\epsilon,3}))} + \frac{b_{\epsilon,4}}{1+\exp(b_{\epsilon,5}(pH - b_{\epsilon,6}))} + b_{\epsilon,7}$$

and k_{neq} was a rate constant for the bond-breakage and coating degradation phenomena. In the limit that $k_{neq} \to \infty$ the value of ϵ attains its equilibrated value

$$\epsilon = \epsilon_{eq} \tag{11-15}$$

In the limit that $k_{neq} \rightarrow 0$ then

$$\frac{\partial \epsilon}{\partial t} \approx 0 \tag{11-16}$$

and the value of the local porosity is unchanged.

Equation (11-14) was recast in terms of φ as

$$\frac{\partial \varphi^{2/3}}{\partial t} = -k_{neq}\left(\varphi^{2/3} - \varphi_{eq}^{2/3}\right) \tag{11-17}$$

where φ_{eq} was

$$\varphi_{eq}^{2/3} = \frac{b_{\epsilon,1}}{1 + b_{\epsilon,8} c_{OH^-}^{-b_{\epsilon,2}}} + \frac{b_{\epsilon,4}}{1 + b_{\epsilon,9} c_{OH^-}^{-b_{\epsilon,5}}} + b_{\epsilon,7} \tag{11-18}$$

and $b_{\epsilon,8}$ and $b_{\epsilon,9}$ were given by equations (11-12) and (11-13), respectively.

11.3 Method of Solution

The governing equation for the c_i was

$$\begin{aligned} \frac{\partial\left(\varphi^{2/3} c_i\right)}{\partial t} &= z_i D_i c_i \varphi \frac{\partial^2 \phi}{\partial x^2} + z_i D_i \varphi \frac{\partial c_i}{\partial x}\frac{\partial \phi}{\partial x} + D_i \varphi \frac{\partial^2 c_i}{\partial x^2} \\ &+ z_i D_i c_i \frac{\partial \phi}{\partial x}\frac{\partial \varphi}{\partial x} + D_i \frac{\partial c_i}{\partial x}\frac{\partial \varphi}{\partial x} + S_i \end{aligned} \tag{11-19}$$

obtained by substituting the flux of a species N_i in one-dimension

$$N_i = -z_i D_i c_i \frac{d\phi}{dx} - D_i \frac{dc_i}{dx} \tag{11-20}$$

into the general form of the governing equation for c_i, equation (11-4).

The system of governing equations in the delamination zone consisted of equations (11-5), (11-6), (11-7), and (11-9) written in the form of equation (11-19), the equation for the electroneutrality condition, equation (11-2), and an equation for the porosity-pH relationship. When the porosity was assumed to attain its equilibrium value instantaneously the equilibrium ϵ-pH relationship, equation (11-11), was used as the governing equation for ϵ. When the non-equilibrium ϵ-pH relationship was included, equation (11-17) was used as the governing equation for ϵ.

The system of governing equations were discretized at each node in the domain using approximations. The first order temporal derivative in time was given by

$$\frac{\partial\left(\varphi^{2/3}c_i\right)}{\partial t} = \frac{(\varphi^{2/3}c_i)^{(n+1)} - (\varphi^{2/3}c_i)^{(n)}}{\triangle t} \tag{11-21}$$

where the superscripts in brackets n and $n+1$ represented the conditions at a given time t and a time one time step ahead, $t + \triangle t$. Terms of the order $(\triangle t)$ and higher were neglected in the temporal derivative. The spatial derivatives for a non-boundary node m used the central finite difference equations

$$\frac{\partial^2 f_{(m)}^{(n)}}{\partial x^2} = \frac{f_{(m+1)}^{(n)} - 2f_{(m)}^{(n)} + f_{(m-1)}^{(n)}}{(\triangle x)^2} \tag{11-22}$$

$$\frac{\partial f_{(m)}^{(n)}}{\partial x} = \frac{f_{(m+1)}^{(n)} - f_{(m-1)}^{(n)}}{2\triangle x} \tag{11-23}$$

and for the boundary node m_{max} the backward difference equation

$$\frac{df_{(m_{max})}^{(n)}}{dx} = \frac{f_{(m_{max}-2)}^{(n)} - 4f_{(m_{max}-1)}^{(n)} + 3f_{(m_{max})}^{(n)}}{2\triangle x} + O(\triangle x)^2 \tag{11-24}$$

where f was a generic variable for c_i , ϕ, and φ. Terms of the order $(\triangle x)^2$ and higher were neglected in the spatial derivatives.

Newton's method was used to solve the system of coupled, non-linear, partial differential equations.[84] The details of this procedure are given in Appendix C. The governing equations were discretized using temporal and spatial approximations. The discretized equations were used to construct the global function vector $\boldsymbol{F}_N$ and the global jacobian matrix $\boldsymbol{J}_N$. The vector $\boldsymbol{F}_N$ and matrix $\boldsymbol{J}_N$ were functions of the dependent variables given by vector $\boldsymbol{C}_N$ where

$$\boldsymbol{C}_N^{(n)} = \left[\mathbb{C}_{(1)}^{(n)}\, \mathbb{C}_{(2)}^{(n)}\, \cdots\, \mathbb{C}_{(m_{max})}^{(n)}\right]^T \tag{11-25}$$

and

$$\mathbb{C}_{(m)}^{(n)} = \left[c_{1(m)}^{(n)}\, c_{2(m)}^{(n)}\, c_{3(m)}^{(n)}\, c_{4(m)}^{(n)}\, \phi_{(m)}^{(n)}\, \varphi_{(m)}^{(n)}\right]^T \tag{11-26}$$

To a first approximation

$$\boldsymbol{F}_N\left(\boldsymbol{C}_N^{(n+1)}\right) \approx \boldsymbol{F}_N\left(\boldsymbol{C}_N^{(n+1),o}\right) + \boldsymbol{J}_N\left(\boldsymbol{C}_N^{(n+1),o}\right) \cdot \triangle \boldsymbol{C}_N \tag{11-27}$$

where $\boldsymbol{C}_N^{(n+1),o}$

$$\boldsymbol{C}_N^{(n+1),o} = \left[\mathbb{C}_{(1)}^{(n+1),o} \ \cdots \ \mathbb{C}_{(m_{max})}^{(n+1),o}\right]^T \tag{11-28}$$

was an approximation for $\boldsymbol{C}_N^{(n+1)}$ and

$$\triangle \boldsymbol{C}_N = \boldsymbol{C}_N^{(n+1)} - \boldsymbol{C}_N^{(n+1),o} \tag{11-29}$$

Given that

$$\boldsymbol{F}_N\left(\boldsymbol{C}_N^{(n+1)}\right) = 0 \tag{11-30}$$

then

$$\boldsymbol{F}_N\left(\boldsymbol{C}_N^{(n+1),o}\right) + \boldsymbol{J}_N\left(\boldsymbol{C}_N^{(n+1),o}\right) \cdot \triangle \boldsymbol{C}_N = 0 \tag{11-31}$$

It follows that for a non-singular $\boldsymbol{J}_N$

$$\triangle \boldsymbol{C}_N = \boldsymbol{J}_N^{-1} \cdot \boldsymbol{F}_N \tag{11-32}$$

A closer approximation for $\boldsymbol{C}_N^{(n+1)}$ was given by

$$\boldsymbol{C}_N^{(n+1)} = \boldsymbol{C}_N^{(n+1),o} + \triangle \boldsymbol{C}_N^o \tag{11-33}$$

The algorithm for the calculation of $\boldsymbol{C}_N^{(n+1)}$ given $\boldsymbol{C}_N^{(n)}$ is presented in Figure 11-2 and summarized below:

1. The initial guess for $\boldsymbol{C}_N^{(n+1),o}$ was obtained from the values of the dependent variables at the current time-step, $\boldsymbol{C}_N^{(n)}$.

2. The global function vector $\boldsymbol{F}_N$ and global Jacobian matrix $\boldsymbol{J}_N$ were assembled.

3. Equation (11-32) was solved to yield $\triangle \boldsymbol{C}_N$. This solution was achieved using a LAPACK solver that was based on LU decomposition with partial pivoting and row interchanges.[53,54]

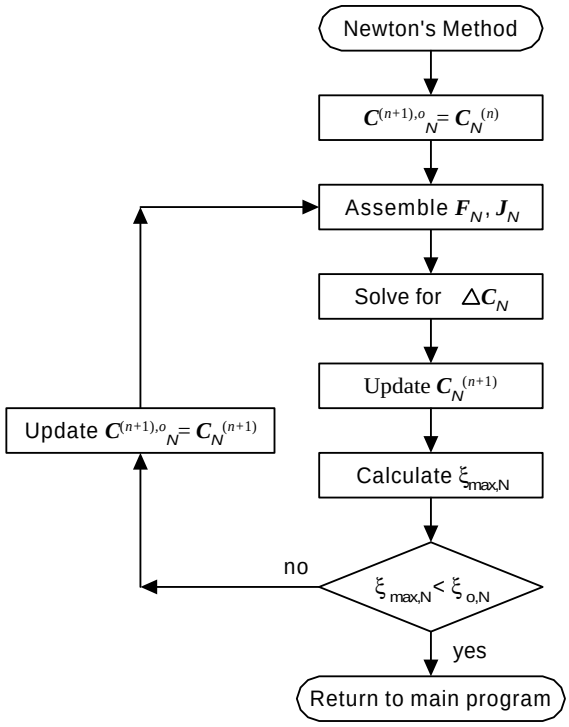

Figure 11-2: Algorithm for Newton's Method used in CADEM.

4. The solution for $\boldsymbol{C}_N^{(n+1)}$ was updated using equation (11-33).

5. The maximum percentage difference $\xi_{max,N}$ between $\boldsymbol{C}_N^{(n+1)}$ and $\boldsymbol{C}_N^{(n+1),o}$ was calculated, where the percentage difference ξ_N was given by

$$\xi_N = 100 \left| \frac{f^{(n+1)} - f^{(n+1),o}}{f^{(n+1),o}} \right| \tag{11-34}$$

where $f^{(n+1)}$ and f^o were corresponding components in $\boldsymbol{C}_N^{(n+1)}$ and $\boldsymbol{C}_N^{(n+1),o}$, respectively.

6. The criterion $\xi_{max,N}$ was compared with a a given convergence criterion $\xi_{o,N}$. If $\xi_{max,N} > \xi_{o,N}$ then the approximate $\boldsymbol{C}_N^{(n+1),o}$ was updated with $\boldsymbol{C}_N^{(n+1)}$ and control returned to Step 2. If $\xi_{max,N} < \xi_{o,N}$ then the procedure was continued.

7. Control was returned to the main program.

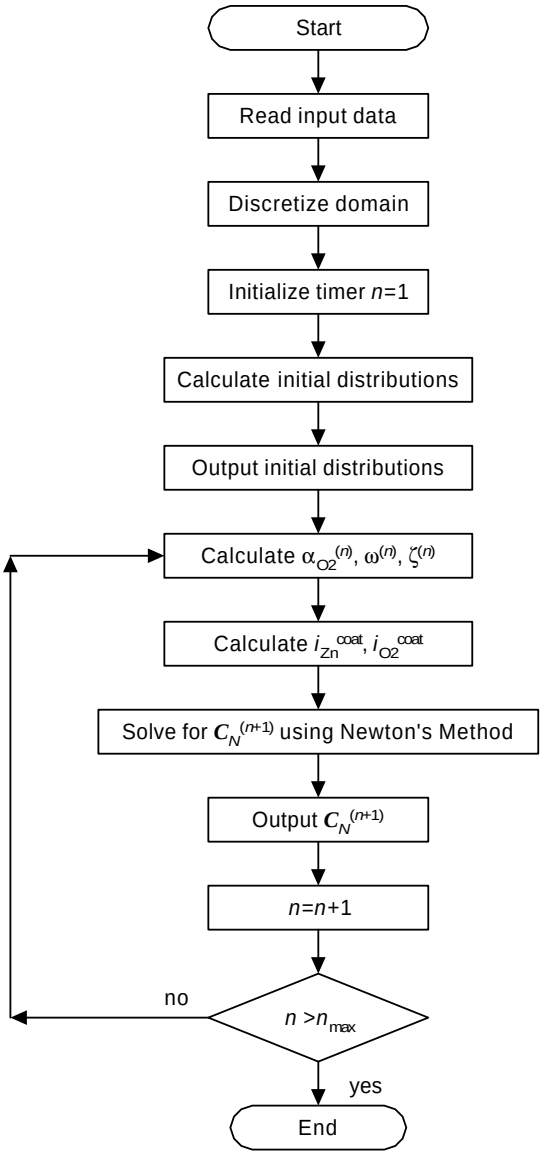

Figure 11-3: The algorithm for the mathematical model CADEM.

11.4 Algorithm for CADEM

A time-stepping algorithm was used to calculate the evolution of the conditions in the delamination zone for a given set of initial conditions. The algorithm for CADEM is presented in Figure 11-3 and summarized below. The program listing for CADEM is given in Appendix D.

1. The data required for the model was input. The concentration parameter data consisted of values for $c_{Na^+,k}$, $c_{Cl^-,k}$, and $c_{OH^-,k}$ where $k = I, II, III, IV, V$.

The fitting parameter data included parameters for ϵ, ω, α_{O_2}, and ζ . The geometry data consisted of the lengths of the delaminated l_{del}, front l_{fro}, semi-intact l_{sem}, and fully-intact regions l_{int}, and the thickness of the gel-medium g_m and coating a_c. The calculation data consisted of the time-step $\triangle t$, the grid spacing $\triangle x$, the simulation time t_{sim}, and the convergence criterion $\xi_{o,N}$.

2. The delamination zone was discretized into nodes using the value of $\triangle x$.

3. The time variable t and counter n were initialized. The counter n corresponded to the current time step and $n+1$ to the time stepped forward in time by $\triangle t$. The number of time steps required n_{max} was also calculated where

$$n_{max} = \frac{t_{sim}}{\triangle t} \tag{11-35}$$

4. The initial distributions for the dependent variables and α_{O_2}, ω, and ζ were calculated. The initial distributions for c_i and ϵ were calculated using the formulated equations given in sections 10.3 and 10.4, respectively. The distributions for α_{O_2}, ω, and ζ were calculated using the formulations given in sections 10.5. The initial distribution for ϕ was calculated using the method described in section 10.6.

5. The initial distributions calculated were output to files.

6. The parameters ω, α_{O_2}, and ζ at the current time were calculated as functions of position in the delamination zone.

7. The current densities $i_{O_2}^{coat}$ and i_{Zn}^{coat} at the current time were calculated as functions of position in the delamination zone.

8. The values of the dependent variables at the time $t^{(n+1)}$ were calculated using Newton's method and returned as $\boldsymbol{C}_N^{(n+1)}$.

9. The calculated values associated with $\boldsymbol{C}_N^{(n+1)}$ were output to files.

10. Increment n by 1.

11. The decision to terminate was determined. If $n \leq n_{max}$ then control was returned to Step 6. If $n > n_{max}$ then the procedure was terminated.

11.5 Summary

The mathematical model CADEM for the propagation of the front along the metal-coating interface of coated zinc during cathodic delamination process was presented. The model accounted for electroneutrality and the mass-transfer of species in the porous delamination zone. The hypothesis that the interfacial porosity of the delamination zone contributed to the propagation of the front was considered by including porosity explicitly as a function of pH. The model was developed to accommodate equilibrium and non-equilibrium relationships between ϵ and pH. The hypothesis that the interfacial polarization kinetics was pH dependent was also included in the development. A time-stepping algorithm was presented that employed Newton's method in the solution of the governing equations at a given time.

CHAPTER 12
CATHODIC DELAMINATION ELECTROCHEMISTRY

The mathematical model CADEM was used to calculate the transient conditions associated with the cathodic delamination system for a given set of initial conditions. The transient conditions included the distributions of the concentrations of the species, the solution potential, the interfacial porosity, and the polarization parameters used in expressions for the interfacial polarization kinetics. The calculated distributions satisfied the coupled phenomena of species mass-transfer and electroneutrality, together with the assumed pH-dependencies of interfacial porosity and interfacial polarization kinetics. Simulated results are presented and discussed in this chapter.

12.1 Model Parameters

The geometry of the delamination zone consisted of a coating thickness $a_c = 45$ μm, a gel-medium thickness $g_m = 5$ μm, and a delamination zone length $l_{delz} = 4.0$ cm. The delamination zone length was divided into lengths at the initial time. These lengths included $l_{del} = 0.1$ cm, $l_{fro} = 0.025$ cm, $l_{sem} = 0.025$ cm, and $l_{int} = 0.25$ cm for the delaminated, front, semi-intact, and fully-intact regions, respectively.

The initial distributions for the concentrations of species were calculated using the concentration parameter data given in Table 12.1. This data included values for the concentrations $c_{Na^+,k}$, $c_{Cl^-,k}$, and $c_{OH^-,k}$ at specific position indicated by the subscript k where $k = I, II, III, IV, IV$. The initial distribution for the interfacial porosity was calculated using fitting parameter data given in Table 12.2. The initial distributions for the polarization parameters α_{O_2}, ω, and ζ were calculated using

Table 12.1: Concentration parameter data for cathodic delamination simulation.

k	$c_{Na^+,k}$ (M)	$c_{Cl^-,k}$ (M)	$c_{OH^-,k}$ (M)
I	0.01	1×10^{-3}	0.01
II	0.001	1×10^{-4}	0.001
III	1×10^{-5}	1×10^{-6}	1×10^{-5}
IV	1×10^{-7}	1×10^{-7}	5×10^{-6}
V	1×10^{-7}	1×10^{-7}	5×10^{-6}

Table 12.2: Fitting parameter data for cathodic delamination simulation.

k	$b_{\epsilon,k}$	$b_{\alpha,k}$	$b_{\omega,k}$	$b_{\zeta,k}$
1	0.0054	1	0.02	9×10^{-12}
2	-5.0	100	-6	-4
3	10.5	11	11.5	10.5
4	0.0045	1	0.01	9×10^{-11}
5	-4.1	24	-4	-7
6	11.4	10	11.1	10.5
7	0.001	0.0001	0.0001	1×10^{-12}
8	-	1×10^{-6}	-	-

fitting parameters given in in Table 12.2. The concentration of dissolved oxygen at the surface of the coating was 1.26×10^{-3} M and corresponded to saturated water at 25^{o}C and 1 atm.[12]

The calculation data for the numerical method included the grid size $\triangle x = 10$ μm , the time step $\triangle t = 0.1$ s, the convergence criterion $\xi_{o,N} = 0.001$, and the simulation time $t_{sim} = 30$ min. The potential of the metal was chosen as $\Psi = -0.955$ V_{SCE}. The values of the parameters used in the polarization expressions for zinc dissolution were $\beta_{Zn} = 0.04$ $V/decade$, $i_{o,Zn} = 0.2$ A/cm^2, and $E^o_{Zn} = -0.763$ V_{SHE}.[85] The values for D_i are given in Table 5.1 and were obtained from TECTRAN.[55] The value of $D_{O_2} = 1.9 \times 10^{-5}$ cm^{2}s^{-1} was used and corresponded to the diffusion coefficient in saturated water at a partial pressure of one atmosphere.[12]

The ϵ-pH relationship was considered at equilibrium and at non-equilibrium conditions as discussed in section 11.2.3. Numerous simulations were performed using CADEM and the results for one simulation where the ϵ-pH relationship was assumed to be in equilibrium are presented in section 12.3. This simulation was

designated Simulation A. The influence of the non-equilibrium ϵ-pH relationship was investigated by comparing the simulated results for two non-equilibrium simulations with that of Simulation A. The non-equilibrium simulations included k_{neq} values of 0.01 and 0.001 and were designated Simulations B and C, respectively. The comparison of the simulated results for Simulations A, B, and C are presented in section 12.4. Non-equilibrium simulations were also performed for k_{neq} values of 0.1 and 0.005. The results for the equilibrium and non-equilibrium porosity-pH relationships were used to demonstrate the influence of the bond-breakage phenomena associated with the cathodic delamination process.

12.2 Initial Conditions

The input data were used to calculate the initial distributions for c_i , ϵ, and the polarization parameters ω, α_{O_2}, and ζ. These initial distributions were used to calculate the initial distribution for Φ using the method described in section 10.6.

12.2.1 Concentrations

The concentration parameters given in Table 12.1 were used to calculate the initial distributions for c_i that are shown in Figure 12-1. The procedure for the construction of these distributions was given in section 10.3. The values of c_{Na^+}, c_{Cl^-}, and c_{OH^-} decreased with position monotonically in the delaminated, front, and semi-intact regions. The variations with position for these concentrations were linear in the delaminated region and exponential in the front and semi-intact regions. In the fully-intact region, the values of c_{Na^+}, c_{Cl^-}, and c_{OH^-} reached asymptotic values. The lowest pH of 8.7 was in the fully-intact region. The values for c_{Na^+} and c_{OH^-} were assumed to be equated at any position in the delaminated and front regions at the initial time. The distribution for $c_{Zn^{+2}}$ satisfied electroneutrality at a given position.

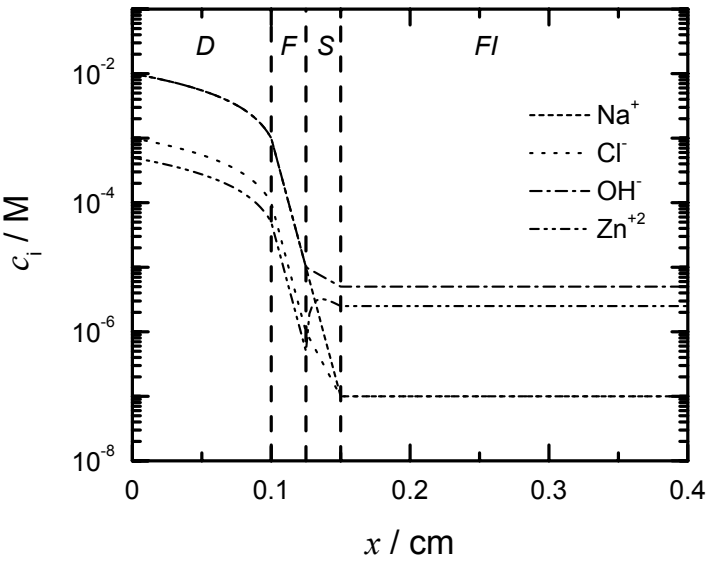

Figure 12-1: The initial distributions of concentrations along the metal-coating interface. The dashed lines separate the delamination zone into the delaminated region D, the front region F, the semi-intact region S and the fully-intact region FI.In the delaminated and front regions the distributions of the sodium and hydroxide ions superimposed.

12.2.2 Porosity-pH

The procedure for the construction of the initial distribution for ϵ was given in section 10.4. The fitting parameters for the ϵ-pH relationship are given in Table 12.2 and were used in equation (10-21) to construct the equilibrium ϵ-pH relationship. The value of the equilibrium ϵ is shown in Figure 12-2 as a function of pH. The value of the equilibrium ϵ is shown in Figure 12-2 as a function of position at $t = 0$, the initial ϵ distribution. There was a slight linear decrease in porosity with position in the delaminated region. There were large non-linear decreases with position for ϵ in the front and semi-intact regions. The porosity in the fully-intact region was uniform.

12.2.3 Polarization-pH parameters

The fitting parameters for the ω-pH, α_{O_2}-pH, and ζ-pH relationships are given in Table 12.2. The procedures given in section 10.5 were used to construct the

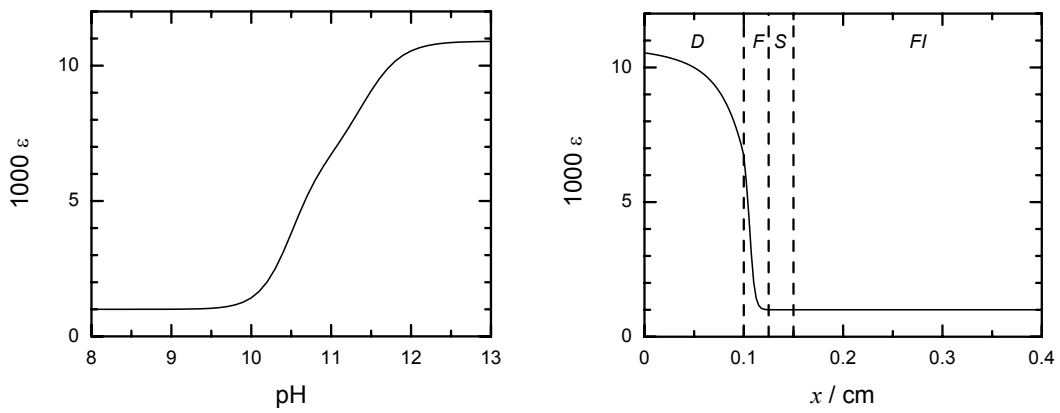

(a) (b)

Figure 12-2: Calculated values of the interfacial porosity (a) as a function of pH and (b) as a function of position along the metal-coating interface at the initial time. The dashed lines separate the delamination zone into the delaminated region *D*, the front region *F*, the semi-intact region *S* and the fully-intact region *FI*.

distributions of ω,α_{O_2}, and ζ as functions of pH that are shown in Figures 12-3(a), 12-4(a), and 12-5(a), respectively. The initial distributions for ω, α_{O_2}, and ζ are shown in Figures 12-3(b), 12-4(b), and 12-5(b).

The polarization parameters α_{O_2}, ω, and ζ were used to calculate the current densities of the zinc dissolution and oxygen reduction electrochemical reactions at the metal-coating interface. The expressions presented for α_{O_2}, ω, and ζ were used together with the current density equations, equations (10-9) and (10-12), to yield polarization plots of the metal-coating interface as functions of pH. These plots are shown in Figure 12-6. A given plot was described using the corrosion potential value V_{corr} and the value for $i^{\text{coat}}_{\text{lim},O_2}$.

The pH values of 8.7 and 9 corresponded to positions in the fully-intact and semi-intact regions, respectively. The value of ω was unchanged over the pH range 8.7 to 9 as seen in Figure 12-3(a). Similarly the values of α_{O_2} and ζ were unchanged for the pH range 8.7 to 9 (see Figures 12-4(a) and 12-5(a)). Therefore there was not much difference in the polarization kinetics for the pH values of 8.7 and 9

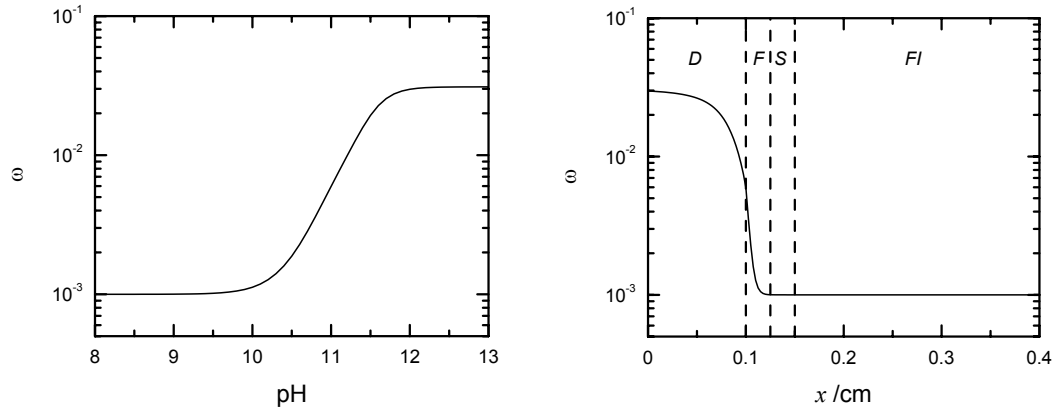

(a) (b)

Figure 12-3: Calculated value for surface area polarization parameter (a) as a function of pH and (b) as a function of position along the metal-coating interface at the initial time. The dashed lines separate the delamination zone into the delaminated region *D*, the front region *F*, the semi-intact region *S* and the fully-intact region *FI*.

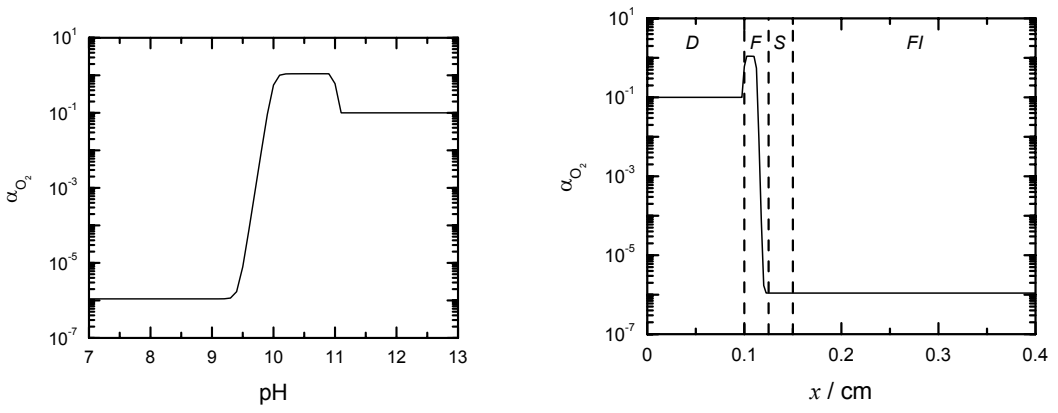

(a) (b)

Figure 12-4: Calculated value of the blocking polarization parameter (a) as a function of pH and (b) as a function of position along the metal-coating interface at the initial time. The dashed lines separate the delamination zone into the delaminated region *D*, the front region *F*, the semi-intact region *S* and the fully-intact region *FI*.

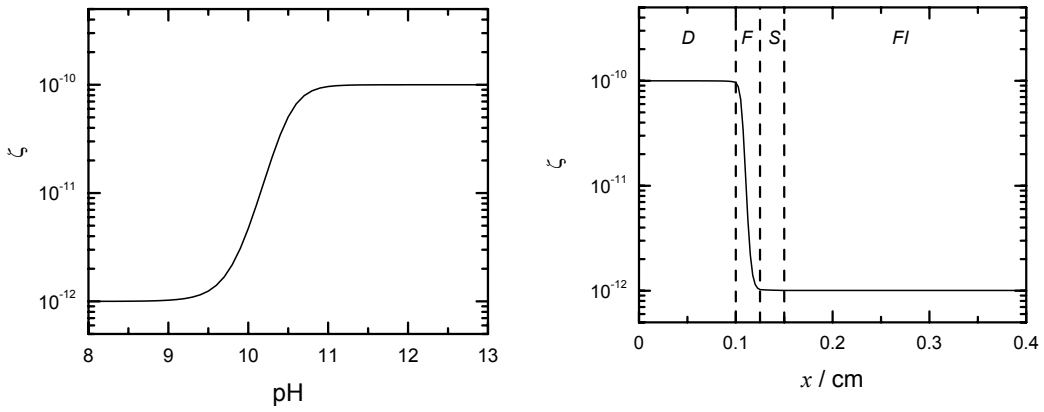

(a) (b)

Figure 12-5: Calculated value of the poisoning polarization parameter for zinc dissolution (a) as a function of pH and (b) as a function of position along the metal-coating interface at the initial time.The dashed lines separate the delamination zone into the delaminated region *D*, the front region *F*, the semi-intact region *S* and the fully-intact region *FI*.

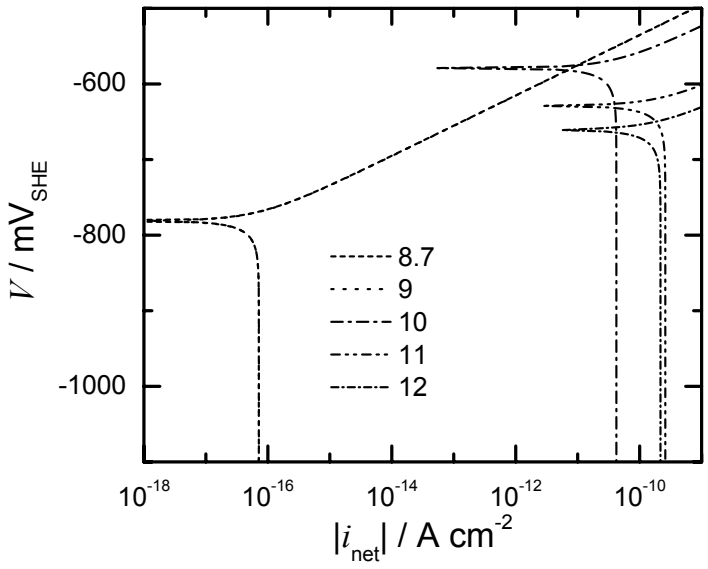

Figure 12-6: Interfacial potential as a function of absolute net current density with local pH as a parameter. The distributions associated with the pH values of 8.7 and 9 superimposed.

as seen in Figure 12-6 where the distributions associated with these pH values superimposed. In these regions there was very little electrochemical activity as the oxygen reduction reaction was limited by the poisoned zinc dissolution reaction.

The values for V_{corr} and i^{coat}_{lim,O_2} were larger for a pH of 10 as compared to a pH of 9. A pH of 10 corresponded to a position in the front region where oxygen reduction was not limited by zinc dissolution. There was a large increase in the value of α_{O_2} over the pH range 9 to 10, as seen in Figure 12-4(a) and this accounted for the increase in i^{coat}_{lim,O_2} seen in Figure 12-6. The zinc dissolution reaction was considered to be inhibited in the front region over the pH range 9 to 10 and there was little change in the value of ζ as seen in Figure 12-5(a). The larger value for i^{coat}_{lim,O_2} at pH 10 required a more positive V_{corr} as seen in Figure 12-6.

The pH range 10 to 11 corresponded to a pH range across the front region. The polarization plots for pH values of 10 and 11 were such that V_{corr} was more negative and i^{coat}_{lim,O_2} increased as the pH went from 10 to 11. The value of ζ increased as a function of pH for the range of 10 to 11, see Figure 12-5(a). This increase represented the reduction in the poisoning of zinc dissolution in the front region. Therefore, a more negative corrosion potential was required for the pH of 11 as compared to that of 10. The increase in i^{coat}_{lim,O_2} was due to the increase in ω as a function of pH over the pH range 10 to 11.

The values of V_{corr} and i^{coat}_{lim,O_2} were more negative and smaller, respectively, for pH 12 as compared to pH 11. The pH change of 11 to 12 represented the change in position from the front region to the delaminated region. The blocking parameter α_{O_2} was assumed to be smaller in the delaminated region as compared to the front region. This facilitated the assumption that in the delaminated region there would be deposits whereas in the front region there would be an absence of deposits. The reduction in the value of α_{O_2} for the pH going from 11 to 12 as seen in Figure

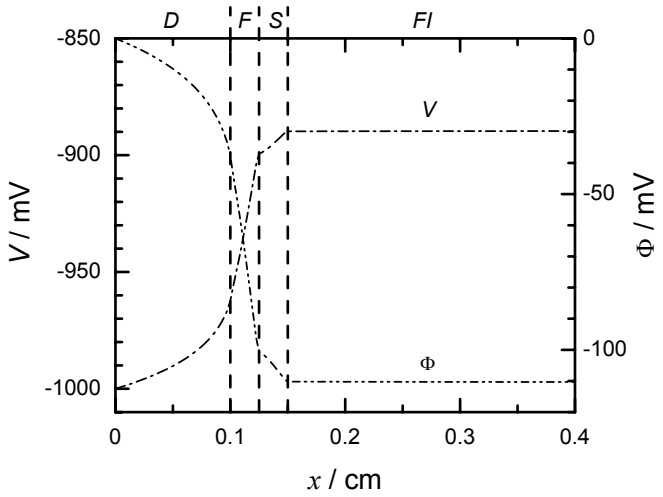

Figure 12-7: The initial distributions of the solution potential and the interfacial potential along the metal-coating interface. The dashed lines separate the delamination zone into the delaminated region *D*, the front region *F*, the semi-intact region *S* and the fully-intact region *FI*.

12-4(a) translated into the reduction of $i^{\text{coat}}_{\text{lim},O_2}$ as seen in Figure 12-6. This reduction in α_{O_2} resulted in the more negative V_{corr} required for a net zero current.

12.2.4 Potential

The calculated initial distribution for Φ is shown in Figure 12-7. Also shown in this figure is the distribution for the interfacial potential at the metal-coating interface V where $V = \Psi - \Phi$. The interfacial potential V was used in the presentation and discussion of the simulations. The value of V and the gradient of V increased non-linearly with position in the delaminated region. In the front region, the value of V increased with position and the gradient of V was approximately constant. The value of V increased with position in the semi-intact region and the gradient of V decreased with position. The value of V was constant in the fully-intact region.

12.3 Equilibrium Porosity-pH

The results for a simulation obtained using CADEM are presented in this section when the ϵ-pH relationship was in equilibrium.

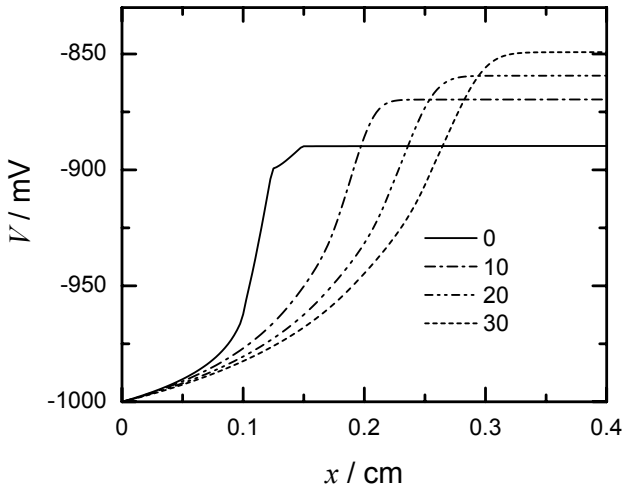

Figure 12-8: Calculated distributions of the interfacial potential along the metal-coating interface with elapsed time in minutes as a parameter.

12.3.1 Potential Distribution

The experimental interfacial potential results reported by Furbeth and Stratmann[10] were discussed in section 9.2.3. The simulated results for V were compared qualitatively with these experimental results using the three features associated with the experimental interfacial potential results. These features included the approximately constant gradient of V in the delaminated and front regions, the formation of distinct regions, and the approximately constant value of V in the fully-intact region.

The distributions calculated for the interfacial potential V are shown in Figure 12-8 with elapsed time as a parameter. The feature of distinct regions was not maintained as the delaminated/front boundary became less distinct with elapsed time. The position of 0.05 cm was located in the delaminated region at $t = 0$ and throughout the 30 min simulation. The gradient of V at this position reduced with time which indicated that the gradient of V in the delaminated region was not approximately constant with time. For a given distribution, the position at which the gradient of V was the largest was located in the front region. As seen in Figure 12-8, the gradient of V in the front region reduced with time.

The shape of the distribution of V was maintained approximately throughout the simulation with the gradients of V being reduced slightly in the delaminated and front regions over the course of the simulation. This result was consistent with experimental observations reported by Furbeth and Stratmann.[10] The maintenance of the shape indicated that the phenomena considered in the model could sustain the profile of V while the delamination front propagated along the metal-coating interface.

The current density in the fully-intact region was several orders of magnitude less than in the other regions. This enabled the fully-intact region to be part of the system but to contribute negligibly to the current requirements of the system. The cathodic delamination system included the defect and delamination zones. The current density of the cathodic oxygen reduction in the delamination zone was balanced by the anodic zinc dissolution in the defect zone. A galvanic couple was formed between the zones. The model was developed for the delamination zone with the assumption that the conditions for the dependent variables be fixed at the defect-delamination zone boundary. For the results presented in Figure 12-8, there was a 40 mV increase over the 30 min simulation in the fully-intact region. This increase was attributed to the fixed conditions at the defect/delamination zone boundary.

Following the approach of Leng and Stratmann the V-distributions were differentiated with respect to position to yield distributions of dV/dx as shown in Figure 12-9 with elapsed time as a parameter.[6] The position x_{del} of the peak of a dV/dx distribution represented the point of inflexion for the V distribution and was located in the front region. The value of x_{del} increased with time indicating that the front propagated along the metal-coating interface. The rate of this propagation was approximately 2.4 mm/hr. The rate of propagation for the experi-

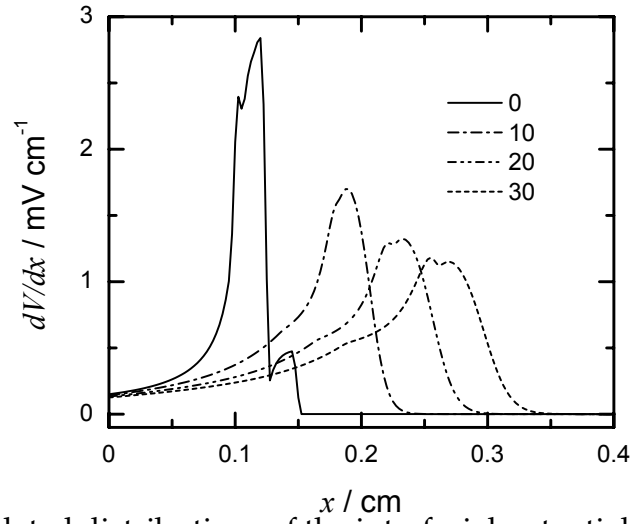

Figure 12-9: Calculated distributions of the interfacial potential gradient along the metal-coating interface with elapsed time in minutes as a parameter.

mental results reported by Furbeth and Stratmann was on the order of mm/hr.[10] These experiments were conducted using poor coatings, *i.e.,* coatings which were highly permeable to oxygen transport. The similarity between the simulated and experimental rate of propagation demonstrated that the hypotheses that the interfacial porosity and polarization kinetics were pH dependent contributed to the propagation of the front along the metal-coating interface.

The peak height corresponded to the value of dV/dx at the peak position x_{del} and decreased with time for the simulated results. The trend of decreasing peak height with time was consistent with the experimental results reported for the cathodic delamination of coated iron.[6] The explanation given by Leng and Stratmann to account for this trend was that, with time, there was a more gradual change in the conditions across the front and semi-intact regions.[6] The simulated results presented below supported this explanation. The coupling of mass-transfer and electroneutrality with the pH-dependent interfacial porosity and pH-dependent interfacial polarization kinetics resulted in the reduction of the differences of the dependent variables c_i , Φ, and ϵ between the delaminated and fully-

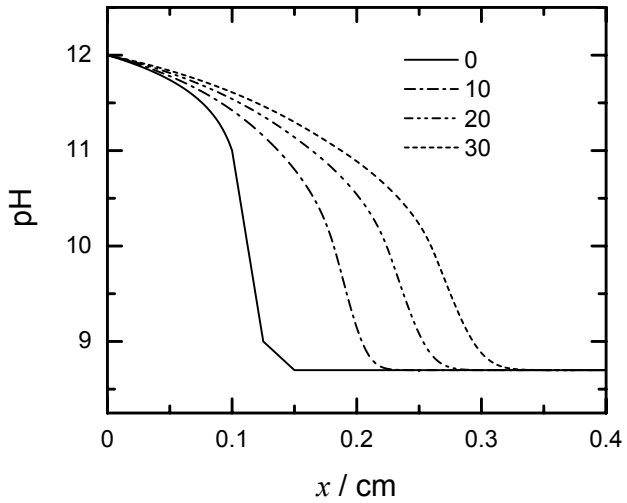

Figure 12-10: Calculated distributions of pH along the metal-coating interface with elapsed time in minutes as a parameter.

intact regions. The width of the dV/dx distribution increased with time as seen in Figure 12-9. This result was not consistent with the experimental results on iron.[6]

12.3.2 Concentration Distributions

The simulated concentration distributions are presented in this section. The initial distributions for c_i were discussed in section 12.2.1. The different regions for the distributions of c_i were distinct at $t = 0$ but as time elapsed only the fully-intact region was distinct. The front region was identified by a position such that the gradient of c_i was the most negative.

The distribution for pH is shown in Figure 12-10 with elapsed time as a parameter. The initial pH distribution included a non-linear decrease with position for the delaminated region and a linear decrease with position in the front and semi-intact regions. The pH in the fully-intact region was a constant value. There were three trends associated with the pH distributions shown in Figure 12-10. A trend that the general shape of the pH distribution was maintained throughout the simulation. A trend that the pH at any position in the delaminated, front, and semi-intact regions increased with time and the pH in the fully-intact region re-

mained unchanged. A trend that the change in pH per unit time was the largest for the positions in the semi-intact region immediately adjacent to the fully-intact region.

The calculated distributions for c_{Na^+} and c_{Cl^-} are shown in Figure 12-11 with elapsed time as a parameter. The trends associated with the c_{Na^+} distributions were consistent with the trends seen in the pH distributions. The trends associated with the distributions of c_{Cl^-} were similar to the trends seen in the pH distributions. A feature of the c_{Cl^-} distributions was that the value of c_{Cl^-} slightly decreased with position for part of the semi-intact region and then slightly increased with position. This feature was attributed to the production of OH^- ions by oxygen reduction in the semi-intact region.

The calculated distribution for $c_{Zn^{+2}}$ is shown in Figure 12-12 with elapsed time as a parameter. Over the first 10 min of simulation, the distribution for $c_{Zn^{+2}}$ changed greatly. The shape of the distribution was maintained for the remainder of the simulation. In the semi-intact region the value of $c_{Zn^{+2}}$ increased with position for part of the region and decreased with position for the other part of the region. This was attributed to the production of Zn^{+2} ions in the semi-intact region. During the course of the simulation the change of $c_{Zn^{+2}}$ with position across the delaminated, front, and semi-intact regions became more gradual as the front propagated into the fully-intact region as was seen for c_{Na^+} , c_{Cl^-}, and c_{OH^-}.

12.3.3 Flux Distributions

The increase in pH at any position in the delaminated, front, and semi-intact regions was attributed to the electrochemical production of OH^- and the flux of OH^- into the delamination zone. The production of OH^- by oxygen reduction along the metal-coating interface can be seen in the distribution of the absolute value of $i_{O_2}^{coat}$ along the metal-coating interface. The absolute value of $i_{O_2}^{coat}$ as a

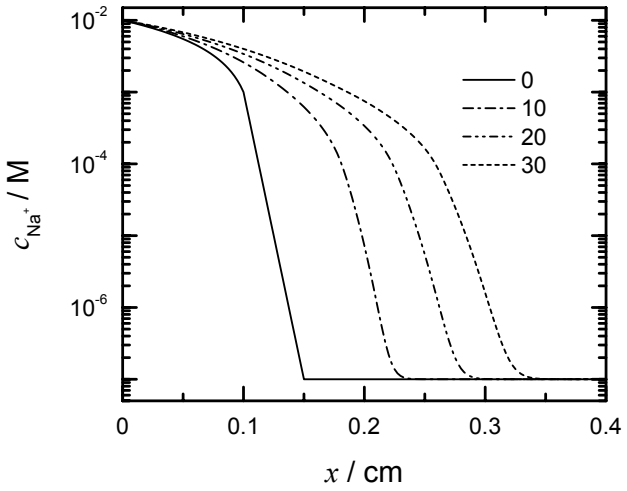

(a)

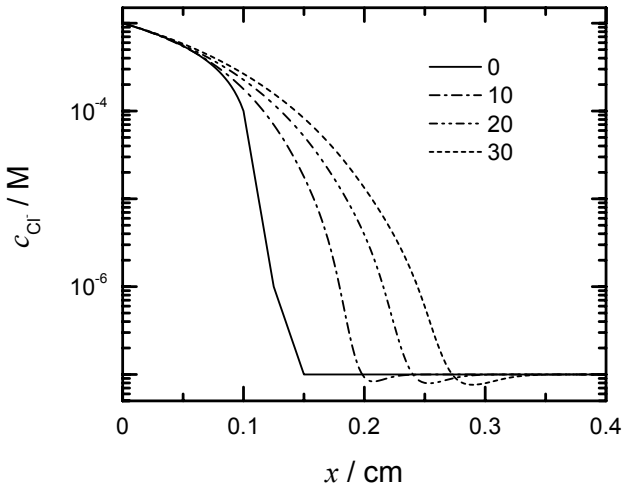

(b)

Figure 12-11: Calculated distributions of concentrations along the metal-coating interface with elapsed time in minutes as a parameter. (a) sodium ion and (b) chloride ion.

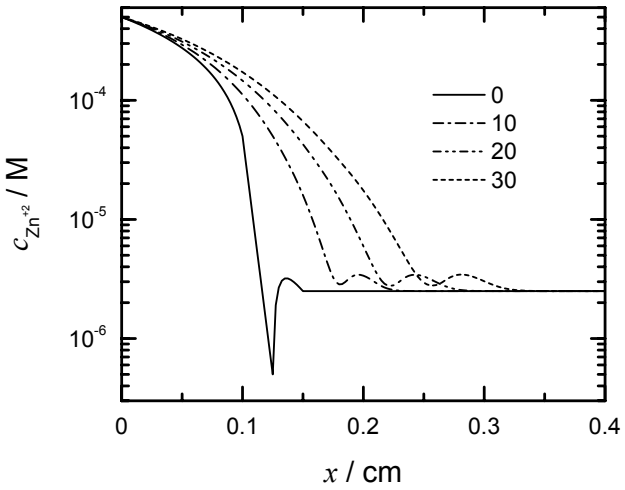

Figure 12-12: Calculated distributions of the zinc ion concentration along the metal-coating interface with elapsed time in minutes as a parameter.

function of position is shown in Figure 12-13. There was an increase in the electrochemical reactivity at the metal-coating interface as the delamination front propagated into the fully-intact region. The distribution of N_{OH^-} is shown in Figure 12-14 with elapsed time as a parameter. The distribution for $t = 0$ was not smooth over positions ranging from 0.075 to 0.125 cm. This distribution corresponded to the initial conditions of c_i , ϵ, and polarization kinetics imposed on the system. The distribution for N_{OH^-} became smooth within a couple of time steps and remained smooth during the remainder of the 30 min simulation. This demonstrated that the model was not sensitive to the initial conditions used. For a given distribution, except that associated with $t = 0$, the value of N_{OH^-} decreased with position in the front and semi-intact regions. The value of N_{OH^-} was approximately 10^{-18} mols^{-1}cm^{-2} for positions in the fully-intact region. The value of N_{OH^-} for a position in the delaminated region decreased with time and for positions in the front and semi-intact region N_{OH^-} increased slightly with time.

The increase in the concentration of the negatively charged OH^- specie at any position in the delaminated, front, and semi-intact regions required the increase in the concentration of a positively charged specie to maintain electroneutrality. The

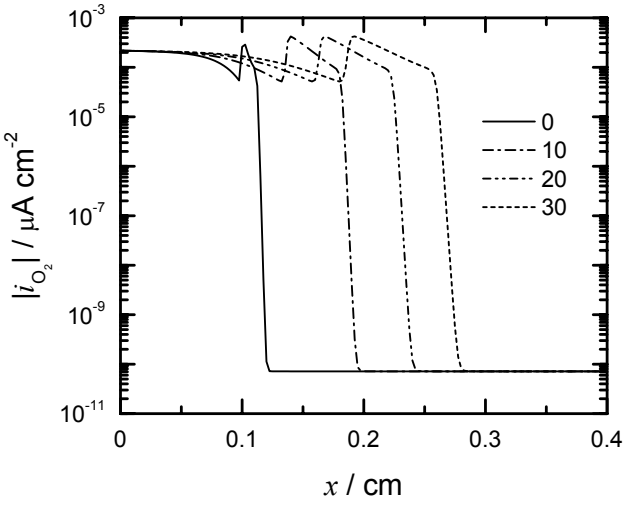

Figure 12-13: Calculated distribution of the oxygen reduction current density along the metal-coating interface with elapsed time in minutes as a parameter.

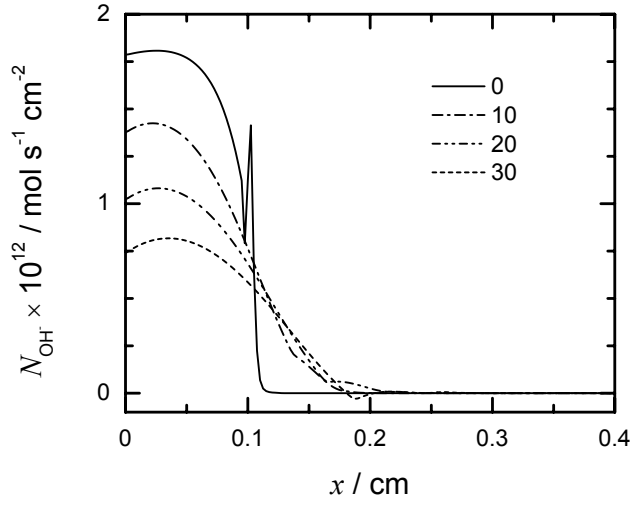

Figure 12-14: Calculated distribution of the hydroxide ion flux along the metal-coating interface with elapsed time in minutes as a parameter.

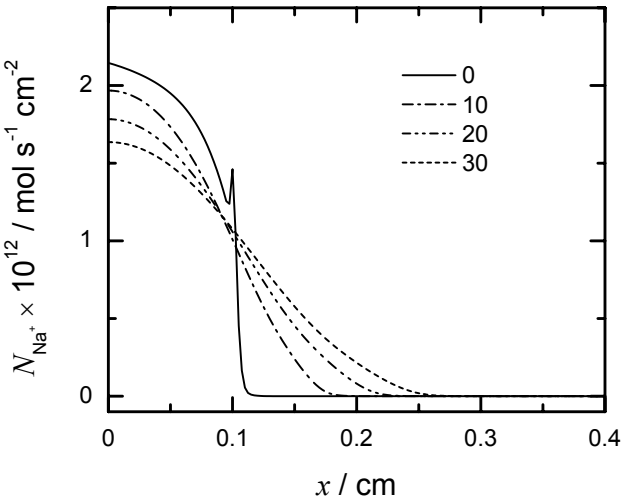

Figure 12-15: Calculated distribution of the sodium ion flux along the metal-coating interface with elapsed time in minutes as a parameter.

zinc dissolution reaction was poisoned at the metal-coating interface. Therefore, to satisfy electroneutrality a net flux of Na^+ into the delamination zone was needed. The flux of Na^+ included the migration of Na^+ facilitated by the positive electric field dV/dx and the diffusion of Na^+ due to the negative concentration gradient of Na^+ in the delamination zone. The increases in the values of c_{Na^+} and c_{OH^-} per unit time, that were seen in Figures 12-11(a) and 12-10, were approximately equal at any given position in the delaminated, front, or semi-intact regions.

The distribution of the flux of Na^+ is shown in Figure 12-15 with elapsed time as a parameter. A positive value for Na^+ indicated a net transport of Na^+ into the delamination zone. The initial distribution for N_{Na^+} was not smooth similar to the initial distribution for N_{OH^-} . This was attributed to the assumed initial conditions. For a given distribution, except at $t = 0$, the value of N_{Na^+} decreased with position and approached a value on the order of 10^{-18} mols^{-1}cm^{-2} as the fully-intact region was approached.

Although the delaminated/front boundary was not clearly identifiable in the distributions of V it was observed that the value of N_{Na^+} at any position less than

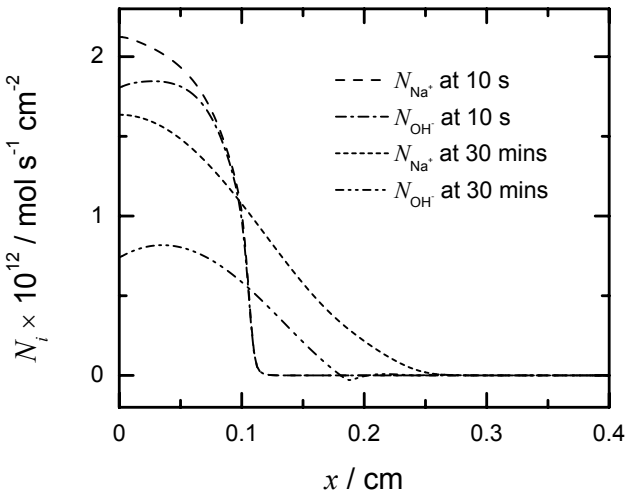

Figure 12-16: Calculated distribution of the sodium ion and hydroxide ion fluxes along the metal-coating interface with elapsed time as a parameter.

0.1 cm decreased with time. Thus the value of N_{Na^+} in the delaminated region reduced with time. The value of N_{Na^+} at any position in the front and semi-intact regions increased with time. The simulated N_{Na^+} distributions in the front and semi-intact regions indicated that the mass-transfer of the positively charged Na^+ specie into these regions was increasing. This increase was required to balance the electrochemical production of the negatively charged OH^- specie in the front and semi-intact regions and to provide transport of Na^+ into the fully-intact region where c_{Na^+} was very small.

The values of N_{Na^+} and N_{OH^-} as functions of position are shown in Figure 12-16 at two values of elapsed times, $t = 10$ s and $t = 30$ min . The distributions for both N_{Na^+} and N_{OH^-} were smooth at $t = 10$ s. At this time the value of N_{Na^+} was greater than N_{OH^-} for positions less than 0.1 cm. The values of N_{Na^+} and N_{OH^-} were approximately equal for positions greater than 0.1 cm . The values of N_{Na^+} and N_{OH^-} at $t = 10$ s were approximately 10^{-18} mol/(s.cm^2) for positions greater than 0.12 cm. During the 30 min simulation the values of N_{Na^+} and N_{OH^-} changed as discussed. For a given position less than 0.125 cm , the value of N_{OH^-} decreased more than the value value of N_{Na^+} . For a given position greater than 0.125 cm

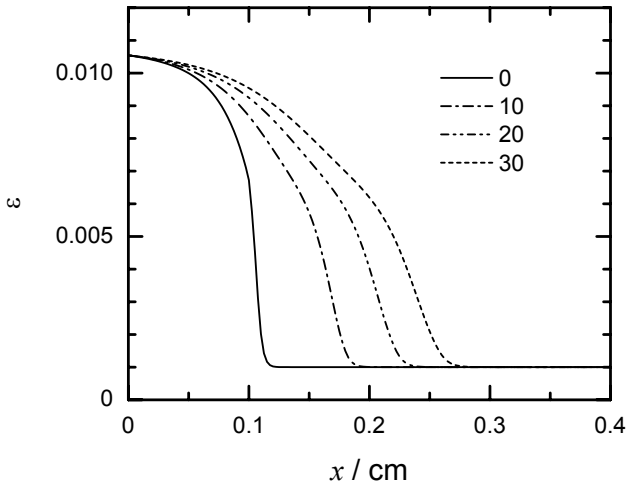

Figure 12-17: Calculated distribution of interfacial porosity along the metal-coating interface with elapsed time in minutes as a parameter.

and less than 0.26 cm, the value of N_{Na^+} increased more than the value value of N_{OH^-}. This difference demonstrated that there was a net flux of positive ions into the delamination zone.

12.3.4 Interfacial Porosity

The calculated distribution for ϵ is shown in Figure 12-17 with elapsed time as a parameter. The initial ϵ-distribution was discussed in section 12.2.2. The shape of the interfacial porosity distribution was maintained throughout the simulation. As the delamination front propagated into the fully-intact region, the porosity increased to satisfy the equilibrium ϵ-pH relationship. The increase in the value of ϵ with time at any position in the front and semi-intact regions was reflected in large changes in the flux of species in these regions. This was seen in the distributions of N_{Na^+} and N_{OH^-} shown in Figures 12-15 and 12-14, respectively.

The calculated distribution of the interfacial porosity gradient along the metal-coating interface is shown in Figure 12-18 with elapsed time in minutes as a parameter. The peak associated with a given distribution corresponded to the front of the interfacial porosity. The velocity of the interfacial porosity front can be asso-

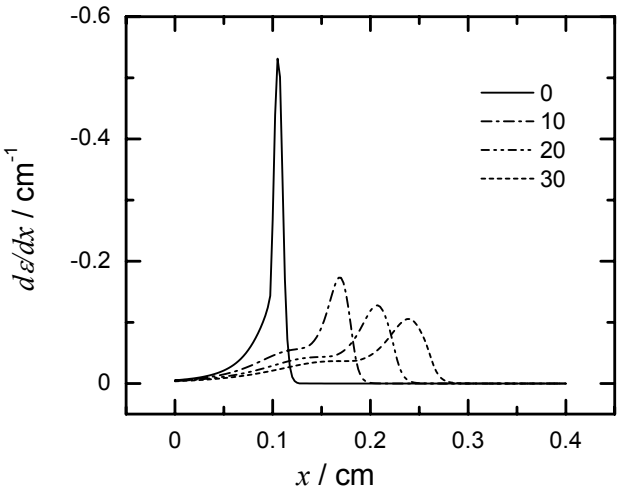

Figure 12-18: Calculated distribution of the interfacial porosity gradient along the metal-coating interface with elapsed time in minutes as a parameter.

ciated with the degradation of the coating and the breakage of the adhesive bonds between the metal and the coating. Thus, the velocity of the interfacial porosity front represents the true delamination rate. For the condition where the interfacial porosity was assumed to be in equilibrium with the local pH, the velocities of the interfacial porosity and interfacial potential fronts were approximately equal. The results associated with the condition where the interfacial porosity and local pH were not at equilibrium is presented in the following section.

12.3.5 Polarization Kinetics

The polarization parameters α_{O_2}, ω, and ζ were assumed to be pH-dependent and expressions for these dependencies were assumed and discussed in section 12.2.3. The distributions for α_{O_2}, ω, and ζ are shown in Figure 12-19 with elapsed time as a parameter. The shape of the distribution for a given parameter was maintained throughout the simulation. This maintenance was attributed to the shape of the pH-distribution being maintained throughout the simulation. The delaminated region, front and semi-intact regions, and fully-intact region were identified in the distributions for α_{O_2}. The delaminated region and front and semi-intact regions grew in length with time. The fully-intact region decreased in length

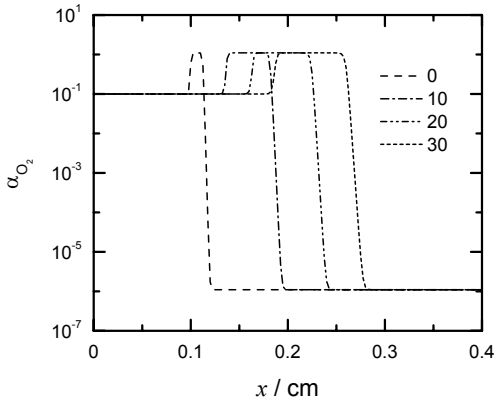

(a)

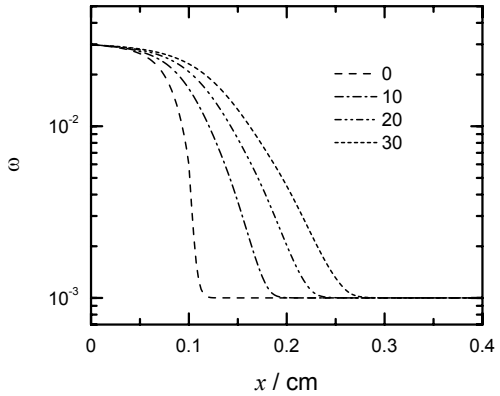

(b)

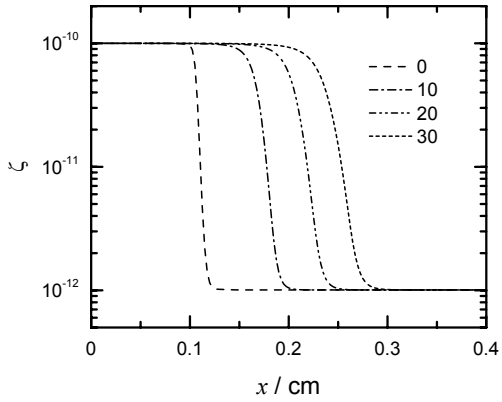

(c)

Figure 12-19: Calculated distributions of polarization parameters along the metal-coating interface with elapsed time as a parameter. (a) blocking parameter, (b) surface coverage parameter, and (c) poisoning parameter.

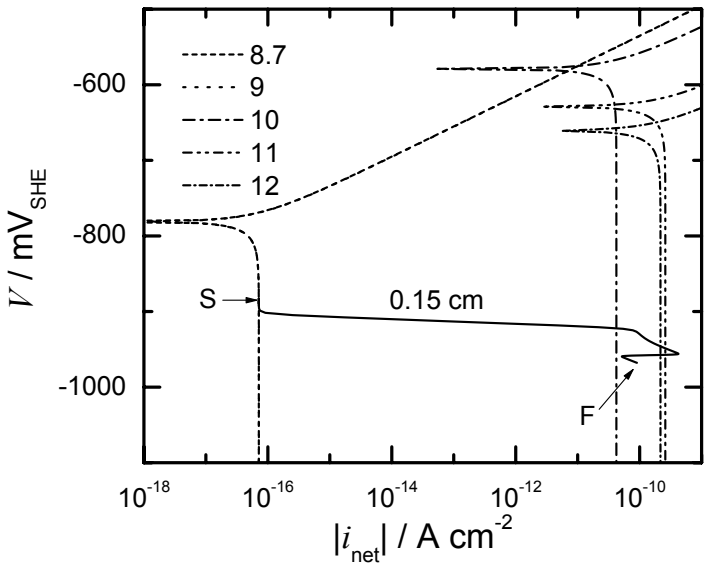

Figure 12-20: Interfacial potential as a function of absolute net current density for the 0.15 cm position. The interfacial potential as a function of pH is included for given pH values. The distributions associated with the pH values of 8.7 and 9 superimposed.

with time as the delamination front propagated into this region.

Polarization parameters were used to describe the polarization kinetics of the metal-coating interface. The interfacial polarization kinetics as a function of pH was shown in Figure 12-6 and discussed in section 12.2.3. The polarization kinetics for the position of 0.15 cm is shown in Figure 12-20 during the 30 min simulation. The 0.15 cm position was located in the fully-intact region at time $t = 0$ with a pH of 8.7 (see Figure 12-10) and an interfacial potential V of approximately -890 mV (see Figure 12-8). This condition is indicated by S in Figure 12-20. After a simulation time of 30 min the position 0.15 cm had the conditions of pH 11.5 and $V = -970$ mV. These conditions are indicated by F in Figure 12-20. The line that connects S to F represents the value of the interfacial potential as a function of the absolute net current density during the 30 min simulation for the 0.15 cm position. This line traverses the family of polarization curves demonstrating that the

polarization kinetics associated with the 0.15 cm position depended on the local pH at the given time.

12.3.6 Oxygen Reduction and Ionic Current Densities

The distribution of $i_{O_2}^{coat}$ is shown in Figure 12-13 with elapsed time as a parameter. The shape of the initial distribution consisted of an approximately constant value in the delaminated region, a value that increased with position in the front region, a value that decreased with position in the semi-intact region, and a constant value in the fully-intact region. The shape of the distribution was maintained throughout the simulation.

Similar to the distributions of α_{O_2} , the delaminated region, front and semi-intact regions, and fully-intact region were identified in the distributions of $i_{O_2}^{coat}$. From these distributions it was observed that the delamination process propagated into the fully-intact region. The increase in lengths of the front and semi-intact regions that was seen in the distributions of α_{O_2} (see Figure 12-19(a)) was also seen in the distributions for $i_{O_2}^{coat}$ because $i_{O_2}^{coat}$ was a function of α_{O_2}.

The ionic current density $\boldsymbol{i}$ represented the current density carried by the charged species in the gel-medium of the delamination zone. The distribution of $\boldsymbol{i}$ along the metal-coating interface is shown in Figure 12-21 with elapsed time as a parameter. The value of $\boldsymbol{i}$ was positive throughout the delamination zone and decreased with position. In the fully-intact region the value of the ionic current density approximated a zero value as the current requirement of the fully-intact region was approximately equal to a zero value. The positive value of $\boldsymbol{i}$ indicated that current was flowing into the delamination zone. This was necessary to balance the negative $i_{O_2}^{coat}$ on the metal-coating interface. The increase in the value of $\boldsymbol{i}$ with time at a given position in the delamination zone was attributed to the increase in $i_{O_2}^{coat}$ with time.

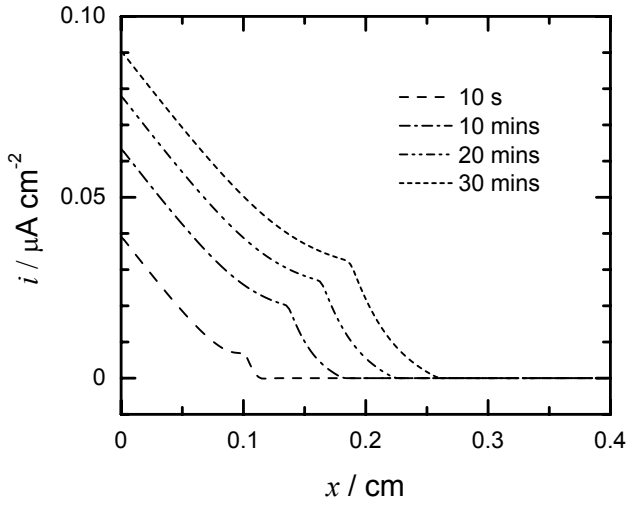

Figure 12-21: Calculated distributions of ionic current density along metal-coating interface with elapsed time as a parameter.

12.4 Non-Equilibrium Porosity-pH

The pH-dependent interfacial porosity represented a novel approach at implicitly accounting for the breakage of adhesive bonds between the coating and the metal. The use of the equilibrium ϵ-pH relationship was under the assumption that the time constants involved in the breakage of the adhesive bonds were sufficiently small such that the local porosity and local pH were at equilibrium at any given time. For the condition where the time constants for bond breakage are large, a non-equilibrium ϵ-pH relationship would be appropriate. The influence of the non-equilibrium ϵ-pH relationship on the transient conditions of the cathodic delamination system is presented in this section. The parameters for these simulations were given before in section 12.1. The relationship for the equilibrium ϵ-pH represented the limit where the rate constant k_{neq} approached infinity.

12.4.1 Interfacial Potential

The interfacial potential distributions calculated for Simulations A, B, and C are shown in Figure 12-22 with elapsed time as a parameter. The same initial conditions were used for the three simulations. The shapes of the potential distribution

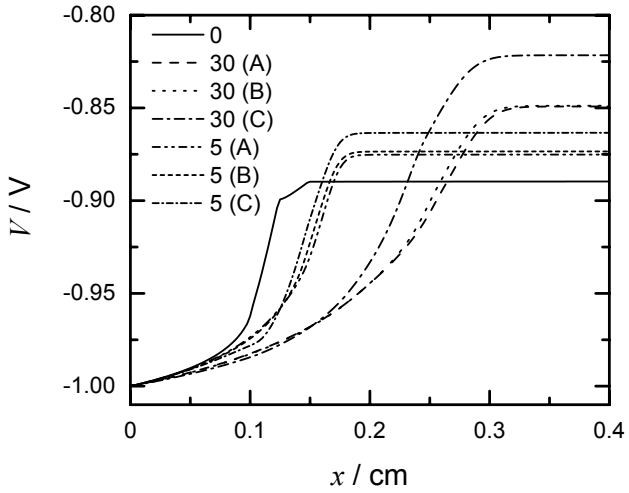

Figure 12-22: Calculated distributions of interfacial potential along the metal-coating interface with elapsed time in minutes and simulation, in brackets, as parameters.

for Simulations B and C were similar to that of Simulation A which was discussed in section 12.3.1. For a given position and elapsed time, more negative values of V were associated with larger rate constants.

The distribution of the interfacial potential gradient dV/dx are presented in Figure 12-23 for the different simulations with elapsed time as a parameter. The shapes of the interfacial potential gradient distribution for Simulations B and C were similar to that of Simulation A that was discussed. The position of the peak x_{del} in the distribution of dV/dx represented the front region. For a given elapsed time, larger values of x_{del} were associated with larger values of the rate constant. Therefore, larger rate constants for the ϵ-pH relationship increased the rate of propagation.

12.4.2 Concentrations and Porosity

The pH and ϵ distributions for simulations A, B, and C are shown in Figure 12-24 and 12-25, respectively. Two general features were associated with the distributions of pH and ϵ. The first was that the shapes of the distributions of Simulations B and C were similar to that of Simulation A, in which the equilibrium

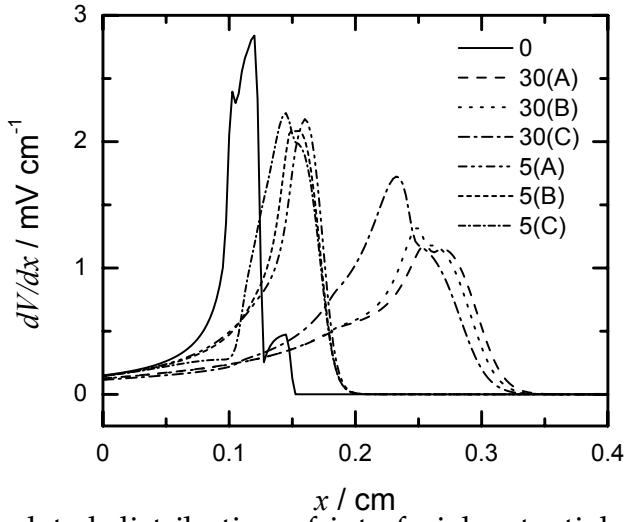

Figure 12-23: Calculated distribution of interfacial potential gradient along the metal-coating interface with elapsed time in minutes and simulation, in brackets, as parameters.

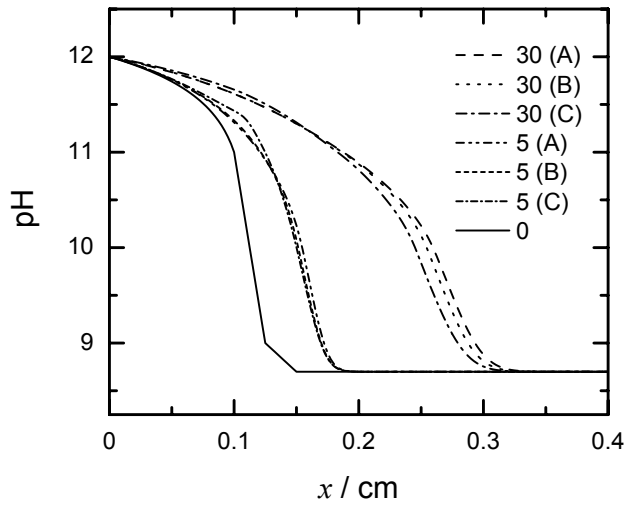

Figure 12-24: Calculated distribution of pH along the metal-coating interface with elapsed time in minutes and simulation, in brackets, as parameters.

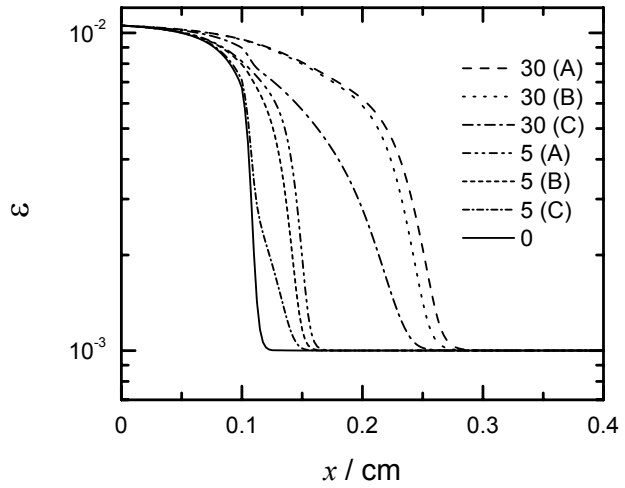

Figure 12-25: Calculated distribution of interfacial porosity along the metal-coating interface with elapsed time in minutes and simulation, in brackets, as parameters.

ϵ-pH relationship was assumed. The second was that, for a given position and elapsed time, a larger change in a given variable was associated with a larger rate constant.

The pH-distribution was related to the electrochemical production of OH^- and the flux of OH^- in the delamination zone, as was discussed in section 12.3.2. The distributions of $i_{O_2}^{coat}$ and N_{OH^-} for simulations A, B, and C are shown in Figures 12-26, and 12-27, respectively. The two general features associated with the pH and ϵdistributions were also seen in the distributions of $i_{O_2}^{coat}$ and N_{OH^-} .

The distribution of c_{Na^+} along the metal-coating interface is shown in Figure 12-28. The two general features associated with the pH and ϵdistributions were seen in the distributions for c_{Na^+}. The distributions of the flux of the sodium ion, which demonstrated the transport of Na^+ ions into the delamination zone, were also consistent with the two general features, as seen in Figure 12-29.

The distributions of N_{Na^+} and N_{OH^-} at an elapsed time of 30 min for Simulations A, B, and C are shown in Figure 12-30. After 30 min of simulation there was a larger spread in the distribution of N_{Na^+} as compared to that of N_{OH^-} for a given

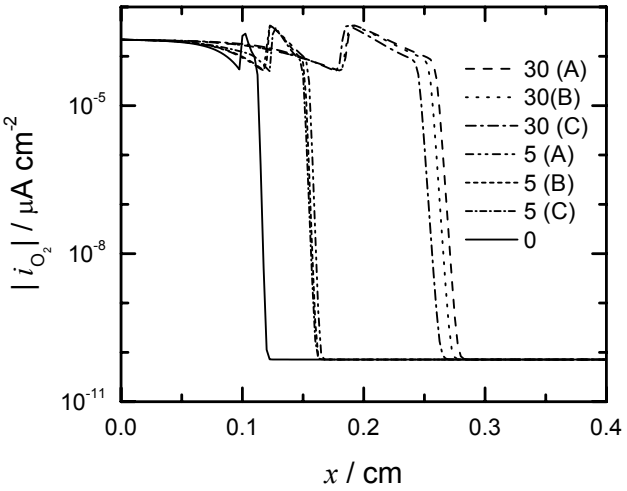

Figure 12-26: Calculated distribution of oxygen reduction current density along the metal-coating interface with elapsed time in minutes and simulation, in brackets, as parameters.

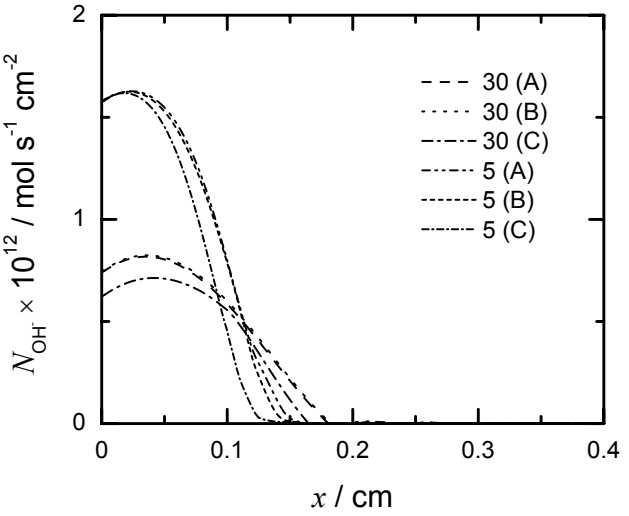

Figure 12-27: Calculated distribution of the hydroxide ion flux along the metal-coating interface with elapsed time in minutes and simulation, in brackets, as a parameter.

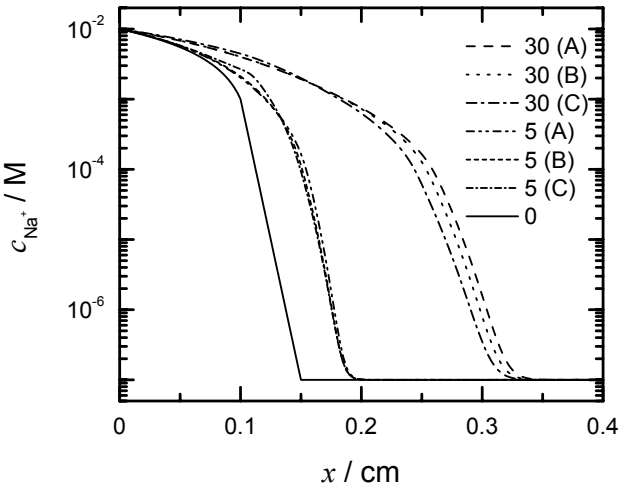

Figure 12-28: Calculated distribution of sodium ion concentration along the metal-coating interface with elapsed time in minutes and simulation, in brackets, as parameters.

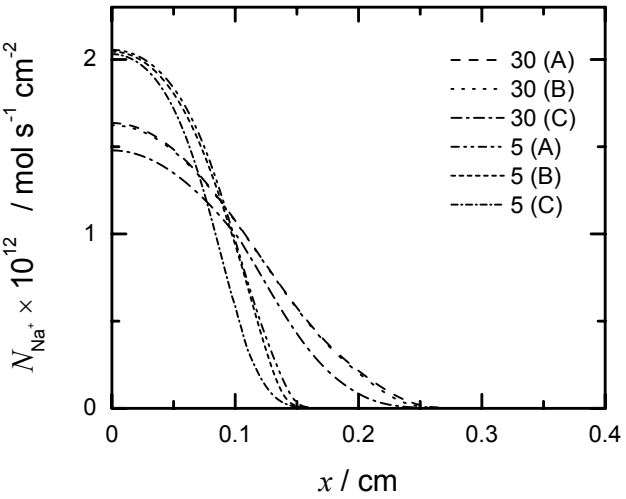

Figure 12-29: Calculated distribution of sodium ion flux along the metal-coating interface with elapsed time in minutes and simulation, in brackets, as parameters.

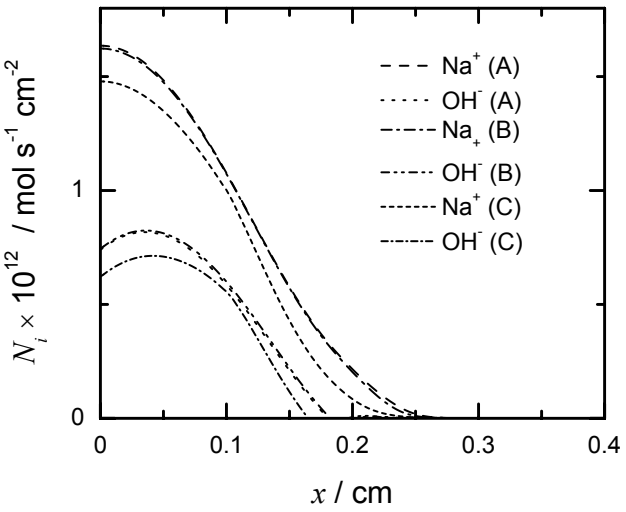

Figure 12-30: Calculated distributions of sodium ion and hydroxide ion flux along the metal-coating interface at an elapsed time of 30min with simulation, in brackets, as a parameter.

simulation. This trend was discussed in section 12.3.2. For a given position smaller values of N_{Na^+} or N_{OH^-} were associated with smaller values of the rate constant. This result is consistent with the influence of the rate constant on the propagation rate.

12.4.3 Bond-breakage Phenomena

The distribution of the gradients of the interfacial potential and interfacial porosity are shown in Figures 12-31 and 12-32, respectively, for an elapsed time period of 15 minutes. The features of these distributions were discussed. The front associated with a given distribution is identified by the peak associated with the distribution. The calculated velocities of the interfacial potential and interfacial porosity fronts are given in Table 12.3 for values of the rate constant k_{neq}. The value of $k_{neq} \rightarrow \infty$ was associated with the condition where the porosity and pH were at equilibrium.

For a given value of k_{neq}, where $k_{neq} > 0.005$, the velocity of the porosity front was slightly less than the velocity of the potential front. For the value of $k_{neq} =$

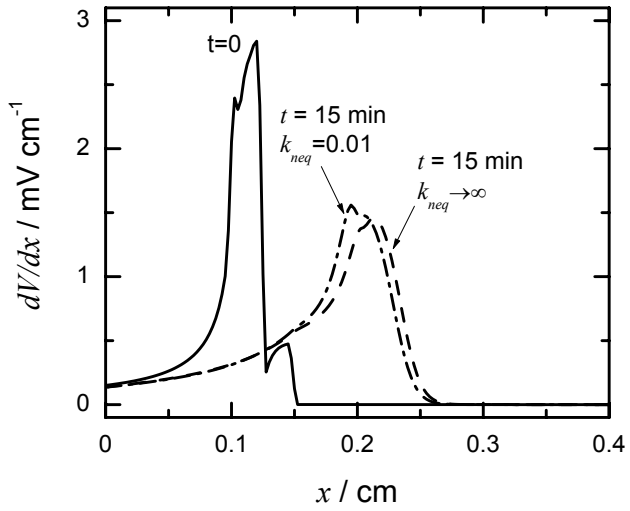

Figure 12-31: Calculated distribution of interfacial potential gradient along the metal-coating interface after 15 minutes of elapsed time with rate constant as a parameter. The distribution associated with the initial time is shown.

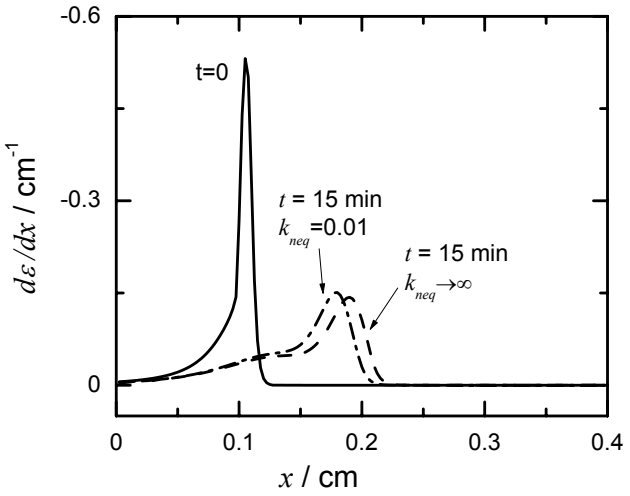

Figure 12-32: Calculated distribution of interfacial porosity gradient along the metal-coating interface after 15 minutes of elapsed time with rate constant as a parameter. The distribution associated with the initial time is shown.

Table 12.3: Calculated front velocity.

Rate constant k_{neq}	Interfacial porosity	Interfacial potential
∞	3.4	4.4
0.1	3.32	4.4
0.01	3.0	3.7
0.005	2.7	3.6
0.001	1.8	3.2

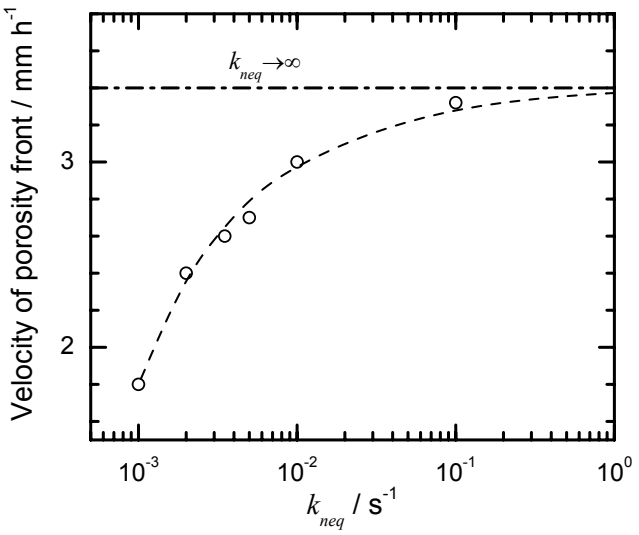

Figure 12-33: Calculated velocity of interfacial porosity front along the metal-coating interface as a function of rate constant. The dashed line shows the general trend between the velocity of the interfacial front and the rate constant. The line at the velocity of 3.4 mm $\cdot$ h^{-1} represented the condition where interfacial porosity and local pH are at equilibrium.

0.001 the velocity of the potential front was 3.2 mm $\cdot$ h^{-1} whereas the velocity of the porosity front was 1.8 mm $\cdot$ h^{-1}. This result indicated that for the value of $k_{neq} = 0.001$, the rate limiting process for cathodic delamination was associated with the breakage of the adhesive bonds between the coating and the metal.

The calculated velocity of the interfacial porosity front along the metal-coating interface as a function of the rate constant k_{neq} is shown in Figure 12-33. The velocity of the porosity front increased with k_{neq} and asymptotically approached a maximum value of 3.4 mm $\cdot$ h^{-1}. This maximum value was associated with the condition where the porosity and pH were assumed to be at equilibrium. The velocity of the porosity front asymptotically approached a value of zero for the condition $k_{neq} \rightarrow 0$. The bond-breakage phenomena was the rate limiting process for cathodic delamination for $k_{neq} < 0.005$, whereas the processes associated with the transport of species and the production of OH^- ions were the rate limiting processes for $k_{neq} > 0.005$. The transport of species included the transport of Na^+

and OH^- along the metal-coating interface and the transport of dissolved oxygen through the coating to the metal-coating interface.

12.5 Discussion

Recent experiments on the cathodic delamination of coated metals have used the Scanning Kelvin Probe to measure the potential distribution at the buried metal-coating interface.[6–11,25,26] The interfacial potential results have shown that there is a propagation of a front during the cathodic delamination of a coated metal. The experiments have also shown that there exists large differences in interfacial potential and concentrations between the delaminated and fully-intact regions.

The initial distributions for the concentrations of species were based on the experimental trends seen in the distributions of Na^+ and Cl^- intensities, and the pH profiles obtained using pH indicator pigments. The distribution of the interfacial porosity was based on the observations of the tensile force required to remove the coating. The distributions of the polarization parameters were assumed using rationale that corresponded to the different regions of the delamination zone. These initial distributions were used in the calculation of the initial interfacial potential distribution. The shape of the calculated interfacial potential distribution was consistent with the shape of the interfacial potentials seen in experiments conducted by Furbeth and Stratmann.[10] This consistency demonstrated that the interfacial potential and concentrations distributions seen in experiments were in agreement. The consistency supported the hypothesized pH dependent phenomena of interfacial porosity and polarization kinetics.

The propagation of the front during the cathodic delamination of coated zinc was simulated by CADEM. This result supported the hypotheses that the interfacial porosity and interfacial polarization kinetics contributed to the front propa-

gation. The simulated distributions for the dependent variables, fluxes of species, and polarization parameters were reconciled to the propagation of the front into the fully-intact region. The flux distributions of Na^+ and OH^- demonstrated that the net transport of the positively charged Na^+ ion was in response to the production of the negatively charged OH^- ion at the interface of the front. This demonstration is consistent with experimental observations.

The pH-dependent interfacial porosity represented a novel approach at implicitly accounting for the breakage of adhesive bonds between the coating and the metal. The results for the non-equilibrium ϵ-pH relationship demonstrated that the propagation rate was sensitive to the rate constant for the non-equilibrium porosity-pH relationship and that the interfacial porosity was a significant contributor to the cathodic delamination system. The results associated with the equilibrium and non-equilibrium conditions for the porosity-pH relationship were used to demonstrate the influence of bond-breakage phenomena on the velocity of the interfacial porosity front, and identify the rate limiting processes associated with the cathodic delamination process.

The mathematical model CADEM is the first model that simulates the propagation of the front during cathodic delamination. In this model only the conditions in the delamination zone were simulated. The galvanic couple between the defect and delamination zones was not accurately accounted for in CADEM as the conditions at the defect-delamination zone boundary were fixed. The coupling of CADEM to a model for the defect zone is the basis of future work.

CHAPTER 13
CONCLUSIONS AND RECOMMENDATIONS

The mathematical models DISCOM and CADEM were applied to systems and the simulated results analyzed. The conclusions derived from these results are presented in the chapters where they are deduced and a summary of the conclusions is presented in this chapter. Recommendations for future work in modeling disbonded coating and cathodic delamination systems are presented in this chapter.

13.1 Conclusions

The mathematical model DISCOM was developed to calculate the steady-state conditions of a radial disbonded coating system on coated steel under cathodic protection. The model accounted for the transport of species by diffusion and migration and satisfied electroneutrality explicitly. The iterative method of solution involved linearization of the coupled, partial differential, and algebraic equations.

Results obtained using DISCOM demonstrated that applied potential, bulk resistivity, gap size, and disbondment length were all contributors to the disbonded coating system. The trends observed for the dependent variables were consistent with simulated and experimental trends reported in literature. Hydrogen evolution was shown to be the significant electrochemical reaction in the disbondment and therefore cannot be neglected when modeling disbonded coating systems. The conditions of the holiday and disbondment were coupled and therefore both should be modeled simultaneously. The contributions of radial diffusion and radial migration current densities in the disbondment were comparable and

therefore concentration gradients in the disbondment should be considered in disbonded coating models.

The quasipotential transformation method for the solution of the steady-state conditions in a two-dimensional system was quantitatively verified for a system where only one specie was being produced by electrochemical reactions. For two-dimensional systems where two species are being produced by electrochemical reactions, such as disbonded coating systems, the quasipotential transformation is inapplicable. However, for one-dimensional systems where two species are being produced by electrochemical reactions the quasipotential transformation was shown to be applicable.

The transient model CADEM simulated the propagation of the front along the metal-coating interface of coated zinc undergoing cathodic delamination. This result supported the hypotheses that the pH-dependent interfacial polarization kinetics and the pH-dependent interfacial porosity contributed to the propagation of the front. The pH-dependent interfacial porosity represented a novel approach at implicitly accounting for the breakage of adhesive bonds between the coating and the metal. The results for the non-equilibrium ϵ-pH relationship demonstrated that the propagation rate was sensitive to the rate constant for the non-equilibrium porosity-pH relationship. This highlighted the contribution of the interfacial porosity towards the propagation of the front in the cathodic delamination system.

13.2 Recommendations for Future Work

Experimental disbonded coating systems reported in literature include disbondment lengths of 10 cm and more.[57 – 60] It is recommended that the model DISCOX be extended to include the hydrogen ion and be used to simulate reported disbonded coating experiments.

In both DISCOM and CADEM models, the method of solution involved casting the governing equations into a system of equations. The solution method for this system used the LAPACK solver which employed LU decomposition. The coefficient matrix of the system of equations for both models was ill-conditioned. Conjugate and biconjugate methods were used to solve the system of equations but these did not provide any improvement to the LAPACK solver. Recently, mathematical models of electrochemical systems without convective contribution have been reported that employ a GMRES Krylov subspace method for the solution of the system of equations.[81,86] It is recommended that this method be implemented in DISCOM and CADEM models. This implementation may permit the inclusion of homogeneous reactions in these systems.

CADEM is the first mathematical model for the propagation of the front during cathodic delamination, and provides a foundation for more sophisticated models. The model was developed for the conditions in the delamination zone with conditions being assumed at the boundary shared by the defect and delamination zones. The coupling of a two-dimensional defect zone with CADEM is recommended for a more sophisticated model. This couple would relax the conditions at the defect/delamination zone boundary and would explicitly account for the galvanic couple between the zones. The influence of this couple on the interfacial potential of the fully-intact region during a simulation would be interesting as the present version of CADEM was unable to simulate the fixed potential condition in the fully-intact region because of the fixed boundary conditions at the defect-delamination zone boundary.

APPENDIX A
DISBONDED COATING SYSTEM SOLUTION METHOD

The non-linear system of governing equations of the disbonded coating system were linearized and cast into a linear system of equations.[12] The details of this procedure are given in this appendix.

The independent spatial variables were r and z for the cylindrical coordinate system. The domain of the disbonded coating system was discretized into a grid and the system of equations were discretized at each node in the domain. The discretized equations were used to construct a global coefficient matrix $\boldsymbol{K}_D$ and global load vector $\boldsymbol{R}_D$.

A.1 Linearization Approximations

The linearization procedure was used under the assumption that known values c_i^o and Φ^o were close to values c_i and Φ that satisfied the system of governing equations such that

$$c_i = c_i^o + \triangle c_i \tag{A-1}$$

$$\phi = \phi^o + \triangle \phi \tag{A-2}$$

The linearization of a non-linear term $c_i\phi$ is given here as an example. Substitution of equations (A-1) and (A-2) into $c_i\phi$ yielded

$$c_i\phi = (c_i^o + \triangle c_i)(\phi^o + \triangle \phi) \tag{A-3}$$

$$= c_i^o\phi^o + c_i^o\triangle\phi + \phi^o\triangle c_i + \triangle c_i\triangle\phi \tag{A-4}$$

The quadratic term $\triangle c_i \triangle \phi$ was neglected and $\triangle c_i$ and $\triangle \phi$ were replaced with $c_i - c_i^o$ and $\phi - \phi^o$, respectively, to recast equation (A-4) as

$$c_i \phi = c_i \phi^o + c_i^o \phi - c_i^o \phi^o \tag{A-5}$$

which represented the approximated linear form of $c_i \phi$.

The approximations used in the linearization of the governing equations for c_i were given by

$$c_i \frac{\partial^2 \phi}{\partial r^2} = c_i^o \frac{\partial^2 \phi}{\partial r^2} + c_i \frac{\partial^2 \phi^o}{\partial r^2} - c_i^o \frac{\partial^2 \phi^o}{\partial r^2} \tag{A-6}$$

$$c_i \frac{\partial^2 \phi}{\partial z^2} = c_i^o \frac{\partial^2 \phi}{\partial z^2} + c_i \frac{\partial^2 \phi^o}{\partial z^2} - c_i^o \frac{\partial^2 \phi^o}{\partial z^2} \tag{A-7}$$

$$c_i \frac{\partial \phi}{\partial r} = c_i^o \frac{\partial \phi}{\partial r} + c_i \frac{\partial \phi^o}{\partial r} - c_i^o \frac{\partial \phi^o}{\partial r} \tag{A-8}$$

$$c_i \frac{\partial \phi}{\partial z} = c_i^o \frac{\partial \phi}{\partial z} + c_i \frac{\partial \phi^o}{\partial z} - c_i^o \frac{\partial \phi^o}{\partial z} \tag{A-9}$$

$$\frac{\partial c_i}{\partial r} \frac{\partial \phi}{\partial r} = \frac{\partial c_i^o}{\partial r} \frac{\partial \phi}{\partial r} + \frac{\partial c_i}{\partial r} \frac{\partial \phi^o}{\partial r} - \frac{\partial c_i^o}{\partial r} \frac{\partial \phi^o}{\partial r} \tag{A-10}$$

and

$$\frac{\partial c_i}{\partial z} \frac{\partial \phi}{\partial z} = \frac{\partial c_i^o}{\partial z} \frac{\partial \phi}{\partial z} + \frac{\partial c_i}{\partial z} \frac{\partial \phi^o}{\partial z} - \frac{\partial c_i^o}{\partial z} \frac{\partial \phi^o}{\partial z} \tag{A-11}$$

A.2 Finite Difference Approximations

Finite difference approximations were employed in discretizing the governing equations for the mass-transfer of species at a node (m, k). The approximations are given here for a generic variable f which represented the dependent variables Φ and c_i . The approximations were correct to order $(\triangle r)^2$ and $(\triangle z)^2$, for the r and z spatial derivatives, respectively. The nodes were either non-boundary or boundary nodes. The boundaries were separated as metal, disbonded coating, vertical coating, and axis boundaries as shown in Figure A-1.

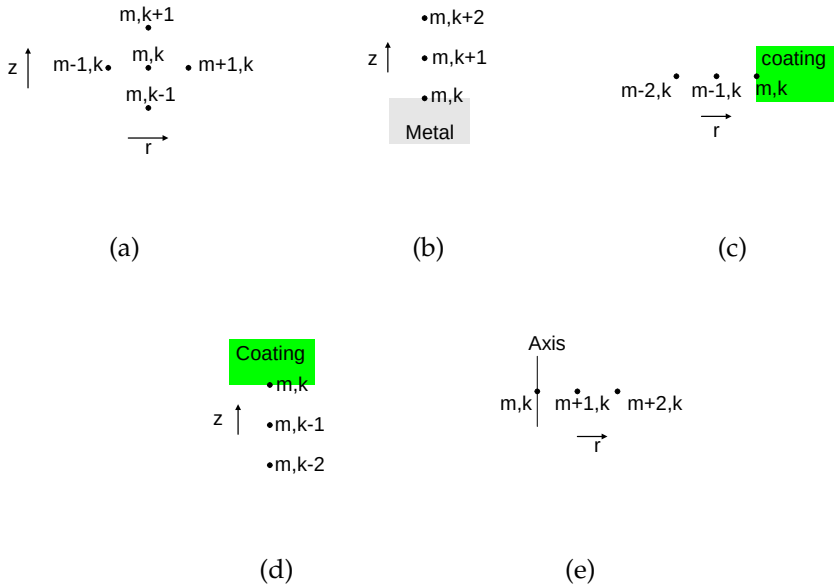

Figure A-1: Positions of non-boundary and boundary nodes. (a) non-boundary node, (b)metal node, (c) vertical coating node, (d) disbonded coating node, and (e) axis node.

The spatial derivatives for non-boundary nodes used the central finite difference approximations

$$\frac{\partial^2 f_{(m,k)}}{\partial r^2} = \frac{f_{(m+1,k)} - 2f_{(m,k)} + f_{(m-1,k)}}{(\triangle r)^2} + O(\triangle r)^2 \tag{A-12}$$

$$\frac{\partial f_{(m,k)}}{\partial r} = \frac{f_{(m+1,k)} - f_{(m-1,k)}}{2\triangle r} + O(\triangle r)^2 \tag{A-13}$$

$$\frac{\partial^2 f_{(m,k)}}{\partial z^2} = \frac{f_{(m,k+1)} - 2f_{(m,k)} + f_{(m,k-1)}}{(\triangle z)^2} + O(\triangle z)^2 \tag{A-14}$$

and

$$\frac{\partial f_{(m,k)}}{\partial z} = \frac{f_{(m,k+1)} - f_{(m,k-1)}}{2\triangle z} + O(\triangle z)^2 \tag{A-15}$$

The backward difference approximations

$$\frac{\partial f_{(m,k)}}{\partial r} = \frac{f_{(m-2,k)} - 4f_{(m-1,k)} + 3f_{(m,k)}}{2\triangle r} + O(\triangle r)^2 \tag{A-16}$$

and

$$\frac{\partial f_{(m,k)}}{\partial z} = \frac{f_{(m,k-2)} - 4f_{(m,k-1)} + 3f_{(m,k)}}{2\triangle z} + O(\triangle z)^2 \tag{A-17}$$

Table A.1: Conventional and computational notations for node position.

Conventional notation	Computational notation
(m,k)	j
$(m,k+1)$	j_1
$(m+1,k)$	j_2
$(m,k-1)$	j_3
$(m-1,k)$	j_4
$(m,k+2)$	j_5
$(m+2,k)$	j_6
$(m,k-2)$	j_7
$(m-2,k)$	j_8

and forward difference approximations

$$\frac{\partial f_{(m,k)}}{\partial r} = \frac{-3f_{(m,k)} + 4f_{(m+1,k)} - f_{(m+2,k)}}{2\triangle r} + O(\triangle r)^2 \tag{A-18}$$

and

$$\frac{\partial f_{(m,k)}}{\partial z} = \frac{-3f_{(m,k)} + 4f_{(m,k+1)} - f_{(m,k+2)}}{2\triangle z} + O(\triangle z)^2 \tag{A-19}$$

were employed in discretizing governing equations for species at nodes located on boundaries.

A.3 System without $Fe(OH)^+$

The discretized equations for non-boundary and boundary nodes of the disbonded coating domain are presented in this section for the system comprised of Na^+, Cl^-, OH^-, and Fe^{+2} . These species were indexed 1, 2, 3, and 4, respectively. The number of dependent variables was $n = 5$. In the development of the discretized equations conventional and computational notations were used. These notations are given in Table A.1.

A.3.1 Non-boundary nodes

The general form of the governing equation for c_i , that was developed in section 4.2, was given by equation (4-26)

$$\begin{aligned} 0 &= z_i D_i c_i \left[\frac{\partial^2\phi}{\partial r^2} + \frac{\partial^2\phi}{\partial z^2}\right] + z_i D_i \left[\frac{\partial c_i}{\partial r}\frac{\partial\phi}{\partial r} + \frac{\partial c_i}{\partial z}\frac{\partial\phi}{\partial z}\right] \\ &+ D_i \left[\frac{\partial^2 c_i}{\partial r^2} + \frac{\partial^2 c_i}{\partial z^2}\right] + z_i D_i c_i \frac{1}{r}\frac{\partial\phi}{\partial r} + D_i \frac{1}{r}\frac{\partial c_i}{\partial r} \end{aligned} \tag{A-20}$$

for the condition where homogeneous reactions were not considered. The discretized form of this equation was

$$\begin{aligned} \mathcal{G}_i &= \mathcal{D}_{i,n}\phi_{(m,k)} + \mathcal{A}_{i,n}\phi_{(m,k+1)} + \mathcal{B}_{i,n}\phi_{(m+1,k)} \\ &+ \mathcal{F}_{i,n}\phi_{(m,k-1)} + \mathcal{H}_{i,n}\phi_{(m-1,k-1)} \\ &+ \mathcal{D}_{i,i}c_{i(m,k)} + \mathcal{A}_{i,i}c_{i(m,k+1)} + \mathcal{B}_{i,i}c_{i(m+1,k)} \\ &+ \mathcal{F}_{i,i}c_{i(m,k-1)} + \mathcal{H}_{i,i}c_{i(m-1,k-1)} \end{aligned} \tag{A-21}$$

where $i = 1, 2, 3, 4$,

$$\mathcal{D}_{i,n} = -2z_i D_i c^o_{i(m,k)} \left[\frac{1}{(\triangle r)^2} + \frac{1}{(\triangle z)^2}\right] \tag{A-22}$$

$$\mathcal{A}_{i,n} = z_i D_i \left[\frac{c^o_{i(m,k)}}{(\triangle z)^2} + \frac{\partial c^o_{i(m,k)}}{\partial z}\frac{1}{2\triangle z}\right] \tag{A-23}$$

$$\mathcal{B}_{i,n} = z_i D_i \left[\frac{c^o_{i(m,k)}}{(\triangle r)^2} + \frac{\partial c^o_{i(m,k)}}{\partial r}\frac{1}{2\triangle r} + \frac{c^o_{i(m,k)}}{2r\triangle r}\right] \tag{A-24}$$

$$\mathcal{F}_{i,n} = z_i D_i \left[\frac{c^o_{i(m,k)}}{(\triangle z)^2} - \frac{\partial c^o_{i(m,k)}}{\partial z}\frac{1}{2\triangle z}\right] \tag{A-25}$$

$$\mathcal{H}_{i,n} = z_i D_i \left[\frac{c^o_{i(m,k)}}{(\triangle r)^2} - \frac{\partial c^o_{i(m,k)}}{\partial r}\frac{1}{2\triangle r} - \frac{c^o_{i(m,k)}}{2r\triangle r}\right] \tag{A-26}$$

$$\begin{aligned} \mathcal{D}_{i,i} &= z_i D_i \left[\frac{\partial^2\phi^o_{(m,k)}}{\partial r^2} + \frac{\partial^2\phi^o_{(m,k)}}{\partial z^2} + \frac{1}{r}\frac{\partial\phi^o_{(m,k)}}{\partial r}\right] \\ &\quad -2D_i \left[\frac{1}{(\triangle r)^2} + \frac{1}{(\triangle z)^2}\right] \end{aligned} \tag{A-27}$$

$$\mathcal{A}_{i,i} = \frac{D_i}{(\triangle z)^2} + \frac{z_i D_i}{2\triangle z}\frac{\partial \phi^o_{(m,k)}}{\partial z} \tag{A-28}$$

$$\mathcal{B}_{i,i} = D_i\left[\frac{1}{(\triangle r)^2} + \frac{1}{2r\triangle r}\right] + \frac{z_i D_i}{2\triangle r}\frac{\partial \phi^o_{(m,k)}}{\partial r} \tag{A-29}$$

$$\mathcal{F}_{i,i} = \frac{D_i}{(\triangle z)^2} - \frac{z_i D_i}{2\triangle z}\frac{\partial \phi^o_{(m,k)}}{\partial z} \tag{A-30}$$

$$\mathcal{H}_{i,i} = D_i\left[\frac{1}{(\triangle r)^2} - \frac{1}{2r\triangle r}\right] - \frac{z_i D_i}{2\triangle r}\frac{\partial \phi^o_{(m,k)}}{\partial r} \tag{A-31}$$

and

$$\begin{aligned}\mathcal{G}_i = {} & z_i D_i c^o_{i(m,k)}\left[\frac{\partial^2 \phi^o_{(m,k)}}{\partial r^2} + \frac{\partial^2 \phi^o_{(m,k)}}{\partial z^2}\right] \\ & + z_i D_i\left[\frac{\partial \phi^o_{(m,k)}}{\partial r}\frac{\partial c^o_{i(m,k)}}{\partial r} + \frac{\partial \phi^o_{(m,k)}}{\partial z}\frac{\partial c^o_{i(m,k)}}{\partial z}\right] \\ & + \frac{z_i D_i c^o_{i(m,k)}}{r}\frac{\partial \phi^o_{(m,k)}}{\partial r}\end{aligned} \tag{A-32}$$

The discretized equation for the electroneutrality condition at a node (m,k) was given by

$$\sum_{i=1}^{i=4} z_i c_{i(m,k)} = 0 \tag{A-33}$$

The discretized governing equations for c_i , equation (A-21), for each specie and electroneutrality, equation (A-33), represented a system of linear equations that governed the steady-state conditions at a at a non-boundary node j . This system of equations was recast using the computational notation as

$$\begin{aligned}\boldsymbol{\mathcal{G}}_j = {} & \boldsymbol{\mathcal{D}}_j \cdot \boldsymbol{\mathcal{C}}_j + \boldsymbol{\mathcal{A}}_j \cdot \boldsymbol{\mathcal{C}}_{j_1} + \boldsymbol{\mathcal{B}}_j \cdot \boldsymbol{\mathcal{C}}_{j_2} \\ & + \boldsymbol{\mathcal{F}} \cdot \boldsymbol{\mathcal{C}}_{j_3} + \boldsymbol{\mathcal{H}}_j \cdot \boldsymbol{\mathcal{C}}_{j_4}\end{aligned} \tag{A-34}$$

where the node solution vector $\boldsymbol{\mathcal{C}}_j$ was given by

$$\boldsymbol{\mathcal{C}}_j = [c_{1(j)}\ c_{2(j)}\ c_{3(j)}\ c_{4(j)}\ \phi_{(j)}]^T \tag{A-35}$$

the node load vector $\boldsymbol{\mathcal{G}}_j$ was given by

$$\boldsymbol{\mathcal{G}}_j = [\mathcal{G}_1\ \mathcal{G}_2\ \mathcal{G}_3\ \mathcal{G}_4\ 0]^T \tag{A-36}$$

the node coefficient matrix $\boldsymbol{\mathcal{D}}_j$ was given by

$$\boldsymbol{\mathcal{D}}_j = \begin{bmatrix} \mathcal{D}_{1,1} & 0 & 0 & 0 & \mathcal{D}_{1,n} \\ 0 & \mathcal{D}_{2,2} & 0 & 0 & \mathcal{D}_{2,n} \\ 0 & 0 & \mathcal{D}_{3,3} & 0 & \mathcal{D}_{3,n} \\ 0 & 0 & 0 & \mathcal{D}_{4,4} & \mathcal{D}_{4,n} \\ z_1 & z_2 & z_3 & z_4 & 0 \end{bmatrix} \tag{A-37}$$

and the node coefficient matrices $\boldsymbol{\mathcal{A}}$, $\boldsymbol{\mathcal{B}}_j$, $\boldsymbol{\mathcal{F}}$, and $\boldsymbol{\mathcal{H}}_j$ were given by

$$\boldsymbol{\mathcal{M}}_j = \begin{bmatrix} \mathcal{M}_{1,1} & 0 & 0 & 0 & \mathcal{M}_{1,n} \\ 0 & \mathcal{M}_{2,2} & 0 & 0 & \mathcal{M}_{2,n} \\ 0 & 0 & \mathcal{M}_{3,3} & 0 & \mathcal{M}_{3,n} \\ 0 & 0 & 0 & \mathcal{M}_{4,4} & \mathcal{M}_{4,n} \\ 0 & 0 & 0 & 0 & 0 \end{bmatrix} \tag{A-38}$$

where $\boldsymbol{\mathcal{M}}$ and $\mathcal{M}$ were generic variables for $\boldsymbol{\mathcal{A}}$ and $\mathcal{A}$, $\boldsymbol{\mathcal{B}}$ and $\mathcal{B}$, $\boldsymbol{\mathcal{F}}$ and $\mathcal{F}$, and $\boldsymbol{\mathcal{H}}$ and $\mathcal{H}$, respectively. In the development of the boundary conditions node coefficient matrices $\boldsymbol{\mathcal{T}}$, $\boldsymbol{\mathcal{U}}$, $\boldsymbol{\mathcal{V}}$, and $\boldsymbol{\mathcal{W}}$ were used which were of the form of $\boldsymbol{\mathcal{M}}$.

A.3.2 Boundary Nodes

The boundaries for the domain consisted of a metal surface OB, the disbonded coating CD, vertical coating BC and DE, and the axis of symmetry OF (see Figure 4-1). The governing equations for nodes located on each of these boundaries are given below. The values of c_i and Φ were known at the mouth FE.

Metal Node

The governing equations for a metal node was

$$-z_i D_i \frac{\partial \phi}{\partial z} - D_i \frac{\partial c_i}{\partial z} = 0 \tag{A-39}$$

for $c_{Na^+}$and c_{Cl^-},

$$-z_{OH^-} D_{OH^-} \frac{\partial \phi}{\partial z} - D_{OH^-} \frac{\partial c_{OH^-}}{\partial z} = \frac{i_{O_2} + i_{H_2}}{-F} \tag{A-40}$$

for c_{OH^-} , and

$$-z_{Fe^{+2}} D_{Fe^{+2}} c_{Fe^{+2}} \frac{\partial \phi}{\partial z} - D_{Fe^{+2}} \frac{\partial c_{Fe^{+2}}}{\partial z} = \frac{i_{Fe}}{2F} \tag{A-41}$$

for $c_{Fe^{+2}}$. The discretized form of these equations was given by

$$\begin{aligned} \mathcal{G}_i &= \mathcal{D}_{i,n}\phi_{(m,k)} + \mathcal{A}_{i,n}\phi_{(m,k+1)} + \mathcal{T}_{i,n}\phi_{(m,k+2)} \\ &+ \mathcal{D}_{i,i}c_{i(m,k)} + \mathcal{A}_{i,i}c_{i(m,k+1)} + \mathcal{T}_{i,i}c_{i(m,k+2)} \end{aligned} \tag{A-42}$$

for $i = 1, 2, 3, 4$, where

$$\mathcal{D}_{i,n} = \frac{3 z_i D_i c^o_{i(m,k)}}{2\triangle z} \tag{A-43}$$

$$\mathcal{A}_{i,n} = \frac{-4 z_i D_i c^o_{i(m,k)}}{2\triangle z} \tag{A-44}$$

$$\mathcal{T}_{i,n} = \frac{z_i D_i c^o_{i(m,k)}}{2\triangle z} \tag{A-45}$$

$$\mathcal{D}_{i,i} = \frac{3 D_i}{2\triangle z} - z_i D_i \frac{\partial \phi^o_{(m,k)}}{\partial z} \tag{A-46}$$

$$\mathcal{A}_{i,i} = \frac{-4 D_i}{2\triangle z} \tag{A-47}$$

$$\mathcal{T}_{i,i} = \frac{D_i}{2\triangle z} \tag{A-48}$$

The term $\mathcal{G}_i$ was given by

$$\mathcal{G}_i = -z_i D_i c^o_{i(m,k)} \frac{\partial \phi^o_{(m,k)}}{\partial z} \tag{A-49}$$

for c_{Na^+} and c_{Cl^-},

$$\mathcal{G}_i = -z_i D_i c^o_{i(m,k)} \frac{\partial \phi^o_{(m,k)}}{\partial z} + \frac{i_{Fe}}{2F} \tag{A-50}$$

for $c_{Fe^{+2}}$, and

$$\mathcal{G}_i = -z_i D_i c^o_{i(m,k)} \frac{\partial \phi^o_{(m,k)}}{\partial z} - \frac{i_{O_2} + i_{H_2}}{-F} \tag{A-51}$$

for c_{OH^-}.

The discretized governing equations for c_i , equation (A-42), and electroneutrality, equation (A-33), at a metal node were cast into matrix form as

$$\boldsymbol{\mathcal{G}}_j = \boldsymbol{\mathcal{D}}_j \cdot \boldsymbol{\mathcal{C}}_j + \boldsymbol{\mathcal{A}}_j \cdot \boldsymbol{\mathcal{C}}_{j_1} + \boldsymbol{\mathcal{T}}_j \cdot \boldsymbol{\mathcal{C}}_{j5} \tag{A-52}$$

where $\boldsymbol{\mathcal{G}}_j$, $\boldsymbol{\mathcal{D}}_j$, and $\boldsymbol{\mathcal{A}}_j$ and $\boldsymbol{\mathcal{T}}_j$ were given by equations (A-36), (A-37), and (A-38), respectively.

Disbonded Coating Node

The governing equation for c_i at a disbonded coating node was

$$-z_i D_i \frac{\partial \phi}{\partial z} - D_i \frac{\partial c_i}{\partial z} = 0 \tag{A-53}$$

where $i = 1, 2, 3, 4$. The discretized form of this equation was

$$\begin{aligned} \mathcal{G}_i &= \mathcal{D}_{i,n}\phi_{(m,k)} + \mathcal{F}_{i,n}\phi_{(m,k-1)} + \mathcal{V}_{i,n}\phi_{(m,k-2)} \\ &+ \mathcal{D}_{i,i}c_{j(m,k)} + \mathcal{F}_{i,i}c_{j(m,k-1)} + \mathcal{V}_{i,i}c_{j(m,k-2)} \end{aligned} \tag{A-54}$$

for $i = 1, 2, 3, 4$ where

$$\mathcal{D}_{i,n} = \frac{-3z_i D_i c^o_{j(m,k)}}{2\triangle z} \tag{A-55}$$

$$\mathcal{F}_{i,n} = \frac{4z_i D_i c^o_{j(m,k)}}{2\triangle z} \tag{A-56}$$

$$\mathcal{V}_{i,n} = \frac{-z_i D_i c^o_{j(m,k)}}{2\triangle z} \tag{A-57}$$

$$\mathcal{D}_{i,i} = \frac{-3D_i}{2\triangle z} - z_i D_i \frac{\partial \phi^o_{(m,k)}}{\partial z} \tag{A-58}$$

$$\mathcal{F}_{i,i} = \frac{4D_i}{2\triangle z} \tag{A-59}$$

$$\mathcal{V}_{i,i} = \frac{-D_i}{2\triangle z} \tag{A-60}$$

$$\mathcal{G}_i = -z_i D_i c^o_{i(m,k)} \frac{\partial \phi^o_{(m,k)}}{\partial z} \tag{A-61}$$

The discretized governing equations for c_i , equation (A-54) and electroneutrality, equation (A-33), at a disbonded coating node were cast into matrix form as

$$\boldsymbol{\mathcal{G}}_j = \boldsymbol{\mathcal{D}}_j \cdot \boldsymbol{\mathcal{C}}_j + \boldsymbol{\mathcal{F}} \cdot \boldsymbol{\mathcal{C}}_{j_3} + \boldsymbol{\mathcal{V}}_j \cdot \boldsymbol{\mathcal{C}}_{j_7} \tag{A-62}$$

where $\boldsymbol{\mathcal{G}}_j$, $\boldsymbol{\mathcal{D}}_j$, and $\boldsymbol{\mathcal{F}}_j$ and $\boldsymbol{\mathcal{V}}_j$ were given by equations (A-36), (A-37), and (A-38), respectively.

Vertical Coating Node

The governing equation for c_i a vertical coating node was

$$-z_i D_i \frac{\partial \phi}{\partial r} - D_i \frac{\partial c_i}{\partial r} = 0 \tag{A-63}$$

for $i = 1, 2, 3, 4$. The discretized form of this equation was

$$\begin{aligned} \mathcal{G}_i &= \mathcal{D}_{i,n}\phi_{(m,k)} + \mathcal{H}_{i,n}\phi_{(m-1,k)} + \mathcal{W}_{i,n}\phi_{(m-2,k)} \\ &+ \mathcal{D}_{i,i}c_{i(m,k)} + \mathcal{H}_{i,i}c_{i(m-1,k)} + \mathcal{W}_{i,i}c_{i(m-2,k)} \end{aligned} \tag{A-64}$$

for $i = 1, 2, 3, 4$ where

$$\mathcal{D}_{i,n} = \frac{-3z_i D_i c^o_{j(m,k)}}{2\triangle r} \tag{A-65}$$

$$\mathcal{H}_{i,n} = \frac{4z_i D_i c^o_{j(m,k)}}{2\triangle r} \tag{A-66}$$

$$\mathcal{W}_{i,n} = \frac{-z_i D_i c^o_{j(m,k)}}{2\triangle r} \tag{A-67}$$

$$\mathcal{D}_{i,i} = \frac{-3D_i}{2\triangle r} - z_i D_i \frac{\partial \phi^o_{(m,k)}}{\partial r} \tag{A-68}$$

$$\mathcal{H}_{i,i} = \frac{4D_i}{2\triangle r} \tag{A-69}$$

$$\mathcal{W}_{i,i} = \frac{-D_i}{2\triangle r} \tag{A-70}$$

$$\mathcal{G}_i = -z_i D_i c^o_{i(m,k)} \frac{\partial \phi^o_{(m,k)}}{\partial r} \tag{A-71}$$

The discretized governing equations for c_i , equation (A-64), and electroneutrality, (A-33), at a vertical coating node were cast into matrix form as

$$\boldsymbol{\mathcal{G}}_j = \boldsymbol{\mathcal{D}}_j \cdot \boldsymbol{\mathcal{C}}_j + \boldsymbol{\mathcal{H}} \cdot \boldsymbol{\mathcal{C}}_{j_4} + \boldsymbol{\mathcal{W}} \cdot \boldsymbol{\mathcal{C}}_{j_8} \tag{A-72}$$

where $\boldsymbol{\mathcal{G}}_j$, $\boldsymbol{\mathcal{D}}_j$, and $\boldsymbol{\mathcal{H}}_j$ and $\boldsymbol{\mathcal{W}}_j$ were given by equations (A-36), (A-37), and (A-38), respectively.

Axis Node

The governing equation for c_i at an axis node was

$$-z_i D_i \frac{\partial \phi}{\partial r} - D_i \frac{\partial c_i}{\partial r} = 0 \tag{A-73}$$

for $i = 1, 2, 3, 4$. The discretized form of this equation was

$$\begin{aligned} \mathcal{G}_i &= \mathcal{D}_{i,5}\phi_{(m,k)} + \mathcal{B}_{i,5}\phi_{(m+1,k)} + \mathcal{U}_{i,5}\phi_{(m+2,k)} \\ &+ \mathcal{D}_{i,i}c_{i(m,k)} + \mathcal{B}_{i,i}c_{i(m+1,k)} + \mathcal{U}_{i,i}c_{i(m+2,k)} \end{aligned} \tag{A-74}$$

for $i = 1, 2, 3, 4$ where

$$\mathcal{D}_{i,5} = \frac{3z_i D_i c^o_{j(m,k)}}{2\triangle r} \tag{A-75}$$

$$\mathcal{B}_{i,5} = \frac{-4z_i D_i c^o_{j(m,k)}}{2\triangle r} \tag{A-76}$$

$$\mathcal{U}_{i,5} = \frac{z_i D_i c^o_{j(m,k)}}{2\triangle r} \tag{A-77}$$

$$\mathcal{D}_{i,i} = \frac{3D_i}{2\triangle r} - z_i D_i \frac{\partial \phi^o_{(m,k)}}{\partial r} \tag{A-78}$$

$$\mathcal{B}_{i,i} = \frac{-4D_i}{2\triangle r} \tag{A-79}$$

$$\mathcal{U}_{i,i} = \frac{D_i}{2\triangle r} \tag{A-80}$$

$$\mathcal{G}_i = -z_i D_i c^o_{i(m,k)} \frac{\partial \phi^o_{(m,k)}}{\partial r} \tag{A-81}$$

The discretized governing equations for c_i , equation (A-74), and electroneutrality, equation (A-33), at an axis node were cast into matrix form as

$$\boldsymbol{\mathcal{G}}_j = \boldsymbol{\mathcal{D}}_j \cdot \boldsymbol{\mathcal{C}}_j + \boldsymbol{\mathcal{B}}_j \cdot \boldsymbol{\mathcal{C}}_{j_2} + \boldsymbol{\mathcal{U}}_j \cdot \boldsymbol{\mathcal{C}}_{j_6} \tag{A-82}$$

where $\boldsymbol{\mathcal{G}}_j$, $\boldsymbol{\mathcal{D}}_j$, and $\boldsymbol{\mathcal{B}}_j$ and $\boldsymbol{\mathcal{U}}_j$ were given by equations (A-36), (A-37), and (A-38), respectively.

A.4 System with $Fe(OH)^+$

The specie $Fe(OH)^+$ was included when the homogeneous reaction given by equation (4-1)

$$Fe^{+2} + OH^- \rightleftharpoons Fe(OH)^+$$

between Fe^{+2} and OH^- was included in the model. The equilibrium relationship for this homogeneous reaction was given by equation (4-12)

$$\frac{c_{Fe(OH)^+}}{c_{OH^-} \cdot c_{Fe^{+2}}} = K_I$$

The equilibrium relationship was linearized as

$$c^o_{OH^-} \cdot c_{Fe^{+2}} K_I + c_{OH^-} \cdot c^o_{Fe^{+2}} K_I - c_{Fe(OH)^+} = c^o_{OH^-} \cdot c^o_{Fe^{+2}} K_I \tag{A-83}$$

where $c^o_{OH^-}$ and $c^o_{Fe^{+2}}$ were assumed values for c_{OH^-} and $c_{Fe^{+2}}$, respectively.

The species considered were Na^+, Cl^-, OH^-, Fe^{+2}, and $Fe(OH)^+$, and these were indexed 1, 2, 3, 4, and 5, respectively. There were $n = 6$ dependent variables in the system.

A.4.1 Non-boundary nodes

The general form for the governing equation for c_i was given by

$$\begin{aligned} 0 &= z_i D_i c_i \left[\frac{\partial^2 \phi}{\partial r^2} + \frac{\partial^2 \phi}{\partial z^2}\right] + z_i D_i \left[\frac{\partial c_i}{\partial r}\frac{\partial \phi}{\partial r} + \frac{\partial c_i}{\partial z}\frac{\partial \phi}{\partial z}\right] \\ &+ D_i \left[\frac{\partial^2 c_i}{\partial r^2} + \frac{\partial^2 c_i}{\partial z^2}\right] + z_i D_i c_i \frac{1}{r}\frac{\partial \phi}{\partial r} + D_i \frac{1}{r}\frac{\partial c_i}{\partial r} + R_i \end{aligned} \tag{A-84}$$

for the condition where homogeneous reactions were considered. The discretized form of this equation was

$$\begin{aligned} \mathcal{G}_i &= \mathcal{D}_{i,n}\phi_{(m,k)} + \mathcal{A}_{i,n}\phi_{(m,k+1)} + \mathcal{B}_{i,n}\phi_{(m+1,k)} \\ &+ \mathcal{F}_{i,n}\phi_{(m,k-1)} + \mathcal{H}_{i,n}\phi_{(m-1,k-1)} \\ &+ \mathcal{D}_{i,i}c_{i(m,k)} + \mathcal{A}_{i,i}c_{j(m,k+1)} + \mathcal{B}_{i,i}c_{j(m+1,k)} \\ &+ \mathcal{F}_{i,i}c_{i(m,k-1)} + \mathcal{H}_{i,i}c_{i(m-1,k-1)} + R_i \end{aligned} \tag{A-85}$$

where $i = 1, 2, 3, 4, 5$. The coefficients in equation (A-85) were given in section A.3.1. The values of R_i were given by

$$R_1 = 0 \tag{A-86}$$

$$R_2 = 0 \tag{A-87}$$

$$R_3 + R_5 = 0 \tag{A-88}$$

and

$$R_4 + R_5 = 0 \tag{A-89}$$

The discretized form of the governing equation for c_{Na^+} and c_{Cl^-} was given by

$$\begin{aligned}
\mathcal{G}_i &= \mathcal{D}_{i,n}\phi_{(m,k)} + \mathcal{A}_{i,n}\phi_{(m,k+1)} + \mathcal{B}_{i,n}\phi_{(m+1,k)} \\
&+ \mathcal{F}_{i,n}\phi_{(m,k-1)} + \mathcal{H}_{i,n}\phi_{(m-1,k-1)} \\
&+ \mathcal{D}_{i,i}c_{i(m,k)} + \mathcal{A}_{i,i}c_{i(m,k+1)} + \mathcal{B}_{i,i}c_{i(m+1,k)} \\
&+ \mathcal{F}_{i,i}c_{i(m,k-1)} + \mathcal{H}_{i,i}c_{i(m-1,k-1)} \qquad \text{(A-90)}
\end{aligned}$$

The discretized form of the governing equation for c_{OH^-} was given by

$$\begin{aligned}
\mathcal{G}_3 + \mathcal{G}_5 &= \left(\mathcal{D}_{3,n} + \mathcal{D}_{5,n}\right)\phi_{(m,k)} + \left(\mathcal{A}_{3,n} + \mathcal{A}_{5,n}\right)\phi_{(m,k+1)} \\
&+ \left(\mathcal{B}_{3,n} + \mathcal{B}_{5,n}\right)\phi_{(m+1,k)} \\
&+ \left(\mathcal{F}_{3,n} + \mathcal{F}_{5,n}\right)\phi_{(m,k-1)} + \left(\mathcal{H}_{3,n} + \mathcal{H}_{5,n}\right)\phi_{(m-1,k-1)} \\
&+ \mathcal{D}_{3,3}c_{3(m,k)} + \mathcal{A}_{3,3}c_{3(m,k+1)} + \mathcal{B}_{3,3}c_{3(m+1,k)} \\
&+ \mathcal{F}_{3,3}c_{3(m,k-1)} + \mathcal{H}_{3,3}c_{3(m-1,k-1)} \\
&+ \mathcal{D}_{5,5}c_{5(m,k)} + \mathcal{A}_{5,5}c_{5(m,k+1)} + \mathcal{B}_{5,5}c_{5(m+1,k)} \\
&+ \mathcal{F}_{5,5}c_{5(m,k-1)} + \mathcal{H}_{5,5}c_{5(m-1,k-1)} \qquad \text{(A-91)}
\end{aligned}$$

The discretized form of the governing equation for $c_{Fe^{+2}}$ was given by

$$\begin{aligned}
\mathcal{G}_4 + \mathcal{G}_5 &= \left(\mathcal{D}_{4,n} + \mathcal{D}_{5,n}\right)\phi_{(m,k)} + \left(\mathcal{A}_{4,n} + \mathcal{A}_{5,n}\right)\phi_{(m,k+1)} \\
&+ \left(\mathcal{B}_{4,n} + \mathcal{B}_{5,n}\right)\phi_{(m+1,k)} \\
&+ \left(\mathcal{F}_{4,n} + \mathcal{F}_{5,n}\right)\phi_{(m,k-1)} + \left(\mathcal{H}_{4,n} + \mathcal{H}_{5,n}\right)\phi_{(m-1,k-1)} \\
&+ \mathcal{D}_{4,4}c_{4(m,k)} + \mathcal{A}_{4,4}c_{4(m,k+1)} + \mathcal{B}_{4,4}c_{4(m+1,k)} \\
&+ \mathcal{F}_{4,4}c_{4(m,k-1)} + \mathcal{H}_{4,4}c_{4(m-1,k-1)} \\
&+ \mathcal{D}_{5,5}c_{5(m,k)} + \mathcal{A}_{5,5}c_{5(m,k+1)} + \mathcal{B}_{5,5}c_{5(m+1,k)} \\
&+ \mathcal{F}_{5,5}c_{5(m,k-1)} + \mathcal{H}_{5,5}c_{5(m-1,k-1)} \qquad \text{(A-92)}
\end{aligned}$$

The discretized equation for the electroneutrality condition at a node (m,k) was given by

$$\sum_{i=1}^{i=5} z_i c_{i(m,k)} = 0 \tag{A-93}$$

The set of discretized equations for c_i and ϕ at a node j were equations (A-90) for c_{Na^+} and c_{Cl^-}, equation (A-91) for c_{OH^-}, equation (A-92) for $c_{Fe^{+2}}$, equation (A-83), for $c_{Fe(OH)^+}$, and equation (A-93) for electroneutrality. This set of equations were cast cast using the computational notation as

$$\begin{aligned} \boldsymbol{\mathcal{G}}_j &= \boldsymbol{\mathcal{D}}_j \cdot \boldsymbol{\mathcal{C}}_j + \boldsymbol{\mathcal{A}}_j \cdot \boldsymbol{\mathcal{C}}_{j_1} + \boldsymbol{\mathcal{B}}_j \cdot \boldsymbol{\mathcal{C}}_{j_2} \\ &+ \boldsymbol{\mathcal{F}} \cdot \boldsymbol{\mathcal{C}}_{j_3} + \boldsymbol{\mathcal{H}}_j \cdot \boldsymbol{\mathcal{C}}_{j_4} \end{aligned} \tag{A-94}$$

where the node solution vector $\boldsymbol{\mathcal{C}}_j$ was given by

$$\boldsymbol{\mathcal{C}}_j = [c_{1(j)}\ c_{2(j)}\ c_{3(j)}\ c_{4(j)}\ c_{5(j)}\ \phi_{(j)}]^T \tag{A-95}$$

the node load vector $\boldsymbol{\mathcal{G}}_j$ was given by

$$\boldsymbol{\mathcal{G}}_j = \begin{bmatrix} \mathcal{G}_1 \\ \mathcal{G}_2 \\ \mathcal{G}_3 + \mathcal{G}_5 \\ \mathcal{G}_4 + \mathcal{G}_5 \\ c^o_{3(j)} c^o_{4(j)} K_1 \\ 0 \end{bmatrix} \tag{A-96}$$

the node coefficient matrix $\boldsymbol{\mathcal{D}}_j$ was given by

$$\boldsymbol{\mathcal{D}}_j = \begin{bmatrix} \mathcal{D}_{1,1} & 0 & 0 & 0 & 0 & \mathcal{D}_{1,n} \\ 0 & \mathcal{D}_{2,2} & 0 & 0 & 0 & \mathcal{D}_{2,n} \\ 0 & 0 & \mathcal{D}_{3,3} & 0 & \mathcal{D}_{5,5} & \mathcal{D}_{3,n} + \mathcal{D}_{5,n} \\ 0 & 0 & 0 & \mathcal{D}_{4,4} & \mathcal{D}_{5,5} & \mathcal{D}_{4,n} + \mathcal{D}_{5,n} \\ 0 & 0 & c^o_{4(j)} K_I & c^o_{3(j)} K_I & -1 & 0 \\ z_1 & z_2 & z_3 & z_4 & z_5 & 0 \end{bmatrix} \tag{A-97}$$

and the node coefficient matrices $\boldsymbol{\mathcal{A}}_j$, $\boldsymbol{\mathcal{B}}_j$, $\boldsymbol{\mathcal{F}}$, and $\boldsymbol{\mathcal{H}}_j$ were given by

$$\boldsymbol{\mathcal{M}}_j = \begin{bmatrix} \mathcal{M}_{1,1} & 0 & 0 & 0 & 0 & \mathcal{M}_{1,n} \\ 0 & \mathcal{M}_{2,2} & 0 & 0 & 0 & \mathcal{M}_{2,n} \\ 0 & 0 & \mathcal{M}_{3,3} & 0 & \mathcal{M}_{5,5} & \mathcal{M}_{3,n} + \mathcal{M}_{5,n} \\ 0 & 0 & 0 & \mathcal{M}_{4,4} & \mathcal{M}_{5,5} & \mathcal{M}_{4,n} + \mathcal{M}_{5,n} \\ 0 & 0 & 0 & 0 & 0 & 0 \\ 0 & 0 & 0 & 0 & 0 & 0 \end{bmatrix} \tag{A-98}$$

where $\boldsymbol{\mathcal{M}}$ and $\mathcal{M}$ were generic variables for $\boldsymbol{\mathcal{A}}$ and $\mathcal{A}$, $\boldsymbol{\mathcal{B}}$ and $\mathcal{B}$, $\boldsymbol{\mathcal{F}}$ and $\mathcal{F}$, and $\boldsymbol{\mathcal{H}}$ and $\mathcal{H}$, respectively.

A.4.2 Boundary Nodes

The discretized equations for the conditions on the boundaries were constructed using the node coefficient matrix $\boldsymbol{\mathcal{D}}_j$ given by

$$\boldsymbol{\mathcal{D}}_j = \begin{bmatrix} \mathcal{D}_{1,1} & 0 & 0 & 0 & 0 & \mathcal{D}_{1,n} \\ 0 & \mathcal{D}_{2,2} & 0 & 0 & 0 & \mathcal{D}_{2,n} \\ 0 & 0 & \mathcal{D}_{3,3} & 0 & 0 & \mathcal{D}_{3,n} \\ 0 & 0 & 0 & \mathcal{D}_{4,4} & 0 & \mathcal{D}_{4,n} \\ 0 & 0 & c^o_{4(j)} K_I & c^o_{3(j)} K_I & -1 & 0 \\ z_1 & z_2 & z_3 & z_4 & z_5 & 0 \end{bmatrix} \tag{A-99}$$

and

$$\boldsymbol{\mathcal{M}}_j = \begin{bmatrix} \mathcal{M}_{1,1} & 0 & 0 & 0 & 0 & \mathcal{M}_{1,n} \\ 0 & \mathcal{M}_{2,2} & 0 & 0 & 0 & \mathcal{M}_{2,n} \\ 0 & 0 & \mathcal{M}_{3,3} & 0 & 0 & \mathcal{M}_{3,n} \\ 0 & 0 & 0 & \mathcal{M}_{4,4} & 0 & \mathcal{M}_{4,n} \\ 0 & 0 & 0 & 0 & 0 & 0 \\ 0 & 0 & 0 & 0 & 0 & 0 \end{bmatrix} \tag{A-100}$$

where $\boldsymbol{\mathcal{M}}$ and $\mathcal{M}$ were generic variables for $\boldsymbol{\mathcal{A}}$ and $\mathcal{A}$, $\boldsymbol{\mathcal{B}}$ and $\mathcal{B}$, $\boldsymbol{\mathcal{F}}$ and $\mathcal{F}$, $\boldsymbol{\mathcal{H}}_j$ and $\mathcal{H}$, $\boldsymbol{\mathcal{T}}$ and $\mathcal{T}$, $\boldsymbol{\mathcal{U}}$ and $\mathcal{U}$, $\boldsymbol{\mathcal{V}}$ and $\mathcal{V}$, and $\boldsymbol{\mathcal{W}}$ and $\mathcal{W}$, respectively.

The node load vector $\boldsymbol{\mathcal{G}}_j$ was given by

$$\boldsymbol{\mathcal{G}}_j = \begin{bmatrix} \mathcal{G}_1 \\ \mathcal{G}_2 \\ \mathcal{G}_3 \\ \mathcal{G}_4 \\ c^o_{3(j)} c^o_{4(j)} K_1 \\ 0 \end{bmatrix} \tag{A-101}$$

Metal Node

The governing equations for a metal node for $c_{Na^+}$and c_{Cl^-}, c_{OH^-}, and $c_{Fe^{+2}}$were equations (A-39), (A-40), and (A-41), respectively. These equation were discretized to give equation (A-42). The discretized governing equation for $c_{Fe(OH)^+}$ was equation (A-83) and for electroneutrality was equation (A-93). The discretized governing equations at a metal node were cast into matrix form as equation (A-52) where $\boldsymbol{\mathcal{G}}_j$, $\boldsymbol{\mathcal{D}}_j$, and $\boldsymbol{\mathcal{A}}_j$ and $\boldsymbol{\mathcal{T}}_j$ were given by equations (A-101), (A-99), (A-100), respectively.

Disbonded Coating Node

The governing equation for c_i at a disbonded coating node was given by equation (A-53) for c_{Na^+}, c_{Cl^-}, c_{OH^-}, and $c_{Fe^{+2}}$. The discretized form of this equation was given by equation (A-54). The discretized governing equation for $c_{Fe(OH)^+}$ was equation (A-83) and for electroneutrality was equation (A-93). The discretized governing equations at a disbonded coating node were cast into matrix form as equation (A-62) where $\boldsymbol{\mathcal{G}}_j$, $\boldsymbol{\mathcal{D}}_j$, and $\boldsymbol{\mathcal{F}}_j$ and $\boldsymbol{\mathcal{V}}_j$ were given by equations (A-101), (A-99), (A-100), respectively.

Vertical Coating Node

The governing equation for c_i a vertical coating node was given by equation (A-63) and the discretized form of this equation was given by equation (A-64). The discretized governing equation for $c_{Fe(OH)^+}$ was equation (A-83) and for electroneutrality was equation (A-93). The discretized governing equations at a vertical coating node were cast into matrix form as equation (A-72) where $\boldsymbol{\mathcal{G}}_j$, $\boldsymbol{\mathcal{D}}_j$, and $\boldsymbol{\mathcal{H}}_j$ and $\boldsymbol{\mathcal{W}}_j$ were given by equations (A-101), (A-99), (A-100), respectively.

Axis Node

The governing equation for c_i at an axis node was given by equation (A-73). The discretized form of this equation was given by equation (A-74). The discretized governing equation for $c_{Fe(OH)^+}$ was equation (A-83) and for electroneutrality was equation (A-93). The discretized governing equations at a vertical coating node were cast into matrix form as equation (A-82) where $\boldsymbol{\mathcal{G}}_j$, $\boldsymbol{\mathcal{D}}_j$, and $\boldsymbol{\mathcal{B}}_j$ and $\boldsymbol{\mathcal{U}}_j$ were given by equations (A-101), (A-99), (A-100), respectively.

A.5 Assembly

The governing equations for c_i and ϕ at a given node in the domain were discretized and cast into a matrix form as described above for non-boundary and boundary nodes. The node coefficient matrices and node load vectors at each node were used to construct the global coefficient matrix $\boldsymbol{K}_D$ and global load vector $\boldsymbol{R}_D$ such that the governing equations for the system were cast into a matrix form of

$$\boldsymbol{K}_D \cdot \boldsymbol{C}_D = \boldsymbol{R}_D \tag{A-102}$$

where $\boldsymbol{C}_D$ was the global solution vector.

The assembled $\boldsymbol{K}_D$ and $\boldsymbol{R}_D$ are given for the discretized domain shown in Figure A-2. In this domain there were 11 nodes. Node 5 was the only non-boundary

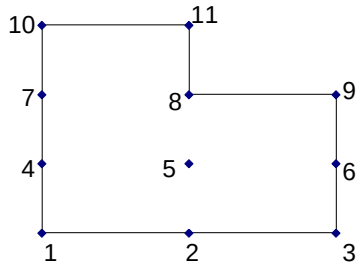

Figure A-2: Example of discretized domain.

node. Nodes 1, 2, and 3 were metal nodes, node 6 was a vertical coating node, nodes 8 and 9 were disbonded coating nodes, and nodes 4 and 7 were axis nodes. Nodes 10 and 11 were bulk boundary nodes where the conditions were known.

The global coefficient matrix $\boldsymbol{K}_D$ was constructed using the node coefficient matrices as

$$\boldsymbol{K}_D = \begin{bmatrix}
\boldsymbol{\mathcal{D}}_1 & 0 & 0 & 0 & \boldsymbol{\mathcal{A}}_1 & 0 & \boldsymbol{\mathcal{T}}_1 & 0 & 0 & 0 & 0 \\
0 & \boldsymbol{\mathcal{D}}_2 & 0 & 0 & 0 & \boldsymbol{\mathcal{A}}_2 & 0 & \boldsymbol{\mathcal{T}}_2 & 0 & 0 & 0 \\
0 & 0 & \boldsymbol{\mathcal{D}}_3 & 0 & 0 & 0 & \boldsymbol{\mathcal{A}}_3 & 0 & \boldsymbol{\mathcal{T}}_3 & 0 & 0 \\
0 & 0 & 0 & \boldsymbol{\mathcal{D}}_4 & \boldsymbol{\mathcal{B}}_4 & \boldsymbol{\mathcal{U}}_4 & 0 & 0 & 0 & 0 & 0 \\
0 & \boldsymbol{F}_5 & 0 & \boldsymbol{\mathcal{H}}_5 & \boldsymbol{\mathcal{D}}_5 & \boldsymbol{\mathcal{B}}_2 & 0 & \boldsymbol{\mathcal{A}}_8 & 0 & 0 & 0 \\
0 & 0 & 0 & \boldsymbol{\mathcal{W}}_6 & \boldsymbol{\mathcal{H}}_6 & \boldsymbol{\mathcal{D}}_6 & 0 & 0 & 0 & 0 & 0 \\
0 & 0 & 0 & 0 & 0 & 0 & \boldsymbol{\mathcal{D}}_7 & \boldsymbol{\mathcal{B}}_7 & \boldsymbol{\mathcal{U}}_7 & 0 & 0 \\
0 & \boldsymbol{\mathcal{V}}_8 & 0 & 0 & \boldsymbol{F}_8 & 0 & 0 & \boldsymbol{\mathcal{D}}_8 & 0 & 0 & 0 \\
0 & 0 & \boldsymbol{\mathcal{V}}_9 & 0 & 0 & \boldsymbol{F}_9 & 0 & 0 & \boldsymbol{\mathcal{D}}_9 & 0 & 0 \\
0 & 0 & 0 & 0 & 0 & 0 & 0 & 0 & 0 & \boldsymbol{I} & 0 \\
0 & 0 & 0 & 0 & 0 & 0 & 0 & 0 & 0 & 0 & \boldsymbol{I}
\end{bmatrix} \tag{A-103}$$

where $\boldsymbol{I}$ was the identity matrix

The global load vector was constructed using the node load vectors $\boldsymbol{\mathcal{G}}_j$ as

$$\boldsymbol{R}_D = [\boldsymbol{\mathcal{G}}_1 \;\; \boldsymbol{\mathcal{G}}_2 \;\; \boldsymbol{\mathcal{G}}_3 \;\; \boldsymbol{\mathcal{G}}_4 \;\; \boldsymbol{\mathcal{G}}_5 \;\; \boldsymbol{\mathcal{G}}_6 \;\; \boldsymbol{\mathcal{G}}_7 \;\; \boldsymbol{\mathcal{G}}_8 \;\; \boldsymbol{\mathcal{G}}_9 \;\; \boldsymbol{\mathcal{G}}_{10} \;\; \boldsymbol{\mathcal{G}}_{11}]^T \tag{A-104}$$

The global solution vector was constructed using the node solution vectors $\boldsymbol{C}_j$ as

$$\boldsymbol{C}_D = [\boldsymbol{C}_1 \ \boldsymbol{C}_2 \ \boldsymbol{C}_3 \ \boldsymbol{C}_4 \ \boldsymbol{C}_5 \ \boldsymbol{C}_6 \ \boldsymbol{C}_7 \ \boldsymbol{C}_8 \ \boldsymbol{C}_9 \boldsymbol{C}_{10} \ \boldsymbol{C}_{11}]^T \tag{A-105}$$

APPENDIX B
DISCOM PROGRAM LISTING

The program listing for DISCOM is presented in this appendix. A variable listing is given for the the key variables used in the development of DISCOM. DISCOM was developed using using 'Compaq Visual Fortran, Version 6.1' with double precision accuracy. The main program and key subroutines are included as sections. The subroutines associated with the key subroutines are given as sub-sections.

B.1 Variable Listing

The variables used in the program were different from the variables used in the document. The key program and document variables are given in Table B.1.

Table B.1: Variable listing for DISCOM.

Program Variable	Document Variable	Description and/or equation reference
A	$\boldsymbol{\mathcal{A}}$	A-38
akg	$\boldsymbol{K}_D$	global coefficient matrix
B	$\boldsymbol{\mathcal{B}}$	A-38
cin_r	$\frac{\partial \phi}{\partial r}$	A-13, A-16, A-18
cin_z	$\frac{\partial \phi}{\partial z}$	A-15, A-17, A-19
D	$\boldsymbol{\mathcal{D}}$	A-37
F	$\boldsymbol{\mathcal{F}}$	A-38
G	$\boldsymbol{\mathcal{G}}$	A-38
H	$\boldsymbol{\mathcal{H}}$	A-38

continued on next page

Table B.1: *continued*

Program Variable	Document Variable	Description and/or equation reference
phi_r	$\frac{\partial \phi}{\partial r}$	A-13, A-16, A-18
phi_rr	$\frac{\partial^2 \phi}{\partial r^2}$	A-12
phi_z	$\frac{\partial \phi}{\partial z}$	A-15, A-17, A-19
phi_zz	$\frac{\partial^2 \phi}{\partial z^2}$	A-14
rhs	$\boldsymbol{R}_D$	global load vector
sol	$\boldsymbol{C}_D$	global solution vector
T	$\mathcal{T}$	A-38
U	$\mathcal{U}$	A-38
V	$\mathcal{V}$	A-38
W	$\mathcal{W}$	A-38
xi_o_d	$\xi_{o,D}$	convergence criterion

B.2 Program Listing

B.2.1 Main Program

```
!Program to calculate the distributions of concentrations and
!solution potential in a disbonded coating system. The program
!uses the method of finite differences to discretize the
!governing equations for the mass-transfer of species. The
!program accounts for migration and diffusion mass-transfer and
!electroneutrality explicitly.

!This program accepts 'input_data .inp' for input data and
!outputs the calculated results in the file 'output_ss.out'
      use big_stuff
      implicit real*8 (A-H,O-Z)
      allocate (akg(4500,4500),akgtemp(4500,4500))
      call input_data
      call oxygen_distribution
      call disbonded_coating
      call outputfile
      deallocate (akg,akgtemp)
      end
```

B.2.2 Input Data File

```
0.5d0


fe_hydrolysis                no

domain             inn
\
surface                  0.5d0
gap                      0.05d0
coat                     0.05d0
mouth                    0.25d0
\
dhr                      0.0125d0
dhz                      0.025d0
dis_up                   0.00d0
dis_out                  0.0d0
\
fe dissolution       yes
o2 reduction         yes
h2 evolution yes
\
Na+           1.d-3
Cl-           1.d-3
OH-           1.d-7
Fe+2         1.d-10
\
bulko2        2.78d-4
```

B.2.3 Input Data

```
      subroutine input_data
      implicit real*8(A-H,O-Z)
      include 'geometry_data.for'
      include 'data_1.for'
      include 'system_data.for'
      character name*20
      print *,'input_data*****'
!---------------------------------------------------------------------
!Input data read from data file
      open(unit=10,file='input-data.inp',status='unknown')
      rewind 10
      read(10,190)name,pname      ! program name
      read(10,100)name,vapp       ! metal potential
      read(10,100)name,xi_o_d       ! convergence criterion
      read(10,190)name,fe_hydro   ! inclusion of Fe(OH)+
!Inner system or Exended system domain
      read(10,190)name,domain
      read(10,*)line
!domain dimensions
!surface=length of metal surface
      read(10,100)name,surface
      read(10,100)name,gap        ! gap=gap dimension
      read(10,100)name,coat       ! coat=coating thickness
```

```
      read(10,100)name,amouth     ! amouth=mouth length
      read(10,*)line
!grid spacings
      read(10,100)name,dhr        !dhr=spacing in r-direction
      read(10,100)name,dhz        !dhz=spacing in z-direction
      read(10,*)line
!dimensions for Extended domain
      read(10,100)name,dis_up
      read(10,100)name,dis_out
      read(10,*)line
!electrochemical reactions considered
      read(10,190)name,corr       ! iron dissolution
      read(10,190)name,o2red      ! oxygen reduction
      read(10,190)name,h2evo      ! hydrogen evolution
      read(10,*)line
!bulk concentration of speices in M
      do 2 i=1,4
          read(10,*)name,cdata
          con(i)=cdata
2         con(i)=con(i)*0.001d0   ! converting to mol/cm3
      read(10,*)line
! bulko2=bulk O2 concentration in M
      read(10,*)name,bulko2
      bulko2=bulko2*0.001d0       ! mol/dm3 to mol/cm3
      close(10)
!---------------------------------------------------------------
      nspec=4                     ! # species
      nvar=5                      ! # dependent variables
! Charge number for species
      z(1)=1                      ! Na+
      z(2)=-1                     ! Cl-
      z(3)=-1                     ! OH-
      z(4)=2                      ! Fe+2
! diffusion coefficients
      dif(1)=1.3341d-5            ! Na+
      dif(2)=2.0344d-5            ! Cl-
      dif(3)=5.2458d-5            ! OH-
      dif(4)=0.71231d-5           ! Fe+2
      difo2=2.92d-5               ! O2
! index
      ina=1                       ! Na+
      icl=2                       ! Cl-
      ioh=3                       ! OH-
      ife=4                       ! Fe+2
      ifeoh=0
! species identification
      specie(1)='Na+         '
      specie(2)='Cl-         '
      specie(3)='OH-        '
      specie(4)='Fe+2        '
!---------------------------------------------------------------
!inclusion of  FeOH+
      if(fe_hydro(1:3).eq.'yes')then
          specie(5)='FeOH+       '
          ifeoh=5                     ! index for FeOH+
```

```
          z(5)=1                        ! charge number for FeOH+
          nspec=5                       ! # increment species
          nvar=6                        ! # increment variables
          dif(5)=0.71231E-5             ! diffsuion coefficient
!akstar=equilibrium constant
          akstar=(10**(5.7d0))*1000.d0
!Calculation of Fe+2 and Fe(OH)+ from total ferrous ion
          con_fe=con(ife)
          con(ife)=con(ife)/(1.d0+akstar*con(ioh))
          con(ifeoh)=con_fe-con(ife)
      endif
!---------------------------------------------------------------------
! scaling
      dcsc=1.d-5      ! diffusion coefficients
      consc=1.d-10    ! concentrations
!     dcsc=1.d0 !   consc=1.d0

! output of input data on screen
      do i=1,nspec
          print *,i,specie(i),con(i)
          difs(i)=dif(i)/dcsc
          con(i)=con(i)/consc
          zdifs(i)=z(i)*difs(i)
      enddo
      write(*,140)'          surface (cm) =',surface
      write(*,140)'              gap (cm) =',gap
      write(*,140)'             coat      =',coat
      write(*,140)'            mouth      =',amouth
      write(*,140)'              dhr      =',dhr
      write(*,140)'              dhz      =',dhz
! Common terms that include dhr and dhz
      dhrr=dhr**2
      dhzz=dhz**2
      dhr2=dhr*2.d0
      dhz2=dhz*2.d0
! Calculation of variables used to discretize domain shown
!in Figure 6-1.
      nesurf=(surface/dhr)        !# elements on OB
      nnsurf=nesurf+1             !# nodes on OB
      netop=(surface-amouth)/dhr  !# elements on CD
      necoat=coat/dhz             !# elements on DE
      nerhs=(gap/dhz)             !# elements on BC
      nemou=(amouth/dhr)          !# elements on FE
      nelhs=(gap+coat)/dhz        !# elements on OF
      ne_up=dis_up/dhz            !# elements on FR
      ne_out=dis_out/dhr          !ne_out=0
100     format(a21,f8.3)
190     format(a21,a20)
140     format(a40,2x,f8.5)
      return
      end
```

B.2.4 Disbonded Coating

```
!Subroutine to calculate the distributions of concentrations
!and solution potential in the disbonded coating domain.
      subroutine disbonded_coating
      use big_stuff
      implicit real*8 (A-H,O-Z)
      include 'data_1.for'
      include 'geometry_data.for'
      include 'system_data.for'
      print *,'disbonded coating*****'
!Discretize the domain into nodes using mesh.
      call mesh
!Set initial guess.
      call initial_guess
!Set nodes at which dependent variables are unknown.
      call set_unknowns
10  continue !Update cold with cin.
      cold=cin
!Calcuate the current densities of the electrochemical reaction
!as a function of position on the metal surface.
      call current
!Discretized the linearized governing equations.
      call governing_equations
!Solve the system of linear equations.
      call solver
!Calculate convergence criterion.
      call compare_ss
      print *,emax
!Determine whether to repeat or end iterative procedure.
      if(dabs(emax).gt.conv)goto 10
      return
      end
```

Mesh

```
!Subroutine that discretizes the domain into nodes.
      subroutine mesh
      implicit real*8 (A-H,O-Z)
      include 'geometry_data.for'
      dimension np(4)
      print *,'   mesh*****'
!mesh_data.out is an output file for the node positions. cord
!stores the r and z position of a node.inode stores the node
!positions for the nodes surrounding a given node that are used in
!the discretization of governing !equations.
      open(unit=10,file='mesh_data.inp',status='unknown')
      close(unit=10,status='delete')
      open(unit=10,file='mesh_data.inp',status='unknown')
      ic=0    !node counter
!Nodes on metal surface
      do i=1,nnsurf
          np=0
          ic=ic+1
          np(1)=nnsurf+i
```

```
          if(i.ne.nnsurf)np(2)=ic+1
          np(4)=ic-1
          rd=(i-1)*dhr
          zd=0.d0
          write(10,100)ic,rd,zd,(np(ij),ij=1,4)
          cord(ic,1)=rd
          cord(ic,2)=zd
          do 10 ik=1,4
10            inode(ic,ik)=np(ik)
      enddo
!Nodes with 0<z<gap
      do j=2,nerhs
          zd=(j-1)*dhz
          k=nnsurf*j
          do i=1,nnsurf
              np=0
              ic=ic+1
              np(1)=k+i
              if(j.eq.nerhs+1.and.i.gt.nemou+1)np(1)=0
              if(i.ne.nnsurf)np(2)=ic+1
              np(3)=ic-nnsurf
              np(4)=ic-1
              if(i.eq.1)np(4)=0
              rd=(i-1)*dhr
              write(10,100)ic,rd,zd,(np(ij),ij=1,4)
              cord(ic,1)=rd
              cord(ic,2)=zd
              do 20 ik=1,4
20                inode(ic,ik)=np(ik)
          enddo
      enddo
!Nodes with z=gap
      j=nerhs+1
      zd=(j-1)*dhz
      k=nnsurf*j
      do i=1,nnsurf
          ic=ic+1
          np=0
          np(1)=k+i
          if(i.gt.nemou+1)np(1)=0
          if(i.ne.nnsurf)np(2)=ic+1
          np(3)=ic-nnsurf
          np(4)=ic-1
          if(i.eq.1)np(4)=0
          rd=(i-1)*dhr
          write(10,100)ic,rd,zd,(np(ij),ij=1,4)
          cord(ic,1)=rd
          cord(ic,2)=zd
          do 30 ik=1,4
30            inode(ic,ik)=np(ik)
      enddo
!Nodes with z>gap
      do j=1,necoat
          np=0
          zd=((j+nerhs+1)-1)*dhz
```

```
            do i=1,nemou+1
                np=0
                ic=ic+1
                if(j.ne.necoat)np(1)=ic+nemou+1
                if(i.ne.nemou+1)np(2)=ic+1
                np(3)=ic-(nemou+1)
                if(j.eq.1)np(3)=ic-nnsurf
                if(i.ne.1)np(4)=ic-1
                rd=(i-1)*dhr
                write(10,100)ic,rd,zd,(np(ij),ij=1,4)
                cord(ic,1)=rd
                cord(ic,2)=zd
                do 40 ik=1,4
40                  inode(ic,ik)=np(ik)
            enddo
        enddo
        close(10)
        nodes=ic        ! nodes=total number of nodes
        print *,'   total # nodes=',nodes
100     format(i4,2x,2(e12.5,2x),5(i5,2x))
        close(10)
        return
        end
```

Initialize guess

```
!Subroutine to initialize the dependent variables.
        subroutine initial_guess
        implicit real*8 (A-H,O-Z)
        include 'data_1.for'
        include 'system_data.for'
        include 'geometry_data.for'
        do jn=1,nodes
            do is=1,nspec
                cin(is,jn)=con(is)
            enddo
            cin(nvar,jn)=0.d0
        enddo
        return
        end
```

Set unknowns

```
!Subroutine that calculates the total number of nodes where
!there are unknowns and
        subroutine set_unknowns
        use big_stuff
        implicit real*8 (A-H,O-Z)
        include 'data_1.for'
        include 'geometry_data.for'
        include 'system_data.for'
        iun_new=0
        do jn=nodes-nemou,nodes
            iun_new(jn)=1
        enddo
```

```
!where for a node j iun_new(j)=1 if the conditions are known
!and iun_new(j)=0 if the conditions are unknown
      iut_new=nodes-(nemou+1)
!where iut_new is the number of nodes where there are unknowns
      ik=0
      iun_con=0
      do i=1,nodes
          do is=1,nvar
              ik=ik+1
              if(iun_new(i).eq.1)iun_con(ik)=1
          enddo
      enddo
!where if the dependent variable is known then iun_con(j)=0,
!else iun_con(j)=1
    return
    end
```

Compare

```
!Subroutine to calculate the convergence criterion
      subroutine compare
      use big_stuff
      implicit real*8 (A-H,O-Z)
      include 'data_1.for'
      include 'geometry_data.for'
      include 'system_data.for'
      emax_ss=0.d0
!where emax_ss stores the maximum percentage difference for each
!dependent variable between calculated and guess values
!Calculation of emax_ss
      do jn=1,nodes
          do is=1,nvar
              perc=0.d0
              if(cold(is,jn).ne.0.d0)then
              perc=(100.d0*(cin(is,jn)-cold(is,jn))/cold(is,jn))
              endif
             if(dabs(perc).gt.dabs(emax_ss(is)))emax_ss(is)=perc
              cin(is,jn)=we*cin(is,jn)+(1.d0-we)*cold(is,jn)
          enddo
      enddo
      emax=0.d0
!where emax is the convergence criterion
      do is=1,nvar
          if(dabs(emax_ss(is)).gt.dabs(emax))emax=emax_ss(is)
      enddo
!Checking for negative concentrations
      do jn=1,nodes
          do is=1,nspec
              if(cin(is,jn).lt.0.)then
                  print *,is,cin(is,jn)
                  print *,cord(jn,1),cord(jn,2)
                  print *,'   '
              endif
          enddo
      enddo
```

```
      return
      end
```

Current

```
!Subroutine to calculate the current densities of the
!electrochemical reaction as a function of position on the metal
!surface.
      subroutine current
      implicit real*8 (A-H,O-Z)
      include 'geometry_data.for'
      include 'system_data.for'
      include 'data_1.for'
      vappt=vapp*1000.d0  !Conversion from volts to mV
      do j=1,nnsurf
          ailim=ailimg(j)
          aife=0.d0
          aio2=0.d0
          aih2=0.d0
          phi=cin(nvar,j)*1000.d0*(gas*temp)/far
!where phi is the dimensionless potential
          aa=(vappt-phi-eqpot_fe)/beta_fe
          bb=(vappt-phi-eqpot_o2)/beta_o2
          cc=-(vappt-phi-eqpot_h2)/beta_h2
!where aa, bb, and cc are exponents used in the polarization
!expressions for the current densities of the electrochemical
!reactions. Current density calculated in A/cm2. !anodic =>
positive ;cathodic => negative
          if(corr(1:3).eq.'yes')aife=(10**aa)*1.e-6
!where aife is the iron dissolution current density at node j
          if(o2red(1:3).eq.'yes')
     *      aio2=-1.d0*(1.d0/((1.d0/ailim)+10**bb))*1.e-6
!where aio2 is the oxygen reduction current density at node j
          if(h2evo(1:3).eq.'yes')aih2=-1.d0*(10**(cc))*1.e-6
!where aih2 is the hydrogen evolution current density at node j
          fxoh(j)=(aio2+aih2)/(-1.d0*far)
!where the flux of hdroxide ion is stored in fxoh
          fxfe(j)=aife/(2.d0*far)
!where the flux of ferrous ion is stored in fxfe
          fxo2(j)=aio2/(4.d0*far)
!where the flux of hydroxide ion due to oxygen reduction stored in
!fxo2
          cde(j)=aife+aio2+aih2
!where the net current density stored in cde
      enddo
      return
      end
```

B.2.5 Solver

```
!Subroutine that solves the  system of linear equations for a
!given a coefficient matrix akg and a load vector rhs using the
!LAPACK solver.
      subroutine solver
```

```
      use big_stuff
      implicit real*8 (A-H,O-Z)
      include 'data_1.for'
      include 'system_data.for'
      include 'geometry_data.for'
      dimension np(4)
      call set_sol
      call load_vector
      call coeff_matrix
      n=iut_new*nvar
      call LAPACK_link(rhsnew,dd,n,nmax)
      k=0
      do jn=1,nodes
          if(iun_new(jn).eq.0)then
              do is=1,nvar
                  k=k+1
                  cin(is,jn)=rhsnew(k)
              enddo
          endif
      enddo
      return
      end
```

Load vector

```
!Subroutine that reduces the load vector correcting for known
!concentrations.
    subroutine load_vector
    use big_stuff
    implicit real*8 (A-H,O-Z)
    include 'data_1.for'
    include 'system_data.for'
    include 'geometry_data.for'
    do ir=1,nodes*nvar
        sum=0.d0
        do jc=1,nodes*nvar
            if(iun_con(jc).eq.1)then
                sum=sum+akg(ir,jc)*sol(jc)
            endif
        enddo
        rhs(ir)=rhs(ir)-sum
    enddo
    i=0
    rhsnew=0.d0
    do ir=1,nodes*nvar
        if(iun_con(ir).eq.0)then
            i=i+1
            rhsnew(i)=rhs(ir)
        endif
    enddo
    return
    end
```

Coeff matrix

```
!Subroutine that reduces the coefficient matrix by removing
!columns and rows of essential nodes.
    subroutine coeff_matrix
    use big_stuff
    implicit real*8 (A-H,O-Z)
    include 'data_1.for'
    include 'system_data.for'
    include 'geometry_data.for'
    akgtemp=0.d0            !initialize akgtemp
    ic=0
    do ir=1,nodes*nvar      !keeping rows
        if(iun_con(ir).eq.0)then
            ic=ic+1
            do jc=1,nvar*nodes
                akgtemp(ic,jc)=akg(ir,jc)
            enddo
        endif
    enddo
    akg=0.d0
    ic=0
    do ir=1,nodes*nvar      !keeping columns
        if(iun_con(ir).eq.0)then
            ic=ic+1
            do jc=1,nvar*nodes
                akg(jc,ic)=akgtemp(jc,ir)
            enddo
        endif
    enddo
    return
    end
```

Set sol

```
!Subroutine that sets up a global solution vector.
    subroutine set_sol
    use big_stuff
    implicit real*8 (A-H,O-Z)
    include 'data_1.for'
    include 'geometry_data.for'
    include 'system_data.for'
    k=0
    do jn=1,nodes
        do is=1,nvar
            k=k+1
            sol(k)=cin(is,jn)
        enddo
    enddo
    return
    end
```

LAPACK link

```
!Subroutine that calls the LaPACK solver.
    subroutine LAPACK_link(B,D,N,NX)
    use big_stuff
    real*8 B(NX),TOL,D,C
    real*8, ALLOCATABLE :: Bnew(:),Anew(:,:)
    integer, ALLOCATABLE :: indx(:),ipiv(:)
    integer lda,ldb
    ALLOCATE(Bnew(N), Anew(N,N))
    ALLOCATE(indx(n), ipiv(n))
    Bnew=0.d0
    Anew=0.d0
    Bc=0.d0
    do i=1,N
        do j=1,N
            Anew(i,j)=akg(i,j)
        enddo
        Bnew(i)=B(i)
    enddo
    nrhs=1
    lda=n
    ldb=n
!Call to LAPACK.  LAPACK not included in listing. Obtained from
!www.netlib.org
    call DGESV( N, NRHS, Anew, LDA, IPIV, Bnew, LDB, INFO )
    B=0.d0
    do i=1,n
        B(i)=bnew(i)
    enddo
    DEALLOCATE(Bnew,Anew , ipiv, indx)
    return
    end
```

B.2.6 Governing Equations

```
!Subrountine to discretize the linearized governing equations.
      subroutine governing_equations
      use big_stuff
      implicit real*8 (A-H,O-Z)
      include 'data_1.for'
      include 'geometry_data.for'
      include 'system_data.for'
      dimension np(4)
      print *,'   gov_eqs_lin***'
!Initializing to zero value.
      akg=0.d0            ! akg=global coefficient matrix
      rhs=0.d0            ! rhs=global load vector
      do jn=1,nodes
!where nodes is the total number of nodes in the domain
!Initialize node coefficient matrices and node load vector
         call initialize_2d
         do i=1,4
            np(i)=inode(jn,i)
```

```
          enddo
!where inode(jn,i) in terms of computational notation is
!inode(jn,1)=j1; inode(jn,2)=j2; inode(jn,3)=j3; inode(jn,4)=j4
          call nacl_gov_eqs(jn,np)
          call oh_gov_eq(jn,np)
          call fe_gov_eq(jn,np)
          call feoh_gov_eq(jn,np)
          call neutrality_gov_eq(jn)
          call assemble(jn)
      enddo
      return
      end
```

NaCl gov eqs

```
!Subroutine for the stagnant species.
      subroutine nacl_gov_eqs(jn,nv)
      implicit real*8 (A-H,O-Z)
      include 'data_1.for'
      include 'system_data.for'
      include 'geometry_data.for'
      dimension np(4),nv(4)
      np=nv
      is=ina
      call discretize_eq(is,jn,np)
      is=icl
      call discretize_eq(is,jn,np)
      return
      end
```

FeOH gov eq

```
!Subroutine for the discretization of the equilibrium
!relationship for the homogeneous reaction.
      subroutine feoh_ss_lin(jn,nv)
      implicit real*8 (A-H,O-Z)
      include 'geometry_data.for'
      include 'data_1.for'
      include 'system_data.for'
      dimension np(4),nv(4)
      if(ifeoh.eq.0)return
      ig=ifeoh
      akstar=(10.d0**(5.7d0))*1000.d0*consc
      D(ig,ifeoh)=1.d0
      D(ig,ife)=-akstar*cin(ioh,jn)
      D(ig,ioh)=-akstar*cin(ife,jn)
      G(ig)=-akstar*cin(ife,jn)*cin(ioh,jn)
      return
      end
```

OH gov eq

```
!Subroutine for the conservation of hydroxide species.
      subroutine oh_gov_eq(jn,nv)
```

```
      implicit real*8 (A-H,O-Z)
      include 'geometry_data.for'
      include 'data_1.for'
      include 'system_data.for'
      dimension np(4),nv(4)
      np=nv
      is=ioh
      ig=is
      call discretize_eq(is,jn,np)
! boundary condition for node is on metal surface
      if(np(3).eq.0)then
          if(cord(jn,2).eq.0.)then
              G(ig)=G(ig)+fxoh(jn)/(consc*dcsc)
          endif
          return
      endif
      if(np(1).eq.0)return
      if(np(2).eq.0)return
      if(np(4).eq.0)return
      is=ifeoh
      if(is.ne.0)then
          cf=+1.d0
          call non_boundary_node(jn,ig,np,is,cf)
      endif
      return
      end
```

Fe gov eq

```
!Subroutine for conservation of ferrous species.
      subroutine fe_gov_eq(jn,nv)
      implicit real*8 (A-H,O-Z)
      include 'geometry_data.for'
      include 'data_1.for'
      include 'system_data.for'
      dimension np(4),nv(4)
      np=nv
      is=ife
      ig=is
      if(is.ne.0)call discretize_eq(is,jn,np)
      if(np(3).eq.0)then
          if(cord(jn,2).eq.0.)then
!on metal surface
              G(ig)=G(ig)+fxfe(jn)/(consc*dcsc)
          endif
          return
      endif
      if(np(1).eq.0.or.np(2).eq.0.or.np(4).eq.0)return
      is=ifeoh
      if(is.ne.0)then
          cf=+1.d0
          call non_boundary_node(jn,ig,np,is,cf)
      endif
      return
      end
```

Neutrality gov eq

```
!Subroutine to discretize electroneutrality condition.
      subroutine neutrality_ss_lin(jn)
      implicit real*8 (A-H,O-Z)
      include 'data_1.for'
      include 'system_data.for'
      include 'geometry_data.for'
      ig=nvar
      do i=1,nspec
          D(ig,i)=z(i)
      enddo
      return
      end
```

Discretize eq

```
!Subroutine to discretize governing equation for mass-transfer.
      subroutine discretize_eq(is,jn,np)
      implicit real*8 (A-H,O-Z)
      include 'data_1.for'
      include 'system_data.for'
      include 'geometry_data.for'
      dimension np(4)
      ig=is
!initialize node load vector G
      G(ig)=0.d0
      if(np(3).eq.0)then
          call metal_node(jn,ig,np)
          return
      elseif(np(1).eq.0)then
          call coat_node(jn,ig,np)
          return
      elseif(np(2).eq.0)then
          call vertical_node(jn,ig,np)
          return
      elseif(np(4).eq.0)then
          call axis_node(jn,ig,np)
          return
      else
!non-boundary node
          cf=+1.d0
          call non_boundary_node(jn,ig,np,is,cf)
      endif
      return
      end
```

Non boundary node

```
!Subroutine to calculate elements of node coefficient matrices
!and node load vectors of a non-boundary node.
      subroutine non_boundary_node(jn,ig,np,is,cf)
      implicit real*8 (A-H,O-Z)
      include 'data_1.for'
      include 'system_data.for'
```

```
      include 'geometry_data.for'
      dimension np(4)
!cin_z= partial c/partial z
      cin_z=(cin(is,np(1))-cin(is,np(3)))/dhz2
!cin_r= partial c/partial r
      cin_r=(cin(is,np(2))-cin(is,np(4)))/dhr2
!phi_z= partial phi/partial z
      phi_z=(cin(nvar,np(1))-cin(nvar,np(3)))/dhz2
!phi_r= partial phi/partial r
      phi_r=(cin(nvar,np(2))-cin(nvar,np(4)))/dhr2
!phi_rr= partial 2 phi/partial r2
      phi_rr=(cin(nvar,np(2))-2.d0*cin(nvar,jn)
     *                       +cin(nvar,np(4)))/dhrr
!phi_zz= partial 2 phi/partial z2
      phi_zz=(cin(nvar,np(1))-2.d0*cin(nvar,jn)
     *                       +cin(nvar,np(3)))/dhzz
      rdis=cord(jn,1)
      A_is=difs(is)/dhzz + zdifs(is)*phi_z/dhz2
      A_temp=zdifs(is)*(cin(is,jn)/dhzz   + cin_z/dhz2)
      A(ig,is)=A_is*cf
      A(ig,nvar)=A(ig,nvar)+cf*A_temp
      B_is=difs(is)/dhrr + zdifs(is)*phi_r/dhr2
      B_temp=zdifs(is)*(cin(is,jn)/dhrr   + cin_r/dhr2)
      B_is=B_is+difs(is)/(rdis*2.d0*dhr)
      B_temp=B_temp+zdifs(is)*cin(is,jn)/(rdis*2.d0*dhr)
      B(ig,is)=B_is*cf
      B(ig,nvar)=B(ig,nvar)+cf*B_temp
      D_is=-2.d0*difs(is)*(1.d0/dhrr + 1.d0/dhzz)
     *      + zdifs(is)*(phi_rr+phi_zz)
     *      + zdifs(is)*phi_r/rdis
      D_temp=-2.d0*zdifs(is)*cin(is,jn)
     *          *(1.d0/dhrr + 1.d0/dhzz)
      D(ig,is)=D_is*cf
      D(ig,nvar)=D(ig,nvar)+cf*D_temp
      F_is=difs(is)/dhzz - zdifs(is)*phi_z/dhz2
      F_temp=zdifs(is)*(cin(is,jn)/dhzz   - cin_z/dhz2)
      F(ig,is)=F_is*cf
      F(ig,nvar)=F(ig,nvar)+cf*F_temp
      H_is=difs(is)/dhrr - zdifs(is)*phi_r/dhr2
      H_temp=zdifs(is)*(cin(is,jn)/dhrr   - cin_r/dhr2)
      H_is=H_is - difs(is)/(rdis*2.d0*dhr)
      H_temp=H_temp -zdifs(is)*cin(is,jn)/(rdis*2.d0*dhr)
      H(ig,is)=H_is*cf
      H(ig,nvar)=H(ig,nvar)+cf*H_temp
      G(ig)=zdifs(is)*(cin_r*phi_r+cin_z*phi_z
     *          +cin(is,jn)*(phi_rr+phi_zz))
     *          + zdifs(is)*cin(is,jn)*phi_r/rdis
      return
      end
```

Metal node

```
!Subroutine to calculate elements of node coefficient matrices
!and node load vectors on metal surface.
      subroutine metal_node(jn,ig,np)
```

```
      implicit real*8 (A-H,O-Z)
      include 'data_1.for'
      include 'system_data.for'
      include 'geometry_data.for'
      dimension np(4)
      is=ig
      phi_z=(-3.d0*cin(nvar,jn)+4.d0*cin(nvar,np(1))-
     *          cin(nvar,np(1)+nnsurf))/dhz2
      T(ig,is)=difs(is)/dhz2
      T(ig,nvar)=zdifs(is)*cin(is,jn)/dhz2
      A(ig,is)=-4.d0*difs(is)/dhz2
      A(ig,nvar)=-4.d0*zdifs(is)*cin(is,jn)/dhz2
      D(ig,is)=3.d0*difs(is)/dhz2 - zdifs(is)*phi_z
      D(ig,nvar)=3.d0*zdifs(is)*cin(is,jn)/dhz2
      G(ig)=-zdifs(is)*cin(is,jn)*phi_z
      return
      end
```

Coat node

```
!Subroutine to calculate elements of node coefficient matrices
!and node load vectors on bulk boundary.
      subroutine coat_node(jn,ig,np)
      implicit real*8 (A-H,O-Z)
      include 'data_1.for'
      include 'system_data.for'
      include 'geometry_data.for'
      dimension np(4)
      if(np(1).eq.0)then
          if(cord(jn,2).eq.gap)then
              if(cord(jn,1).gt.amouth)then
                  is=ig
                  phi_z=(3.d0*cin(nvar,jn)-4.d0*cin(nvar,np(3))+
     *            cin(nvar,np(3)-nnsurf))/dhz2
                  D(ig,is)=-3.d0*difs(is)/dhz2 - zdifs(is)*phi_z
                  D(ig,nvar)=-3.d0*zdifs(is)*cin(is,jn)/dhz2
                  F(ig,is)=4.d0*difs(is)/dhz2
                  F(ig,nvar)=4.d0*zdifs(is)*cin(is,jn)/dhz2
                  V(ig,is)=-difs(is)/dhz2
                  V(ig,nvar)=-zdifs(is)*cin(is,jn)/dhz2
                  G(ig)=-zdifs(is)*cin(is,jn)*phi_z
                  return
              endif
          endif
      endif
      return
      end
```

Vertical node

```
!Subroutine to calculate elements of node coefficient matrices
!and node load vectors on vertical section boundary.
      subroutine vertical_node(jn,ig,np)
      implicit real*8 (A-H,O-Z)
      include 'data_1.for'
```

```
      include 'system_data.for'
      include 'geometry_data.for'
      dimension np(4)
      is=ig
      phi_r=(3.d0*cin(nvar,jn)-4.d0*cin(nvar,np(4))+
     *          cin(nvar,np(4)-1))/dhr2
      D(ig,is)=-3.d0*difs(is)/dhr2 -zdifs(is)*phi_r
      D(ig,nvar)=-3.d0*zdifs(is)*cin(is,jn)/dhr2
      H(ig,is)=4.d0*difs(is)/dhr2
      H(ig,nvar)=4.d0*zdifs(is)*cin(is,jn)/dhr2
      W(ig,is)=-difs(is)/dhr2
      W(ig,nvar)=-zdifs(is)*cin(is,jn)/dhr2
      G(ig)=-zdifs(is)*cin(is,jn)*phi_r
      return
      end
```

Axis node

```
!Subroutine to calculate elements of node coefficient matrices
!and node load vectors on axis boundary.
      subroutine axis_node(jn,ig,np)
      implicit real*8 (A-H,O-Z)
      include 'data_1.for'
      include 'system_data.for'
      include 'geometry_data.for'
      dimension np(4)
      is=ig
      phi_r=(-3.d0*cin(nvar,jn)+4.d0*cin(nvar,np(2))-
     *          cin(nvar,np(2)+1))/dhr2
      U(ig,is)=difs(is)/dhr2
      U(ig,nvar)=zdifs(is)*cin(is,jn)/dhr2
      B(ig,is)=-4.d0*difs(is)/dhr2
      B(ig,nvar)=-4.d0*zdifs(is)*cin(is,jn)/dhr2
      D(ig,is)=3.d0*difs(is)/dhr2 - zdifs(is)*phi_r
      D(ig,nvar)=3.d0*zdifs(is)*cin(is,jn)/dhr2
      G(ig)=-zdifs(is)*cin(is,jn)*phi_r
      return
      end
```

Assemble

```
!Subroutine to assemble the node coefficient matrices and node
!load vector into the global coefficient  matrix and global
!load vector, respectively.
      subroutine assemble(jn)
      use big_stuff
      implicit real*8 (A-H,O-Z)
      include 'geometry_data.for'
      include 'data_1.for'
      include 'system_data.for'
      dimension np(4)
      np=0
      do i=1,4
          np(i)=inode(jn,i)
      enddo
```

```
      ic=jn
      i=0
      ifst=(jn-1)*nvar+1
      isec=(jn-1)*nvar+nvar
      do ir=ifst,isec
          i=i+1
          do j=1,nvar
              akg(ir,(ic-1)*nvar+j)=D(i,j)
              if(np(2).ne.0)akg(ir,(np(2)-1)*nvar+j)=B(i,j)
              if(np(1).ne.0)akg(ir,(np(1)-1)*nvar+j)=A(i,j)
              if(np(4).ne.0)akg(ir,(np(4)-1)*nvar+j)=H(i,j)
              if(np(3).ne.0)akg(ir,(np(3)-1)*nvar+j)=F(i,j)
              if(np(3).eq.0)akg(ir,(np(1)+nnsurf-1)*nvar+j)
     *                                        =T(i,j)
              if(np(4).eq.0)akg(ir,(np(2)-1+1)*nvar+j)=U(i,j)
              if(np(2).eq.0)akg(ir,(np(4)-1-1)*nvar+j)=W(i,j)
              if(np(1).eq.0)then
                  if(cord(jn,2).eq.gap)then
                      if(cord(jn,1).gt.amouth)then
                          akg(ir,(np(3)-nnsurf-1)*nvar+j)
     *                                        =V(i,j)
                      endif
                  endif
              endif
          enddo
      enddo
      do i=1,nvar
          rhs((jn-1)*nvar+i)=G(i)
      enddo
      return
      end
```

Initialize 2D

```
!Subroutine to initialize elements of node coefficient matrices
!and node load vector to 0.
      subroutine initialize_2d
      use big_stuff
      implicit real*8 (A-H,O-Z)
      include 'data_1.for'
      T=0.d0
      U=0.d0
      V=0.d0
      W=0.d0
      A=0.d0
      B=0.d0
      G=0.d0
      D=0.d0
      F=0.d0
      H=0.d0
      return
      end
```

B.2.7 Oxygen Distribution

```
!Subroutine to calculate the distribution of oxygen in the
!domain of the disbonded coating system.
      subroutine oxygen_distribution
      use big_stuff
      implicit real*8 (A-H,O-Z)
      include 'geometry_data.for'
      if(o2red(1:2).eq.'no')return
      print *,'oxygen_fdm*****'
      call mesh
      call set_conditions_o2
      call o2_driver
      call solver_o2
      call calculate_ilim
      return
      end
```

Set conditions o2

```
!Subroutine to set the conditions of oxygen concentration at the
!nodes and to construct the array that identifies the nodes
!where the concentrations are known and unknown.
      subroutine set_conditions_o2
      use big_stuff
      implicit real*8 (A-H,O-Z)
      include 'data_1.for'
      include 'geometry_data.for'
      include 'system_data.for'
      iun_o2=0
!where inu_o2 is an array such that for a given node j the
!condition iun_o2(j)=1 and iun_o2(j)=0 corresponds to the oxygen
!concentration known and the flux of oxygen is known, respectively

!For the nodes on the metal surface and at the bulk boundary the
!oxygen concentration is known
      do jn=1,nnsurf
          iun_o2(jn)=1
      enddo
      do jn=nodes-nemou,nodes
          iun_o2(jn)=1
      enddo
      iut_o2=nodes-(nemou+1)-nnsurf
!where iut_o2=# nodes where flux is known or concentration is
!unknown. Initialize sol where sol stores the concentration of
!oxygen at the nodes
      sol=0.d0
!For the nodes on the bulk boundary set the concentration to the
!bulk value.
      do j=nodes-(nemou+1),nodes
          sol(j)=bulko2
      enddo
      return
      end
```

O2 driver

```
!Subroutine that calculates the values of the elements in the
!coefficient matrix.
      subroutine o2_driver
      implicit real*8 (A-H,O-Z)
      include 'geometry_data.for'
      include 'system_data.for'
      include 'data_1.for'
      dimension np(4)
      print *,'   o2_driver_Oh2***'
!Initialize global coefficient matrix akg and global load vector
!rhs.
      akg=0.d0
      rhs=0.d0
!For all the nodes
      do jn=1,nodes
          call initialize_o2
!Obtain the addresses of surrounding nodes
          do i=1,4
              np(i)=inode(jn,i)
          enddo
          if(np(3).eq.0)then
!on metal surface
              T_o2=1.d0/dhz2
              A_o2=-4.d0/dhz2
              D_o2=3.d0/dhz2
          elseif(np(1).eq.0)then
!bulk or coating boundary
              D_o2=-3.d0/dhz2
              F_o2=4.d0/dhz2
              V_o2=-1.d0/dhz2
          elseif(np(2).eq.0)then
!vertical section boundary
              D_o2=-3.d0/dhr2
              H_o2=4.d0/dhr2
              W_o2=-1.d0/dhr2
          elseif(np(4).eq.0)then
!symmetry axis boundary
              U_o2=1.d0/dhr2
              B_o2=-4.d0/dhr2
              D_o2=3.d0/dhr2
          else
!non-boundary node
              A_o2=1.d0/dhzz
              B_o2=1.d0/dhrr
              D_o2=-2.d0*(1.d0/dhrr + 1.d0/dhzz)
              F_o2=1.d0/dhzz
              H_o2=1.d0/dhrr
              rdis=cord(jn,1)
              B_o2=B_o2+1.d0/(rdis*2.d0*dhr)
              H_o2=H_o2-1.d0/(rdis*2.d0*dhr)
          endif
          G_o2=0.d0
          call assemble_o2_Oh2(jn,np)
      enddo
```

```
      return
      end
```

Solver o2

```
!Subroutine that solves the Laplace equation for the oxygen
!concentration given a coefficient matrix akg and a load vector
!rhs.
      subroutine solver_o2
      use big_stuff
      implicit real*8 (A-H,O-Z)
      include 'data_1.for'
      include 'system_data.for'
      include 'geometry_data.for'
      print *,'   solver_o2***'
!Reduce global load vector correcting for known concentrations
      call load_vector_o2
!Reduce global coefficient matrix
      call coeff_matrix_o2
      print *,'   iut_o2=',iut_o2
      call LAPACK_link(rhsnew,dd,iut_o2,nmax)
      i=0
      do ir=1,nodes
          if(iun_o2(ir).eq.0)then
              i=i+1
              sol(ir)=rhsnew(i)
          endif
      enddo
      return
      end
```

Load vector o2

```
!Subroutine that reduces the load vector correcting for known
!concentrations.
      subroutine load_vector_o2
      use big_stuff
      implicit real*8 (A-H,O-Z)
      include 'data_1.for'
      include 'system_data.for'
      include 'geometry_data.for'
      dimension np(4)
      print *,'   load_vector_o2***'
      rhsnew=0.d0
      do ir=1,nodes
          sum=0.d0
          do jc=1,nodes
              if(iun_o2(jc).eq.1)then
                  sum=sum+akg(ir,jc)*sol(jc)
              endif
          enddo
          rhs(ir)=rhs(ir)-sum
      enddo
      i=0
      rhsnew=0.d0
```

```
      do ir=1,nodes
          if(iun_o2(ir).eq.0)then
              i=i+1
              rhsnew(i)=rhs(ir)
          endif
      enddo
      return
      end
```

Coeff matrix o2

```
!Subroutine that reduces the coefficient matrix by removing
!columns and rows of essential nodes
      subroutine coeff_matrix_o2
      use big_stuff
      implicit real*8 (A-H,O-Z)
      include 'data_1.for'
      include 'system_data.for'
      include 'geometry_data.for'
      dimension np(4)
      print *,'   coeff_matrix_o2***'
      ic=0
      akgtemp=0.d0
      do ir=1,nodes       !striking rows
          if(iun_o2(ir).eq.0)then
              ic=ic+1
              do jc=1,nodes
                  akgtemp(ic,jc)=akg(ir,jc)
              enddo
          endif
      enddo
      akg=0.d0
      ic=0
      do ir=1,nodes       !striking columns
          if(iun_o2(ir).eq.0)then
              ic=ic+1
              do jc=1,nodes
                  akg(jc,ic)=akgtemp(jc,ir)
              enddo
          endif
      enddo
      return
      end
```

Calculate ilim

```
!Subroutine that calculates the mass-transfer-limited current
!density for oxygen reduction on nodes of the metal surface.
      subroutine calculate_ilim
      use big_stuff
      implicit real*8 (A-H,O-Z)
      include 'data_1.for'
      include 'system_data.for'
      include 'geometry_data.for'
      dimension np(4)
```

```
      do j=1,nnsurf
          do i=1,4
              np(i)=inode(j,i)
          enddo
!where np holds the addresses for nodes surrounding node j
          k=np(1)+nnsurf
          dco2dy=(-sol(k)+4.d0*sol(np(1))-3.d0*sol(j))
     *              /(2.d0*dhz)
!where dco2dy (mol/cm3)/cm is the gradient of concentration
!normal to the metal surface using backward difference !equation.
          ailimg(j)=4*far*difo2*dco2dy*1e6
!where ailimg(jn) is the value of the mass-transfer-limited
!current density for O2 reduction at node j in microA/cm2.
      enddo

!Writing values of ailimg to output file.
      open(unit=10,file='ilimo2.out',status='unknown')
      close(unit=10,status='delete')
      open(unit=10,file='ilimo2.out',status='unknown')
      do j=1,nnsurf
          write(10,*),(j-1)*dhr,ailimg(j)
      enddo
      close(10)
      return
      end
```

Assemble o2

```
!Subroutine that assembles the elements of the coefficient matrix
!akg and load vector rhs.
      subroutine assemble_o2(jn,np)
      use big_stuff
      implicit real*8 (A-H,O-Z)
      include 'data_1.for'
      include 'system_data.for'
      include 'geometry_data.for'
      dimension np(4)
      ic=jn
      ir=jn
      akg(ir,ic)=D_o2
      if(np(2).ne.0)akg(ir,np(2))=B_o2
      if(np(1).ne.0)akg(ir,np(1))=A_o2
      if(np(4).ne.0)akg(ir,np(4))=H_o2
      if(np(3).ne.0)akg(ir,np(3))=F_o2
      if(np(3).eq.0)akg(ir,(np(1)+nnsurf))=T_o2
      if(np(4).eq.0)akg(ir,(np(2)+1))=U_o2
      if(np(2).eq.0)akg(ir,(np(4)-1))=W_o2
      if(np(1).eq.0)then
          if(cord(jn,2).eq.gap)then
              if(cord(jn,1).gt.amouth)then
                  akg(ir,(np(3)-nnsurf))=V_o2
              endif
          endif
      endif
      rhs(jn)=G_o2
```

```
      return
      end
```

Initialize o2

```
!Subroutine that initializes the variables for the coefficient
!matrix elements.
      subroutine initialize_o2
      use big_stuff
      implicit real*8 (A-H,O-Z)
      include 'data_1.for'
      A_o2=0.d0
      B_o2=0.d0
      G_o2=0.d0
      D_o2=0.d0
      F_o2=0.d0
      H_o2=0.d0
      T_o2=0.d0
      U_o2=0.d0
      V_o2=0.d0
      W_o2=0.d0
      return
      end
```

B.2.8 Output Data

```
!Output data stored in file 'output_ss.out'.

    subroutine outputfile
    implicit real*8 (A-H,O-Z)
    include 'data_1.for'
    include 'geometry_data.for'
    include 'system_data.for'
!Deleting old output_ss.out file.
      open(unit=10,file='output_ss.out',status='unknown')
      close(unit=10,status='delete')
      open(unit=10,file='output_ss.out',status='unknown')
!Headings for data
      write(10,355)'r','(',vapp,'V)'
     *             ,'E,mV ','(',vapp,'V)'
     *             ,'pot,mV','(',vapp,'V)'
     *             ,'ph','(',vapp,'V)'
     *             ,(specie(i)(1:12),'(',vapp,'V)',i=1,nspec)
!For each node on the metal surface
      do j=1,nnsurf
          ph=14.d0+log10(cin(ioh,j)*consc*1000.d0)
!where ph is the calculated pH at node j
          write(10,750)
!the position r
     *      dhr*(j-1)
!the potential V in mV
     *      ,1000.d0*(vapp-cin(nvar,j)*gas*temp/far)
!the solution potential in mV
     *      ,1000.d0*cin(nvar,j)*gas*temp/far
!the pH
```

```
     *      ,ph
!the species concentrations in M
     *      ,(cin(i,j)*consc*1000.d0,i=1,nspec)
       enddo
       write(10,*),'  '
!Data headings
       write(10,355)'r','(',vapp,'V)'
     *              ,'cde      ','(',vapp,'V)'
     *              ,'i_fe     ','(',vapp,'V)'
     *              ,'i_o2     ','(',vapp,'V)'
     *              ,'i_h2     ','(',vapp,'V)'
     *              ,'i_lim_o2 ','(',vapp,'V)'

       do j=1,nnsurf
           aife=2.d0*far*fxfe(j)
           aio2=4.d0*far*fxo2(j)
           aih2=-1*far*fxoh(j)-aio2
           write(10,750)dhr*(j-1)
!absolute value of net current density in microA per cm2
     *      ,dabs(cde(j)*1.e6)
!iron dissolution current density in microA/cm2
     *      ,aife*1.e6
!oxygen reduction current density in microA/cm2
     *      ,-aio2*1.e6
!hydrogen evolution current density in microA/cm2
     *      ,-aih2*1.e6
!mass-transfer-limited current density for oxygen reduction
!in microA/cm2
     *      ,ailimg(j)
       enddo
       close(10)
355    format(1x,a5,a1,f6.3,a2,2x,12(2x,a12,a1,f6.3,a2))
750      format(e15.8,2x,12(2x,e15.8,6x))
       return
       end
```

B.2.9 External Dependencies

Data 1

```
       common/data_1/cin(20,2000),cold(20,2000)
       common/data_2/A(20,20),B(20,20),D(20,20),F(20,20)
     * ,H(20,20),G(20)
       common/data_3/T(20,20),U(20,20),V(20,20),W(20,20)
       common/data_4/emax,we,emax_ss(20),perc_max
       common/data_5/rhsnew(4500),rhs(4500),akappa(4500)
       common/data_6/indx(4500),soltemp(4500),sol(4500)
       common/data_7/bulko2,difo2,ailimg(1000),efield(4500)
       common/data_8/A_o2,B_o2,D_o2,F_o2,H_o2,G_o2
       common/data_9/T_o2,U_o2,V_o2,W_o2
       parameter(nmax=4500)
```

Geometry data

```
      common/g_1/surface,gap,coat,amouth,dhr,dhz,dhrr
      common/g_2/dhzz,dhr2,dhz2,dis_up,dis_out,xi_o_d
      common/g_3/nelms,nesurf,nnsurf,nerhs,netop,necoat
      common/g_4/ne_up,ne_out,nelhs,nemou
      common/g_5/vapp
      common/g_7/update,corr,o2red,h2evo,fe_hydro,domain
      common/g_8/nodes,iut,iut_new,iut_o2,iun_new(4500)
      common/g_10/cord(4500,2),iele(2500,4),inode(4500,4)
      common/g_11/iun(4500),iun_con(4500),iun_o2(4500)
      character*20 update,domain,pname,answer,fe_hydro
     * ,corr,o2red,h2evo
      character line*80
      parameter(pi=3.141592653589793d0)
```

System data

```
      common/blkvar/nvar,nspec,ina,icl,ioh,ife,ifeoh
      common/info/dif(40),con(40)
      common/names/specie,mfile
      common/scsc/dcsc,consc,difs(40),z(40),zdifs(20)
      common/fluxes/fxoh(1500),fxfe(1500),fxo2(1500)
      common/c_data1/fx_specie(10,1000),cde(1500)
      parameter(far=96487.d0,gas=8.314d0,temp=298.d0)
      parameter(eqpot_h2=-870.d0,beta_h2=132.d0
     * ,eqpot_fe=-475.d0
     * ,beta_fe=62.6d0,eqpot_o2=-500.d0,beta_o2=66.5d0)
      character*20 mfile
      character*12 specie(40)
```

APPENDIX C
CATHODIC DELAMINATION SYSTEM SOLUTION METHOD

Newton's method was used to solve the system of coupled, non-linear, partial differential equations of the cathodic delamination system.[84] The details of this procedure are given in this appendix.

The dependent variables included c_{Na^+}, c_{Cl^-}, c_{OH^-}, $c_{Zn^{+2}}$, ϕ, and φ and were indexed 1 to 6, respectively. The independent variables were time t and position x. The domain was discretized into a grid and the system of governing equations were discretized at each node in the domain using approximations for the derivatives. The discretized equations were used to construct the global function vector $\boldsymbol{F}_N$ and the global jacobian matrix $\boldsymbol{J}_N$.

C.1 Function Vector

The construction of the global function vector is given in this section. The discretization of the governing equations for non-boundary nodes m and the boundary node m_{max} are presented.

C.1.1 Non-boundary Node

The governing equation for c_i at a non-boundary node was

$$\begin{aligned}\frac{\partial\left(\varphi^{2/3}c_i\right)}{\partial t} &= z_i D_i c_i \varphi \frac{\partial^2\phi}{\partial x^2} + z_i D_i \varphi \frac{\partial c_i}{\partial x}\frac{\partial\phi}{\partial x} + D_i\varphi\frac{\partial^2 c_i}{\partial x^2} \\ &+ z_i D_i c_i \frac{\partial\phi}{\partial x}\frac{\partial\varphi}{\partial x} + D_i\frac{\partial c_i}{\partial x}\frac{\partial\varphi}{\partial x} + S_i \end{aligned} \tag{C-1}$$

Employing the approximations of the derivatives the discretized form of equa-

tion (C-1) at a non-boundary node m was given by

$$\begin{aligned} -\frac{(\varphi^{2/3}c_i)^{(n)}_{(m)}}{\triangle t} - S^{(n)}_{i(m)} &= \mathbb{H}_{i,5}\phi^{(n+1)}_{(m-1)} + \mathbb{D}_{i,5}\phi^{(n+1)}_{(m)} + \mathbb{B}_{i,5}\phi^{(n+1)}_{(m+1)} \\ &+ \mathbb{H}_{i,i}c^{(n+1)}_{i(m-1)} + \mathbb{D}_{i,i}c^{(n+1)}_{i(m)} + \mathbb{B}_{i,i}c^{(n+1)}_{i(m+1)} \end{aligned} \tag{C-2}$$

where $i = 1, 2, 3, 4$ and

$$\mathbb{B}_{i,5} = z_i D_i \left[\frac{(c_i\varphi)^{(n+1)}}{(\triangle x)^2} + \frac{\varphi^{(n+1)}}{2\triangle x}\frac{\partial c^{(n+1)}_{i(m)}}{\partial x} + \frac{c^{(n+1)}_{i(m)}}{2\triangle x}\frac{\partial \varphi^{(n+1)}}{\partial x} \right] \tag{C-3}$$

$$\mathbb{D}_{i,5} = \frac{-2z_i D_i (c_i\varphi)^{(n+1)}}{(\triangle x)^2} \tag{C-4}$$

$$\mathbb{H}_{i,5} = z_i D_i \left[\frac{\left(c_i\varphi_{(m)}\right)^{(n+1)}}{(\triangle x)^2} - \frac{\varphi^{(n+1)}_{(m)}}{2\triangle x}\frac{\partial c^{(n+1)}_{i(m)}}{\partial x} - \frac{c^{(n+1)}_{i(m)}}{2\triangle x}\frac{\partial \varphi^{(n+1)}_{(m)}}{\partial x} \right] \tag{C-5}$$

$$\mathbb{B}_{i,i} = \frac{\varphi^{(n+1)}_{(m)} D_i}{(\triangle x)^2} + \frac{D_i}{2\triangle x}\frac{\partial \varphi^{(n+1)}_{(m)}}{\partial x} \tag{C-6}$$

$$\mathbb{D}_{i,i} = \frac{-2D_i\varphi^{(n+1)}_{(m)}}{(\triangle x)^2} - \frac{\left(\varphi^{2/3}\right)^{(n+1)}_{(m)}}{\triangle t} \tag{C-7}$$

$$\mathbb{H}_{i,i} = \frac{\varphi^{(n+1)}_{(m)} D_i}{(\triangle x)^2} - \frac{D_i}{2\triangle x}\frac{\partial \varphi^{(n+1)}_{(m)}}{\partial x} \tag{C-8}$$

$$\frac{\partial c^{(n+1)}_{i(m)}}{\partial x} = \frac{c^{(n+1)}_{i(m+1)} - c^{(n+1)}_{i(m-1)}}{2\triangle x} \tag{C-9}$$

$$\frac{\partial \varphi^{(n+1)}_{(m)}}{\partial x} = \frac{\varphi^{(n+1)}_{(m+1)} - \varphi^{(n+1)}_{(m-1)}}{2\triangle x} \tag{C-10}$$

The discretized equation for the electroneutrality condition was

$$\sum_{i=1}^{4} \mathbb{D}_{5,i} c^{(n+1)}_{i(m)} = 0 \tag{C-11}$$

where

$$\mathbb{D}_{5,i} = z_i \tag{C-12}$$

The equation

$$\left(\varphi^{2/3}\right)^{(n+1)}_{(m)} = \frac{b_{\epsilon,1}}{1 + b_{\epsilon,8}\left(c^{-b_{\epsilon,2}}_{\mathrm{OH^-}}\right)^{(n+1)}} - \frac{b_{\epsilon,4}}{1 + b_{\epsilon,9}\left(c^{-b_{\epsilon,5}}_{\mathrm{OH^-}}\right)^{(n+1)}} + b_{\epsilon,7} \tag{C-13}$$

was used when the equilibrium ϵ-pH relationship was considered.

The equation

$$\begin{aligned}\frac{\left(\varphi^{2/3}\right)_{(m)}^{(n+1)}}{\triangle t} &= -\left(\varphi^{2/3}\right)_{(m)}^{(n+1)}\left(k_{neq}+\frac{1}{\triangle t}\right)\\ &+ \frac{b_{\epsilon,1}}{1+b_{\epsilon,8}\left(c_{\mathrm{OH^-}}^{-b_{\epsilon,2}}\right)^{(n+1)}}-\frac{b_{\epsilon,4}}{1+b_{\epsilon,9}\left(c_{\mathrm{OH^-}}^{-b_{\epsilon,5}}\right)^{(n+1)}}+b_{\epsilon,7}\end{aligned} \tag{C-14}$$

was used when the non-equilibrium ϵ-pH was considered.

The function for c_i at a non-boundary node m was given by $F_{i(m)}$ where

$$\begin{aligned}\mathbb{F}_{i(m)} &= \mathbb{H}_{i,5}\phi_{(m-1)}^{(n+1)}+\mathbb{D}_{i,5}\phi_{(m)}^{(n+1)}+\mathbb{B}_{i,5}\phi_{(m+1)}^{(n+1)}\\ &+ \mathbb{H}_{i,i}c_{i(m-1)}^{(n+1)}+\mathbb{D}_{i,i}c_{i(m)}^{(n+1)}+\mathbb{B}_{i,i}c_{i(m+1)}^{(n+1)}+\frac{\left(\varphi^{2/3}c_i\right)_{(m)}^{(n)}}{\triangle t}+S_{i(m)}^{(n)}\end{aligned} \tag{C-15}$$

where $i=1,2,3,4$.

The function for the electroneutrality condition was

$$\mathbb{F}_{5(m)}=\sum_{i}^{4}\mathbb{D}_{5,i}c_{i(k)} \tag{C-16}$$

The function for the equilibrium ϵ-pH relationship was

$$\mathbb{F}_{6(m)}=\varphi^{2/3}-\frac{b_{\epsilon,1}}{1+b_{\epsilon,8}\left(c_{OH^-}^{-b_{\epsilon,2}}\right)^{(n+1)}}-\frac{b_{\epsilon,4}}{1+b_{\epsilon,9}\left(c_{\mathrm{OH^-}}^{-b_{\epsilon,5}}\right)^{(n+1)}}+b_{\epsilon,7} \tag{C-17}$$

and the function for the non-equilibrium ϵ-pH relationship was

$$\begin{aligned}\mathbb{F}_{6(m)} &= -\left(\varphi^{2/3}\right)_{(m)}^{(n+1)}\left(k+\frac{1}{\triangle t}\right)\\ &+\frac{b_{\epsilon,1}}{1+b_{\epsilon,8}\left(c_{3}^{-b_{\epsilon,2}}\right)^{(n+1)}}-\frac{b_{\epsilon,4}}{1+b_{\epsilon,9}\left(c_{\mathrm{OH^-}}^{-b_{\epsilon,5}}\right)^{(n+1)}}+b_{\epsilon,7}\\ &-\frac{\left(\varphi^{2/3}\right)_{(m)}^{(n)}}{\triangle t}\end{aligned} \tag{C-18}$$

The subscripts of the coefficients of the dependent variables in equations (C-15) and (C-16) were used to designate the element position in node coefficient matrices $\mathbb{B}_m$, $\mathbb{H}_m$, and $\mathbb{D}_m$ where

$$\mathbb{B}_m=\begin{bmatrix}\mathbb{B}_{1,1} & \cdots & \mathbb{B}_{1,6}\\ \vdots & & \vdots\\ \mathbb{B}_{6,1} & \cdots & \mathbb{B}_{6,6}\end{bmatrix} \tag{C-19}$$

$$\mathbb{H}_m = \begin{bmatrix} \mathbb{H}_{1,1} & \dots & \mathbb{H}_{1,6} \\ \vdots & & \vdots \\ \mathbb{H}_{6,1} & \dots & \mathbb{H}_{6,6} \end{bmatrix} \tag{C-20}$$

and

$$\mathbb{D}_m = \begin{bmatrix} \mathbb{D}_{1,1} & \dots & \mathbb{D}_{1,6} \\ \vdots & & \vdots \\ \mathbb{D}_{6,1} & \dots & \mathbb{D}_{6,6} \end{bmatrix} \tag{C-21}$$

The functions $\mathbb{F}_{i(m)}$ at a non-boundary node were cast into matrix form as

$$\mathbb{F}_m = \mathbb{H}_m \cdot \mathbb{C}_{(m-1)}^{(n+1)} + \mathbb{D}_m \cdot \mathbb{C}_{(m)}^{(n+1)} + \mathbb{B}_m \cdot \mathbb{C}_{(m+1)}^{(n+1)} + \mathbb{R}_m \tag{C-22}$$

where the node function vector $\mathbb{F}_m$ was given by

$$\mathbb{F}_m = \begin{bmatrix} \mathbb{F}_{1(m)} & \mathbb{F}_{2(m)} & \mathbb{F}_{3(m)} & \mathbb{F}_{4(m)} & \mathbb{F}_{5(m)} & \mathbb{F}_{6(m)} \end{bmatrix}^T \tag{C-23}$$

the node solution vector $\mathbb{C}_{(m)}^{(n+1)}$ was given by

$$\mathbb{C}_{(m)}^{(n+1)} = \begin{bmatrix} c_{1(m)}^{(n+1)} & c_{2(m)}^{(n+1)} & c_{3(m)}^{(n+1)} & c_{4(m)}^{(n+1)} & \phi_{(m)}^{(n+1)} & \varphi_{(m)}^{(n+1)} \end{bmatrix}^T \tag{C-24}$$

and the node load vector $\mathbb{R}_m$ was given by

$$\mathbb{R}_m = \begin{bmatrix} \frac{\left(\varphi^{2/3} c_1\right)_{(m)}^{(n)}}{\triangle t} + S_{1(m)}^{(n)} \\ \frac{\left(\varphi^{2/3} c_2\right)_{(m)}^{(n)}}{\triangle t} + S_{2(m)}^{(n)} \\ \frac{\left(\varphi^{2/3} c_3\right)_{(m)}^{(n)}}{\triangle t} + S_{3(m)}^{(n)} \\ \frac{\left(\varphi^{2/3} c_4\right)_{(m)}^{(n)}}{\triangle t} + S_{4(m)}^{(n)} \\ 0 \\ \mathbb{F}_{6(m)} \end{bmatrix} \tag{C-25}$$

C.1.2 Boundary node

The no-flux condition for c_i at the boundary was

$$0 = -z_i D_i c_i \varphi \frac{d\phi}{dx} - D_i \varphi \frac{dc_i}{dx} \tag{C-26}$$

This equation was discretized as

$$\begin{aligned} 0 &= \mathbb{W}_{i,5}\phi^{(n+1)}_{(m_{max}-2)} + \mathbb{H}_{i,5}\phi^{(n+1)}_{(m_{max}-1)} + \mathbb{D}_{i,5}\phi^{(n+1)}_{(m_{max})} \\ &+ \mathbb{W}_{i,i}c^{(n+1)}_{i(m_{max}-2)} + \mathbb{H}_{i,i}c^{(n+1)}_{i(m_{max}-1)} + \mathbb{D}_{i,i}c^{(n+1)}_{i(m_{max})} \end{aligned} \tag{C-27}$$

where $i = 1, 2, 3, 4$ and

$$\mathbb{W}_{i,5} = \frac{-z_i D_i \left(c_i \varphi\right)^{(n+1)}_{max}}{2\triangle x} \tag{C-28}$$

$$\mathbb{H}_{i,5} = \frac{4 z_i D_i \left(c_i \varphi\right)^{(n+1)}_{max}}{2\triangle x} \tag{C-29}$$

$$\mathbb{D}_{i,5} = \frac{-3 z_i D_i \left(c_i \varphi\right)^{(n+1)}_{max}}{2\triangle x} \tag{C-30}$$

$$\mathbb{W}_{i,i} = \frac{-D_i \varphi^{(n+1)}_{(m_{max})}}{2\triangle x} \tag{C-31}$$

$$\mathbb{H}_{i,i} = \frac{4 D_i \varphi^{(n+1)}_{(m_{max})}}{2\triangle x} \tag{C-32}$$

$$\mathbb{D}_{i,i} = \frac{-3 D_i \varphi^{(n+1)}_{(m_{max})}}{2\triangle x} \tag{C-33}$$

The governing equations for the electroneutrality condition and the ϵ-pH relationship were used to complete the system of equations at the boundary node.

The functions at the boundary node were

$$\begin{aligned} \mathbb{F}_{i(m_{max})} &= \mathbb{W}_{i,5}\phi^{(n+1)}_{(m_{max}-2)} + \mathbb{H}_{i,5}\phi^{(n+1)}_{(m_{max}-1)} + \mathbb{D}_{i,5}\phi^{(n+1)}_{(m_{max})} \\ &+ \mathbb{W}_{i,i}c^{(n+1)}_{i(m_{max}-2)} + \mathbb{H}_{i,i}c^{(n+1)}_{i(m_{max}-1)} + \mathbb{D}_{i,i}c^{(n+1)}_{i(m_{max})} \end{aligned} \tag{C-34}$$

for the no-flux condition for c_i

$$\mathbb{F}_{5(m_{max})} = \sum_{i=1}^{4} \mathbb{D}_{5,i} c^{(n+1)}_{i(m_{max})} \tag{C-35}$$

for the condition of electroneutrality, and

$$\mathbb{F}_{6(m_{max})} = \left(\varphi^{2/3}\right)^{(n+1)}_{(m_{max})} - \frac{b_{\epsilon,1}}{1 + b_{\epsilon,8}\left(c^{-b_{\epsilon,2}}_{3(m_{max})}\right)^{(n+1)}} - \frac{b_{\epsilon,4}}{1 + b_{\epsilon,9}\left(c^{-b_{\epsilon,5}}_{3(m_{max})}\right)^{(n+1)}} + b_{\epsilon,7} \tag{C-36}$$

for the equilibrium ϵ-pH condition or

$$\begin{aligned}\mathbb{F}_{6(m_{max})} &= -\left(\varphi^{2/3}\right)^{(n+1)}_{(m_{max})}\left(k_{neq}+\frac{1}{\triangle t}\right) \\ &+\frac{b_{\epsilon,1}}{1+b_{\epsilon,8}\left(c^{-b_{\epsilon,2}}_{3(m_{max})}\right)^{(n+1)}}-\frac{b_{\epsilon,4}}{1+b_{\epsilon,9}\left(c^{-b_{\epsilon,5}}_{3(m_{max})}\right)^{(n+1)}}+b_{\epsilon,7} \\ &-\frac{\left(\varphi^{2/3}\right)^{(n)}_{(m_{max})}}{\triangle t}\end{aligned} \tag{C-37}$$

for the non-equilibrium ϵ-pH condition.

The functions at the boundary node were cast into matrix form as

$$\mathbb{F}_{m_{max}} = \mathbb{W}_{m_{max}}\cdot\mathbb{C}^{(n+1)}_{(m-2)}+\mathbb{H}_{m_{max}}\cdot\mathbb{C}^{(n+1)}_{(m_{max}-1)}+\mathbb{D}_{m_{max}}\cdot\mathbb{C}^{(n+1)}_{(m_{max})}+\boldsymbol{R}_{m_{max}} \tag{C-38}$$

where

$$\mathbb{W}_{m_{max}} = \begin{bmatrix} \mathbb{W}_{1,1} & \cdots & \mathbb{W}_{1,6} \\ \vdots & & \vdots \\ \mathbb{W}_{6,1} & \cdots & \mathbb{W}_{6,6} \end{bmatrix} \tag{C-39}$$

$$\mathbb{H}_{m_{max}} = \begin{bmatrix} \mathbb{H}_{1,1} & \cdots & \mathbb{H}_{1,6} \\ \vdots & & \vdots \\ \mathbb{H}_{6,1} & \cdots & \mathbb{H}_{6,6} \end{bmatrix} \tag{C-40}$$

$$\mathbb{D}_{m_{max}} = \begin{bmatrix} \mathbb{D}_{1,1} & \cdots & \mathbb{D}_{1,6} \\ \vdots & & \vdots \\ \mathbb{D}_{6,1} & \cdots & \mathbb{D}_{6,6} \end{bmatrix} \tag{C-41}$$

and

$$\mathbb{R}_{m_{max}} = \begin{bmatrix}0\,0\,0\,0\,0\,\mathbb{F}_{6(m_{max})}\end{bmatrix}^T \tag{C-42}$$

C.1.3 Global Function Vector

The node vector functions were assembled to give the global function vector $\boldsymbol{F}_N$

$$\boldsymbol{F}_N = \begin{bmatrix} \mathbb{F}_1 \\ \mathbb{F}_2 \\ \vdots \\ \mathbb{F}_{m_{max}} \end{bmatrix} \tag{C-43}$$

where the conditions at the first node were known with

$$\mathbb{F}_1 = [0\ 0\ 0\ 0\ 0\ 0]^T \tag{C-44}$$

C.2 Jacobian Matrix

The Jacobian matrix for non-boundary and boundary nodes are presented in this section.

C.2.1 Non-boundary node

The elements of a node function vector $\mathbb{F}_m$ at a non-boundary node m were functions of the dependent variables with

$$\mathbb{F}_{i(m)} = \mathbb{F}_{i(m)}\left(\mathbb{G}_m^{(n+1)}\right) \tag{C-45}$$

where

$$\mathbb{G}_m^{(n)} = \left(\mathbb{C}_{(m-1)}^{(n)}, \mathbb{C}_{(m)}^{(n)}, \mathbb{C}_{(m+1)}^{(n)}\right) \tag{C-46}$$

To a first approximation

$$\begin{aligned} \mathbb{F}_{i(m)}\left(\mathbb{G}_m^{(n+1)}\right) &= \mathbb{F}_{i(m)}\left(\mathbb{G}_m^{(n+1),o}\right) \\ &+ \sum_{j=m-1}^{j=m+1}\left(\sum_{i=1}^{4}\frac{\partial \mathbb{F}_{i(m)}}{\partial c_{i(j)}}\triangle c_{i(j)} + \frac{\partial \mathbb{F}_{i(m)}}{\partial \phi_{(j)}}\triangle \phi_{(j)} + \frac{\partial \mathbb{F}_{i(m)}}{\partial \varphi_{(j)}}\triangle \varphi_{(j)}\right) \end{aligned} \tag{C-47}$$

where

$$\triangle c_{i(j)} = c_{i(j)}^{(n+1)} - c_{i(j)}^{(n+1),o} \tag{C-48}$$

$$\triangle \phi_{(j)} = \phi_{(j)}^{(n+1)} - \phi_{(j)}^{(n+1),o} \tag{C-49}$$

$$\triangle \varphi_{(j)} = \varphi_{(j)}^{(n+1)} - \varphi_{(j)}^{(n+1),o} \tag{C-50}$$

$\mathbb{G}_m^{(n+1),o}$ was an approximation to $\mathbb{G}_{(m)}^{(n+1)}$, and $c_{i(m)}^{(n+1),o}$, $\phi_{(m)}^{(n+1),o}$ and $\varphi_{(m)}^{(n+1),o}$ were approximations for $c_{i(m)}^{(n+1)}$, $\phi_{(m)}^{(n+1)}$ and $\varphi_{(m)}^{(n+1)}$, respectively.

The first approximation of $\mathbb{F}_m$ was given by

$$\mathbb{F}_m\left(\mathbb{G}_m^{(n+1)}\right) = \mathbb{F}_m\left(\mathbb{G}^{(n+1),o}\right) + \mathbb{J}_m\left(\mathbb{G}_m^{(n+1),o}\right) \cdot \triangle \mathbb{G} \tag{C-51}$$

where

$$\triangle \mathbb{G} = \mathbb{G}_m^{(n+1)} - \mathbb{G}_m^{(n+1),o} \tag{C-52}$$

and $\mathbb{J}_m$ was the node jacobian matrix.

The node jacobian matrix $\mathbb{J}_m$ was partioned as

$$\mathbb{J}_m \;=\; [\mathbb{T}_m\, \mathbb{U}_m\, \mathbb{V}_m] \tag{C-53}$$

where $\mathbb{T}_m$, $\mathbb{U}_m$, and $\mathbb{V}_m$ were given by

$$\mathbb{T}_m = \begin{bmatrix} \frac{\partial \mathbb{F}_1}{\partial c_{1(m-1)}} & \frac{\partial \mathbb{F}_1}{\partial c_{2(m-1)}} & \frac{\partial \mathbb{F}_1}{\partial c_{3(m-1)}} & \frac{\partial \mathbb{F}_1}{\partial c_{4(m-1)}} & \frac{\partial \mathbb{F}_1}{\partial \phi_{(m-1)}} & \frac{\partial \mathbb{F}_1}{\partial \varphi_{(m-1)}} \\ \vdots & \vdots & \vdots & \vdots & \vdots & \vdots \\ \frac{\partial \mathbb{F}_6}{\partial c_{1(m-1)}} & \frac{\partial \mathbb{F}_6}{\partial c_{2(m-1)}} & \frac{\partial \mathbb{F}_6}{\partial c_{3(m-1)}} & \frac{\partial \mathbb{F}_6}{\partial c_{4(m-1)}} & \frac{\partial \mathbb{F}_6}{\partial \phi_{(m-1)}} & \frac{\partial \mathbb{F}_6}{\partial \varphi_{(m-1)}} \end{bmatrix} \tag{C-54}$$

$$\mathbb{U}_m = \begin{bmatrix} \frac{\partial \mathbb{F}_1}{\partial c_{1(m)}} & \frac{\partial \mathbb{F}_1}{\partial c_{2(m)}} & \frac{\partial \mathbb{F}_1}{\partial c_{3(m)}} & \frac{\partial \mathbb{F}_1}{\partial c_{4(m)}} & \frac{\partial \mathbb{F}_1}{\partial \phi_{(m)}} & \frac{\partial \mathbb{F}_1}{\partial \varphi_{(m)}} \\ \vdots & \vdots & \vdots & \vdots & \vdots & \vdots \\ \frac{\partial \mathbb{F}_6}{\partial c_{1(m)}} & \frac{\partial \mathbb{F}_6}{\partial c_{2(m)}} & \frac{\partial \mathbb{F}_6}{\partial c_{3(m)}} & \frac{\partial \mathbb{F}_6}{\partial c_{4(m)}} & \frac{\partial \mathbb{F}_6}{\partial \phi_{(m)}} & \frac{\partial \mathbb{F}_6}{\partial \varphi_{(m)}} \end{bmatrix} \tag{C-55}$$

and

$$\mathbb{V}_m = \begin{bmatrix} \frac{\partial \mathbb{F}_1}{\partial c_{1(m+1)}} & \frac{\partial \mathbb{F}_1}{\partial c_{2(m+1)}} & \frac{\partial \mathbb{F}_1}{\partial c_{3(m+1)}} & \frac{\partial \mathbb{F}_1}{\partial c_{4(m+1)}} & \frac{\partial \mathbb{F}_1}{\partial \phi_{(m+1)}} & \frac{\partial \mathbb{F}_1}{\partial \varphi_{(m+1)}} \\ \vdots & \vdots & \vdots & \vdots & \vdots & \vdots \\ \frac{\partial \mathbb{F}_6}{\partial c_{1(m+1)}} & \frac{\partial \mathbb{F}_6}{\partial c_{2(m+1)}} & \frac{\partial \mathbb{F}_6}{\partial c_{3(m+1)}} & \frac{\partial \mathbb{F}_6}{\partial c_{4(m+1)}} & \frac{\partial \mathbb{F}_6}{\partial \phi_{(m+1)}} & \frac{\partial \mathbb{F}_6}{\partial \varphi_{(m+1)}} \end{bmatrix} \tag{C-56}$$

The elements of $\mathbb{T}_m$, $\mathbb{U}_m$, and $\mathbb{V}_m$ were calculated using the equations

$$\frac{\partial \mathbb{F}_i}{\partial \phi_{(m+1)}} = \mathbb{B}_{i,5} \tag{C-57}$$

$$\frac{\partial \mathbb{F}_i}{\partial \phi_{(m)}} = \mathbb{D}_{i,5} \tag{C-58}$$

$$\frac{\partial \mathbb{F}_i}{\partial \phi_{(m-1)}} = \mathbb{H}_{i,5} \tag{C-59}$$

$$\frac{\partial \mathbb{F}_i}{\partial c_{i(m+1)}} = \frac{\partial \mathbb{B}_{i,5}}{\partial c_{i(m+1)}}\phi_{(m+1)}^{(n+1),o} + \frac{\partial \mathbb{D}_{i,5}}{\partial c_{i(m+1)}}\phi_{(m)}^{(n+1),o} + \frac{\partial \mathbb{H}_{i,5}}{\partial c_{i(m+1)}}\phi_{(m-1)}^{(n+1),o} + \mathbb{B}_{i,i} \tag{C-60}$$

$$\frac{\partial \mathbb{F}_i}{\partial c_{i(m)}} = \frac{\partial \mathbb{B}_{i,5}}{\partial c_{i(m)}}\phi_{(m+1)}^{(n+1),o} + \frac{\partial \mathbb{D}_{i,5}}{\partial c_{i(m)}}\phi_{(m)}^{(n+1),o} + \frac{\partial \mathbb{H}_{i,5}}{\partial c_{i(m)}}\phi_{(m-1)}^{(n+1),o} + \mathbb{D}_{i,i} \tag{C-61}$$

$$\frac{\partial \mathbb{F}_i}{\partial c_{i(m-1)}} = \frac{\partial \mathbb{B}_{i,5}}{\partial c_{i(m-1)}}\phi_{(m+1)}^{(n+1),o} + \frac{\partial \mathbb{D}_{i,5}}{\partial c_{i(m-1)}}\phi_{(m)}^{(n+1),o} + \frac{\partial \mathbb{H}_{i,5}}{\partial c_{i(m-1)}}\phi_{(m-1)}^{(n+1),o} + \mathbb{H}_{i,i} \tag{C-62}$$

$$\begin{aligned}\frac{\partial \mathbb{F}_i}{\partial \varphi_{(m+1)}} = {} & \frac{\partial \mathbb{B}_{i,5}}{\partial \varphi_{(m+1)}}\phi_{(m+1)}^{(n+1),o} + \frac{\partial \mathbb{D}_{i,5}}{\partial \varphi_{(m+1)}}\phi_{(m)}^{(n+1),o} + \frac{\partial \mathbb{H}_{i,5}}{\partial \varphi_{(m+1)}}\phi_{(m-1)}^{(n+1),o} \\ & + \frac{\partial \mathbb{B}_{i,i}}{\partial \varphi_{(m+1)}}c_{i(m+1)}^{(n+1),o} + \frac{\partial \mathbb{D}_{i,i}}{\partial \varphi_{(m+1)}}c_{i(m)}^{(n+1),o} + \frac{\partial \mathbb{H}_{i,i}}{\partial \varphi_{(m+1)}}c_{i(m-1)}^{(n+1),o}\end{aligned} \tag{C-63}$$

$$\begin{aligned}\frac{\partial \mathbb{F}_i}{\partial \varphi_{(m)}} = {} & \frac{\partial \mathbb{B}_{i,5}}{\partial \varphi_{(m)}}\phi_{(m+1)}^{(n+1),o} + \frac{\partial \mathbb{D}_{i,5}}{\partial \varphi_{(m)}}\phi_{(m)}^{(n+1),o} + \frac{\partial \mathbb{H}_{i,5}}{\partial \varphi_{(m)}}\phi_{(m-1)}^{(n+1),o} \\ & + \frac{\partial \mathbb{B}_{i,i}}{\partial \varphi_{(m)}}c_{i(m+1)}^{(n+1),o} + \frac{\partial \mathbb{D}_{i,i}}{\partial \varphi_{(m)}}c_{i(m)}^{(n+1),o} + \frac{\partial \mathbb{H}_{i,i}}{\partial \varphi_{(m)}}c_{i(m-1)}^{(n+1),o}\end{aligned} \tag{C-64}$$

and

$$\begin{aligned}\frac{\partial \mathbb{F}_i}{\partial \varphi_{(m-1)}} = {} & \frac{\partial \mathbb{B}_{i,5}}{\partial \varphi_{(m-1)}}\phi_{(m+1)}^{(n+1),o} + \frac{\partial \mathbb{D}_{i,5}}{\partial \varphi_{(m-1)}}\phi_{(m)}^{(n+1),o} + \frac{\partial \mathbb{H}_{i,5}}{\partial \varphi_{(m-1)}}\phi_{(m-1)}^{(n+1),o} \\ & + \frac{\partial \mathbb{B}_{i,i}}{\partial \varphi_{(m-1)}}c_{i(m+1)}^{(n+1),o} + \frac{\partial \mathbb{D}_{i,i}}{\partial \varphi_{(m-1)}}c_{i(m)}^{(n+1),o} + \frac{\partial \mathbb{H}_{i,i}}{\partial \varphi_{(m-1)}}c_{i(m-1)}^{(n+1),o}\end{aligned} \tag{C-65}$$

The following equations were used in the calculation of the elements of the $\mathbb{T}_m$, $\mathbb{U}_m$, and $\mathbb{V}_m$:

$$\frac{\partial \mathbb{B}_{i,5}}{\partial c_{i(m+1)}} = \frac{z_i D_i \varphi_{(m)}^{(n+1),o}}{4(\triangle x)^2} \tag{C-66}$$

$$\frac{\partial \mathbb{B}_{i,5}}{\partial c_{i(m)}} = z_i D_i \left[\frac{\varphi_{(m)}^{(n+1),o}}{(\triangle x)^2} + \frac{1}{2\triangle x}\frac{\partial \varphi_{(m)}^{(n+1),o}}{\partial x}\right] \tag{C-67}$$

$$\frac{\partial \mathbb{B}_{i,5}}{\partial c_{i(m-1)}} = -\frac{z_i D_i \varphi_{(m)}^{(n+1),o}}{4(\triangle x)^2} \tag{C-68}$$

$$\frac{\partial \mathbb{B}_{i,5}}{\partial \varphi_{(m+1)}} = \frac{z_i D_i c_{i(m)}^{(n+1),o}}{4(\triangle x)^2} \tag{C-69}$$

$$\frac{\partial \mathbb{B}_{i,5}}{\partial \varphi_{(m)}} = z_i D_i \left[\frac{c_{i(m)}^{(n+1),o}}{(\triangle x)^2} + \frac{1}{2\triangle x} \frac{\partial c_{i(m)}^{(n+1),o}}{\partial x} \right] \tag{C-70}$$

$$\frac{\partial \mathbb{B}_{i,5}}{\partial \varphi_{(m-1)}} = -\frac{z_i D_i c_{i(m)}^{(n+1),o}}{4(\triangle x)^2} \tag{C-71}$$

$$\frac{\partial \mathbb{D}_{i,5}}{\partial c_{i(m+1)}} = 0 \tag{C-72}$$

$$\frac{\partial \mathbb{D}_{i,5}}{\partial c_{i(m)}} = \frac{-2 z_i D_i \varphi_{(m)}^{(n+1),o}}{(\triangle x)^2} \tag{C-73}$$

$$\frac{\partial \mathbb{D}_{i,5}}{\partial c_{i(m-1)}} = 0 \tag{C-74}$$

$$\frac{\partial \mathbb{D}_{i,5}}{\partial \varphi_{i(m+1)}} = 0 \tag{C-75}$$

$$\frac{\partial \mathbb{D}_{i,5}}{\partial \varphi_{(m)}} = \frac{-2 z_i D_i c_{i(m)}^{(n+1),o}}{(\triangle x)^2} \tag{C-76}$$

$$\frac{\partial \mathbb{D}_{i,5}}{\partial \varphi_{i(m-1)}} = 0 \tag{C-77}$$

$$\frac{\partial \mathbb{H}_{i,5}}{\partial c_{i(m+1)}} = -\frac{z_i D_i \varphi_{(m)}^{(n+1),o}}{4(\triangle x)^2} \tag{C-78}$$

$$\frac{\partial \mathbb{H}_{i,5}}{\partial c_{i(m)}} = z_i D_i \left[\frac{\varphi_{(m)}^{(n+1),o}}{(\triangle x)^2} - \frac{1}{2\triangle x} \frac{\partial \varphi_{(m)}^{(n+1),o}}{\partial x} \right] \tag{C-79}$$

$$\frac{\partial \mathbb{H}_{i,5}}{\partial c_{i(m-1)}} = \frac{z_i D_i \varphi_{(m)}^{(n+1),o}}{4(\triangle x)^2} \tag{C-80}$$

$$\frac{\partial \mathbb{H}_{i,5}}{\partial \varphi_{(m+1)}} = -\frac{z_i D_i c_{i(m)}^{(n+1),o}}{4(\triangle x)^2} \tag{C-81}$$

$$\frac{\partial \mathbb{H}_{i,5}}{\partial \varphi_{(m)}} = z_i D_i \left[\frac{c_{i(m)}^{(n+1),o}}{(\triangle x)^2} - \frac{1}{2\triangle x} \frac{\partial c_{i(m)}^{(n+1),o}}{\partial x} \right] \tag{C-82}$$

$$\frac{\partial \mathbb{H}_{i,5}}{\partial \varphi_{(m-1)}} = \frac{z_i D_i c_{i(m)}^{(n+1),o}}{4(\triangle x)^2} \tag{C-83}$$

$$\frac{\partial \mathbb{B}_{i,i}}{\partial \varphi_{(m+1)}} = \frac{D_i}{4(\triangle x)^2} \tag{C-84}$$

$$\frac{\partial \mathbb{B}_{i,i}}{\partial \varphi_{(m)}} = \frac{D_i}{(\triangle x)^2} \tag{C-85}$$

$$\frac{\partial \mathbb{B}_{i,i}}{\partial \varphi_{(m-1)}} = -\frac{D_i}{4(\triangle x)^2} \tag{C-86}$$

$$\frac{\partial \mathbb{D}_{i,i}}{\partial \varphi_{(m+1)}} = 0 \tag{C-87}$$

$$\frac{\partial \mathbb{D}_{i,i}}{\partial \varphi_{(m)}} = -\frac{2D_i}{(\triangle x)^2} - \frac{\left(\varphi^{2/3}\right)_{(m)}^{(n+1),o}}{\triangle t} \tag{C-88}$$

$$\frac{\partial \mathbb{D}_{i,i}}{\partial \varphi_{(m-1)}} = 0 \tag{C-89}$$

$$\frac{\partial \mathbb{H}_{i,i}}{\partial \varphi_{(m+1)}} = -\frac{D_i}{4(\triangle x)^2} \tag{C-90}$$

$$\frac{\partial \mathbb{H}_{i,i}}{\partial \varphi_{(m)}} = \frac{D_i}{(\triangle x)^2} \tag{C-91}$$

and

$$\frac{\partial \mathbb{H}_{i,i}}{\partial \varphi_{(m-1)}} = \frac{D_i}{4(\triangle x)^2} \tag{C-92}$$

C.2.2 Boundary node

The elements of a node function vector $\mathbb{F}_{i(m_{max})}$ at the boundary node were functions of the dependent variables with

$$\mathbb{F}_{i(m_{max})} = \mathbb{F}_{i(m_{max})}\left(\mathbb{G}_{(m_{max})}^{(n+1)}\right) \tag{C-93}$$

where

$$\mathbb{G}_{(m_{max})}^{(n+1)} = \left(\mathbb{C}_{(m_{max})-2)}^{(n+1)}, \mathbb{C}_{(m_{max})-1)}^{(n+1)}, \mathbb{C}_{(m_{max}))}^{(n+1)}\right) \tag{C-94}$$

To a first approximation

$$\begin{aligned}\mathbb{F}_{i(m_{max})} &= \mathbb{F}_{i(m_{max})}\left(\mathbb{G}_{m_{max}}^{(n+1),o}\right) \\ &+ \sum_{j=m_{max}-2}^{j=m_{max}}\left(\sum_{i=1}^{4}\frac{\partial \mathbb{F}_{i(m)}}{\partial c_{i(j)}}\triangle c_{i(j)} + \frac{\partial \mathbb{F}_{i(m)}}{\partial \phi_{(j)}}\triangle \phi_{(j)} + \frac{\partial \mathbb{F}_{i(m)}}{\partial \varphi_{(j)}}\triangle \varphi_{(j)}\right)\end{aligned} \tag{C-95}$$

The governing equations for the dependent variables at the boundary node m_{max} was cast as

$$\mathbb{F}_{m_{max}} = \mathbb{F}_{m_{max}}\left(\mathbb{G}_{m_{max}}^{(n+1),o}\right) + \mathbb{J}_{max}\left(\mathbb{G}_{m_{max}}^{(n+1),o}\right) \cdot \triangle \mathbb{G}_{m_{max}} \tag{C-96}$$

where

$$\triangle \mathbb{G}_{m_{max}} = \mathbb{G}_{m_{max}}^{(n+1)} - \mathbb{G}_{m_{max}}^{(n+1),o} \tag{C-97}$$

The jacobian matrix $\mathbb{J}_{m_{max}}$ was partioned as

$$\mathbb{J}_{m_{max}} = \left[\mathbb{A}_{m_{max}}\ \mathbb{T}_{m_{max}}\ \mathbb{U}_{m_{max}}\right] \tag{C-98}$$

where $\mathbb{A}_{m_{max}}$, $\mathbb{T}_{m_{max}}$, and $\mathbb{U}_{m_{max}}$ for $m = m_{max}$ were given by

$$\mathbb{A}_{m_{max}} = \begin{bmatrix} \frac{\partial \mathbb{F}_1}{\partial c_{1(m-2)}} & \frac{\partial \mathbb{F}_1}{\partial c_{2(m-2)}} & \frac{\partial \mathbb{F}_1}{\partial c_{3(m-2)}} & \frac{\partial \mathbb{F}_1}{\partial c_{4(m-2)}} & \frac{\partial \mathbb{F}_1}{\partial \phi_{(m-2)}} & \frac{\partial \mathbb{F}_1}{\partial \varphi_{(m-2)}} \\ \vdots & \vdots & \vdots & \vdots & \vdots & \vdots \\ \frac{\partial \mathbb{F}_6}{\partial c_{1(m-2)}} & \frac{\partial \mathbb{F}_6}{\partial c_{2(m-2)}} & \frac{\partial \mathbb{F}_6}{\partial c_{3(m-2)}} & \frac{\partial \mathbb{F}_6}{\partial c_{4(m-2)}} & \frac{\partial \mathbb{F}_6}{\partial \phi_{(m-2)}} & \frac{\partial \mathbb{F}_6}{\partial \varphi_{(m-2)}} \end{bmatrix} \tag{C-99}$$

$$\mathbb{T}_{m_{max}} = \begin{bmatrix} \frac{\partial \mathbb{F}_1}{\partial c_{1(m-1)}} & \frac{\partial \mathbb{F}_1}{\partial c_{2(m-1)}} & \frac{\partial \mathbb{F}_1}{\partial c_{3(m-1)}} & \frac{\partial \mathbb{F}_1}{\partial c_{4(m-1)}} & \frac{\partial \mathbb{F}_1}{\partial \phi_{(m-1)}} & \frac{\partial \mathbb{F}_1}{\partial \varphi_{(m-1)}} \\ \vdots & \vdots & \vdots & \vdots & \vdots & \vdots \\ \frac{\partial \mathbb{F}_6}{\partial c_{1(m-1)}} & \frac{\partial \mathbb{F}_6}{\partial c_{2(m-1)}} & \frac{\partial \mathbb{F}_6}{\partial c_{3(m-1)}} & \frac{\partial \mathbb{F}_6}{\partial c_{4(m-1)}} & \frac{\partial \mathbb{F}_6}{\partial \phi_{(m-1)}} & \frac{\partial \mathbb{F}_6}{\partial \varphi_{(m-1)}} \end{bmatrix} \tag{C-100}$$

$$\boldsymbol{U}_{m_{max}} = \begin{bmatrix} \frac{\partial \mathbb{F}_1}{\partial c_{1(m)}} & \frac{\partial \mathbb{F}_1}{\partial c_{2(m)}} & \frac{\partial \mathbb{F}_1}{\partial c_{3(m)}} & \frac{\partial \mathbb{F}_1}{\partial c_{4(m)}} & \frac{\partial \mathbb{F}_1}{\partial \phi_{(m)}} & \frac{\partial \mathbb{F}_1}{\partial \varphi_{(m)}} \\ \vdots & \vdots & \vdots & \vdots & \vdots & \vdots \\ \frac{\partial \mathbb{F}_6}{\partial c_{1(m)}} & \frac{\partial \mathbb{F}_6}{\partial c_{2(m)}} & \frac{\partial \mathbb{F}_6}{\partial c_{3(m)}} & \frac{\partial \mathbb{F}_6}{\partial c_{4(m)}} & \frac{\partial \mathbb{F}_6}{\partial \phi_{(m)}} & \frac{\partial \mathbb{F}_6}{\partial \varphi_{(m)}} \end{bmatrix} \tag{C-101}$$

The elements of $\mathbb{A}_{m_{max}}$, $\mathbb{T}_{m_{max}}$, and $\mathbb{U}_{m_{max}}$ were calculated using the equations

$$\frac{\partial \mathbb{F}_i}{\partial \phi_{(m_{max})-2)}} = \mathbb{W}_{i,5} \tag{C-102}$$

$$\frac{\partial \mathbb{F}_i}{\partial \phi_{(m_{max})-1)}} = \mathbb{H}_{i,5} \tag{C-103}$$

$$\frac{\partial \mathbb{F}_i}{\partial \phi_{(m_{max}))}} = \mathbb{D}_{i,5} \tag{C-104}$$

$$\frac{\partial \mathbb{F}_i}{\partial c_{i(m_{max})-2)}} = \mathbb{W}_{i,i} \tag{C-105}$$

$$\frac{\partial \mathbb{F}_i}{\partial c_{i(m_{max})-1)}} = \mathbb{H}_{i,i} \tag{C-106}$$

$$\begin{aligned} \frac{\partial \mathbb{F}_i}{\partial c_{i(m_{max}))}} &= \mathbb{D}_{i,i} + \frac{\partial \mathbb{W}_{i,5}}{\partial c_{i(m_{max})}} \phi_{(m_{max})-2)} \\ &\quad + \frac{\partial \mathbb{H}_{i,5}}{\partial c_{i(m_{max})}} \phi_{(m_{max})-1)} + \frac{\partial \mathbb{D}_{i,5}}{\partial c_{i(m_{max}))}} \phi_{(m_{max}))} \end{aligned} \tag{C-107}$$

and

$$\begin{aligned}\frac{\partial \mathbb{F}_i}{\partial \varphi} &= \frac{\partial \mathbb{W}_{i,5}}{\partial \varphi}\phi_{(m_{max}-2)} + \frac{\partial \mathbb{H}_{i,5}}{\partial \varphi}\phi_{(m_{max}-1)} + \frac{\partial \mathbb{D}_{i,5}}{\partial \varphi}\phi_{(m_{max})} \\ &+ \frac{\partial \mathbb{W}_{i,i}}{\partial \varphi}c_{i(m_{max}-2)} + \frac{\partial \mathbb{H}_{i,i}}{\partial \varphi}c_{i(m_{max}-1)} + \frac{\partial \mathbb{D}_{i,i}}{\partial \varphi}c_{i(m_{max})}\end{aligned} \tag{C-108}$$

Equations that were used in equations (C-102) to (C-108) were

$$\frac{\partial \mathbb{W}_{i,5}}{\partial c_{i(m_{max})}} = \frac{-z_i D_i \varphi_{(m_{max})}}{2\triangle x} \tag{C-109}$$

$$\frac{\partial \mathbb{H}_{i,5}}{\partial c_{i(m_{max})}} = \frac{4z_i D_i \varphi_{(m_{max})}}{2\triangle x} \tag{C-110}$$

$$\frac{\partial \mathbb{D}_{i,5}}{\partial c_{i(m_{max})}} = \frac{-3z_i D_i \varphi_{(m_{max})}}{2\triangle x} \tag{C-111}$$

$$\frac{\partial \mathbb{W}_{i,5}}{\partial \varphi_{(m_{max})}} = \frac{-z_i D_i c_{i(m_{max})}}{2\triangle x} \tag{C-112}$$

$$\frac{\partial \mathbb{H}_{i,5}}{\partial \varphi_{(m_{max})}} = \frac{4z_i D_i c_{i(m_{max})}}{2\triangle x} \tag{C-113}$$

$$\frac{\partial \mathbb{D}_{i,5}}{\partial \varphi_{(m_{max})}} = \frac{3z_i D_i c_{i(m_{max})}}{2\triangle x} \tag{C-114}$$

C.2.3 Global Jacobian Matrix

The node jacobian matrices were assembled to give the global jacobian matrix J_N

$$J_N = \begin{bmatrix} 0 & 0 & 0 & \cdots & 0 \\ 0 & \mathbb{J}_2 & 0 & \cdots & 0 \\ 0 & 0 & \mathbb{J}_3 & \cdots & 0 \\ \vdots & \vdots & \vdots & \ddots & \vdots \\ 0 & 0 & 0 & \cdots & \mathbb{J}_{m_{max}} \end{bmatrix} \tag{C-115}$$

APPENDIX D
CADEM PROGRAM LISTING

The program listing for CADEM is presented in this appendix. A variable listing is given for the the key variables used in the development of CADEM. CADEM was developed using using 'Compaq Visual Fortran, Version 6.1' with double precision accuracy. The main program and key subroutines are included as sections. The subroutines associated with the key subroutines are given as subsections.

D.1 Variable Listing

The variables used in the program were different from the variables used in the document. The important program and document variables are given in Table D.1.

Table D.1: Variable listing for CADEM.

Program Variable	Document Variable	Description and/or equation reference
a_kv	k_{neq}	rate constant, 11-14
aint_surf	l_{sem}	initial length of semi-intact region
alambda_cl_fro	$\lambda_{Na^+,fro}$	10-17
alambda_na_fro	$\lambda_{Cl^-,fro}$	10-17
alambda_oh_fro	$\lambda_{OH^-,fro}$	10-17
alambda_cl_int	$\lambda_{Na^+,sem}$	10-19
alambda_na_int	$\lambda_{Cl^-,sem}$	10-19
alambda_oh_int	$\lambda_{OH^-,sem}$	10-19
B_j	$\mathbb{B}_{i,i}$	C-6

continued on next page

Table D.1: *continued*

Program Variable	Document Variable	Description and/or equation reference
B_j_vm	$\frac{\partial \mathbb{B}_{i,i}}{\partial \varphi_{i(m)}}$	C-85
B_j_vmm1	$\frac{\partial \mathbb{B}_{i,i}}{\partial \varphi_{i(m-1)}}$	C-86
B_j_vmp1	$\frac{\partial \mathbb{B}_{i,i}}{\partial \varphi_{i(m+1)}}$	C-84
B_phi	$\mathbb{B}_{i,5}$	C-3
B_phi_cm	$\frac{\partial \mathbb{B}_{i,5}}{\partial c_{i(m)}}$	C-67
B_phi_cmm1	$\frac{\partial \mathbb{B}_{i,5}}{\partial c_{i(m-1)}}$	C-68
B_phi_cmp1	$\frac{\partial \mathbb{B}_{i,5}}{\partial c_{i(m+1)}}$	C-66
B_phi_vm	$\frac{\partial \mathbb{B}_{i,5}}{\partial \varphi_{(m)}}$	C-70
B_phi_vmm1	$\frac{\partial \mathbb{B}_{i,5}}{\partial \varphi(m-1)}$	C-71
B_phi_vmp1	$\frac{\partial \mathbb{B}_{i,5}}{\partial \varphi_{(m+1)}}$	C-69
bint_surf	l_{int}	initial length of fully-intact region
b_alpha	$b_{\alpha,j}$	fitting parameter for α_{O_2}
b_por	$b_{\epsilon,j}$	fitting parameter for ϵ
b_omega	$b_{\omega,j}$	fitting parameter for ω
b_zeta	$b_{\zeta,j}$	fitting parameter for ζ
chi_cl	χ_{Cl^-}	10-15
chi_na	χ_{Na^+}	10-15
chi_oh	χ_{OH^-}	10-15
cin_del	$\boldsymbol{C}_N^{(n+1)}$	11-25
cin_org	$c_{i,k}$	concentration parameters
cold_del	$\boldsymbol{C}_N^{(n)}$	11-25
czero_del	$\boldsymbol{C}_N^{o}$	11-25
D_j	$\mathbb{D}_{i,i}$	C-7

continued on next page

Table D.1: *continued*

Program Variable	Document Variable	Description and/or equation reference
D_j_vm	$\frac{\partial \mathbb{D}_{i,i}}{\partial \varphi_{i(m)}}$	C-88
D_j_vmm1	$\frac{\partial \mathbb{D}_{i,i}}{\partial \varphi_{i(m-1)}}$	C-89
D_j_vmp1	$\frac{\partial \mathbb{D}_{i,i}}{\partial \varphi_{i(m+1)}}$	C-87
D_phi	$\mathbb{D}_{i,5}$	C-4
D_phi_cm	$\frac{\partial \mathbb{D}_{i,5}}{\partial c_{i(m)}}$	C-73
D_phi_cmm1	$\frac{\partial \mathbb{D}_{i,5}}{\partial c_{i(m-1)}}$	C-74
D_phi_cmp1	$\frac{\partial \mathbb{D}_{i,5}}{\partial c_{i(m+1)}}$	C-72
D_phi_vm	$\frac{\partial \mathbb{D}_{i,5}}{\partial \varphi_{i(m)}}$	C-76
D_phi_vmm1	$\frac{\partial \mathbb{D}_{i,5}}{\partial \varphi_{i(m-1)}}$	C-77
D_phi_vmp1	$\frac{\partial \mathbb{D}_{i,5}}{\partial \varphi_{i(m+1)}}$	C-75
dc_dx	$\frac{\partial c_{i(m)}^{(n+1)}}{\partial x}$	C-9
del_surf	l_{del}	initial length of delaminated region
dhx	$\triangle x$	node spacing
dif	D_i	diffusion coefficient of species i
dtstep	$\triangle t$	time-step
dvar_dx	$\frac{\partial \varphi_{(m)}^{(n+1)}}{\partial x}$	C-10
fro_surf	l_{fro}	initial length of front region
FV	$\mathbb{F}_m$	node function vector, C-22
g_coat	a_c	coating thickness
g_med	g_m	gel-medium thickness
GFM	$\boldsymbol{F}_N$	global function vector, C-43
GJM	$\boldsymbol{J}_N$	global jacobian matrix, C-115
H_j	$\mathbb{H}_{i,i}$	C-8

continued on next page

Table D.1: *continued*

Program Variable	Document Variable	Description and/or equation reference
H_j_vm	$\frac{\partial \mathbb{H}_{i,i}}{\partial \varphi_{i(m)}}$	C-91
H_j_vmm1	$\frac{\partial \mathbb{H}_{i,i}}{\partial \varphi_{i(m-1)}}$	C-92
H_j_vmp1	$\frac{\partial \mathbb{H}_{i,i}}{\partial \varphi_{i(m+1)}}$	C-90
H_phi	$\mathbb{H}_{i,5}$	C-5
H_phi_cm	$\frac{\partial \mathbb{H}_{i,5}}{\partial c_{i(m)}}$	C-79
H_phi_cmm1	$\frac{\partial \mathbb{H}_{i,5}}{\partial c_{i(m-1)}}$	C-80
H_phi_cmp1	$\frac{\partial \mathbb{H}_{i,5}}{\partial c_{i(m+1)}}$	C-78
H_phi_vm	$\frac{\partial \mathbb{H}_{i,5}}{\partial \varphi_{i(m)}}$	C-82
H_phi_vmm1	$\frac{\partial \mathbb{H}_{i,5}}{\partial \varphi_{i(m-1)}}$	C-83
H_phi_vmp1	$\frac{\partial \mathbb{H}_{i,5}}{\partial \varphi_{i(m+1)}}$	C-81
ivalue	t_{sim}	simulation time
m_max	m_{max}	node position of external boundary
ninv	n_{sim}	number of time steps
T(k,i)	$\frac{\partial F_k}{\partial c_{i(m-1)}}$	C-54
U(k,i)	$\frac{\partial F_k}{\partial c_{i(m)}}$	C-55
V(k,i)	$\frac{\partial F_k}{\partial c_{i(m+1)}}$	C-56
vapp	Ψ	applied potential
xi_o_n	$\xi_{o,N}$	convergence criterion for time-steps
xi_o_w	$\xi_{o,W}$	convergence criterion for initial Φ

D.2 Program Listing

D.2.1 Main Program

```
!Program to simulate the electrochemistry during cathodic
!delmaination of coated zinc.  The program uses Newton's method
!to solve the system of governing equations.
      program CADEM
      use big_stuff
      implicit real*8 (A-H,O-Z)
!Use of dynamic storage
      allocate (akg(2000,2000),akgtemp(2000,2000)
     *          ,akg_nr(2000,2000),GJM(2000,2000))
!Read input data
      call Input_Data
!Discretize delamination zone
      call Grid_1d
!Initialize the concentration distributions
      call Initialize_Concentrations
!Initialize porosity
      call Calculate_Porosity
!Initialize polarization parameters
      call Calculate_Parameters
!Calculate initial potential distribution
      call Initialize_Potential
!Add porosity as a dependent variable
      call Include_Porosity
!Time-stepping routine
      call Transient_State
      deallocate (akg,akgtemp,akg_nr,GJM)
      end
```

D.2.2 Input Data

```
!Subroutine that reads input data from input file.
      subroutine input_data
      implicit real*8(A-H,O-Z)
      include 'geometry_data.for'
      include 'data_1.for'
      include 'system_data.for'
      character name*20
      print *,'input_data*****'
      open(unit=10,file='delamination-30.inp',status='unknown')
      rewind 10
!Read program name:pname
      read(10,190)name,pname
!Read metal potential relative to SHE:vapp
      read(10,100)name,vapp
!Read weighting:we
      read(10,100)name,we
!Read time step in seconds:dtstep
      read(10,100)name,dtstep
!Read convergence criterion:conv
      read(10,100)name,xi_o_n
!Read convergence criterion:conv
```

```
      read(10,100)name,xi_o_w
!Read por_ph_eq
      read(10,190)name,por_ph_eq
!where por_ph_eq='yes' then use equilibrium condition for
!pH-porosity relationship !and !por_ph_eq='no' then use
non-equilibrium condition for !pH-porosity relationship

!Read parameter for non-equilibrium condition:ak_v
      read(10,100)name,ak_v
      read(10,*)line
      read(10,*)line
      read(10,90)name,imax_del
!imax_del is the # nodes per mm
      print *,name
      read(10,100)name,surface_del
      read(10,100)name,g_coat
      read(10,100)name,g_med
      read(10,100)name,def_surf
      read(10,100)name,del_surf
      read(10,100)name,fro_surf
      read(10,100)name,aint_surf
      read(10,100)name,bint_surf
      read(10,*)line
!Input of fitting parameter data for porosity
      do 1 i=1,7
1         read(10,100)name,b_por(i)
      read(10,*)line
!Input of fitting parameter data for blocking factor
      do 2 i=1,8
2         read(10,100)name,b_alpha(i)
      read(10,*)line
! Input of fitting parameter data for surface area
      do 3 i=1,8
3         read(10,100)name,b_omega(i)
      read(10,*)line
!Input of fitting parameter data for poisoning factor
      do 4 i=1,7
4         read(10,100)name,b_zeta(i)
      read(10,*)line
      gamma_org=0.d0
!Input of simulation time
      read(10,90)name,ivalue
      ninv=ivalue/dtstep
      read(10,*)line
!-----------------------------------------------------------------
!Input of concentration parameter data in M and converted to
!mol/cm3
      do 5 i=1,4
         read(10,*)name,cdata
5        cin_org(i,1)=cdata/1000.d0
      read(10,*)line
      do 6 k=2,5
         read(10,*)name,cdata
         cin_org(1,k)=cdata/1000.d0
         read(10,*)name,cdata
```

```
          cin_org(2,k)=cdata/1000.d0
          read(10,*)name,cdata
          cin_org(3,k)=cdata/1000.d0
6         read(10,*)line
!-----------------------------------------------------------------
!Input of oxygen concentration at coating surface
      read(10,*)name,bulko2
      bulko2=bulko2*0.001d0   !mol/dm3 to mol/cm3
      nspec=4
!where nspec is the number of species
      nvar=5
!where nvar is the nspec+1
      npor=6
!where npor is # depenedent variables
!Charge numbers
      z(1)=1      ! for Na+
      z(2)=-1     ! for Cl-
      z(3)=-1     ! for OH-
      z(4)=2      ! for Zn+2
!Diffusion coefficients
      dif(1)=1.3341d-5    ! for Na+
      dif(2)=2.0344d-5    ! for Cl-
      dif(3)=5.2458d-5    ! for OH-
      dif(4)=0.71231d-5   ! for Zn+2
      difo2=1.90000d-5    ! for O2
      difo2_org=difo2
!Index for dependent variables
      ina=1   ! for na=
      icl=2   ! for Cl-
      ioh=3   ! for OH-
      izn=4   ! for Zn+2
      iphi=5  ! for solution potential
      ipor=6  ! for porosity
      vapp_org=vapp
!Scaling values
      consc=1.d0
      dcsc=1.d0
      dtsc=dtstep*dcsc
      dts=dtstep*dcsc
      do i=1,nspec
          difs(i)=dif(i)/dcsc
      enddo
      difs_org=difs
      specie(1)='Na+         '
      specie(2)='Cl-         '
      specie(3)='OH-         '
      specie(4)='Zn+2        '
!Scaling of concentration parameters
      cin_org=cin_org/consc
      close(10)
90    format(a21,i7)
100   format(a21,f8.3)
190   format(a21,a20)
      return
      end
```

D.2.3 Grid 1d

```
!Subroutine that calculates the initial number of nodes in each
!region.
      subroutine Grid_1d
      use big_stuff
      implicit real*8 (A-H,O-Z)
      include 'geometry_data.for'
      include 'system_data.for'
      include 'data_1.for'
      print *,'   grid_1d*****'
!imax_del is the number of nodes per mm
!dhx is the node spacing
      dhx=0.1d0/(imax_del-1)
      dxi=dhx
!nodes_del+1 is # nodes in the delaminated region initially
      nodes_del=del_surf/dhx
!nodes_del+1 is # nodes in the front region initially
      nodes_fro=fro_surf/dhx
!nodes_del+1 is # nodes in the semi-intact region initially
      nodes_int=aint_surf/dhx
!nodes_del+1 is # nodes in the fully-intact region initially
      nodes_bin=bint_surf/dhx
      j_del=nodes_del
      j_fro=nodes_fro
      j_int=nodes_int
      j_bin=nodes_bin
!nodes_total is # nodes in delamination zone
      nodes_total=nodes_del+nodes_fro+nodes_int+nodes_bin+1
      print *,'nodes_total=',nodes_total,nodes_total*(nvar+1)
      return
      end
```

D.2.4 Initialize Concentrations

```
!Subroutine to initialize the concentration distributions in the
!delamination zone.
      subroutine Initialize_Concentrations
      print *,'initialize_delaminate*****'
      call initialize_parameters
      call conc_delaminated
      call conc_front
      call conc_semi_intact
      call conc_fully_intact
      return
      end
```

Initialize parameters

```
!Subroutine that calculates the parameters used in constructing
!the initial distributions for the concentrations of species.
      subroutine initialize_parameters
      use big_stuff
      implicit real*8 (A-H,O-Z)
      include 'data_1.for'
```

```
      include 'geometry_data.for'
      include 'system_data.for'
      print *,'   '
      print *,'initialize_parameters*****'
      chi_na=(cin_org(ina,2)-cin_org(ina,1))/del_surf
      chi_cl=(cin_org(icl,2)-cin_org(icl,1))/del_surf
      chi_oh=(cin_org(ioh,2)-cin_org(ioh,1))/del_surf
      alambda_na_fro=(dlog(cin_org(ina,3)/cin_org(ina,2)))
     *                     /fro_surf
      alambda_cl_fro=(dlog(cin_org(icl,3)/cin_org(icl,2)))
     *                     /fro_surf
      alambda_oh_fro=(dlog(cin_org(ioh,3)/cin_org(ioh,2)))
     *                     /fro_surf
      alambda_na_sem=(dlog(cin_org(ina,4)/cin_org(ina,3)))
     *                     /aint_surf
      alambda_cl_sem=(dlog(cin_org(icl,4)/cin_org(icl,3)))
     *                     /aint_surf
      alambda_oh_sem=(dlog(cin_org(ioh,4)/cin_org(ioh,3)))
     *                     /aint_surf
      alambda_na_int=(dlog(cin_org(ina,5)/cin_org(ina,4)))
     *                     /bint_surf
      alambda_cl_int=(dlog(cin_org(icl,5)/cin_org(icl,4)))
     *                     /bint_surf
      alambda_oh_int=(dlog(cin_org(ioh,5)/cin_org(ioh,4)))
     *                     /bint_surf
      return
      end
```

Conc delaminated

```
!Subroutine that calculates the concentration distributions in
!the delaminated region.
      subroutine conc_delaminated
      implicit real*8 (A-H,O-Z)
      include 'data_1.for'
      include 'system_data.for'
      include 'geometry_data.for'
      cin_del(ina,1)=cin_org(ina,1)
      cin_del(icl,1)=cin_org(icl,1)
      cin_del(ioh,1)=cin_org(ioh,1)
      cin_del(izn,1)=0.5d0*
     *      (cin_del(icl,1)+cin_del(ioh,1)-cin_del(ina,1))

      js=nodes_del+1
      cin_del(ina,js)=cin_org(ina,2)
      cin_del(icl,js)=cin_org(icl,2)
      cin_del(ioh,js)=cin_org(ioh,2)
      cin_del(izn,js)=0.5d0*
     *      (cin_del(icl,js)+cin_del(ioh,js)-cin_del(ina,js))

      js=nodes_del+1
      do j=2,nodes_del+1
          cin_del(ina,j)=cin_del(ina,1)+(j-1)*dxi*chi_na
          cin_del(icl,j)=cin_del(icl,1)+(j-1)*dxi*chi_cl
          cin_del(ioh,j)=cin_del(ioh,1)+(j-1)*dxi*chi_oh
```

```
          cin_del(izn,j)=0.5d0*
     *          (cin_del(icl,j)+cin_del(ioh,j)-cin_del(ina,j))
       enddo
       return
       end
```

Conc front

```
!Subroutine that calculates the concentration distributions in
!the front region.
       subroutine conc_front
       implicit real*8 (A-H,O-Z)
       include 'data_1.for'
       include 'system_data.for'
       include 'geometry_data.for'
       js=nodes_del+1
       do 10 is=1,nspec
10         cin_fro(is,1)=cin_del(is,js)
       jf=nodes_fro+1
       do 20 j=1,jf
           x_v=dxi*(j-1)
           cin_fro(ina,j)=cin_org(ina,2)*dexp(x_v*alambda_na_fro)
           cin_fro(icl,j)=cin_org(icl,2)*dexp(x_v*alambda_cl_fro)
           cin_fro(ioh,j)=cin_org(ioh,2)*dexp(x_v*alambda_oh_fro)
20         cin_fro(izn,j)=0.5d0*
     *       (cin_fro(icl,j)+cin_fro(ioh,j) - cin_fro(ina,j))
       do 30 j=2,jf
           k=j+nodes_del
           do 30 is=1,nspec
30             cin_del(is,k)=cin_fro(is,j)
       return
       end
```

Conc semi intact

```
!Subroutine that calculates the concentration distributions in
!the semi-intact region.
       subroutine conc_semi_intact
       implicit real*8 (A-H,O-Z)
       include 'data_1.for'
       include 'system_data.for'
       include 'geometry_data.for'
       js=nodes_del+1+nodes_fro
       do 10 is=1,nspec
10         cin_int(is,1)=cin_del(is,js)
       jf=nodes_int+1
       do 20 j=1,jf
           x_v=dxi*(j-1)
           cin_int(ina,j)=cin_org(ina,3)*dexp(x_v*alambda_na_sem)
           cin_int(icl,j)=cin_org(icl,3)*dexp(x_v*alambda_cl_sem)
           cin_int(ioh,j)=cin_org(ioh,3)*dexp(x_v*alambda_oh_sem)
20         cin_int(izn,j)=0.5d0*
     *       (cin_int(icl,j)+cin_int(ioh,j)-cin_int(ina,j))
       do 30 j=2,jf
           k=j+nodes_del+nodes_fro
```

```
          do 30 is=1,nspec
30            cin_del(is,k)=cin_int(is,j)
      return
      end
```

Conc fully intact

```
!Subroutine that calculates the concentration distributions in
!the fully-intact region.
      subroutine conc_fully_intact
      implicit real*8 (A-H,O-Z)
      include 'data_1.for'
      include 'system_data.for'
      include 'geometry_data.for'
      js=nodes_del+1+nodes_fro+nodes_int
      do 10 is=1,nspec
10        cin_bin(is,1)=cin_del(is,js)
      jf=nodes_bin+1
      do 20 j=1,jf
          do 20 is=1,nvar
20            cin_bin(is,j)=cin_bin(is,1)
      do 30 j=2,jf
          k=j+nodes_del+nodes_fro+nodes_int
          do 30 is=1,nspec
30            cin_del(is,k)=cin_bin(is,j)
      return
      end
```

D.2.5 Calculate Porosity

```
!Subroutine that calculates the value of porosity at the nodes.
      subroutine calculate_porosity
      use big_stuff
      implicit real*8 (A-H,O-Z)
      include 'data_1.for'
      include 'geometry_data.for'
      include 'system_data.for'
      do 10 j=1,nodes_total
          ph_v=14.d0+dlog10(cin_del(ioh,j)*consc*1000.d0)
          s_1=b_por(1)
     *      /(1.d0+dexp(b_por(2)*(ph_v-b_por(3))))
          s_2=b_por(4)
     *      /(1.d0+dexp(b_por(5)*(ph_v-b_por(6))))
10        por(j)=s_1 + s_2 + b_por(7)
      por_coat=por(nodes_total)
      var_coat=por_coat**(1.5d0)
      do 20 j=1,nodes_total
20        var(j)=por(j)**(1.5d0)
!where var is the dependent variable representing porosity
      return
      end
```

D.2.6 Calculate Parameters

```
!Subroutine that calculates the polarization parameters given
!the pH at the nodes.
      subroutine Calculate_Parameters
      use big_stuff
      implicit real*8 (A-H,O-Z)
      print *,'calculate_parameters*****'
      call calculate_alpha
      call calculate_omega
      call calculate_zeta
      call calculate_ilim
      return
      end
```

Calculate alpha

```
      subroutine calculate_alpha
      use big_stuff
      implicit real*8 (A-H,O-Z)
      include 'data_1.for'
      include 'geometry_data.for'
      include 'system_data.for'
      do 10 j=1,nodes_total
          ph_v=14.d0+dlog10(cin_del(ioh,j)*consc*1000.d0)
          s_1=dexp(-b_alpha(2)*(ph_v-b_alpha(3)))
          s_2=b_alpha(1)*s_1/(1.d0+s_1)
          s_3=1.d0/( (1.d0/b_alpha(4))
     *          + dexp(-b_alpha(5)*(ph_v-b_alpha(6))) )
10        alpha_o2(j)= (s_2+b_alpha(7)) * (s_3+b_alpha(8))
      return
      end
```

Calculate omega

```
!Subrotuine that calculates the value of the surface area
!polarization parameter.
      subroutine Calculate_omega
      use big_stuff
      implicit real*8 (A-H,O-Z)
      include 'data_1.for'
      include 'geometry_data.for'
      include 'system_data.for'
      do 10 j=1,nodes_total
          ph_v=14.d0+dlog10(cin_del(ioh,j)*consc*1000.d0)
          s_1=b_omega(1)/
     *      (1.d0+dexp(b_omega(2)*(ph_v-b_omega(3))))
          s_2=b_omega(4)/
     *      (1.d0+dexp(b_omega(5)*(ph_v-b_omega(6))))
10        omega(j)= s_1 + s_2 + b_omega(7)
       return
      end
```

Calculate zeta

```
!Subroutine that calculates the value of the poisoning factor !for
zinc dissolution at the nodes on the metal-coating !interface.
      subroutine calculate_zeta
      use big_stuff
      implicit real*8 (A-H,O-Z)
      include 'data_1.for'
      include 'geometry_data.for'
      include 'system_data.for'
      do 10 j=1,nodes_total
          ph_v=14.d0+dlog10(cin_del(ioh,j)*consc*1000.d0)
          s_1=b_zeta(1)/(1.d0+dexp(b_zeta(2)*(ph_v-b_zeta(3))))
          s_2=b_zeta(4)/(1.d0+dexp(b_zeta(5)*(ph_v-b_zeta(6))))
10        zeta(j)= s_1 + s_2 + b_zeta(7)
       return
      end
```

Calculate ilim

```
!Subroutine that calculates the mass-transfer-limited current
!density for oxygen reduction at nodes on the metal-coating
!interface.
      subroutine Calculate_ilim
      use big_stuff
      implicit real*8 (A-H,O-Z)
      include 'data_1.for'
      include 'geometry_data.for'
      include 'system_data.for'
      do 10 j=1,nodes_total
          var_med=var(j)
          anum=var_coat*var_med
          dnum=var_med*(g_coat-g_med)+var_coat*g_med
          ailimg_v=4.d0*far*difo2_org*bulko2*anum/dnum
10        ailimg_del(j)=ailimg_v*((10.d0)**(6.d0))! in uA/cm2
      return
      end
```

D.2.7 Initialize Potential

```
!Subroutine that calculates the initial distribution of solution
!potential at the metal-coating interface.
      subroutine Initialize_Potential
      implicit real*8 (A-H,O-Z)
      include 'data_1.for'
      include 'system_data.for'
      include 'geometry_data.for'
      print *,'initialize_potential***'
!Calculate the conductivity in the control volumes
      call sigma_values
!Calculate the diffusion current entering control volumes
      call diffusion_current
      cde=0.d0
      phi_cal=0.d0
      phi_old=phi_cal
```

```
!phi_cal:array for storing phi values on metal-coating interface

!Calculate initial distribution for phi
      call initial_phi
!Calculate percentage error
      call phi_error
      print *,'phi_emax=',phi_emax
10    phi_old=phi_cal !Calculate current density on metal-coating
interface
      call current_Zn_del
!Calculate the current density entering each control volume
      call anet_values
!Calculate initial distribution for phi
      call initial_phi
!Calculate percentage error
      call phi_error
      print *,'phi_emax=',phi_emax
      if(phi_emax.gt.xi_o_w)goto 10
!Calculate initial flux profiles
      call calculate_flux_del
!Output initial distributions to files
      nt1=0
      att1=0.d0
      call output_data(nt1,att1)
!Output potential value at delaminated/front boundary
      print *,'       Phi(del)='
     *      ,phi_cal(j_del+1)*(gas*temp/far)*1000.d0

!Output potential value at front/semi-intact boundary
      print *,'       Phi(fro)='
     *      ,phi_cal(j_del+j_fro+1)*(gas*temp/far)*1000.d0

!Output potential value at semi-intact/fully-intact boundary
      print *,'       Phi(int)='
     *  ,phi_cal(j_del+j_fro+j_int+1)*(gas*temp/far)*1000.d0

!Output potential value at external boundary of fully-intact
region
      print *,'       Phi(bin)='
     *  ,phi_cal(j_del+j_fro+j_int+j_bin+1)*(gas*temp/far)*1000.d0

      return
      end
```

Sigma values

```
!Subroutine that calculates the conductivity averaged over the
!pores per unit volume.
      subroutine sigma_values
      implicit real*8 (A-H,O-Z)
      include 'data_1.for'
      include 'system_data.for'
      include 'geometry_data.for'
      sigma=0.d0
      do 20 j=1,nodes_total
```

```
          sum=0.d0
          do 10 is=1,nspec
10            sum=sum+z(is)*z(is)*difs(is)*cin_del(is,j)
          sigma(j)=sum*var(j)*far
       enddo
       return
       end
```

Diffusion current

```
!Subroutine that calculates the diffusion current entering a
!control volume.
       subroutine diffusion_current
       implicit real*8 (A-H,O-Z)
       include 'data_1.for'
       include 'system_data.for'
       include 'geometry_data.for'
       adiff=0.d0
       j=1
       do is=1,nspec
           pc_px=(-3.d0*cin_del(is,j)+4.d0*cin_del(is,j+1)
     *                                    -cin_del(is,j+2))
     *                        /(2.d0*dhx)
           adiff(j)=adiff(j)
     *      +z(is)*difs(is)*pc_px*0.5d0*(var(j)+var(j+1))
       enddo
       adiff(j)=adiff(j)*far
       do j=2,nodes_total-1
           do is=1,nspec
                  pc_px=(cin_del(is,j+1)-cin_del(is,j-1))
     *                        /(2.d0*dhx)
             adiff(j)=adiff(j)
     *      +z(is)*difs(is)*pc_px*0.5d0*(var(j+1)+var(j))
           enddo
           adiff(j)=adiff(j)*far
       enddo
       j=nodes_total
       do is=1,nspec
           pc_px=(cin_del(is,j-2)-4.d0*cin_del(is,j-1)
     *                               +3.d0*cin_del(is,j))
     *                        /(2.d0*dhx)
           adiff(j)=adiff(j)
     *      +z(is)*difs(is)*pc_px*0.5d0*(var(j-1)+var(j))
       enddo
       adiff(j)=adiff(j)*far
       return
       end
```

Anet values

```
!Subroutine that calculates the net current density entering a
!control volume.
       subroutine anet_values
       implicit real*8 (A-H,O-Z)
       include 'data_1.for'
```

```
      include 'system_data.for'
      include 'geometry_data.for'
      anet=0.d0
      do k=1,nodes_total-1
          sum=0.d0
          do j=k,nodes_total
              sum=sum+cde(j)*dhx
          enddo
          anet(k)=sum/(0.0005d0*consc*dcsc)
      enddo
      return
      end
```

Initial phi

```
      subroutine initial_phi
      implicit real*8 (A-H,O-Z)
      include 'data_1.for'
      include 'system_data.for'
      include 'geometry_data.for'
      include 'parameter_data.for'
!Calculate initial distribution for phi
      do j=2,nodes_total
          dphi_dx=adiff(j)/-sigma(j)
!where dphi_dx is the gradient of phi across a control volume
          phi_cal(j)=phi_cal(j-1)+dphi_dx*dhx
      enddo
!Enter calculated initial phi distribution into dependent
!variable storage
      do 4 j=1,nodes_total
4         cin_del(nvar,j)=phi_cal(j)
      return
      end
```

Phi error

```
!Subroutine that calculates percentage error between guess and
!calculated values of solution potential.
      subroutine phi_error
      implicit real*8 (A-H,O-Z)
      include 'data_1.for'
      include 'system_data.for'
      include 'geometry_data.for'
      include 'parameter_data.for'
      phi_emax=0.d0
      do j=2,nodes_total
          perc=dabs(100*(phi_cal(j)-phi_old(j))/phi_cal(j) )
          if(perc.gt.phi_emax)phi_emax=perc
      enddo
      return
      end
```

D.2.8 Include Porosity

```
!Subroutine that adds varphi as a dependent variable.
      subroutine Include_Porosity
      use big_stuff
      implicit real*8 (A-H,O-Z)
      include 'data_1.for'
      include 'geometry_data.for'
      include 'system_data.for'
      print *,'   '
      print *,'include_porosity*****'
      cold_del=cin_del
      cin_del=0.d0
      do j=1,nodes_total
          do is=1,nvar
              cin_del(is,j)=cold_del(is,j)
          enddo
          cin_del(nvar+1,j)=var(j)
      enddo
      cold_del=cin_del
      return
      end
```

D.2.9 Transient State

```
!Subroutine for time-stepping.
      subroutine transient_state
      use big_stuff
      implicit real*8 (A-H,O-Z)
      include 'data_1.for'
      include 'geometry_data.for'
      include 'system_data.for'
      print *,'transient_state*****'
!telap:elapsed time
      telap=0.d0
!   call set_unknowns
      int=0
      do jtime=1,ninv
!increment time
          telap=telap+dtstep
          print *,'   '
          print *,'/////telap=',telap
!Update dependent variables
          cold_del=cin_del
!var_old stores the values of var at the present time
          var_old=var
!por_old stores the values of porosity at the present time
          por_old=por
!Calculate polarization parameters at present time
          call calculate_parameters
!-------------------------------------------------------------
!Output data about current time step
          print *,'Phi=',1000.d0*
```

```
     *      cin_del(nvar,nodes_total)*gas*temp/far
            print *,
     *   'E=',1000.d0*
     *   (vapp-cin_del(nvar,nodes_total)*gas*temp/far)
         ph=14.d0+dlog10(cin_del(ioh,nodes_total)
     *       *consc*1000.d0)
            print *,'ph=',ph
            print *,'cd=',cde(nodes_total)
            j=nodes_total
            aio2=-1.d0*far*fxoh(j)
            aizn=   fxzn(j)*(2.d0*far)
            print *,'aio2=',aio2
            print *,'aizn=',aizn
!-----------------------------------------------------------------
!Calculate the dependent variables values at next time-step
            call time_step
!Calculate flux distributions at next time step
            call calculate_flux
!Calculate ionic current distribution at next time step
            call ionic_current
!-----------------------------------------------------------------
!Output data every 100 time steps
            nt=jtime
            att=telap
            int=int+1
            if(int.eq.100)then
                call output_data(nt,att)
                int=0
            endif
!-----------------------------------------------------------------
      enddo
      return
      end
```

Time step

```
!Subroutine to calculate conditions at next time step cin_del
!given conditions at current time step cold_del.
      subroutine time_step
      use big_stuff
      implicit real*8 (A-H,O-Z)
      include 'data_1.for'
      include 'geometry_data.for'
      include 'system_data.for'
!Output subroutine name
      print *,'   time_step_nr***'
!Construct global degree of freedom vector
      call set_unknowns_nr_por
!Calculate current densities at metal-coating interface
      call current_zn_del
!Construct global solution vector
10    call set_sol_del_por
!Update guess for czero with cin_del
      czero=cin_del
!Discretize the governing equations and construct global
```

```
!coefficient matrix and global function vector.
      call governing_equations
!Calculate improved cin_del
      call solver
!Compare cin_del with guess czero
      call compare_por
!Update arrays var and por with calculated values
      do 20 j=1,nodes_total
          var(j)=cin_del(ipor,j)
20        por(j)=var(j)**(2.d0/3.d0)
!Determine if calculated cin_del is satisfactory
      ifg=0
      do 30 is=1,npor
30        if(emax_lin(is).gt.xi_o_n)ifg=1
      if(ifg.eq.1)goto 10
      return
      end
```

Set sol del por

```
!Subroutine to construct the global solution array sol_del using
!the conditions at the nodes.
      subroutine set_sol_del_por
      use big_stuff
      implicit real*8 (A-H,O-Z)
      include 'data_1.for'
      include 'geometry_data.for'
      include 'system_data.for'
!Initialize sol_del
      sol_del=0.d0
      k=0
      do 10 j=1,nodes_total
          do 10 is=1,npor
              k=k+1
10            sol_del(k)=cin_del(is,j)
      return
      end
```

Compare por

```
!Subroutine to compare calculated cin_del with guess czero.
      subroutine compare_por
      use big_stuff
      implicit real*8 (A-H,O-Z)
      include 'data_1.for'
      include 'geometry_data.for'
      include 'system_data.for'
!Initialize emax_lin
      emax_lin=0.d0
!where emax_lin is a one-dimensional array that holds the values
!of the largest percentage difference between calculated and
!guess values for each dependent variable.

!Calculation of percentage differences between calculated and
!guess value for variable is at node j
```

```
      do 10 j=2,nodes_total
          do 10 is=1,npor
              perc=dabs(100.d0*(cin_del(is,j)
     *          -czero(is,j))/czero(is,j))
!Compare perc for variable is with current maximum and update if
!perc is greater than maximum.
10              if(perc.gt.emax_lin(is))emax_lin(is)=perc


!Output maximum percentage differences for variables.
      print *,'emax_lin,cin_del(is,nodes_total)'
      do 20 is=1,npor
20        print *,is,emax_lin(is),cin_del(is,nodes_total)
      return
      end
```

Set unknowns nr por

```
!Subroutine to construct the array that identifies the nodes
!where the conditions are known and unknown.
      subroutine set_unknowns_nr_por
      use big_stuff
      implicit real*8 (A-H,O-Z)
      include 'data_1.for'
      include 'geometry_data.for'
      include 'system_data.for'
      iun_new=0
      iun_new(1)=1
!where inu_new is an array such that for a given node j the
!condition iun_new(j)=1 and iun_new(j)=0 corresponds to known
!and unknown conditions, respectively.
      iut_new=nodes_total-1
!where iut_new=# nodes where condition is unknown

!Construction of degree of freedom vector iun_con.

!iun_con is an array such that for a given node j and dependent
!variable i. The conditions iun_con((j-1)*npor+i)=1 and
!iun_con((j-1)*npor+i)=0  correspond to known and unknown
!variables, respectively.
      ik=0
      iun_con=0       !initialize iun_con
      do j=1,nodes_total
          do is=1,npor
              ik=ik+1
!determine if node j has known or unknown conditions
              if(iun_new(j).eq.1)iun_con(ik)=1
          enddo
      enddo
      return
      end
```

Current zn del

```
!Subroutine to calculate the current densities of zinc
!dissolution  and oxygen reduction at the metal-coating surface.
      subroutine current_zn_del
      implicit real*8 (A-H,O-Z)
      include 'geometry_data.for'
      include 'system_data.for'
      include 'data_1.for'
      external zinc_current
!Output applied potential in SHE and SCE
      print *,vapp,'SHE'
      print *,vapp-0.241d0,'SCE'
!Conversion from volts to mV SHE to mV SCE
      vappt=(vapp-0.241d0)*1000.d0
!Calculate for all nodes
      do j=1,nodes_total
!conversion of ilim from uA/cm2 to A/cm2
         ailim=ailimg_del(j)*(10.d0**-6)
!Calculation of solution potential phi in mV from !dependent
variable for potential.
         phi=cin_del(nvar,j)*(gas*temp/far)*1000.d0
!       Current density is in A/cm2
         aizn=zinc_current(vappt,phi)
!where aizn is the current density due to zinc dissolution
         aio2=-ailim
!where aio2 is the current density due to oxygen reduction
!Scale current densities with polarization parameters at node j
         aizn=aizn*zeta(j)*omega(j)
         aio2=aio2*alpha_o2(j)*omega(j)
!Calculate net current density at node j and store in array cde
         cde(j)=aizn+aio2
!Calculate flux of hydroxide ions at node j and store in array
!fxoh
         fxoh(j)=(aio2)/(-1.d0*far)
!Calculate flux of zinc ions at node j and store in array fxzn
         fxzn(j)=aizn/(2.d0*far)
      enddo
      return
      end
```

Zinc current

```
!function to calculate the zinc dissolution current density.
      double precision function zinc_current(vappt,phi)
      implicit real*8 (A-H,O-Z)
      include 'geometry_data.for'
      aa=(vappt-phi-eqpot_zn)/beta_zn
      zinc_current=zn_io*(10**aa)
      return
      end
```

Set unknowns

```
!Subrountie that sets array to identify known and unknown
!conditions.
      subroutine set_unknowns
      use big_stuff
      implicit real*8 (A-H,O-Z)
      include 'data_1.for'
      include 'geometry_data.for'
      include 'system_data.for'
      iun_new=0
!where inu_new is an array such that for a given node j the
!condition iun_new(j)=1 and iun_new(j)=0 corresponds to known
!and unknown conditions, respectively.
      iun_new(1)=1
!conditions known at node m=1
      iut_new=nodes_total-1
!where iut_new=# nodes where condition is unknown
      ik=0
      iun_con=0
      do 10 i=1,nodes_total
          do 10 is=1,nvar
              ik=ik+1
 10         if(iun_new(i).eq.1)iun_con(ik)=1
      return
      end
```

Calculate flux

```
!Subroutine to calculate the flux of species.
      subroutine calculate_flux
      implicit real*8 (A-H,O-Z)
      include 'data_1.for'
      include 'system_data.for'
      include 'geometry_data.for'
      print *,'   calculate_flux_del***'
      ohmic=0.d0
      ohm_mig=0.d0
      ohm_dif=0.d0
!Flux at boundary node m_1
      j=1
      dphi_dx=( -3.d0*cin_del(iphi,j) + 4.d0*cin_del(iphi,j+1)
     *          - cin_del(nvar,j+2))/(2.d0*dhx)
      do is=1,nspec
          zdifs=z(is)*difs(is)
          dc_dx=( -3.d0*cin_del(is,j) + 4.d0*cin_del(is,j+1)
     *          - cin_del(is,j+2))/(2.d0*dhx)
          fx_specie(is,j)=-zdifs*var(j)*cin_del(is,j)*dphi_dx
     *          - var(j)*difs(is)*dc_dx
          fx_specie(is,j)=fx_specie(is,j)*consc*dcsc
          ohmic(j)=far*z(is)*fx_specie(is,j)+ohmic(j)
          a_mig=-zdifs*var(j)*cin_del(is,j)*dphi_dx*consc*dcsc
          a_dif=- var(j)*difs(is)*dc_dx*consc*dcsc
          ohm_mig(j)=far*z(is)*a_mig+ohm_mig(j)
          ohm_dif(j)=far*z(is)*a_dif+ohm_dif(j)
```

```
      enddo
!Flux at non-boundary nodes
      do j=2,nodes_total-1
          dphi_dx=( cin_del(iphi,j+1) - cin_del(iphi,j-1))
     *                          /(2.d0*dhx)
          d2phi_dx2=( cin_del(iphi,j-1) - 2.d0*cin_del(iphi,j)
     *                     + cin_del(iphi,j+1))
     *                          /(dhx**2)
          do is=1,nspec
              zdifs=z(is)*difs(is)
              dc_dx=( cin_del(is,j+1) - cin_del(is,j-1))
     *                          /(2.d0*dhx)
              d2c_dx2=( cin_del(is,j-1) - 2.d0*cin_del(is,j)
     *                   + cin_del(is,j+1))
     *                          /(dhx**2)

           fx_specie(is,j)=-zdifs*var(j)*cin_del(is,j)*dphi_dx
     *          - var(j)*difs(is)*dc_dx
              fx_specie(is,j)=fx_specie(is,j)*consc*dcsc
          a_mig=-zdifs*var(j)*cin_del(is,j)*dphi_dx*consc*dcsc
              a_dif=-var(j)*difs(is)*dc_dx*consc*dcsc
              ohmic(j)=far*z(is)*fx_specie(is,j)+ohmic(j)
              ohm_mig(j)=far*z(is)*a_mig+ohm_mig(j)
              ohm_dif(j)=far*z(is)*a_dif+ohm_dif(j)
          enddo
      enddo
!Flux at boundary node m_max
      j=nodes_total
      dphi_dx=( cin_del(nspec+1,j-2) - 4.d0*cin_del(nspec+1,j-1)
     *          + 3.d0*cin_del(nspec+1,j))/(2.d0*dhx)
      do is=1,nspec
          zdifs=z(is)*difs(is)
          dc_dx=( cin_del(is,j-2) - 4.d0*cin_del(is,j-1)
     *          + 3.d0*cin_del(is,j))/(2.d0*dhx)
          fx_specie(is,j)=-zdifs*var(j)*cin_del(is,j)*dphi_dx
     *          - var(j)*difs(is)*dc_dx
          fx_specie(is,j)=fx_specie(is,j)*consc*dcsc
          ohmic(j)=far*z(is)*fx_specie(is,j)+ohmic(j)
          a_mig=-zdifs*var(j)*cin_del(is,j)*dphi_dx*consc*dcsc
          a_dif=- var(j)*difs(is)*dc_dx*consc*dcsc
          ohm_mig(j)=far*z(is)*a_mig+ohm_mig(j)
          ohm_dif(j)=far*z(is)*a_dif+ohm_dif(j)
      enddo
      return
      end
```

D.2.10 Governing Equations

```
!Subroutine to discretize the governing equations and assemble the
!global function vector and the global jacobian matrix.npor= 6
!nspec=4 ; nvar=5
      subroutine governing_equations
      use big_stuff
      implicit real*8 (A-H,O-Z)
      include 'data_1.for'
```

```
      include 'geometry_data.for'
      include 'system_data.for'
!Initialize GFV and GJM to zero.
      GFV=0.d0
      GJM=0.d0
      do m=1,nodes_total
          call initialize_2d
          call na_gov_eq(m)
          call cl_gov_eq(m)
          call oh_gov_eq(m)
          call zn_gov_eq(m)
          call neutrality_gov_eq(m)
          if(por_ph_eq(1:3).eq.'yes')call porosity_eq(m)
          if(por_ph_eq(1:2).eq.'no')call porosity_noneq(m)
          call assemble_GFV(m)
          call assemble_GJM(m)
      enddo
      return
      end
```

Porosity eq

```
!Calculate the elements of the node function vector and node
!jacobian matrix when the condition of equilibrium por-pH
!relationship is used.
      subroutine porosity_eq(j)
      implicit real*8 (A-H,O-Z)
      include 'data_1.for'
      include 'system_data.for'
      include 'geometry_data.for'
      ig=ipor
      D(ig,ig)=1.d0
      b_por(8)=(dexp(-b_por(2)*b_por(3)
     *      +14.d0*b_por(2)))*(10.d0**b_por(2))
      b_por(9)=(dexp(-b_por(5)*b_por(6)
     *      +14.d0*b_por(5)))*(10.d0**b_por(5))
      ph_v=14.d0+dlog10(cin_del(ioh,j)*consc*1000.d0)
      s_1=b_por(1)/(1.d0+dexp(b_por(2)*(ph_v-b_por(3))))
      s_2=b_por(4)/(1.d0+dexp(b_por(5)*(ph_v-b_por(6))))
      por_v=s_1+s_2+b_por(7)
      por_eq=por_v
      var_v=por_v**(1.5d0)
      FV(ig)=cin_del(ipor,j)-var_v
      U(ig,ig)=(2.d0/3.d0)*(var(j)**-(1.d0/3.d0))
      U_max(ig,ig)=(2.d0/3.d0)*(var(j)**-(1.d0/3.d0))

      c_oh=(cin_del(ioh,j)*consc*1000.d0)
      anum=b_por(1)*b_por(2)*b_por(8)*c_oh**(-(b_por(2)+1.d0))
      dnom=(1.d0+b_por(8)*(c_oh**(-b_por(2))))**2.d0
      s_1=anum/dnom

      anum=b_por(4)*b_por(9)*b_por(5)*c_oh**(-(b_por(5)+1.d0))
      dnom=(1.d0+b_por(9)*(c_oh**(-b_por(5))))**2.d0
      s_2=anum/dnom
      U(ig,ioh)=s_1+s_2
```

```
      U_max(ig,ioh)=s_1+s_2
      return
      end
```

Porosity noneq

```
!Calculate the elements of the node function vector and node
!jacobian matrix when the condition of non-equilibrium por-pH
!relationship is used.
      subroutine porosity_noneq(j)
      implicit real*8 (A-H,O-Z)
      include 'data_1.for'
      include 'system_data.for'
      include 'geometry_data.for'
      ig=ipor
      D(ig,ig)=1.d0
      b_por(8)=(dexp(-b_por(2)*b_por(3)+14.d0*b_por(2)))
     *      *(10.d0**b_por(2))
      b_por(9)=(dexp(-b_por(5)*b_por(6)+14.d0*b_por(5)))
     *      *(10.d0**b_por(5))
      ph_v=14.d0+dlog10(cin_del(ioh,j)*consc*1000.d0)
      s_1=b_por(1)/(1.d0+dexp(b_por(2)*(ph_v-b_por(3))))
      s_2=b_por(4)/(1.d0+dexp(b_por(5)*(ph_v-b_por(6))))
      por_v=s_1+s_2+b_por(7)
      por_eq=por_v
      var_v=por_v**(1.5d0)
      var_eq=por_eq**(1.5d0)
      anum=por_old(j)/dtstep + ak_v*por_eq
      dnom=ak_v + 1.d0/dtstep
      por_v=anum/dnom
      FV(ig)=+(cin_del(nvar+1,j))**(2.d0/3.d0)
     *          *(ak_v + 1.d0/dtstep)
     *      -(por_old(j)/dtstep + ak_v*por_eq)
      U(ig,ig)=(2.d0/3.d0)*(var(j)**-(1.d0/3.d0))
   *          *(ak_v+1.d0/dtstep)
      U_max(ig,ig)=(2.d0/3.d0)*(var(j)**-(1.d0/3.d0))
   *          *(ak_v+1.d0/dtstep)

      c_oh=(cin_del(ioh,j)*consc*1000.d0)
      anum=b_por(1)*b_por(2)*b_por(8)*c_oh**(-(b_por(2)+1.d0))
      dnom=(1.d0+b_por(8)*(c_oh**(-b_por(2))))**2.d0
      s_1=anum/dnom

      anum=b_por(4)*b_por(9)*b_por(5)*c_oh**(-(b_por(5)+1.d0))
      dnom=(1.d0+b_por(9)*(c_oh**(-b_por(5))))**2.d0
      s_2=anum/dnom
      U_max(ig,ioh)=-ak_v*(s_1+s_2)
      U(ig,ioh)=-ak_v*(s_1+s_2)
      return
      end
```

Na gov eq

```
!Subroutine to calculate the elements for the gov. eq. of cNa+.
      subroutine na_tr_nr_por(j)
```

```
      implicit real*8 (A-H,O-Z)
      include 'data_1.for'
      include 'system_data.for'
      include 'geometry_data.for'
      is=ina
      if(j.eq.nodes_total)then
          call boundary_node(is,is,j)
      else
          call non_boundary_node(is,is,j)
      endif
      return
      end
```

Cl gov eq

```
!Subroutine to calculate  elements for the gov. eq. of cCl-.
      subroutine cl_tr_nr_por(m)
      implicit real*8 (A-H,O-Z)
      include 'data_1.for'
      include 'system_data.for'
      include 'geometry_data.for'
      is=icl
      if(m.eq.nodes_total)then
          call boundary_node(is,is,m)
      else
          call non_boundary_node(is,is,m)
      endif
      return
      end
```

OH gov eq

```
!Subroutine to calculate the elements for the gov. eq. of cOH-.
      subroutine oh_tr_nr_por(m)
      implicit real*8 (A-H,O-Z)
      include 'data_1.for'
      include 'system_data.for'
      include 'geometry_data.for'
      is=ioh
      if(m.eq.nodes_total)then
          call boundary_node(ioh,is,m)
      else
          call non_boundary_node(ioh,is,m)
      endif
      if(m.ne.1.and.m.ne.nodes_total)then
          FV(ioh)=FV(ioh)+fxoh(m)/(g_med*consc*dcsc)
      endif
      return
      end
```

Zn gov eq

```
!Subroutine to calculate the elements for the gov. eq. of cZn+2.
      subroutine zn_gov_eq(m)
```

```
      implicit real*8 (A-H,O-Z)
      include 'data_1.for'
      include 'system_data.for'
      include 'geometry_data.for'
      is=izn
      if(m.eq.nodes_total)then
          call boundary_node(is,is,m)
      else
          call non_boundary_node(is,is,m)
      endif
      if(m.ne.1.and.m.ne.nodes_total)then
          FV(izn)=FV(izn)+fxzn(m)/(g_med*consc*dcsc)
      endif
      return
      end
```

Neutrality gov eq

```
!Subroutine to calculate the elements for the gov. eq.of the
!electroneutrality condition.
      subroutine neutrality_gov_eq(m)
      implicit real*8 (A-H,O-Z)
      include 'data_1.for'
      include 'system_data.for'
      ig=iphi
      do 10 i=1,nspec
          D(ig,i)=z(i)
          U(ig,i)=z(i)
10        U_max(ig,i)=z(i)
      sum=0.d0
      do 20 is=1,nspec
20        sum=sum+D(ig,is)*cin_del(is,m)
      FV(ig)=sum
      return
      end
```

Non boundary node

```
!Subroutine to calculate the elements for a species with index is
!at a non-boundary node.
      subroutine non_boundary_node(ig,is,m)
      implicit real*8 (A-H,O-Z)
      include 'data_1.for'
      include 'system_data.for'
      include 'geometry_data.for'
!The boundary node is m=1
      if(m.eq.1)return
!caculate the gradient of c_i
      dc_dx=(cin_del(is,m+1) - cin_del(is,m-1))/(2.d0*dhx)
!calculate the gradient of phi
      dphi_dx=(cin_del(iphi,m+1) - cin_del(iphi,m-1))/(2.d0*dhx)
!calculate the gradient of varphi
      dvar_dx=(cin_del(ipor,m+1) - cin_del(ipor,m-1))/(2.d0*dhx)
      zdifs=z(is)*difs(is)
      B_phi_1=zdifs*(cin_del(is,m)/(dhx**2)
```

```
*      + dc_dx/(2.d0*dhx))
 B_phi_2=zdifs*cin_del(is,m)/(2.d0*dhx)
 B_phi=cin_del(ipor,m)*B_phi_1+dvar_dx*B_phi_2
 B_phi_cmp1=zdifs*cin_del(ipor,m)/(4.d0*(dhx**2))
 B_phi_cm=zdifs*(cin_del(ipor,m)/(dhx**2)
*          +dvar_dx/(2.d0*dhx))
 B_phi_cmm1=-B_phi_cmp1
 B_phi_vmp1=zdifs*cin_del(is,m)/(4.d0*(dhx**2))
 B_phi_vm=zdifs*( cin_del(is,m)/(dhx**2)+dc_dx/(2.d0*dhx))
 B_phi_vmm1=-B_phi_vmp1
 H_phi_1=zdifs*(cin_del(is,m)/(dhx**2) - dc_dx/(2.d0*dhx))
 H_phi_2=-zdifs*cin_del(is,m)/(2.d0*dhx)
 H_phi=cin_del(ipor,m)*H_phi_1+dvar_dx*H_phi_2
 H_phi_cmp1=-B_phi_cmp1
 H_phi_cm=zdifs*(cin_del(ipor,m)/(dhx**2)
*              - dvar_dx/(2.d0*dhx))
 H_phi_cmm1=B_phi_cmp1
 H_phi_vmp1=-zdifs*cin_del(is,m)/(4.d0*(dhx**2.d0))
 H_phi_vm=zdifs* ( cin_del(is,m)/(dhx**2)
*                 - dc_dx/(2.d0*dhx) )
 H_phi_vmm1=-H_phi_vmp1
 D_phi_1=-2.d0*zdifs*cin_del(is,m)/(dhx**2)
 D_phi=cin_del(ipor,m)*D_phi_1
 D_phi_cmp1=0.d0
 D_phi_cm=-2.d0*zdifs*cin_del(ipor,m)/(dhx**2)
 D_phi_cmm1=0.d0
 D_phi_vmp1=0.d0
 D_phi_vm=-2.d0*zdifs*cin_del(is,m)/(dhx**2.d0)
 D_phi_vmm1=0.d0
 H_j_1= difs(is)/(dhx**2)
 H_j_2=-difs(is)/(2.d0*dhx)
 H_j=var(m)*H_j_1 + dvar_dx*H_j_2
 D_j_1=-2.d0*difs(is)/(dhx**2)
 D_j_2=0.d0
 D_j=var(m)*D_j_1 + dvar_dx*D_j_2
 B_j_1=difs(is)/(dhx**2)
 B_j_2=difs(is)/(2.d0*dhx)
 B_j=var(m)*B_j_1 + dvar_dx*B_j_2
 B_j_vmp1=difs(is)/(4.d0*(dhx**2.d0))
 B_j_vm=difs(is)/(dhx**2.d0)
 B_j_vmm1=-B_j_vmp1
 D_j_vmp1=0.d0
 D_j_vm=-2.d0*difs(is)/(dhx**2.d0)
*      -( 2.d0*(var(m)**(-1.d0/3.d0))/(3.d0*dtsc))
 D_j_vmm1=0.d0
 H_j_vmp1=-B_j_vmp1
 H_j_vm=B_j_vm
 H_j_vmm1=-B_j_vmm1
 T(ig,is)=   H_j + cin_del(iphi,m+1)*B_phi_cmm1
*          + cin_del(iphi,m)  *D_phi_cmm1
*          + cin_del(iphi,m-1)*H_phi_cmm1
 T(ig,iphi)=H_phi
 T(ig,ipor)=cin_del(iphi,m+1)  *B_phi_vmm1
*          + cin_del(iphi,m)  *D_phi_vmm1
*          + cin_del(iphi,m-1)*H_phi_vmm1
```

```
*          + cin_del(is,m+1)  *B_j_vmm1
*          + cin_del(is,m)    *D_j_vmm1
*          + cin_del(is,m-1)  *H_j_vmm1
 U(ig,is)=D_j-por_old(m)/dtsc
*          + cin_del(iphi,m+1)*B_phi_cm
*          + cin_del(iphi,m)  *D_phi_cm
*          + cin_del(iphi,m-1)*H_phi_cm
 U(ig,iphi)=D_phi
 U(ig,ipor)=cin_del(iphi,m+1)*B_phi_vm
*          + cin_del(iphi,m)  *D_phi_vm
*          + cin_del(iphi,m-1)*H_phi_vm
*          + cin_del(is,m+1)  *B_j_vm
*          + cin_del(is,m)    *D_j_vm
*          + cin_del(is,m-1)  *H_j_vm
 V(ig,is)=   B_j + cin_del(iphi,m+1)*B_phi_cmp1
*          + cin_del(iphi,m)  *D_phi_cmp1
*          + cin_del(iphi,m-1)*H_phi_cmp1
 V(ig,iphi)= B_phi
 V(ig,ipor)=  cin_del(iphi,m+1)*B_phi_vmp1
*          + cin_del(iphi,m)  *D_phi_vmp1
*          + cin_del(iphi,m-1)*H_phi_vmp1
*          + cin_del(is,m+1)  *B_j_vmp1
*          + cin_del(is,m)    *D_j_vmp1
*          + cin_del(is,m-1)  *H_j_vmp1
 H(ig,is)=H_j
 H(ig,iphi)=H_phi
 D(ig,is)=D_j-   por_old(m)/dtsc
 D(ig,iphi)=D_phi
 B(ig,is)=B_j
 B(ig,iphi)=B_phi
 FV(ig)=cold_del(is,m)*por_old(m)/dtsc
*      +H(ig,is)*cin_del(is,m-1)
*      + H(ig,iphi)*cin_del(iphi,m-1)
*      +D(ig,is)*cin_del(is,m)
*      + D(ig,iphi)*cin_del(iphi,m)
*      +B(ig,is)*cin_del(is,m+1)
*      + B(ig,iphi)*cin_del(iphi,m+1)
 return
 end
```

Boundary node

```
!Subroutine to calculate the elements for a species at the
!boundary node m_max
      subroutine boundary_node(ig,is,m_max)
      implicit real*8 (A-H,O-Z)
      include 'data_1.for'
      include 'system_data.for'
      include 'geometry_data.for'
      zdifs=z(is)*difs(is)
      dphi_dx=(cin_del(iphi,m_max-2)-4.d0*cin_del(iphi,m_max-1)
     *              +3.d0*cin_del(iphi,m_max))
     *                     /(2.d0*dhx)
      HP_phi=-zdifs*cin_del(is,m_max)/ (2.d0*dhx)
      HP_phi_cm=-zdifs/(2.d0*dhx)
```

```
      HP_j=-difs(is)/(2.d0*dhx)
      H_j=4.d0*difs(is)/(2.d0*dhx)
      H_phi=4.d0*zdifs*cin_del(is,m_max)/ (2.d0*dhx)
      H_phi_cm=4.d0*zdifs/ (2.d0*dhx)
      D_j=-3.d0*difs(is)/(2.d0*dhx)
      D_phi=-3.d0*zdifs*cin_del(is,m_max)/ (2.d0*dhx)
      D_phi_cm=-3.d0*zdifs/ (2.d0*dhx)
      A_max(ig,iphi)=HP_phi
      A_max(ig,is)=HP_j
      T_max(ig,is)=H_j
      T_max(ig,iphi)=H_phi
      U_max(ig,iphi)=D_phi
      U_max(ig,is)=D_j + cin_del(iphi,m_max-2)*HP_phi_cm
     *      + cin_del(iphi,m_max-1)*H_phi_cm
     *      + cin_del(iphi,m_max)  *D_phi_cm
      HP(ig,iphi)=HP_phi
      HP(ig,is)=HP_j
      H(ig,is)=H_j
      H(ig,iphi)=H_phi
      D(ig,iphi)=D_phi
      D(ig,is)=D_j
      FV(ig)=       H(ig,is)*cin_del(is,m_max-1)
     *          + H(ig,iphi) *cin_del(iphi,m_max-1)
     *          + D(ig,is) *cin_del(is,m_max)
     *          + D(ig,iphi) *cin_del(iphi,m_max)
     *          + HP(ig,is)*cin_del(is,m_max-2)
     *          + HP(ig,iphi)*cin_del(iphi,m_max-2)
      return
      end
```

Assemble GFV

```
!Subroutine to assemble node function vector into global
!function vector.
      subroutine assemble_GFV(m)
      use big_stuff
      implicit real*8 (A-H,O-Z)
      include 'geometry_data.for'
      include 'data_1.for'
      include 'system_data.for'
      do 10 i=1,ipor
10        GFV((m-1)*ipor+i)=FV(i)
      return
      end
```

Assemble GJM

```
      subroutine assemble_GJM(m)
      use big_stuff
      implicit real*8 (A-H,O-Z)
      include 'geometry_data.for'
      include 'data_1.for'
      include 'system_data.for'
      i=0
      ifst=(m-1)*(ipor)+1
```

```
      isec=(m-1)*(ipor)+(ipor)
      if(m.eq.1)return
!Non-boundary node
      if(m.ne.1.and.m.ne.nodes_total)then
          do 10 ir=ifst,isec
              i=i+1
              do 10 j=1,(nvar+1)
                  GJM(ir,(m-1-1)*ipor+j)=
     *              GJM(ir,(m-1-1)*ipor+j) + T(i,j)
                  GJM(ir,(m-1)*ipor+j)=
     *              GJM(ir,(m-1)*ipor+j)    + U(i,j)
10                GJM(ir,(m+1-1)*ipor+j)=
     *              GJM(ir,(m+1-1)*ipor+j) + V(i,j)
       endif
!Boundary node
      if(m.eq.nodes_total)then
          do 20 ir=ifst,isec
              i=i+1
              do 20 j=1,ipor
                  GJM(ir,(m-2-1)*ipor+j)=
     *              GJM(ir,(m-2-1)*ipor+j) + A_max(i,j)
                  GJM(ir,(m-1-1)*ipor+j)=
     *              GJM(ir,(m-1-1)*ipor+j) + T_max(i,j)
20                GJM(ir,(m-1)*ipor+j)=
     *              GJM(ir,(m-1)*ipor+j)   + U_max(i,j)
      endif
      return
      end
```

D.2.11 Solver

```
!Subroutine that solves the  system of linear equations for a
!given a  matrix GJM  and a vector GFV using the !LAPACK solver.
      subroutine solver
      use big_stuff
      implicit real*8 (A-H,O-Z)
      include 'data_1.for'
      include 'system_data.for'
      include 'geometry_data.for'
      dimension akgs(2000,2000),rhss(2000)
      call reduce_GFV
      call reduce_GJM
      n=ipor*iut_new
      print *,'n=',n
      akgs=akg
      rhss=rhsnew
      call LAPACK_link(akgs,rhss,n)
      sol_del=0.d0
      i=0
      do ir=1,ipor*(nodes_total)
          if(iun_con(ir).eq.0)then
              i=i+1
              sol_del(ir)=rhss(i)
          endif
```

```
      enddo
      k=0
      do j=1,nodes_total
          do i=1,ipor
              k=k+1
              cin_del(i,j)=sol_del(k)+cin_del(i,j)
          enddo
      enddo
      return
      end
```

Reduce GFV

```
!Subroutine that reduces the vector GFV correcting for known
!conditions.
      subroutine reduce_GFV
      use big_stuff
      implicit real*8 (A-H,O-Z)
      include 'data_1.for'
      include 'system_data.for'
      include 'geometry_data.for'
      i=0
      rhsnew=0.d0
      do ir=1,nodes_total*npor
          if(iun_con(ir).eq.0)then
              i=i+1
              rhsnew(i)=-GFV(ir)
          endif
      enddo
      return
      end
```

Reduce GJM

```
!Subroutine that reduces the GJM by removing columns and rows of
!essential nodes.
      subroutine reduce_GJM
      use big_stuff
      implicit real*8 (A-H,O-Z)
      include 'data_1.for'
      include 'system_data.for'
      include 'geometry_data.for'
      akgtemp=0.d0
      ic=0
      do ir=1,ipor*nodes_total
          if(iun_con(ir).eq.0)then
              ic=ic+1
              do jc=1,ipor*nodes_total
                  akgtemp(ic,jc)=GJM(ir,jc)
              enddo
          endif
      enddo
      akg=0.d0
      ic=0
      do ir=1,ipor*nodes_total        !striking columns
```

```
          if(iun_con(ir).eq.0)then
              ic=ic+1
              do jc=1,ipor*nodes_total
                  akg(jc,ic)=akgtemp(jc,ir)
              enddo
          endif
      enddo
      return
      end
```

LAPACK link

```
!Subroutine that calls the LAPACK solver.
      subroutine LAPACK_link(akgs,rhss,N)
      use big_stuff
      include 'data_1.for'
      real*8 TOL,D,C
      real*8, ALLOCATABLE :: Bnew(:),Anew(:,:)
      integer, ALLOCATABLE :: ipiv(:)
      real*8 akgs(2000,2000),rhss(2000)
      integer lda,ldb
      ALLOCATE(Bnew(N), Anew(N,N))
      ALLOCATE(ipiv(n))
      Bnew=0.d0
      Anew=0.d0
      do i=1,N
          do j=1,N
              Anew(i,j)=akgs(i,j)
          enddo
          Bnew(i)=rhss(i)
      enddo
      nrhs=1
      lda=n
      ldb=n
!Call to LAPACK.  LAPACK not included in listing. Obtained from
!www.netlib.org
      call DGESV( N, NRHS, Anew, LDA, IPIV, Bnew, LDB, INFO )
      print *,'   INFO=',info,n
      do i=1,n
          rhss(i)=bnew(i)
      enddo
      DEALLOCATE(Bnew,Anew , ipiv)
      return
      end
```

D.2.12 External Dependencies

Data 1

```
      common/d_1/cin_int(10,4000),cin_fro(10,4000)
     * ,cin_temp(10,4000),cin_org(10,5)
      common/d_2/cin_bin(10,4000),czero(10,4000)
      common/d_3/cin_del(10,4000),cold_del(10,4000)
      common/d_4/evalue(4000),dedx(4000),flux_del(20)
```

```
      common/d_5/ntimes,ninv
      common/d_6/phi_emax,emax,we,emax_lin(10),xi_o_w,xi_o_n
      common/d_7/B(20,20),D(20,20),H(20,20),HP(20,20)
      common/d_8/T(20,20),U(20,20),V(20,20)
      common/d_9/A_max(20,20),T_max(20,20),U_max(20,20)
      common/g_10/rhsnew(2000),rhs(2000),sol_del(2000)
      common/d_11/indx(2000),soltemp(2000)
      common/d_12/FV(20),GFV(2000)
      parameter(nmax=2000)
```

Geometry data

```
      common/g_1/vapp,telap
      common/g_2/por_ph_eq,corr,o2red
      common/g_3/g_coat,g_med,surface_del,ak_v
      common/g_4/dxi,dhx,dtsc,dtstep
      common/g_5/del_surf,fro_surf,aint_surf,bint_surf
      common/g_6/nodes,iut,imax_del,imax,nodes_total
      common/g_7/iun_con(5000),iun_new(2500),iut_new
      common/g_8/nodes_del,nodes_fro,nodes_int,nodes_bin
      common/g_9/j_del,j_fro,j_int,j_bin
      character*20 por_ph_eq,corr,o2red
      character line*80
```

System data

```
      common/s_1/nvar,nspec,npor,ina,icl,ioh,izn,iphi,ipor
      common/s_2/dif(40),con(40),difs(40),z(40),difs_org(40)
      common/s_3/specie
      common/s_4/dcsc,consc
      common/s_5/bulko2,difo2,difo2_org,ailimg_del(1000)
      common/s_6/fxoh(1500),fxzn(1500),fxo2(1500)
      common/s_7/cde(1500),phi_old(2000),anet(2000)
      common/s_8/sigma(2000),adiff(2000),phi_cal(2000)
      common/s_9/fx_specie(20,2700),ohmic(2700)
      common/s_10/ohm_mig(2700),ohm_dif(2700)
      common/s_11/chi_por,chi_na,chi_cl,chi_oh
      common/s_12/alambda_na_fro,alambda_cl_fro,alambda_oh_fro
      common/s_13/alambda_na_sem,alambda_cl_sem,alambda_oh_sem
      common/s_14/por_mouth,por_coat,var_coat
      common/s_15/b_por(10),b_alpha(10),b_omega(10),b_zeta(10)
      common/s_16/zeta(2000),alpha_o2(2000),omega(2000)
      common/s_17/por(2000),por_old(2000),akr(2000)
      common/s_18/var(2000),var_old(2000)
      character(12) specie(40)
!Setting values for parameters used in calculating the current
!density.
      parameter(eqpot_h2=-870.d0,beta_h2=132.d0,eqpot_fe=-475.d0
     *  ,beta_fe=62.6d0,zn_io=0.2d0
     *  ,eqpot_zn=-1004.d0,beta_zn=40.d0,eqpot_o2=-642.d0
     *  ,beta_o2=93.d0)
      parameter(far=96487.d0,gas=8.314d0,temp=298.d0)
!Faraday's constant=far  Gas constant=gas ; Temperature in
!Kelvin=temp
```

REFERENCES

1. G. Koch, M. Brongers, N. Thompson, Y. Virmani, and J. Payer, *Corrosion Cost and Preventive Strategies in the United States*, Technical report, CC Technologies Laboratories and NACE International, Dublin, OH and Houston, TX (2001).

2. G. M. Sabde, *Study of Current/Potential Distribution in a Cathodically Protected Crevice*, Ph.D. thesis, Clarkson University (1995).

3. D. T. Chin and G. M. Sabde, "Modeling Transport Process and Current Distribution in a Cathodically Protected Crevice," *Corrosion*, **56** (2000) 783–793.

4. F. M. Song, D. W. Kirk, J. W. Graydon, and D. E. Cormack, "Steel Corrosion under a Disbonded Coating with a Holiday-Part 1: The Model and Validation," *Corrosion*, **58** (2002) 1015–1024.

5. F. M. Song, D. W. Kirk, J. W. Graydon, and D. E. Cormack, "Steel Corrosion under a Disbonded Coating with a Holiday-Part 2: Corrosion Behavior," *Corrosion*, **59** (2003) 42–49.

6. A. Leng, H. Streckel, and M. Stratmann, "The Delamination of Polymeric Coatings from Steel. Part 2: First Stage of Delamination, Effect of type and Concentration of Cations on Delamination, Chemical Analysis of the Interface." *Corrosion Science*, **41** (1999) 579–597.

7. A. Leng, H. Streckel, and M. Stratmann, "The Delamination of Polymeric Coatings from Steel. Part 1: Calibration of the Kelvinprobe and Basic Delamination Mechanism." *Corrosion Science*, **41** (1999) 547–578.

8. A. Leng, H. Streckel, K. Hofmann, and M. Stratmann, "The Delamination of Polymeric Coatings from Steel. Part 3: Effect of the Oxygen Partial Pressure on the Delamination Reaction and Current Distribution at the Metal/Polymer Interface." *Corrosion Science*, **41** (1999) 599–620.

9. W. Furbeth and M. Stratmann, "The Delamination of Polymeric Coatings from Electrogalvanised Steel–A Mechanistic Approach. Part 1: Delamination from a Defect with Intact Zinc Layer." *Corrosion Science*, **43** (2001) 207–227.

10. W. Furbeth and M. Stratmann, "The Delamination of Polymeric Coatings from Electrogalvanised Steel–A Mechanistic Approach. Part 3: Delamination Kinetics and Influence of CO2." *Corrosion Science*, **43** (2001) 243–254.

11. W. Furbeth and M. Stratmann, "The Delamination of Polymeric Coatings from Electrogalvanised Steel–A Mechanistic Approach. Part 2: Delamination from a Defect down to Steel." *Corrosion Science*, **43** (2001) 229–241.

12. J. S. Newman, *Electrochemical Engineering*, 2nd edition (Englewood Cliffs, New Jersey: Prentice-Hall, 1991).

13. M. Watson and J. Postlethwaite, "Numerical Simulation of Crevice Corrosion of Stainless Steels and Nickel Alloys in Chloride Solutions," *Corrosion*, **46** (1990) 522–530.

14. M. Verhoff and R. Alkire, "Experimental and Modeling Studies of Single Pits on Pure Aluminum in pH 11 NaCl Solutions I. Lase Initiated Single Pits," *Journal of the Electrochemical Society*, **147** (2000) 1349–1358.

15. M. Verhoff and R. Alkire, "Experimental and Modeling Studies of Single Corrosion Pits on Pure Aluminum in pH 11 NaCl Solutions II. Pit Stability," *Journal of the Electrochemical Society*, **147** (2000) 1359–1365.

16. J. N. Harb and R. C. Alkire, "Transport and Reaction During Pitting Corrosion of Ni in 0.5M NaCl I. Stagnant Fliud," *Journal of the Electrochemical Society*, **138** (1991) 2594–2600.

17. S. M. Sharland and P. W. Tasker, "A Mathematical Model of Crevice and Pitting Corrosion-I. The Physical Model," *Corrosion Science*, **28** (1988) 603–620.

18. M. W. Verbrugge, D. Baker, and J. Newman, "Reaction Distribution in a Corroding Pit," *Electrochimica Acta*, **38** (1993) 1649–1659.

19. A. J. Bard and L. R. Faulkner, *Electrochemical Methods* (New York, New York: John Wiley & Sons, Inc., 1980).

20. J. C. Walton, G. Cragnolino, and S. K. Kalandros, "A Numerical Model of Crevice Corrosion for Passive and Active Metals," *Corrosion Science*, **38** (1996) 1–18.

21. M. Orazem, J. Esteban, K. Kenelley, and R. Degerstedt, "Mathematical Models for Cathodic Protection of an Underground Pipeline with Coating Holidays: Part 1–Theoretical Development," *Corrosion*, **53** (1997) 264–272.

22. J. R. Davis, editor, *Corrosion: Understanding the Basics* (Materials Park, Ohio: ASM International, 2000).

23. K. Nisancioglu, "Predicting the Time Dependence of Polarization on Cathodically Protected Steel in Seawater," *Corrosion*, **43** (1987) 100–111.

24. M. Orazem and J. Esteban, *A Three-Dimensional Model for the Cathodic Protection of an Underground Pipeline*, Final report to the Alyeska Pipeline Service Company, University of Florida, Gainesville, Fl (1994).

25. G. Williams and H. McMurray, "Chromate Inhibition of Corrosion-Driven Organic Coating Delamination Studied Using a Scanning Kelvin Probe Technique," *Journal of the Electrochemical Society*, **148** (2001) B377–B385.

26. D. W. G. Williams, H.N. McMurray, "Cerium(III) Inhibition of Corrosion-Driven Organic Coating Delamination Studied Using a Scanning Kelvin Probe Technique," *Journal of the Electrochemical Society*, **149** (2002) B154–B162.

27. E. Mulder, "A Testing Time," *World Pipelines*, **3** (2003) 39–42.

28. K. Kennelley, L. Bone, and M. Orazem, "Current and Potential Distribution on a Coated Pipeline with Holidays Part I–Model and Experimental Verification." *Corrosion*, **49** (1993) 199–210.

29. M. E. Orazem, K. J. Kennelley, and L. Bone, "Current and Potential Distribution on a Coated Pipeline with Holidays: 2. A Comparison of the Effects of Discrete and Distributed Holidays," *Corrosion*, **49** (1993) 211–219.

30. M. E. Orazem, J. M. Esteban, K. J. Kennelley, and R. M. Degerstedt, "Mathematical Models for Cathodic Protection of an Underground Pipeline with Coating Holidays: 2. Case Studies of Parallel Anode CP Systems," *Corrosion*, **53** (1997) 427–436.

31. D. Riemer and M. Orazem, "Cathodic Protection of Multiple Pipelines with Coating Holidays," in *Procedings of the NACE99 Topical Research Symposium: Cathodic Protection: Modeling and Experiment*, M. E. Orazem, editor, NACE (Houston, TX: NACE International, 1999) 65–81.

32. D. Riemer and M. Orazem, "Development of Mathematical Models for Cathodic Protection of Multiple Pipelines in a Right of Way," in *Proceedings of the 1998 International Gas Research Conference*, Gas Research Institute (Chicago, Illinois: Gas Research Institute, 1998) 117. Paper TSO-19.

33. D. P. Riemer, *Modeling Cathodic Protection for Pipeline Networks*, Ph.D. dissertation, University of Florida, Gainesville, FL (2000).

34. A. Turnbull, "Modeling of Crack Chemistry in Sensitized Stainless Steel in Boiling Water Reactor Environments," *Corrosion Science*, **39** (1997) 789–805.

35. S. M. Sharland, "A Review of the Theoretical Modelling of Crevice and Pitting Corrosion," *Corrosion Science*, **27** (1987) 289–323.

36. A. Turnbull, *Review of Modelling of Pit Propagation Kinetics*, NPL DMM(A)65, National Physical Laboratory, Middlesex, England (1992).

37. N. Sridhar, D. S. Dunn, and M. Seth, "Application of a General Reactive Transport Model to Predict Environment Under Disbonded Coatings," *Corrosion*, **57** (2001) 598–613.

38. N. J. Laycock and S. P. White, "Computer Simulation of Single Pit Propagation in Stainless Steel under Potentiostatic Control," *Journal of the Electrochemical Society*, **148** (2001) B264–B275.

39. J. Newman, D. N. Hanson, and K. Vetter, "Potential Distribution in a Corroding Pit," *Electrochimica Acta*, **22** (1977) 829–831.

40. B. Pillay and J. Newman, "Modeling Diffusion and Migration in Dilute Electrochemical Systems Using the Quasipotential Transformation," *Journal of the Electrochemical Society*, **140** (1993) 414–420.

41. M. W. Verbrugge, D. R. Baker, and J. Newman, "Dependent-Variable Transformation for the Treatment of Diffusion, Migration, and Homogeneous Reactions," *Journal of the Electrochemical Society*, **140** (1993) 2530.

42. J. W. Tester and H. S. Isaacs, "Diffusional Effects in Simulated Localized Corrosion," *Journal of the Electrochemical Society*, **122** (1975) 1438–1445.

43. R. Alkire and D. Siitari, "The Location of Cathodic Reaction during Localized Corrosion," *Journal of the Electrochemical Society*, **126** (1979) 15–22.

44. S. M. Gravano and J. R. Galvele, "Transport Processes in Passivity Breakdown–III. Full Hydrolysis Plus Ion Migration Plus Buffers," *Corrosion Science*, **24** (1984) 517–534.

45. J. R. Galvele, "Transport Processes and the Mechanism of Pitting of Metals," *Journal of the Electrochemical Society*, **123** (1976) 464–474.

46. J. R. Galvele, "Transport Processes in Passivity Breakdown–II. Ful Hydrolysis of the Metal Ions," *Corrosion Science*, **21** (1981) 551–579.

47. S. M. Sharland, "A Mathematical Model of Crevice and Pitting Corrosion–II. The Mathematical Solution," *Corrosion Science*, **28** (1988) 621–630.

48. A. Turnbull and J. G. N. Thomas, "A Model of Crack Electrochemistry for Steels in the Active State Based on Mass Transport by Diffusion and Ion Migration," *Journal of the Electrochemical Society*, **129** (1982) 1412–1422.

49. S. M. Sharland, C. P. Jackson, and A. J. Diver, "A Finite-element Model of the Propogation of Corrosion Crevices and Pits," *Corrosion Science*, **29** (1989) 1149–1166.

50. S. M. Sharland, "A Mathematical Model of the Initiation of Crevice Corrosion in Metals," *Corrosion Science*, **33** (1992) 183–201.

51. M. M. Pariona and I. L. Muller, "Numerical Simulation and Factorial Design of Titanium Crevice Corrosion in Sodium Chloride Solution," *Computers Chemical*, **22** (1998) 377–384.

52. A. Turnbull and D. H. Ferris, "Mathematical Modeling of the Electrochemistry in Corrosion Fatigue Cracks in Structural Steel Cathodically Protected in Sea Water," *Corrosion Science*, **26** (1986) 601–628.

53. "LAPACK," (accessed November 2, 2000). Linear algebra package source code. www.netlib.org/lapack.

54. "BLAS," (accessed November 2, 2000). Basic linear algebra subprograms source code. www.netlib.org/blas.

55. "Tectran Version 1.0," (1999). Developed by N.Sridhar, Center for Nuclear Waste Regulatory Analyses, Southwest Research Institute, San Antonio, Texas.

56. K. Grasshoff, *Marine Electrochemistry* (New York, New York: John Wiley and Sons, 1981) 327–420.

57. D. T. Chin and G. M. Sabde, "Current Distribution and Electrochemical Environment in a Cathodically Protected Crevice," *Corrosion*, **55** (1999) 229–237.

58. J. J. Perdomo and I. Song, "Chemical and electrochemical conditions on steel under disbonded coatings: the effect of applied potential, solution resitivity, crevice thickness and holiday size," *Corrosion Science*, **42** (2000) 1389–1415.

59. F. G. Zhengfeng Li and X. Mao, "A study on cathodic protection against crevice corrosion in dilute NaCl solutions," *Corrosion Science*, **44** (2002) 689–701.

60. R. Brousseau and S. Qian, "Distribution of Steady-State Cathodic Currents Underneath a Disbonded Coating," *Corrosion Science*, **50** (1994) 907–911.

61. W. H. Press, S. A. Teukolsky, W. T. Vetterling, and B. P. Flannery, *Numerical Recipes in Fortran 77*, 2nd edition (Cambridge, UK: Press Syndicate of the University of Cambridge, 1992).

62. D. R. Baker, M. W. Verbrugge, and J. Newman, "A Transformation for the Treatment of Diffusion and Migration. Application to Stationary Disk and Hemispherical Electrodes," *Journal of Electroanalytic Chemistry*, **314** (1991) 23–44.

63. D. R. Baker, "Reducing Nonlinear Systems of Transport Equations to Laplace's Equation," *SIAM Journal of Applied Math*, **53** (1993) 419–439.

64. A. C. West, "Comparison of Modeling Approaches for a Porous Salt Film," *Journal of the Electrochemical Society*, **140** (1993) 403–408.

65. B. Pillay, *Development and Application of the Quasi-Potential Transformation*, Master's thesis, University of California, Berkeley, California (1992).

66. G. Engelhardt, D. D. MacDonald, and M. Urquidi-Macdonald, "A Simplified Method for Estimating Corrosion Cavity Growth Rates," *Corrosion Science*, **39** (1997) 419–441.

67. E. Kreyszig, *Advanced Engineering Mathematics* (New York, New York: John Wiley and Sons, Inc, 1988).

68. J. W. Gibbs, *The Scientific Papers Volume II* (New York, New York: Dover, 1961).

69. H. Leidheiser Jr., "Corrosion of Painted Metals-A Review," *Corrosion*, **38** (1982) 374–383.

70. S. U. and J. I. Skar, "Factors Influencing the Rate of Cathodic Disbonding of Coatings," *Corrosion*, **50** (1994) 934–939.

71. H. Leidheiser and W. Wang, "Some Substrate and Environmental Influences on the Cathodic Delamination of Organic Coatings," *Journal of Coatings Technology*, **53** (1981) 77–84.

72. A. A. Korzhenko, G. S. Shapoval, and A. A. Pud, "Investigation of Processes Occurring at the Metal/Polymer Coating/Electrolyte Interface," *Journal of Adhesion*, **71** (1999) 55–80.

73. J. D. W. R. D. Armstrong, B. W. Johnson, "An Investigation into the Cathodic Delamination of Epoxy-Polyamine Protective Coatings," *Electrochimica Acta*, **36** (1991) 1915–1923.

74. H. Leidheiser, "Mechanisms of De-adhesion of Organic Coatings from Metal Surfaces," in *Polymeric Materials for Corrosion Control*, R. A. Dickie and F. L. Floyd, editors, ACS Symposium Series 322 (Washington, DC: American Chemical Society, 1986) 124–135.

75. G. Grundmeier, C. Reinartz, M. Rohwerder, and M. Stratmann, "Corrosion Properties of Chemically Modefied Metal Surfaces," *Electrochemica Acta*, **43** (1997) 165.

76. J. S. Thornton, J. F. Cartier, and R. W. Thomas, "Cathodic Delamination of Protective Coatings: Cause and Control," in *Polymeric Materials for Corrosion Control*, R. A. Dickie and F. L. Floyd, editors, ACS Symposium Series 322 (Washington, DC: American Chemical Society, 1986) 169–179.

77. R. A. Dickie, "Chemical Studies of the Organic Coating-Steel Interface After Exposure to Aggressive Environments," in *Polymeric Materials for Corrosion Control*, R. A. Dickie and F. L. Floyd, editors, ACS Symposium Series 322 (Washington, DC: American Chemical Society, 1986) 136–154.

78. W. W. and L. H., "A Model for the Quantitative Interpretation of Cathodic Delamination," *Journal of the Electrochemical Society*, **131** (1984) 300C. Abstract.

79. D. A. Jones, *Principles and Prevention of Corrosion* (Upper Saddle River, New Jersey: Prentice Hall, 1996).

80. S. L. Carson and M. E. Orazem, "Time-Dependent Polarization of Behavior of Pipeline-Grade in Low Ionic Strength Environments," *Journal of Applied Electrochemistry*, **29** (1999) 703–717.

81. J. Wu, V. Srinivasan, J. Xu, and C. Y. Wang, "Newton-Krylov-Multigrid Algorithms for Battery Simulation," *Journal of the Electrochemical Society*, **149** (2002) A1342–A1348.

82. T. Duan, J. W. Weidner, and R. E. White, "Extension of Newman's Method to Electrochemical Reaction-Diffusion in a Fule Cell Catlyst Layer," *Journal of Power Sources*, (2002) 24–33.

83. P. M. Gomadam, J. W. Weidner, R. A. Dougal, and R. E. White, "Mathematical Modeling of Lithium-ion and Nickel Battery Systems," *Journal of Power Sources*, **110** (2002) 267–284.

84. J. Stoer and R. Bulirsch, *Introduction to Numerical Amalysis*, volume 12 (New York, New York: Springer-Verlag, 1992).

85. G. Zhnang, *Corrosion and Electrochemistry of Zinc* (New York, New York: Plenum Press, 1996).

86. E. G. Webb and R. C. Alkire, "Pit Initiation at Single Sulfide Inclusions in Stainless Steel III. Mathematical Model," *Journal of the Electrochemical Society*, **149** (2002) B286–B295.

BIOGRAPHICAL SKETCH

Kerry Neil Allahar grew up in Trinidad and Tobago as part of a family of five boys, a school-teacher father, and a housewife mother. He and his brothers attended Presentation College in San Fernando, Trinidad, for their secondary school education. He received a Bachelor of Science degree in chemical and process engineering from the University of the West Indies in 1994. Kerry's grandmother helped him and his family to migrate to the United States where Kerry used the opportunity to pursue graduate school. He began reading for a doctoral degree in chemical engineering in the fall of 1997 at the University of Florida where he was advised by Professor Mark E. Orazem. He graduated in the fall of 2003 after spending the previous six years being educated in chemical and electrochemical engineering and the mathematical modeling of electrochemical systems.